On the Evolution of Planetesimals in Post-Main-Sequence Planetary Systems

by

Catriona Heather McDonald

Thesis

Submitted to the University of Warwick

for the degree of

Doctor of Philosophy

Department of Physics

June 2023

THE UNIVERSITY OF WARWICK

Contents

List of Tables

List of Figures

Acknowledgments

Firstly, I would like to thank my supervisor Dimitri Veras whose support and patience has been instrumental in helping me become the scientist I am today. The last four years have had their challenges, and although we were unable to meet in person for over 500 days, every single science discussion filled me with ideas, enthusiasm and excitement which spurred me on.

The Astronomy & Astrophysics group at Warwick provided a warm and supportive environment for which I will be forever grateful. Special thanks are needed for those who have guided me in my studies; Farzana Meru, Tom Marsh, and Grant Kennedy. Every one of my office mates have made each day a delight through fun distractions, Nerf battles and relentless kindness and support. I am incredibly grateful for all of you, especially Tom, Evie, Rebecca, Pat, and Azib.

Thank you to my friends who have been with me every step of the way cheering me on and reminding me to smile; Lizzie, Leia, Adam, Sam and Tom, and many others.

I owe endless amounts of gratitude to my family, especially my parents and grandparents, for always believing in me even when I didn't believe in myself.

And finally, thank you Will, for filling my days with more love and laughter than I could ever ask for and being so patient and supportive over the last few months.

Declarations

This thesis is submitted to the University of Warwick for the degree of Doctor of Philosophy. I confirm that all work is my own unless otherwise stated and has not been previously submitted for another degree.

A significant amount of this work has been previously published in peer-reviewed journals, in particular;

- Chapter 2 is a reproduction of McDonald and Veras [2021],
- Chapter 3 is a reproduction of McDonald and Veras [2023].

Chapter 2 was prepared in collaboration with D. Veras who derived and produced text surrounding the analytic white dwarf cooling age relation presented in Section 2.2. Further, the discussion around disc lifetimes in Section 2.5 was produced by D. Veras. All other work and writing in this chapter were carried out by myself.

Chapters 3 and 4 were produced in collaboration with D. Veras and A. Bonsor respectively. Although the work was furthered by discussions with these collaborators, all work and writing were produced exclusively by myself.

Abstract

White dwarfs provide unique opportunities to characterize the chemical and architectural diversity of exoplanetary systems. The accretion of planetary material by white dwarfs can allow inferences to be made about the chemical compositions, formation and dynamical evolution of exoplanetary bodies. This thesis aims to contribute to the growing literature surrounding white dwarf planetary systems by exploring the processes that deliver planetary material to white dwarfs.

Firstly, I show how using triaxial ellipsoidal shape models instead of spheres affects the evolution of an asteroid directly approaching a white dwarf. The presented analytic model considers tidal forces from the star, sublimation, and self-gravitation and internal strength of the asteroid to determine how the body disrupts. The model finds that highly elongated asteroids are most susceptible to sublimation and hence predicts there should be vast expanses of gaseous material around white dwarfs with debris discs.

The significant binary fraction of asteroids in the Solar System next motivates a numerical study into the scattering of binary asteroids around white dwarfs. I use simulations to explore how Kuiper Belt analogues with equal-mass binary systems evolve under the influence of planets. Largely, asteroid binarity does not effect the rate at which planetesimals are delivered towards the star, but does influence the architectures of planetesimal reservoirs and could produce interstellar asteroids.

Finally, I present a preliminary model for the tidal migration of a giant planet towards a close orbit around a white dwarf and the effect this has on planetesimals in the system. Results show that the planet's motion efficiently ejects planetesimals from the system, unless they are deeply captured in mean motion resonances. This suggests that the majority of future white dwarfs observed with close planetary companions may not show atmospheric pollution.

Chapter 1

Introduction

The majority of Earth's closest neighbours in the Solar System are bright enough in the night sky to be observed by the naked eye and have long been known as planets similar to our own. Over hundreds of years of dedicated study through telescopes and more recently space missions, the Solar System remains the best studied and understood example of a planetary system and is largely the starting point for all of our planetary knowledge to date.

The Solar System

The Sun is a $\sim$ 4 Gyr G2 type star about halfway through its main sequence lifetime, and will remain in relative stability for the next $\sim$ 6 billion years. After the Sun formed from a rapidly spinning cloud of material, the remnant material formed a protoplanetary disc. The subsequent planet formation within the solar protoplanetary disc created a clearly structured and defined planetary system, which has been further sculpted by dynamical processes in the many years since. Figure 1.1 shows a schematic depiction of the Solar System's structure and is further discussed below.

The very inner region of the planetary system in the range $0.3 - 1.7$ au, is inhabited by the rocky, terrestrial planets; Mercury, Venus, Earth, and Mars, whose orbits are shown by black lines in the left hand panel of Figure 1.1. These planets show a startling diversity in terms of size, surface features and atmospheric conditions. They range from the tiny tidally locked Mercury to the green and life-abundant Earth.

Past the orbit of Mars, we encounter the first large population of Solar System planetesimals in the form of the Main Belt. This region between $\sim 2 - 4.3$ au contains a very large number of small bodies ($>$ 500 000 are currently recorded in the Minor Planet Center database[1] [Wood, 2019]) and is shown by the blue region in the left hand panel of Figure 1.1. These rocky planetesimals are thought to be the remnant building blocks of planet formation which failed to accrete onto a larger body. The majority of bodies in the

[1] https://www.minorplanetcenter.net/iau/MPCORB.html

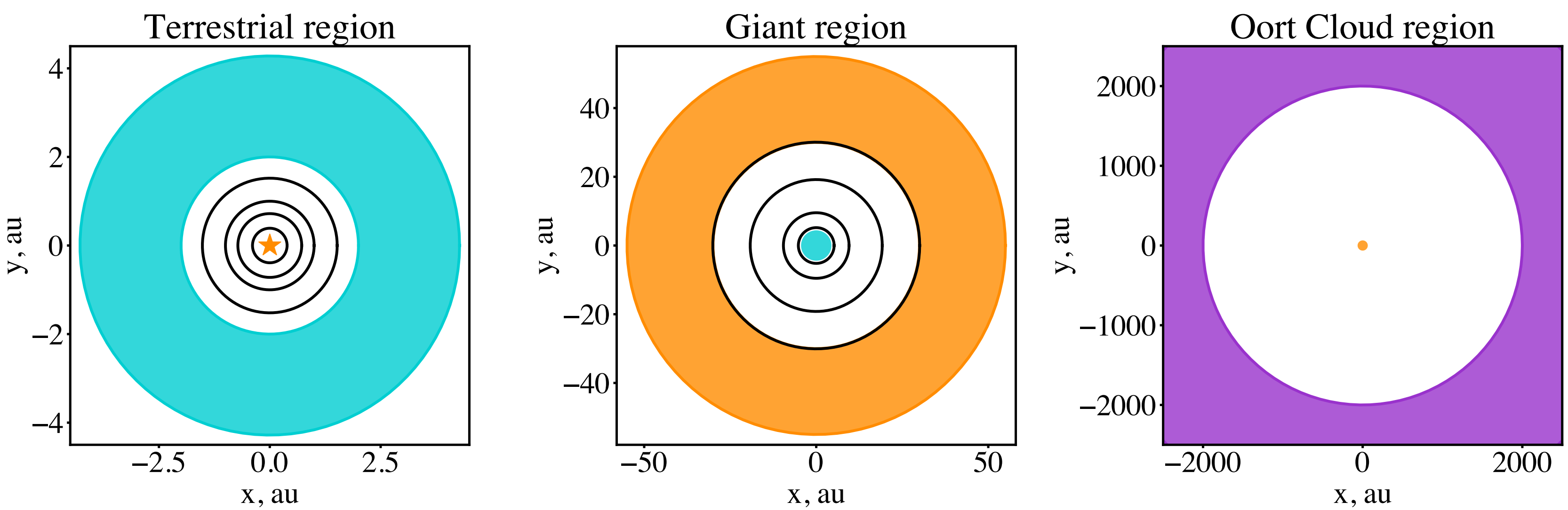

Figure 1.1: The structure of the Solar System. In the left-most panel we start with the inner Solar System, the Sun is indicated by a orange star at the centre of the plot, the four terrestrial planet's orbits are shown by black circles and the approximate region of the Main Belt is shown in blue. The middle panel shows the region occupied by the giant planets whose orbits are again shown in black. The Kuiper Belt region is highlighted in orange here expanding from 30 au to 50 au, the inner boundary of which coincides with the orbit of Neptune. The inner region as shown in the left hand panel is shown by the blue shaded circle at the centre of the middle panel. Finally, in the right hand panel the approximate inner boundary for the Oort Cloud is shown by the purple shaded region, I do not show the outer boundary as this has been theorised to extend out to 100 000 au. The shaded orange region at the centre of this panel encompassses the entirety of the other two panels.

Main Belt are asteroids, in that they are rocky bodies which largely show no activity from sublimating volatiles which would be more indicative of a cometary body.

Next, we encounter the giant planets; Jupiter, Saturn, Uranus and Neptune in the region 5 – 30 au, whose orbits are shown in the centre panel of Figure 1.1. Like the terrestrial planets, the giants show a similar diversity in physical, and orbital, properties. However, they can be largely thought of as being composed of a core of rocky material with a surrounding envelope of gaseous and/or volatile rich material.

Past the giant planets, in the region $\sim 30 - 55$ au [Wood, 2019] we reach the next large population of planetesimals, the Kuiper Belt, shown in orange in the centre panel of Figure 1.1. This population differs from the Main Belt. Firstly, a significant proportion of the Kuiper Belt is thought to be pristine, in that it has remained unprocessed during the Solar System's history and so retains its properties from formation. Secondly, because the planetesimals formed at larger distances from the Sun, the Kuiper Belt's composition is much more volatile rich and icy as they formed beyond many chemical species ice lines (the radial location where the temperature is low enough for gaseous material to condense).

Moving even further out, we reach the Oort Cloud, a tenuous collection of planetesimals in a spherical halo around the Solar System [Oort, 1950], whose inner boundary is depicted in purple in the right hand panel of Figure 1.1. The Oort Cloud is thought to be the origin of long period comets with extremely large semi-major axes on the order of 50 000 au [e.g Fouchard et al., 2014] and could extend out to 100 000 au.

Exoplanetary Systems

Although the existence of the Solar System planets has been known for millennia, the discovery of the first planets outside of our Solar System (so called exoplanets) came in 1992, when two roughly Earth-sized planets were identified orbiting around the pulsar PSR1257+12 [Wolszczan and Frail, 1992]. A signal from a third, moon-sized planet around PSR1257+12 was discovered in 1994 [Wolszczan, 1994]. These planets orbiting around a pulsar, which represents the final stages of a large stars life, provided tantalising evidence for planets around stars like our Sun and beyond.

The first exoplanet discovered around a solar-like star, 51 Pegasi, was confirmed in 1995 [Mayor and Queloz, 1995]. 51 Peg b was discovered by observing Doppler shift in the star's spectrum caused by the planetary mass affecting the orbit of the star, a method now known as Doppler radial velocity. The planet was identified to be roughly the size of Jupiter, but in an orbit closer than that of Mercury. As of 27th April 2023, astronomers around the world have now worked together to confirm the existence of 5338 planets outside of our Solar System[2]. We are quickly discovering a diverse demographic of planets, many of which are unlike anything we have seen in the Solar System.

[2] As collated by the NASA Exoplanet Archive https://exoplanetarchive.ipac.caltech.edu/

Thus, there is a rich and rapidly expanding field of study surrounding exoplanets, through their formation around fledgling stars all the way to their demise around the dying embers of their stars.

This thesis focusses on the evolution of planetesimals around white dwarfs, the dying remnants of intermediate mass stars. In order to fully motivate this area of research, we first need to take a step back in time and interrogate our current knowledge of planetary systems throughout the evolution of their stars.

1.1 The Main Sequence

1.1.1 Stellar Properties and Evoltuion

As stars evolve they undergo changes in luminosity, temperature, size and internal structure. An entire star's evolution can be shown on a Hertzsprung-Russell (HR) diagram such as in Figure 1.2.

The Zero-Age-Main-Sequence (ZAMS) as seen in the HR diagram is the point where a star begins fusing hydrogen into helium. From that point until the hydrogen supply is depleted, a star is said to be on the main sequence. The majority of stars in the Milky Way are evolving on the main sequence and most will spend a large fraction of their lives in this phase of core hydrogen burning.

For stars that are much smaller than the Sun ($M < 0.3 M_\odot$), the energy produced by nuclear reactions in the core are transported outwards by convection, while stars that are more massive develop convective cores while their stellar envelopes remain in radiative equilibrium [Prialnik, 2000]. During all phases of stellar evolution, stars lose mass through stellar winds occurring at their surface (a process which will be discussed further in Section 1.2). Mass loss rates increase with stellar mass [Prialnik, 2000], but only a relatively negligible amount is lost during the main sequence. Main sequence stars will continue quiescently fusing hydrogen to helium in their cores until this fuel reservoir is depleted, at which point they evolve onto the giant branch phases of evolution (see Section 1.2). The amount of time that a star will spend on the main sequence is heavily dependent on the stellar mass, with more massive stars exhausting their fuel reserves sooner.

In the following work, I only consider the evolution of intermediate mass stars ($0.7 M_\odot \lesssim M \lesssim 8 M_\odot$) which will end their lives as white dwarfs.

1.1.2 Planetary Systems

The planets we have so far observed around main sequence stars display a startling variety of sizes, masses and orbital locations compared to the planets of the Solar System. Figure 1.3 shows the distribution in orbital period and mass space for 2170 exoplanets discovered prior to 2023. The Solar System planets are shown by large, labelled orange markers, and the

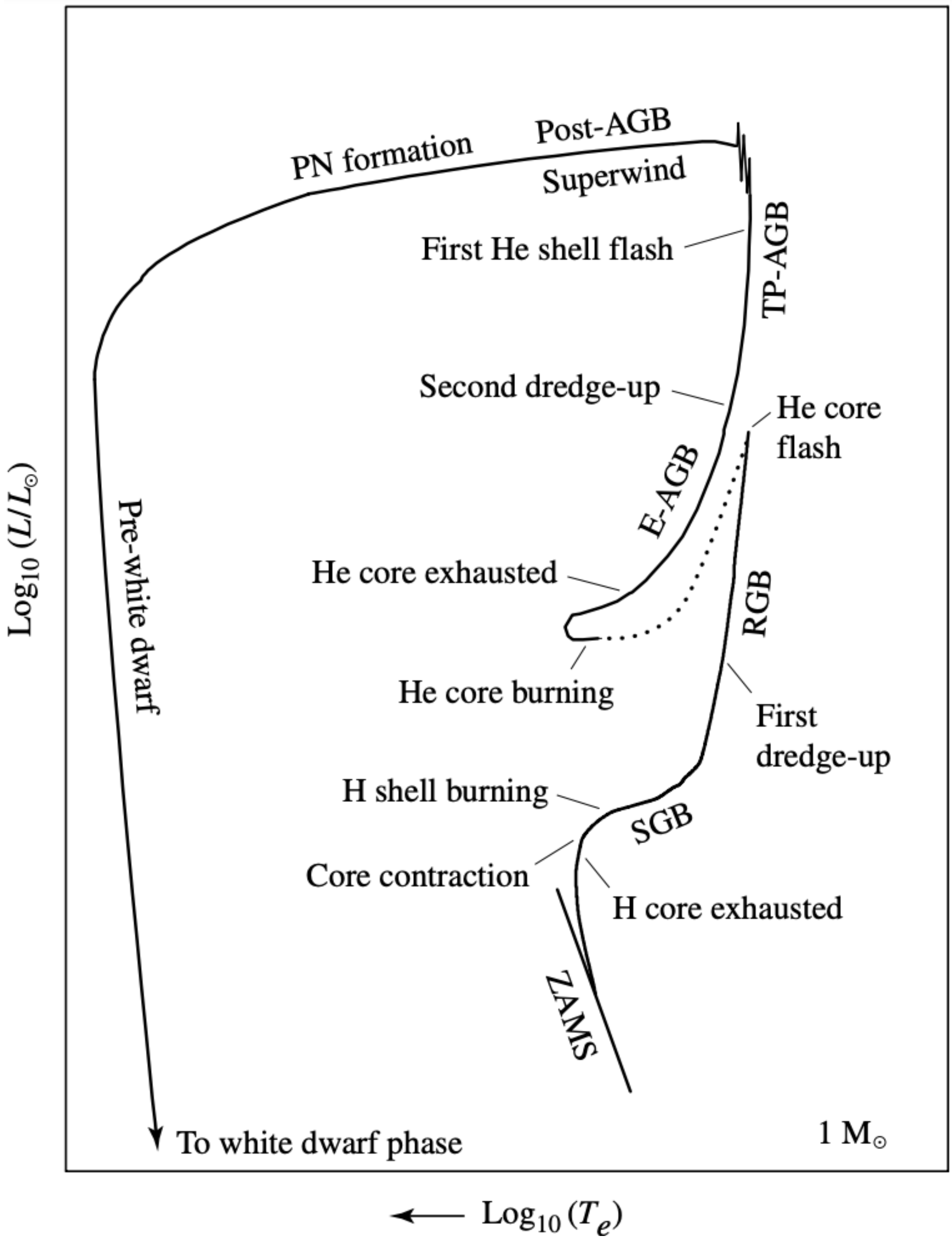

Figure 1.2: A schematic Hertzsprung-Russell diagram depicting the temperature and luminosity evolution of a $1M_\odot$ star from the zero-age-main-sequence (ZAMS), sub- and red-giant branches (SGB, RGB respectively), the various stages of the asymptotic giant branch (AGB), before finally evolving into a white dwarf. Figure is taken from Chapter 13 of Carroll and Ostlie [2013].

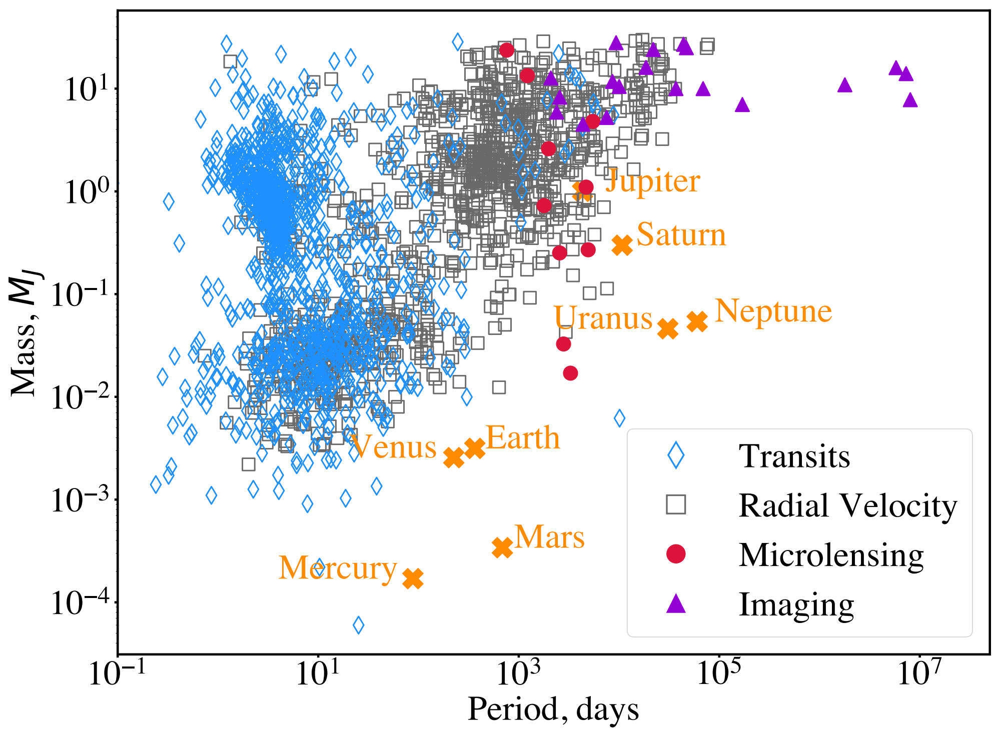

Figure 1.3: Period and masses for a subset of 2170 exoplanets discovered and characterized as of May 2023. The location of the Solar System planets are shown in large, labelled orange markers. The remaining markers, which denote the observed exoplanets, are described in the legend and indicate which observational technique detected them. The clustering of different coloured markers indicate the observational limitations of each detection method. The data used to create this plot was downloaded from the NASA Exoplanet Archive `https://exoplanetarchive.ipac.caltech.edu/`.

smaller markers indicate the detection method used in finding the planets as described in the legend. There has been no true analogue for many of the Solar System planets yet discovered.

The first hint that the Solar System may not be the archetype of all planetary systems came with the discovery of the first planet around a solar-like star, 51 Pegasi b [Mayor and Queloz, 1995]. Although this planet has a roughly similar mass and size to Jupiter, it orbits at a semi-major axis of ~ 0.052 au, well within the Solar System orbit of Mercury and outside of the region where we think Jupiter-sized planets could have formed. Thus, this became the prototype 'hot Jupiter', so called due to their Jupiter-like size ($0.25M_{\rm J} < M \lesssim 13M_{\rm J}$) and their small orbital periods ($P < 10$ days) which puts the surface temperatures at extremely high values [see Dawson and Johnson 2018 for a recent review of Hot Jupiters and Chapter 4 for further discussion].

The discovery of 51 Peg b signified the oncoming onslaught of exoplanet discoveries and the development of a number of discovery techniques which are represented by different markers in Figure 1.3. Each of these techniques favours a different region of space, which is seen by the clustered points in the figure and is hence best at discovering a particular type of planet. The main techniques are briefly described below.

Transit Photometry

The transit photometry technique has massively contributed to the population of known exoplanets thanks to dedicated telescopes such as the Wide Angle Search for Planets (WASP) [Pollacco et al., 2006] and space missions such as *Kepler* [Borucki et al., 2010; Howell et al., 2014] and TESS [Ricker et al., 2015].

The technique involves monitoring a star's brightness and identifying small dips in the incoming flux caused by a planet passing between the observer and the star. Thus, by necessity the planetary system has to be roughly edge-on to the observer for detection. Further, the technique favours the discovery of planets where the ratio between the star and planet size is large such that a measurable amount of flux is blocked during the transit.

The first planet observed via the transit technique was reported in Henry et al. [2000] in the system HD2094586 and described as '51 Peg-like', with a suspected mass of $0.62M_{\rm J}$ and similarly close in orbit.

Doppler Radial Velocity

The Doppler radial velocity technique was behind the discovery of 51 Peg b [Mayor and Queloz, 1995]. The technique exploits the fact that a planetary system collectively orbits around its combined centre of mass, thus stars which have planets can be observed to 'wobble' as the system's centre of mass is not at the centre of the star. As the star then orbits, we can observe red- and blue-shifted light from its motion. Constraints on the planet mass can be found from the radial velocity measurements, although the value is degenerate with inclination.

This method of exoplanet detection is most reliable for large planets, which will significantly shift the centre of mass of the system, and whose signature are easily distinguished from those produced from stellar activity.

Direct Imaging

The ability to directly detect and image an exoplanet is made difficult by the bright light of the central star obscuring the region around it. Coronagraphs which block the light from the central star can allow us to directly detect planets themselves. This process is made more difficult by atmospheric fluctuations and instrumental aberrations which introduce diffracted and scattered light to observations. As the central regions around the star are obscured, a planet has to be sufficiently far from the star to be directly imaged. Further, the planet still needs to be bright in order to stand out. The brightness of the planet can be enhanced by either having a sufficient albedo to reflect enough starlight, or by having an internal heat source such as in young planets actively contracting after formation.

Thus, direct imaging is most effective at observing very large, young planets on wide orbits.

Microlensing

Microlensing exploits the gravitational lensing effect, where a massive foreground object acts as a lens and bends the light from a distant source behind it. This acts to magnify the light of the source star and produce a brightening event. If the lens star hosts a planet, then the observed brightening is accompanied by a smaller, additional brightening caused by the planet.

This method can allow planets to be detected outside of the local Solar neighbourhood, both in the Milky Way and possibly beyond. Microlensing is sensitive to much lower mass planets than other detection methods and thus can help probe a new area of planetary parameters. However, the nature of microlensing events precludes follow up observations of the systems which would allow further characterisation of the planetary bodies.

The upcoming Nancy Grace Roman Space Telescope is predicted to find ~ 1000 microlensing exoplanets with masses larger than $0.02M_{\oplus}$ [Penny et al., 2019; Wilson et al., 2023].

Astrometry

The astrometric method of planetary detection relies on detecting the movement of the star on the background sky, and precisely identifying the component of that motion caused by the motion of the star around the centre of mass of its planetary system. If the astrometric proper motion and parallax are combined with radial velocity measurements to provide line of sight motion from the star, then we are able to determine the full 3D orbits of the system.

Although to date there have been no confirmed planet discoveries using astrometry due to observational difficulties, upcoming data releases from the *Gaia* space telescope are expected to provide such exquisite astrometric data it will allow for the detection of tens of thousands of high mass, long period planets [Perryman et al., 2014].

Debris Discs

Alongside the plethora of planets discovered around main sequence stars, we are also able to observe another important aspect of planetary systems around other stars - debris discs. Planet formation begins in protoplanetary discs with the formation of large numbers of planetesimals, which are small conglomerations of dusty material. While largely these planetesimals are subsumed into the growing planets, a significant amount of planetesimals are left in reservoirs spread throughout the system. Planetesimals are small collections of rock, dust and ice held together by self-gravity in aspherical shapes. As a consequence of their loose physical structure, the bodies show a large variety of densities and porosities [e.g. Carry, 2012].

In the Solar System, these planetesimals can be seen in the reservoirs of the Main Belt and Kuiper Belt. These two reservoirs generally present as chemically different, with the Kuiper Belt possessing more icy, volatile rich material than the mostly dry, rocky bodies of the Main Belt.

Just after formation, while the planetesimal reservoirs are abundant in material, frequent collisions will produce fresh dust, gas and smaller body fragments. These fragments can then go on to collide themselves, initiating a collisional cascade [Kenyon and Bromley, 2017a,b]. Over the disc's lifetime, the material begins to deplete as planetesimals are ground into dust, and dust and gas are removed from the system through processes such as stellar winds, Poynting-Robinson drag and radiation pressure (discussed further in Sections 1.2 and 1.3.2). This remnant material and intact planetesimals persist around main sequence stars as observable debris discs.

The simplest way to observe debris discs is to identify unresolved infrared flux which is above that expected from the star itself, and hence is known as an infrared (IR) excess. We identify these IR excesses by measuring the spectral energy distribution (SED) for the star, which is the distribution of energy emitted by an object across the electromagnetic spectrum. As we can generally model a stellar spectrum as a black body, if we observe a second black body 'hump' at cooler temperatures, this IR excess can be attributed to circumstellar material. There are a number of observational limitations to detecting debris discs around other stars, with more massive and brighly illuminated discs being easier to identify.

Although there are difficulties in observing debris discs, concerted efforts to observe the most massive debris discs can allow us to put some constraints on their occurrence. Massive debris discs were observed via IR excesses around 33 ± 5 per cent of a sample of A-type stars using Spitzer [Su et al., 2006]. Moving to the less massive FGK solar-like stars, the Herschel DEBRIS survey which carried out observations of an unbiased sample of 275 nearby FGK stars had a total detection rate of 17.1 ± 2.4 per cent, with the individual rates descending with spectral type [Sibthorpe et al., 2018]. At even lower stellar masses, the observation rate of debris discs falls even further, with some surveys observing no IR excesses [Gautier et al., 2007], and the Herschel DEBRIS survey observing only two M-dwarf debris discs with an occurrence rate of just $2.2^{+3.4}_{-2.0}$ per cent [Lestrade et al., 2012; Kennedy et al., 2014]. Both Moro-Martín et al. [2015] and Yelverton et al. [2020] find no significant correlation between the existence of planets and debris discs.

Thus, even though we are observationally restricted to detecting the most massive debris discs, a substantial number are detected around massive stars. It is not unreasonable to consider that less massive debris discs are more ubiquitous than suggested by their observations.

1.2 The Giant Branches

1.2.1 Stellar Properties and Evolution

Once a main sequence star has exhausted its supply of hydrogen, it moves onto the giant branch phases of evolution as shown in Figure 1.2.

For stars that are more massive than $2M_{\odot}$, once the core hydrogen supply is exhausted, nuclear energy generation ends, core convection is quenched and the core begins to collapse. Although core fusion has ended, hydrogen burning continues in the surrounding envelope, which drives energy production beyond thermal equilibrium and increases the stellar luminosity. As a consequence, the stellar envelope expands and cools (the radius can increase by a factor of thousands compared to on the main sequence [Veras, 2016]), and the star joins the red giant branch (RGB). While hydrogen burning continues in the stellar envelope, helium is continually deposited in the core, and the increasingly massive core continues to contract. The stellar envelope becomes convective in order to account for the increased need for energy transfer and the span of this convective envelope allows the ashes of hydrogen burning to be 'dredged up' to the stellar surface where they can be observed. Eventually, the stellar core reaches temperatures sufficient for helium burning to begin.

In stars that are less massive than $2M_{\odot}$, degenerate electrons supply sufficient pressure to support the weight of the stellar envelope and so core contraction and the subsequent evolution onto the RGB proceeds slower. Nuclear fusion in degenerate material is thermally unstable and leads to runaway reactions. Thus, the explosive onset of helium burning in low mass stars is known as the helium flash. In just a few seconds, the temperature in the core rises very steeply, the core degeneracy lifts, and the core expands allowing the helium burning to stabilise.

Helium burning on the RGB occurs inside the star's convective core, which is continually replenished by the products of hydrogen burning in the outer shell. As the core material is fused into carbon and oxygen, the helium supply is diminished and convection stops. The CO core proceeds as before, contracting and heating up as the envelope expands and cools and convection begins. The expanding star becomes more red and joins the asymptotic giant branch (AGB) as a supergiant.

As the luminosity of the star approaches the Eddington limit, radiation pressure increases until it is capable of accelerating material outside of the stellar potential well, which drives stellar mass loss through stellar winds. The stellar luminosity on the giant branches can increase by thousands of times compared to the main sequence [Veras et al., 2014a]. Stellar mass loss on the RGB has typically been modelled by Reimer's mass loss formula

$$\frac{dM_*^{\rm RBG}}{dt} = 8\times10^{-14}\frac{M_\odot}{\rm yr}\left(\frac{L_*^{\rm RGB}}{L_\odot}\right)\left(\frac{R_*^{\rm RGB}}{R_\odot}\right)\left(\frac{M_*^{\rm RGB}}{M_\odot}\right)^{-1} \times\left(\frac{T_*^{\rm RGB}}{4000{\rm K}}\right)^{7/2}\left[1+2.3\times10^{-4}\left(\frac{g_*^{\rm RGB}}{g_\odot}\right)^{-1}\right], \quad (1.1)$$

where g is the surface gravity [Kudritzki and Reimers, 1978; Schröder and Cuntz, 2005; Veras, 2016]. On the AGB, Reimer's mass loss formula is no longer valid and instead the following empirical mass loss rate can be adopted

$$\log\dot{M}^{\rm AGB} = -11.4 + 0.0125\,[P - 100\,\max(M_* - 2.5, 0.0)]\,M_\odot{\rm yr}^{-1}, \quad (1.2)$$

where

$$P = \min(3.3, -2.07 - 0.9\,\log M_* + 1.94\,\log R_*) \quad (1.3)$$

is the Mira pulsation period of the star in days [Vassiliadis and Wood, 1993; Bonsor and Wyatt, 2010].

Finally, the mass loss rate for the star reaches its highest value at the tip of the AGB with the onset of the superwind which marks the near end of the star's time on the giant branches. Superwind ejection rates can be on the order of a few times $10^{-5}M_\odot{\rm yr}^{-1}$ and within a factor of 2 of the value $\dot{M} = L_*/cv_{\rm exp}$, where L_* is the stellar luminosity, c is the speed of light and $v_{\rm exp}$ is the stellar wind expansion velocity far from the central star [Vassiliadis and Wood, 1993].

The combination of these different phases of mass loss can lead to a star losing up to 80 per cent of its total mass by the end of the the AGB. Thus, as the AGB phase nears its end, the central star is surrounded by an extended shell of ejected material. The central core expands and the small remnant envelope contracts leading to a distinct separation between the star and its ejected envelope.

When the core temperature reaches around 30 000 K, the emitted photons are energetic enough to cause the ejected material to fluoresce and for observers to see a bright ring of material surrounding the central star as a planetary nebula.

Finally, the central core is surrounded by a thin shell of hydrogen or helium, and with no internal fusion the stellar luminosity drops and the star becomes a white dwarf.

1.2.2 Planetary Systems

While a star is evolving on the giant branches, its planetary system also undergoes drastic changes.

Orbital Expansion

The stellar mass loss drives changes to the orbits of all bodies within the system regardless of their distance from the central star.

If we assume that the mass from the central star is lost isotropically (an appropriate approximation for most post-main-sequence applications [Veras et al., 2013a]), then the change in an orbiting body's semi-major axis and eccentricity can be written as follows

$$\frac{da}{dt} = -\frac{a(1+e^2+2e\cos f)}{1-e^2}\frac{\dot{M}_* + \dot{M}_\mathrm{p}}{M_* + M_\mathrm{p}} \tag{1.4}$$

and

$$\frac{de}{dt} = -(e+\cos f)\frac{\dot{M}_* + \dot{M}_\mathrm{p}}{M_* + M_\mathrm{p}}, \tag{1.5}$$

where M_* and M_p are the masses of the star and planetary object and $\dot{M}$ indicates the mass loss rates [Veras, 2016]. The semi-major axis, eccentricity and true anomaly are given by a, e and f respectively.

Equation 1.4 shows that semi-major axes always increase due to mass loss, and when combined with Equation 1.5, the orbital pericentre also increases. Planetary orbits can grow by $2-5\times$ depending on the amount of mass lost by the central star [Veras et al., 2011; Mustill and Villaver, 2012].

Planetary Engulfment

As the stellar envelope expands outwards, increasing by many orders of magnitude [Veras, 2016], close in planets are at risk of being engulfed by the stellar envelope. Planets in the inner system thus have two competing effects, tidal forces driven by interactions with the turbulent envelope pulling the orbits towards the central star and orbital expansion driven by stellar mass loss. If a planet is in a close-in orbit at the onset of the giant branch phases of stellar evolution, then the orbital decay driven by tides is sufficient to cause the planet to spiral into the stellar envelope.

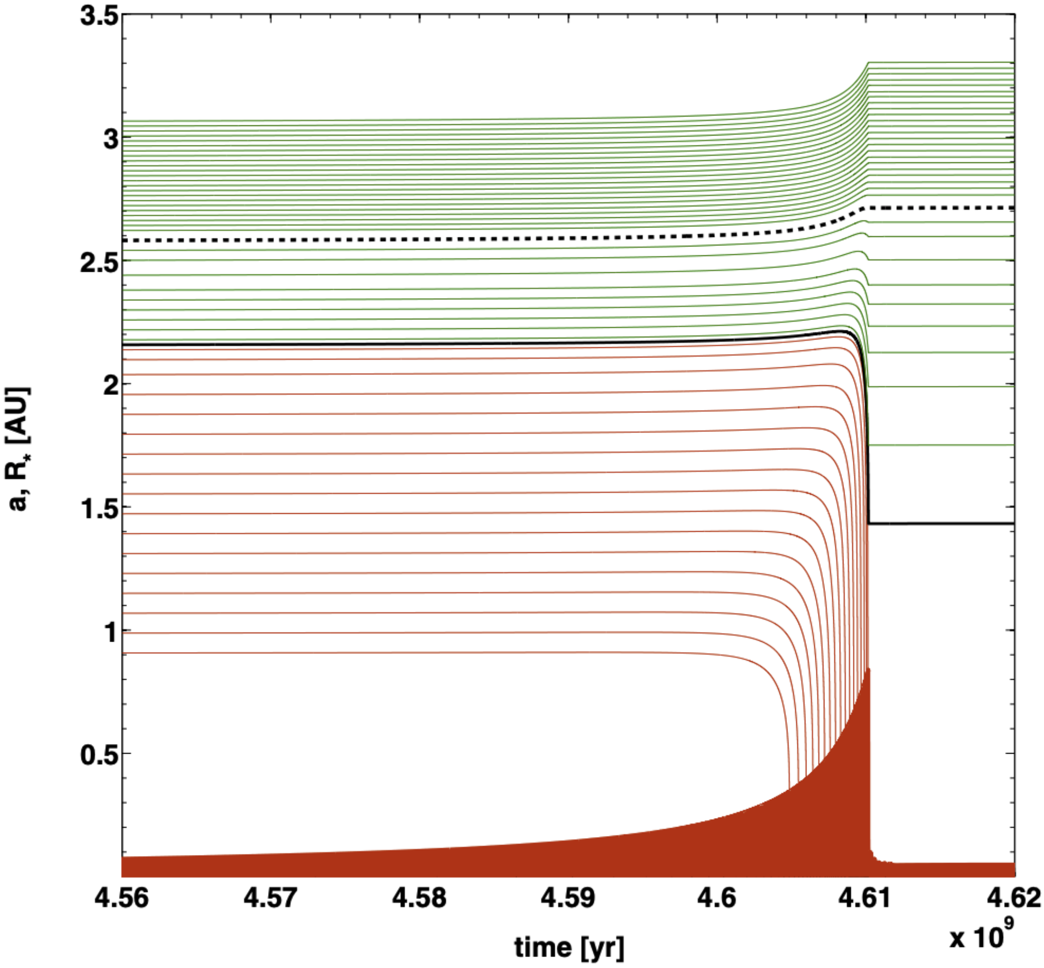

Figure 1.4: The radius evolution of a $1.5M_{\odot}$ star as it reaches the tip of the RGB as indicated by the filled red region. The orbital evolution of a Jupiter-mass planet with varying initial semi-major axis is indicated by the thin lines. The red lines indicate orbits where the planet will be engulfed by the star and green lines show where the planet survives. The solid black line shows the critical distance required for a planet to survive engulfment and the dashed line shows the distance where tidal forces from the star are negligible. Figure taken from Villaver et al. [2014].

Figure 1.4, highlights the results from one study which investigated the orbital evolution of a Jupiter-mass planet as its $1.5M_{\odot}$ central star reaches the tip of the RGB [Villaver et al., 2014]. Planets with initial semi-major axes below ~ 2.15 au will be engulfed by the expanding stellar envelope, and those planets initially beyond that distance will survive. For a small range of initial semi-major axes (2.15 au$< a_i <$ 2.6 au) the planet's orbit is affected by tidal forces and the outward expansion due to mass loss is effectively stalled, allowing them to retain closer orbits than those predicted from stellar mass loss alone.

Villaver et al. [2014] find that the main parameter which affects a planet's survival is its mass, with more massive planets being more likely to be engulfed sooner and at wider distances.

Beyond the RGB, planets can still be at risk of engulfment during the AGB, where the stellar envelope continues to expand and the effect of thermal pulses accelerates tidal decay putting Jupiter-mass planets out to 3.2 au at risk of engulfment [Mustill and Villaver, 2012].

When a planet is engulfed in the stellar envelope its interactions with the stellar medium act to damp its orbit even further and it can quickly merge with the stellar core or be tidally disrupted [Chamandy et al., 2020]. This process acts to increase the energy of the stellar envelope, which can be entirely ejected and the process of tidal engulfment halted if enough energy is deposited [Chamandy et al., 2021].

Thus, we do not expect to see planets in close-in orbits around a newly born white dwarf. Due to the planetary mass dependence on stellar engulfment, we may not expect to see terrestrial planets within 2 au and Jupiter-mass planets within 1.5 au of a white dwarf with a $1M_{\odot}$ main sequence progenitor [Mustill and Villaver, 2012].

Luminosity effects

The increased luminosity during the giant branch phases of stellar evolution can have destructive consequences on minor bodies close to the star.

Jura [2008] provide an estimate for the minimum size an asteroid has to be to survive total sublimation as

$$R_{\min} = \frac{\dot{\sigma}(T)}{\rho_{\mathrm{ast}}} t_{\mathrm{AGB}}, \tag{1.6}$$

where

$$\dot{\sigma}(T) = \dot{\sigma}_0 \sqrt{\frac{T_0}{T}} e^{-T_0/T} \tag{1.7}$$

is the mass production rate from dust per unit area, $\dot{\sigma}_0 = 1.5 \times 10^9$ g cm^{-2} s^{-1}, t_{AGB} is the time the star spends on the asymptotic giant branch phase of evolution, T is the asteroid temperature and $T_0 = 65\,300$ K. Jura [2008] find that depending on the maximum luminosity reached by the star during the AGB, bodies in the size range $1 - 10$ km within $2 - 3$ au of the star are likely to sublimate completely.

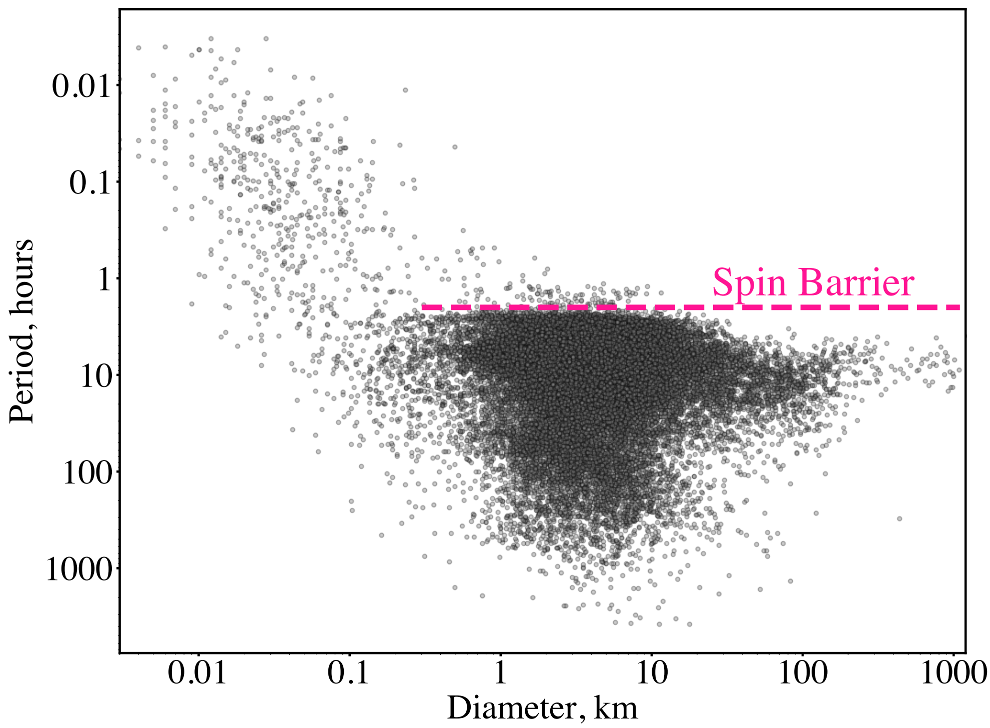

Figure 1.5: The size and spin distribution of ~ 29 000 asteroids highlighting the obvious 'spin barrier' with a dashed, pink line. Few bodies larger than about 300 m in diameter are observed to be rotating with a spin period larger than around 2.2 hours. Data taken from the Asteroid Lightcurve Database [Warner et al., 2009], updated 2023 April 24.

Veras et al. [2014a] further studied the effects of stellar luminosity on the survivability of planetesimals around giant branch stars, by focussing on the YORP (Yarkovsky-O'Keefe-Radvievski-Paddock) effect [Rubincam, 2000]. The YORP effect drives rotational evolution of bodies due to the anisotropic absorption and radiation of light. Due to the rubble pile nature of small bodies, which are essentially piles of regolith held together by self-gravity and little to no tensile strength, it is relatively easy for them to undergo rotational fission.

The rotational fission of asteroids in the Solar System is well evidenced by the existence of the 'rubble pile spin barrier' as seen in Figure 1.5. The clear dearth of planetesimals larger than around a kilometre rotating with a period of more than ~ 2.2 hrs indicates that bodies which spin quicker than that are destroyed, with the YORP effect being one of the drivers of destruction. Although a small number of bodies are observed above the spin barrier in Figure 1.5, it has been suggested that these bodies show unusually high levels of cohesion [e.g. Polishook et al., 2016; Chang et al., 2022], which separate them from the typical rubble piles which constitute the bulk of observed asteroids.

The spin evolution of a body can be described by the following

$$\frac{ds}{dt} = \frac{Y}{2\pi\rho R^2}\left(\frac{F_*}{a^2\sqrt{1-e^2}}\right), \tag{1.8}$$

where R is the body's mean radius, ρ is the density, a is the semi-major axis and e the eccentricity [Veras et al., 2014a]. $Y \in [0, 1]$ is a constant determined by the physical properties of the body and can essentially be thought of as the extent of a body's asymmetry. Finally, F_* is the force due to stellar irradiation, which is a function of many body and stellar properties and is fully described in Equations 23-26 of Scheeres [2007]. In the Solar System, $F_\odot$ is linearly proportional to the Solar radiation constant and is approximately equal to 10^{17} kg m s^{-2}. In extrasolar contexts F_* can be approximated as $F_* = F_\odot(L_*/L_\odot)$.

Veras et al. [2014a] simulated the rotational evolution of asteroids under increased luminosity as their host star leaves the main sequence. They find that even slightly asymmetric bodies as large as 10 km which orbit at 7 au will undergo rotational fission. Thus, the inner planetary regions around giant branch stars are likely to be devoid of planetesimals around 10 km and smaller out to about 7 au.

Planet occurrence

Although the destructive giant branch phases of stellar evolution should act to reduce and remove planetary material from the inner regions of a system, a number of observations have been made of planetary mass companions around giant branch stars. Sabine Reffert maintains a database of credible substellar companions to giant branch stars at www.lsw.uni-heidelberg.de/users/sreffert/giantplanets.html. As of 23rd March 2023, there are 128 known giant branch companions with $M_\mathrm{p} < 13M_\mathrm{J}$ recorded in the database. Of these substellar companions, all are observed within 5.7 au and around 7.8 per cent are within 0.5 au.

Although the number of known giant branch planets remains relatively low in comparison to main sequence planets, studies are beginning to make inferences of population wide statistics. Grunblatt et al. [2019] sampled 2476 low-luminosity RGB stars observed by the K2 mission and found 0.49 ± 0.28 per cent of the sample hosted planets with $M > 1M_\mathrm{J}$ and periods less than 10 days. Giant branch planets appear to preferentially inhabit higher eccentricity orbits than their main sequence counterparts [Grunblatt et al., 2018, 2023], with 60 per cent of the companions in the Reffert database having $e > 0.1$.

One particular post-main-sequence planetary system of interest is BD+48 740, which hosts a $1.6M_\mathrm{J}$ planet on a highly eccentric ($e = 0.67 \pm 0.17$) orbit at 1.89 au [Adamów et al., 2012]. Alongside this eccentric planet which may be undergoing tidal circularisation and may eventually be engulfed, the star shows a heightened lithium abundance. As the lithium abundance of stars is expected to drop as they enter the giant branches, the observed overabundance of lithium could be indicative of a second planet in the system which has already been engulfed and provided the enrichment [Adamów et al., 2012].

Debris Discs

Observations of debris discs around giant branch stars are sparse but existing.

The first GB debris disc was resolved around the sub-giant κ Coronae Borealis with Herschel [Bonsor et al., 2013; Lovell et al., 2022]. Although it is impossible to determine the exact architecture of this system, observations suggest there is at least one planet coexistent with the disc.

A further survey of 35 sub-giant stars identified three more debris disc hosts, two of which also host planets [Bonsor et al., 2014]. Thus, planets and planetary material can still persist around giant branch stars.

1.3 The White Dwarf Phase

At the end of the AGB phase of stellar evolution, the star embarks on its next, and final, stage by becoming a white dwarf. There are a few key properties of white dwarfs which help describe their subsequent evolution and that of their remnant planetary systems.

1.3.1 Stellar Properties and Evolution

White Dwarf Masses

The observed mass distribution of hydrogen-rich (top panel) and helium-rich white dwarfs (bottom panel) is shown in Figure 1.6. Both distributions exhibit a narrow peak centred around $0.6M_{\odot}$, with tails out to about $0.8M_{\odot}$. Recent dedicated surveys of the local 40 pc sample of white dwarfs similarly find a peak mass of $M_{\rm WD} \sim 0.63M_{\odot}$ [McCleery et al., 2020; O'Brien et al., 2023].

White dwarfs could form with masses up to $M_{\rm WD} > 1.4M_{\odot}$ but these are not largely represented in the current observed mass distribution. Additionally, the time required for a main sequence progenitor to evolve into a white dwarf with $M_{\rm WD} < 0.4M_{\odot}$ is longer then the current age of the universe, and hence no white dwarf should currently exist below this mass if it evolved as a single star. Lower masses could be explained by having formed in a binary, where some of its mass was stripped by the companion star during a common envelope phase of evolution [Veras, 2016].

The relationship between a white dwarf's mass and that of its progenitor is known as the initial-to-final-mass relation (IFMR) and has been widely studied and empirically measured.

One such measurement can be made by exploiting the fact that all stars in a stellar cluster formed at the same time and hence are the same age. Then the time a white dwarf

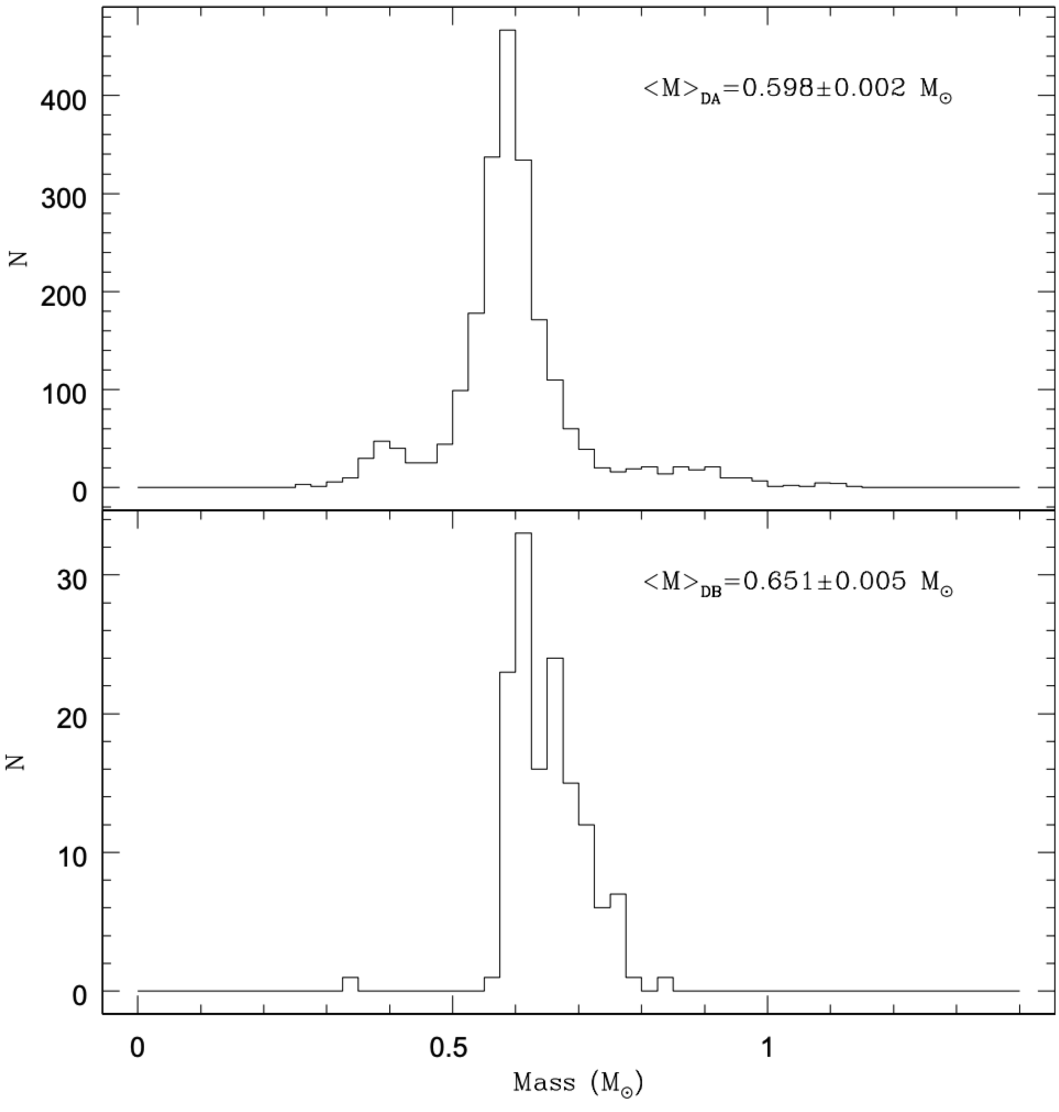

Figure 1.6: The mass distribution of hydrogen rich white dwarfs with $T_{\rm eff} > 13\,000$ K (top panel) and helium rich white dwarfs with $T_{\rm eff} > 16\,000$ K (bottom panel) observed in SDSS DR7. Figure taken from Kleinman et al. [2013].

spent on the main sequence can be estimated as

$$t_{\mathrm{prog}} = t_{\mathrm{cluster}} - t_{\mathrm{WD}}, \tag{1.9}$$

where t_{prog}, t_{cluster} and t_{WD} are the lifetime of the main sequence progenitor, the age of the cluster and the white dwarf cooling age respectively. It is then possible to estimate the initial mass of the white dwarf progenitor by comparing t_{prog} to single star evolutionary models [Raddi et al., 2016].

However, this method is age limited as older white dwarfs are harder to observe, thus the IFMR calculated from stellar clusters is most accurate for clusters whose most massive stars are newly born white dwarfs. The increased accuracy and completeness of observations of white dwarfs by the *Gaia* space telescope is improving measurements [El-Badry et al., 2018].

Alternatively, estimates of the IFMR can be made by examining white dwarfs in wide binaries with main sequence companions. The main sequence lifetime of such a white dwarf can be estimated by finding the age of the main sequence companion through chromospheric activity and then subtracting the cooling age of the white dwarf. As before, the initial mass of the progenitor can then be estimated by comparing with stellar evolution models [Zhao et al., 2012].

From an empirically calculated IFMR, expressions can be found which estimate the mass of the white dwarf formed from a given main sequence mass such as [Wood, 1992; Frewen and Hansen, 2014]

$$M_{\mathrm{WD}} = 0.49 \exp\left[0.095 M_{\mathrm{MS}}\right]. \tag{1.10}$$

Understanding the mass of a white dwarf progenitor can help inform initial conditions for models of post-main-sequence planetary systems.

White Dwarf Radii

Due to the nature of white dwarfs, their physical radii are closely linked with their mass.

One mass-radius relation is given by Verbunt and Rappaport [1988] as

$$\frac{R_{\mathrm{WD}}}{R_{\odot}} = 0.0114 \left[\left(\frac{M_{\mathrm{WD}}}{M_{\mathrm{c}}}\right)^{-2/3} - \left(\frac{M_{\mathrm{WD}}}{M_{\mathrm{c}}}\right)^{2/3}\right]^{1/2} \times \left[1 + 3.5\left(\frac{M_{\mathrm{WD}}}{M_{\mathrm{p}}}\right)^{-2/3} + \left(\frac{M_{\mathrm{WD}}}{M_{\mathrm{p}}}\right)^{-1}\right]^{-2/3}, \tag{1.11}$$

where $M_{\mathrm{c}} = 1.44 M_{\odot}$ is the Chandrasekhar mass limit and $M_{\mathrm{p}} = 0.00057 M_{\odot}$ is a constant.

Table 1.1: Summary of the white dwarf classification scheme first proposed by Sion et al. [1983], with additional single letter magnetic classifications as described in Koester [2013].

Classification	Description
DA	Balmer lines, no He or metals
DB	He I lines, no H or metals
DC	continuous spectrum
DO	strong He II lines, He I or H also present
DZ	metal lines, no H or He
DQ	Ca features
H	magnetic with Zeeman splitting
P	magnetic with polarisation

An alternative expression given by Nauenberg [1972] is

$$\frac{R_{\mathrm{WD}}}{R_\odot} \approx 0.0127 \left(\frac{M_{\mathrm{WD}}}{M_\odot}\right)^{-1/3} \sqrt{1 - 0.607 \left(\frac{M_{\mathrm{WD}}}{M_\odot}\right)^{4/3}}, \tag{1.12}$$

assuming a mean molecular weight per electron of 2 [Hamada and Salpeter, 1961].

Using a typical white dwarf mass of $M_{\mathrm{WD}} = 0.6M\odot$, Equation 1.12 suggests $R_{\mathrm{WD}} \sim 0.012R\odot \sim 1.31R_\oplus$. Thus, white dwarfs have about half the mass of the Sun squeezed into a sphere only a little bigger than the Earth and subsequently have extremely high surface gravities. The surface gravity of a white dwarf can be determined by examining measured spectral lines which are highly sensitive to the surface gravity through the density of particles in the atmosphere. An average surface gravity for a white dwarf is $\log g \sim 8$ whereas $\log g \sim 4.4$ for the Sun [Fontaine et al., 2001].

White Dwarf Compositions

As stars leave the AGB, they have CO cores and are losing mass through stellar winds while alternately burning hydrogen or helium in thin shells [Prialnik, 2000]. As mass loss ceases during a random phase of a thermal pulse, a white dwarf could be left with either a helium or hydrogen outer shell. However, helium burning only takes up a small fraction of the pulse cycle and so stars are proportionally more likely to end the AGB with a hydrogen envelope. Thus, around 85 per cent of white dwarfs observed have hydrogen rich atmospheres [Althaus et al., 2010].

White dwarfs can be classified based on the elements observed within their atmospheres. This classification scheme was first described by Sion et al. [1983] and is summarized in Table 1.1. In these classifications, the initial capital D refers to the white dwarf being a degenerate star and the second letter to its most prominent spectral feature. If more than one spectral feature from the table is observed, then the weaker components letter can be added to the stronger, for example if a white dwarf is observed with strong Balmer lines and weaker lines of iron, the star could be classified as a DAZ. Further classifications for white dwarfs with observed magnetism through either Zeeman splitting observed in spectral lines or polarisation was later added and described in Koester [2013].

Thus, white dwarfs are classified by measuring a spectrum from the star, and identifying atmospheric absorption lines to infer the stellar composition.

White Dwarf Temperatures

As white dwarfs are no longer actively undergoing fusion in their cores, they monotonically cool for the rest of their lifetimes. Dedicated models of how white dwarfs cool allow us to use observed temperatures to estimate how long a particular star has been a white dwarf, which is known as the cooling age $\tau_{\rm cool}$. Figure 1.7 shows the luminosity and effective temperature evolution for a number of different mass DA white dwarfs based on the models of Fontaine et al. [2001]. The plot clearly shows the steadily declining temperature of the white dwarf and indicates a number of important evolutionary events which are further discussed below.

For very high luminosities and consequently high effective temperatures ($T_{\rm eff} >$ 25 000K), indicative of white dwarfs which have just departed from the planetary nebula phase, the core temperatures are high enough for neutrinos to be produced in abundance and escape directly from the core, hence dominating the heat transfer [Fontaine et al., 2013]. The point where neutrino cooling ceases to be the dominant heat loss mechanism in favour of thermal cooling is indicated by the open circles at the top left hand corner of Figure 1.7, the markers for the two most massive white dwarf models are beyond the limits of this particular plot.

As the white dwarf cools and loses thermal energy due to radiation at the surface, the core material has its kinetic energy reduced and eventually it will evolve from a gas to a fluid and then finally to a solid. The final transition from a liquid to a solid is accompanied by a release of a significant amount of latent heat which can act to considerably slow down the cooling process [Fontaine et al., 2001]. This process is known as crystallization and can be observed by an overabundance of white dwarfs with a specific cooling age [Tremblay et al., 2019]. The onset of crystallization is shown in Figure 1.7 by the filled circles. More massive white dwarfs which have higher internal densities, develop crystallized cores at higher effective temperatures.

For the effective temperature range in which the bulk of white dwarfs exist 16 000K $<$ $T_{\rm eff} <$ 18 000K, the temperatures in the degenerate core can vary between $\sim 5\times10^{6}$K -2×10^{7}K [Fontaine et al., 2001]. This large temperature difference between the core and outer envelopes can drive the formation of convective zones in the envelope, which play a key role in the cooling process. As the base of these convection zones can reach all the way to the upper boundary of the core, the rate of heat energy transfer across the convective zones can exceed that which would be possible from radiation alone. The onset of convection is shown in Figure 1.7 by the labelled opened circles towards the center of the plot.

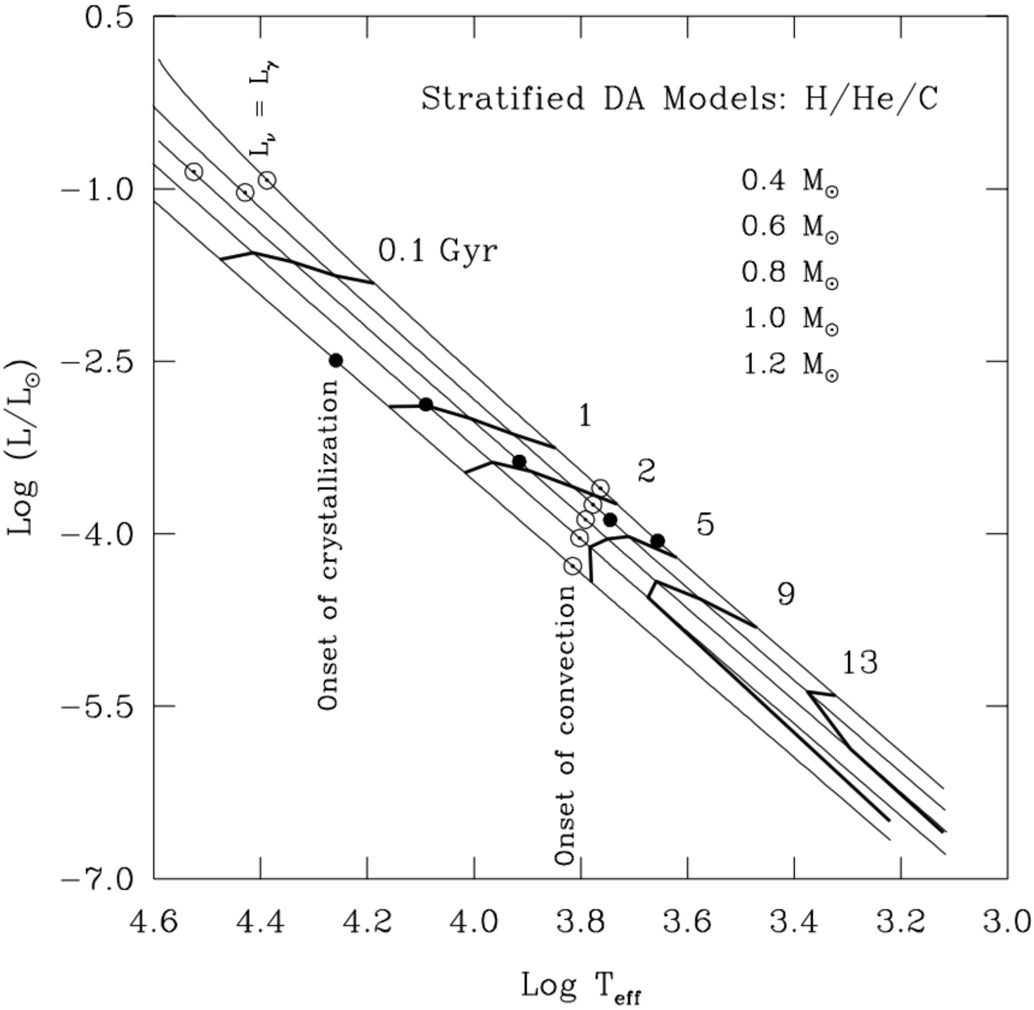

Figure 1.7: Model evolutionary tracks for five different DA white dwarf masses ($M = 0.4, 0.6, 0.8, 1.0, 1.2 M_\odot$, top to bottom) are shown in the diagonal solid lines. The thick lines indicate isochrones, which intersect with the different evolutionary tracks at the same $\tau_{\rm cool}$, which is indicated by the number next to the thick curve in units of Gyr. The unfilled circles at high luminosities indicate the transition between neutrino cooling and thermal cooling phases. The solid circles show the onset of crystallization and the slightly smaller unfilled circles show where the core and envelope are coupled through convection. Figure taken from Fontaine et al. [2013], originally published in Fontaine et al. [2001].

Once the white dwarfs entire thermal energy reservoir is depleted, the crystallised object is no longer visible and becomes known as a black dwarf.

1.3.2 Planetary Systems

Around 95 per cent of all stars in the Milky Way are destined to become white dwarfs [Althaus et al., 2010]. Thus these small, dim, stellar objects form an important stellar population. Equipped with the knowledge discussed in Section 1.2.2 that planets and planetary material can exist around GB stars and the different ways that stellar evolution immediately preceding the white dwarf phase can erode these systems, we are now able to examine the evidence for planetary systems around white dwarfs.

Photospheric Pollution

Almost 80 years before the discovery of 51 Peg b, astronomer Adriaan van Maanen discovered a star with large proper motions that he initially classified as an F0-type star [van Maanen, 1917, 1919]. It is likely that this initial classification was made due to the presence of strong Ca ɪɪ H and K absorption lines in the observed spectrum, a feature that is typical for F-type stars. Later in 1922, the star (now known as van Maanen's star or vMa2) was reclassified as one of the first three white dwarfs, then described as faint A-type stars with high proper motions [Luyten, 1922]. In 2016, the original spectroscopic plates recorded for vMa2 were reinspected by Farihi [2016], and the clearly visible Ca ɪɪ absorption lines were identified as evidence for atmospheric pollution.

Spectral absorption lines are caused when photons are absorbed by material in a star's atmosphere and produce dips in the measured spectrum. As discussed in Section 1.3.1, the only chemical elements expected to be visible in a white dwarf's atmosphere is H or He. Thus, the material causing these absorption lines is said to 'pollute' the white dwarf. As different chemical species absorb particular wavelengths, the observed absorption lines indicate the chemical make up of the material polluting the stellar atmosphere. Figure 1.8 shows observed spectra for two white dwarfs (G74-7 top, GD 362 bottom) which both show evidence for metallic absorption lines, the labelled tick marks indicate lines associated with specific metals.

I now discuss some of the processes necessary to understand atmospheric pollution of white dwarfs.

Atmospheric Processing

For most white dwarfs, their extreme surface gravities will act to stratify their atmospheres and effectively drag elements heavier than H or He into their cores. Extremely young white dwarfs may still display heavy elements in their photospheres through radiative levitation [e.g. Michaud et al., 1979; Vennes et al., 1988; Chayer et al., 1995], and older white dwarfs

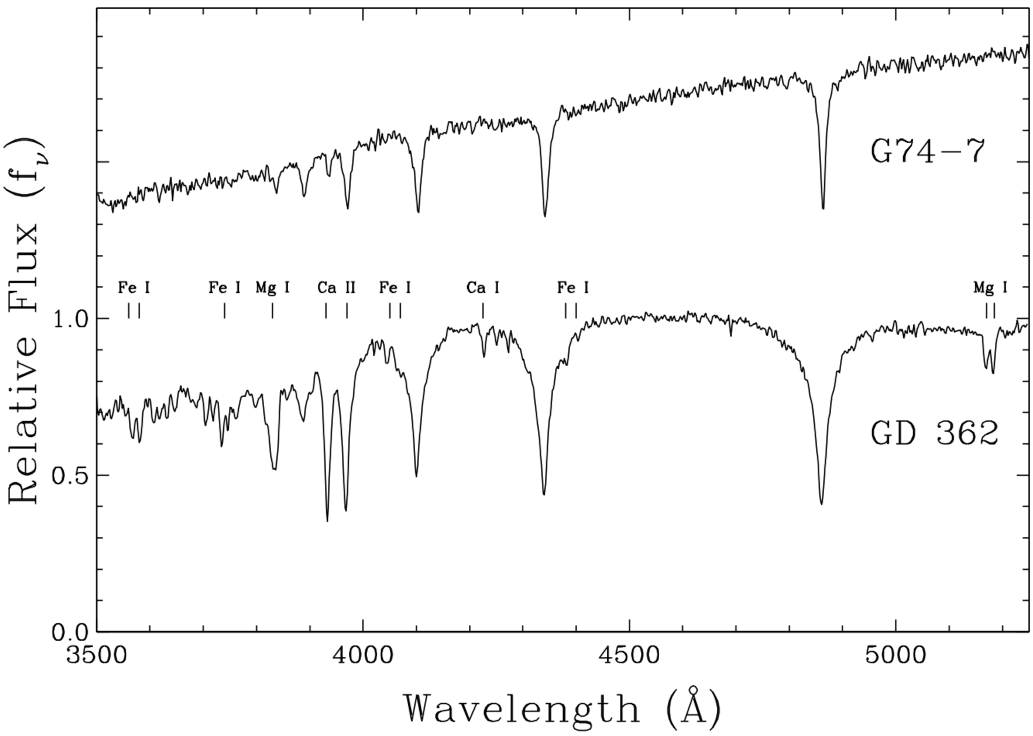

Figure 1.8: Optical spectra for two white dwarfs; G74-7 (top), and GD 362 (bottom). Metallic absorption lines can clearly be seen in both spectra and specific lines in the GD 362 spectrum are highlighted by labelled tick marks. Figure taken from Gianninas et al. [2004].

may have core carbon dredged up into their atmospheres [e.g. Koester et al., 1982; Fontaine et al., 1984; Pelletier et al., 1986]. The time it takes for a white dwarf to remove pollutant material from its atmosphere is so much faster than the cooling age that we should only expect to observe metal pollution in under 0.1 per cent of white dwarfs [Veras, 2016]. Thus, the fact that we observe metal pollution in between a quarter and half of all DA white dwarfs [Zuckerman et al., 2010; Koester et al., 2014; Kepler et al., 2015, 2016; Coutu et al., 2019], suggests that this material is being continually deposited on the surface and processed by the atmosphere.

The timescale for a particular element to diffuse out of the photosphere, τ_{diff}, can be described by the following expression

$$\tau_{\text{diff}} = \frac{M_{\text{cvz}}}{4\pi r^2 \rho\, v_{\text{diff}}}, \tag{1.13}$$

where M_{cvz} is the mass of the white dwarf's convective zone, r is the local radius at the base of the convective zone, ρ is the local mass density and v_{diff} is the diffusion velocity [Paquette et al., 1986a,b]. Koester [2009] presents τ_{diff} values for atmospheric models of both DA and DB white dwarfs and a number of different chemical species. For calcium within a DA white dwarf atmosphere they find the diffusion time can vary from the order of days for a 25 000 K white dwarf to thousands of years for cooler 6 000 K stars. The situation is different for DB white dwarfs which have deeper convective zones. A 25 000 K DB would diffuse calcium in tens of years, while cooler DBs could take Myrs.

If a particular chemical species, j, is being accreted at a constant rate, $\dot{M}_j$, the specific mass abundance of the element in the convection zone at a time t can be found by the following

$$X(j,t) = X(j,0)e^{-t/\tau_j} + \frac{\tau_j \dot{M}_j}{M_{\text{cvz}}}\left[1 - e^{-t/\tau_j}\right], \tag{1.14}$$

where τ_j is the diffusion time for the species. The process of elemental accretion can be described in three stages; onset, steady-state and trailing, each phase can be seen in the top panel of Figure 1.9. At the onset of accretion, elemental abundances increase linearly. During the steady-state phase, diffusion through the base of the convective zone is balanced by accretion at the surface. Finally, in the trailing phase, surface accretion ends and the abundances decrease exponentially.

By assuming that the observed accretion is in the steady-state phase, which is a reasonable assumption for DA white dwarfs where diffusion times are short, the observed elemental abundances can be used to directly estimate the abundances of the progenitor body. The total accretion rate onto the star can be found by summing the individual chemical species' contribution [Bauer and Bildsten, 2018]. Estimates for the accretion rates for a number of white dwarfs find rates in the range $10^5 - 10^8$ g s^{-1} [Koester et al., 2014].

For DB white dwarfs which have much deeper convective zones and slower diffusion times than their DA counterparts, the pollution observed in their atmospheres can act as a

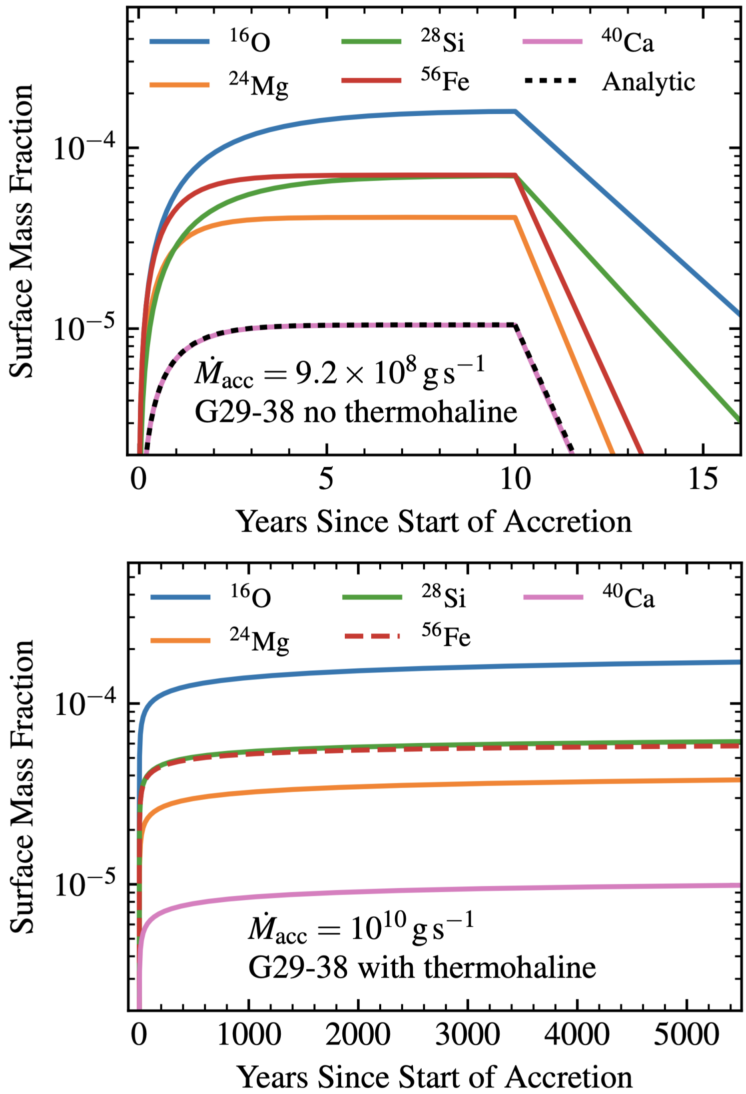

Figure 1.9: Metallic abundances within the `MESA` modelled atmosphere of white dwarf G 29-38 under constant accretion. The top panel considers only gravitational settling and shows the characteristic onset phase of accretion at early times with abundances asymptotically approaching the steady-state phase before exponentially decreasing in the trailing phase. The lower panel displays the results for a model which includes the effect of thermohaline convection, which shows that the steady-state phase of accretion persists for much longer compared to pure gravitational settling models. Both panels from Bauer and Bildsten [2018].

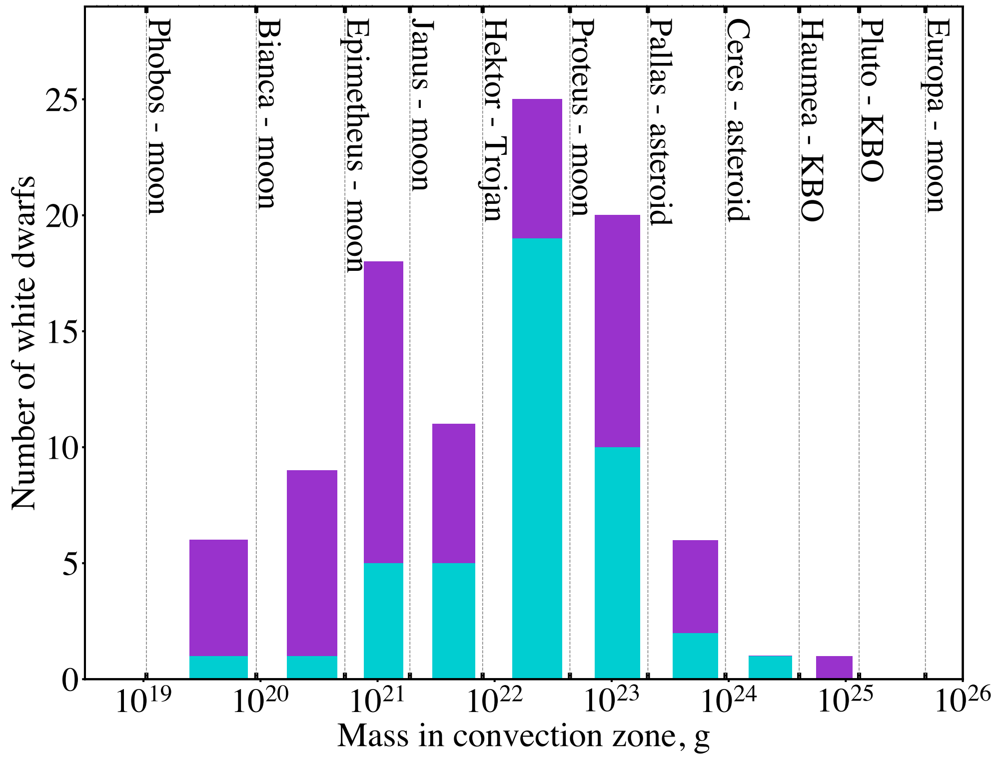

Figure 1.10: Histogram showing the lower bounds on total accreted mass for a number of white dwarfs in two separate samples; data from Xu and Jura [2012] is shown in blue and from Girven et al. [2012] in purple. The data is binned between different Solar System body masses which are shown by vertical grey annotated lines. Figure cosmetically enhanced from Veras [2016].

record for the past ~Myr of evolution. Thus, observations of DB white dwarfs can allow us to place lower bounds on the total mass that has been accreted by the white dwarf. Figure 1.10 shows the lower bounds for the total material accreted by two different samples of DB white dwarfs. The histogram bins are sized according to the masses of different Solar System minor bodies as displayed on the top axis. The total observed mass accretion estimates are in line with the masses of asteroids, Kuiper Belt objects (KBOs) and even small moons of the Solar System.

The above discussion of metallic diffusion only considers the effect of gravitational settling directly, yet recent improvements to atmospheric modelling efforts have highlighted two potential complications to this simple picture, which may affect calculated accretion rates.

The first is the idea of thermohaline convection, which enhances levels of atmospheric mixing due to a metallicity gradient between layers of the atmosphere [Traxler et al., 2011; Brown et al., 2013]. This leads to layers of the white dwarf's upper atmosphere which have accreted heavy elements diffusing through the atmosphere faster than predicted by diffusion alone [Deal et al., 2013; Bauer and Bildsten, 2018, 2019]. Bauer and Bildsten [2018] find that for DA white dwarfs with $T_{\rm eff} > 10\,000$ K, inferred accretion rates can increase by several orders of magnitude when including effects of thermohaline convection. However, for DB white dwarfs with $T_{\rm eff} < 18\,000$ K, the effect of thermohaline convection is likely to be insignificant due to the large size of the surface convection zones [Bauer and Bildsten, 2019].

Secondly, is the idea of convective overshoot, where significant atmospheric mixing can occur below the formally defined zones of convective instability increasing the efficiency of diffusion [Freytag et al., 1996; Tremblay et al., 2015; Bauer and Bildsten, 2019; Cunningham et al., 2019]. Both Bauer and Bildsten [2019] and Cunningham et al. [2019] find that incorporating convective overshoot into atmospheric models can increase diffusion times by up to two orders of magnitude.

Understanding the atmospheric processes of gravitational settling, thermohaline convection, and convective overshoot can provide us with information about how often and how much material is being accreted by a white dwarf.

Pollution Composition

Combining information about what material, and how much of it, is being accreted can tell us important information about the progenitor body. By 2021, 23 separate chemical species had been identified in the atmospheres of white dwarfs with effective temperatures below 25 000 K. Table 1.2 details the year in which each individual chemical species was first identified and in which white dwarf.

Figure 1.11 shows the mass fraction of chemical elements observed within the atmospheres of a number of polluted white dwarfs, alongside the mass fractions within bulk Earth and the Comet Halley. Largely, the material seen to be polluting white dwarfs is in line with the compositions of rocky Solar System bodies, and resembles bulk Earth to zeroth order [Jura and Young, 2014; Xu et al., 2019]. The majority of DZ white dwarfs investigated by Harrison et al. [2021a] had compositions which appear to be primitive material like that expected from asteroids. Thus, it is commonly assumed that the observed pollution originates from asteroids. Although, Brouwers et al. [2023a] note that the composition of accreted material may vary with time, such that instantaneous abundances may not be reflective of the progenitors bulk composition.

However, to date there has been a wide variety of elements observed in the atmospheres of white dwarfs, including rock forming elements (Si, Fe, Mg and O), refractory lithophiles (Ca, Al and Ti), volatile elements (C, N, P and S) and core-loving siderophiles (Cr, Mn, S and Ni) [Veras, 2016]. Using derived chemical abundances of the accreted material can allow us to make inferences about the progenitor body.

Firstly, the chemical species present can indicate where the body formed. Planetesimals form inside the protoplanetary disc and so their composition is determined by

Table 1.2: Chemical elements discovered in the atmospheres of white dwarfs with $T_{\mathrm{eff}} <$ 25 000 K prior to 2021. Data was collected by and initially presented in Klein et al. [2021], references for each of these discoveries are available in the original publication. Question marks indicate that the detection was originally reported with ambiguity.

Discovery	Element	WD
1917	Ca	vMa2
1941	Mg?	Ross 640
1956	Fe	vMa2
1960	Mg	vMa2
1976	Na	G165-7
1980	Si	Ross 640
1980	Cr	G165-7
1991	C?	G238-44
1995	C, O?, Al?	GD40
1998	Al	G238-44
2007	Sc, Ti, V, Mn, Co, Ni, Cu, Sr	GD 362
2008	O, S	GD 378, GD 61
2012	P	GD 40, G241-6, GALEXJ1931
2017	N	G200-39
2021	Li, K	WDJ1644, LHS 2534 and others
2021	Be	GALEXJ2339, GD378

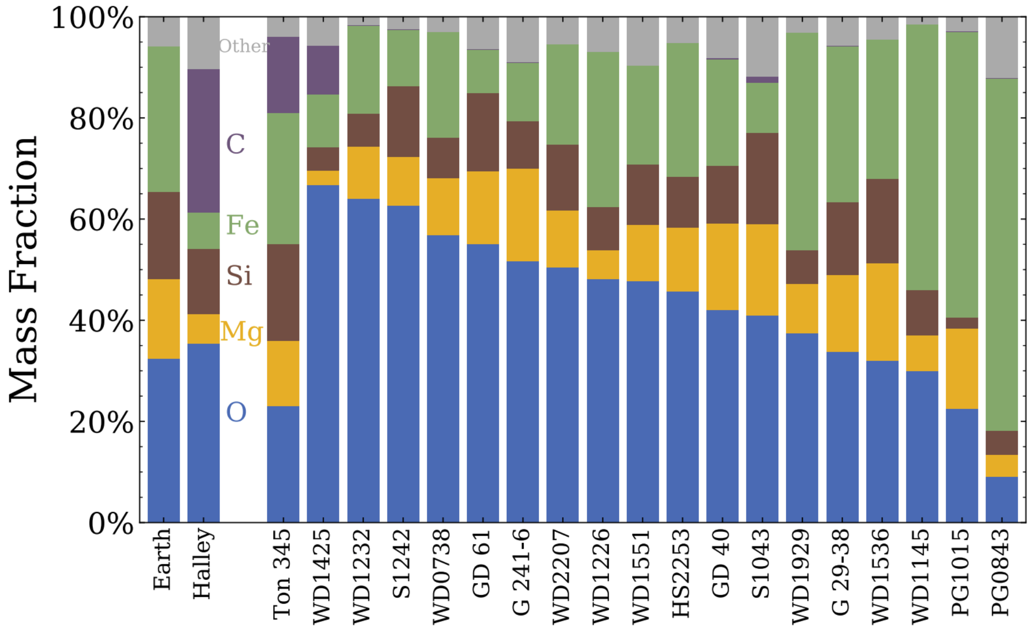

Figure 1.11: The mass fraction of chemical elements (O, Mg, Si, Fe, C and *other*) observed in the atmospheres of polluted white dwarfs as named in the x-axis. The leftmost side of the plot shows the mass fraction for the same elements in Earth and Comet Halley. Broadly, most white dwarfs have accreted material similar to bulk Earth or other rocky planetesimals. Figure taken from Xu and Bonsor [2021].

what material is at that disc location. The chemistry within the disc is heavily dependent on the temperature driven by the stellar radiation. An ice line describes a radial disc location where the temperature is low enough for a particular chemical species to condense [Kennedy and Kenyon, 2008]. The ice lines for more volatile materials, which sublimate at lower temperatures are thus further out in the protoplanetary disc.

Thus, we expect planetesimals with high concentrations of volatile material or ices to have formed in the outer regions of a planetary system, such as the Solar System's Kuiper Belt. Heavily volatile-depleted planetesimals could have formed much closer to the host star, undergone partial surface vaporisation during giant branch phases of stellar evolution [Harrison et al., 2018] or had a dynamically active past where impacts removed volatiles [Harrison et al., 2021b].

A number of white dwarfs have so far been observed with metal pollution indicative of a volatile-rich progenitor body [Farihi et al., 2013; Raddi et al., 2015; Gentile Fusillo et al., 2017; Xu et al., 2017; Hoskin et al., 2020; Izquierdo et al., 2021; Johnson et al., 2022; Brouwers et al., 2023b]. As an example, GD 61 displays an excess in oxygen in its atmosphere, which suggests that the progenitor had up to 26 per cent of its initial mass in the form of water. By considering the total material accreted by a white dwarf, any oxygen observed in the atmosphere can be distributed amongst the other elements to form oxides which were likely present in the progenitor. If there is a significant amount of oxygen in excess of what could have been held in oxides, it's likely that this was accreted in the form of water. Although the lack of C observed in GD 61 suggests the body is more akin to a body from the Solar System's outer main belt rather than a comet [Farihi et al., 2013]. Additionally, the pollution observed in WD 1425+540 displays a N mass fraction of ~ 2 per cent, which is similar to comet Halley, which suggests the pollution may come from a KBO analogue [Xu et al., 2017]. Finally, G 238-44 appears to show spectroscopic signatures from both an icy KBO, and a heavily iron enriched object with similar composition to that inferred for Mercury [Johnson et al., 2022].

Detailed modelling of the pollution's composition can indicate whether or not the parent body was differentiated during formation. The process of differentiation in a forming planet is primarily driven by heating which leads to certain chemical species preferentially accumulating in different areas of the body's interior, such as iron in the core, magnesium in the mantle and silicates in the crust [Jura et al., 2014]. Thus, if we can measure the abundance ratios between specific materials accreted by a white dwarf, we can identify if it was more likely a core or mantle fragment.

Additionally, large planetesimals may be differentiated if they form early enough for their cores to be sufficiently heated by radioactive decay of ^{26}Al [Bonsor et al., 2023]. Bonsor et al. [2020] carried out a number of N-body simulations which tracked the levels of core and mantle material in fragments produced during the break up of a differentiated body and found that the majority of fragments maintain core fractions similar to their parent body, although a few fragments may be extremely core or mantle rich compared to the bulk of their parent. Thus, even white dwarfs thought to be accreting the remnants of planetesimals could show evidence for differentiation.

Such signatures of planetary differentiation have been detected in the atmospheric pollution of white dwarfs. Of 17 white dwarf systems investigated by Harrison et al. [2018], up to 9 of the stars showed evidence for having accreted core- or mantle-like material.

The white dwarf NLTT 43806 shows pollution rich in Al and poor in Fe, which may be indicative of crustal material [Zuckerman et al., 2011; Harrison et al., 2018]. Hollands et al. [2021] report four white dwarfs whose pollution exhibits Li signatures alongside a depletion in Ca, which best matches the composition expected for a planetary crust. The simultaneous detection of K in the atmosphere of one of the white dwarf bolsters the conclusion that the white dwarfs have recently accreted a fragment of planetary crust.

Buchan et al. [2022] present a model which places constraints on the mass of progenitor bodies based on the observed abundances of certain elements. During the differentiation process, elements such as Ni, Cr and Si preferentially settle based on the pressures in the environment, which then affects their core-mantle abundances. As internal pressure is dictated by the body mass, the abundances of these elements may allow us to constrain the mass of the progenitor.

Finally, recent studies have claimed the discovery of material likely accreted from the tidally disrupted remnants of a giant planet's moon through the detection of atmospheric Be [Klein et al., 2021]. The production of Be at the levels required for this detection require an environment where high energy particle collisions produce Be through spallation. Doyle et al. [2021] argue that such an abundance of Be could only be formed through the irradiation of ice and rock by energetic protons. Such a situation could occur within the radiation belt of a giant planet, where rings of ice can then form a moon. They claim that a mid-sized Saturnian analogue icy moon matches observations both in terms of mass and composition, and thus argue that the Be detections constitute the first detection of an exo-moon.

All indications thus point to the fact that the metallic material we observe polluting the atmospheres of white dwarfs originate from the disrupted remnants of planets or planetesimals which initially survived the violent giant branch phases of evolution before reaching their final demise around white dwarfs. Before we consider how the planetary material is delivered close to the white dwarf, we first need to examine the processes that lead to accretion.

Debris Discs

In 1987, a significant excess of infrared radiation was detected around the white dwarf G 29-38 [Zuckerman and Becklin, 1987]. As discussed in Section 1.1.2, a measured IR excess can be indicative of a disc of cooler material orbiting around the central star. Although the detection at G 29-38 was originally explained by the presence of a companion brown dwarf, we now know that this was the first detection of a debris disc around a white dwarf. Nearly two decades later, the next white dwarf debris disc was observed around GD362 [Becklin et al., 2005; Kilic et al., 2005] and the link between dusty debris discs and the pollution we observe in white dwarf atmospheres rapidly became clear. The link is bolstered even further by the fact that to date there has been no confident report of a debris disc detection around an unpolluted white dwarf [Veras, 2016]. Here I discuss the observational evidence for debris discs around white dwarfs and the theoretical work aiming to model these systems.

Debris Disc Observations

Observations indicate that $1-3$ per cent of white dwarfs display signatures of dusty debris discs [Rebassa-Mansergas et al., 2019] and only $0.04-0.1$ per cent show evidence for gaseous circumstellar material [Manser et al., 2020]. The inferred link between polluted white dwarfs and debris discs suggests that every polluted white dwarf we observe should have a related disc [Bonsor et al., 2017], but up to 90 per cent of these discs may be currently unobservable [Rocchetto et al., 2015].

As mentioned above and first discussed in Section 1.1.2, one of the most widely used methods for detecting debris discs is by looking for IR excesses in SEDs. The discs we observe around white dwarfs are vastly different from those around main sequence stars. Debris discs around main sequence stars are thought to be massive planetesimal belts not dissimilar from the Solar System's Kuiper Belt, while the discs we observe around white dwarfs are much smaller and exist at distances much closer to their host star. Figure 1.12 shows SEDs observed by *Spitzer* for the first two white dwarf debris disc systems (G29-38 and GD 362), the excess infrared emission is clearly distinguishable from the model white dwarf atmospheres shown by the dotted grey lines.

Dedicated studies which have searched for IR excesses around white dwarfs have proven successful. A recent study which combined data from the Large Sky Area Multi-Object Fibre Spectroscopic Telescope (LAMOST) with that from the Wide-field Infrared Survey Explorer (WISE) fit SEDs for 846 white dwarfs [Wang et al., 2023]. The authors report the detection of 12 candidate debris disc systems, including eight which were previously undetected, thus suggesting an occurrence rate of ~ 1.4 per cent. While a combination of space-based photometry from *Spitzer* and ground-based infrared observations for 174 white dwarfs investigated in Lai et al. [2021] find 52 IR excesses of interest which may prove to be debris discs after further observations.

A smaller number of discs around white dwarfs have also been observed with gaseous components, starting with the discovery of gas in the white dwarf disc system SDSS J1228+1040 [Gänsicke et al., 2006]. Observations of this particular white dwarf displayed double peaked emission lines from the Ca II triplet. This is expected from rotating gaseous discs where light is blue- or red-shifted by the disc components rotating towards or away from the observer. The Ca II triplet emission lines are shown in Figure 1.13, where the

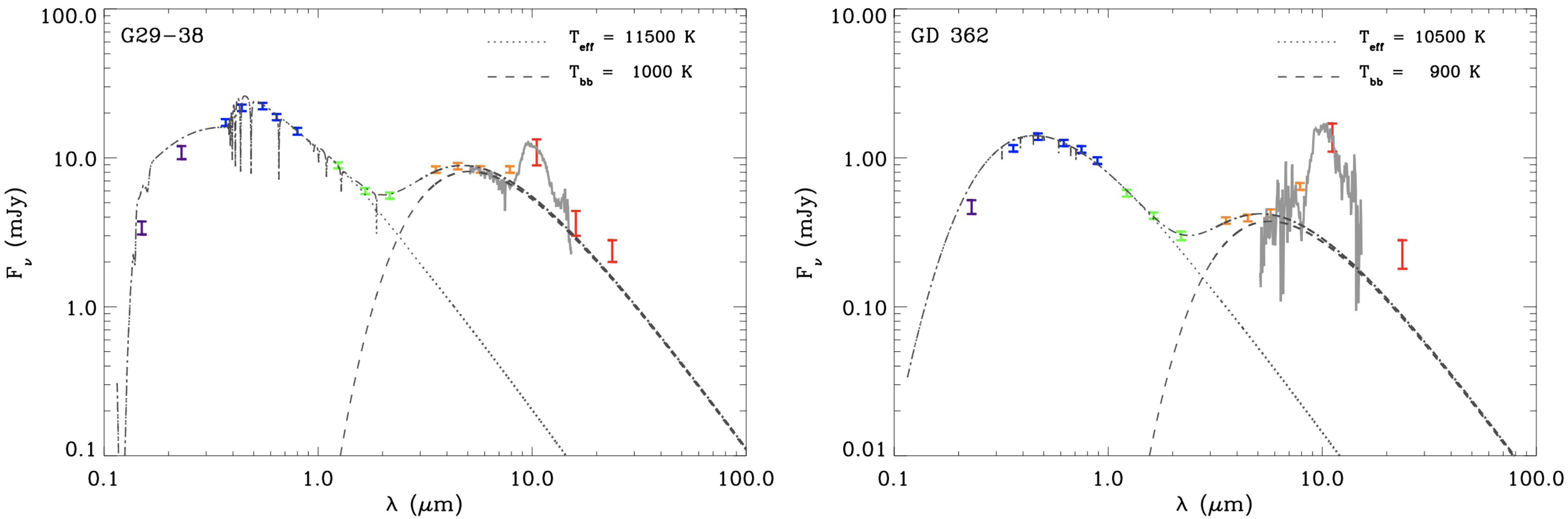

Figure 1.12: Spectral energy distributions of the first two white dwarfs with detected debris discs from *Spitzer*. The photometric data is shown by colour error bars, where the colour changes with the observed wavelength range. The solid grey lines show spectra measured with IRS, the dotted grey line indicates a model white dwarf atmosphere at the temperature indicated on each panel, and the dashed grey shows a black body model to approximate the temperature of the disc's dust. Figures taken from Farihi [2016].

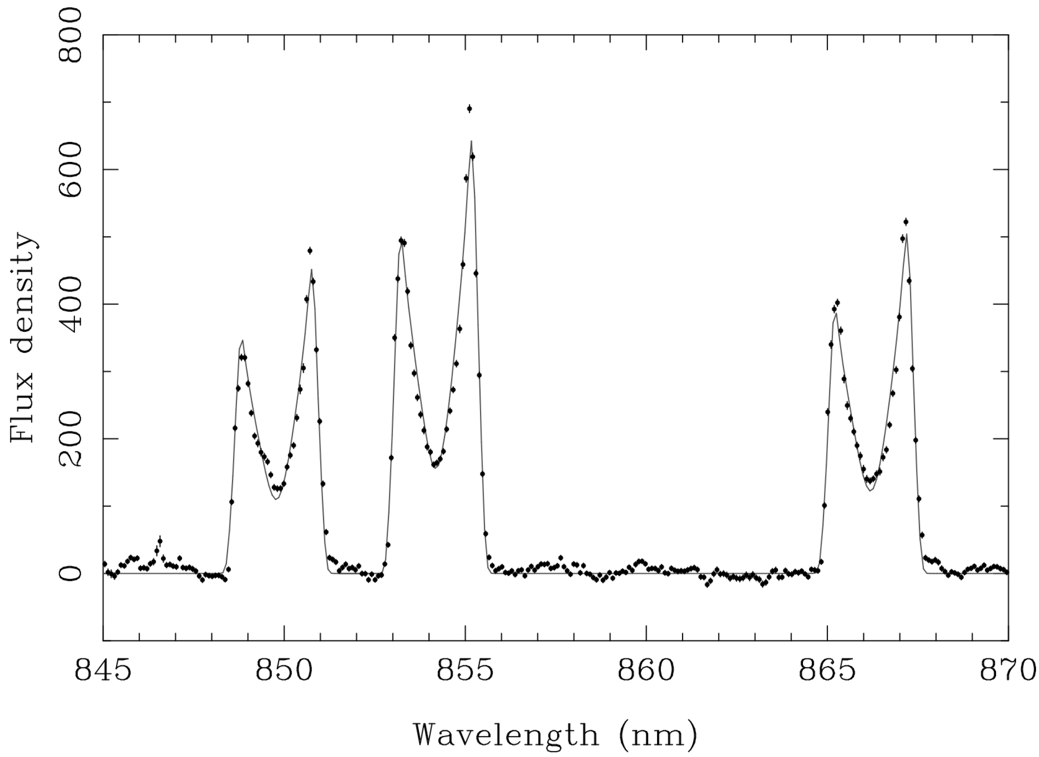

Figure 1.13: The observed double-peaked emission lines of the Ca II triplet for SDSS J1228+1040. The asymmetric profiles are due to the blue- and red-shifted light measured for the rotating gas. The data shown by the diamond markers have been overlaid by a disc model further discussed in Gänsicke et al. [2006]. Figures taken from Gänsicke et al. [2006].

observed data is shown by diamond markers and is overlaid by a debris disc model which constrains the outer radius of the disc at $\sim 1.2R_{\odot}$.

In early 2020, there had only been seven confirmed gaseous debris discs through the detection of double-peaked emission lines. This small number of detections implies an occurrence rate of gaseous debris discs detectable through Ca II emission lines as $0.067\pm^{0.042}_{0.025}$ per cent [Manser et al., 2020]. However, recent advances have greatly increased the number of known gaseous debris discs. In 2020 alone, 16 new gaseous debris discs were added to the literature [Melis et al., 2020; Dennihy et al., 2020; Gentile Fusillo et al., 2021], with all systems displaying gaseous emission lines, IR excesses from a dusty component and atmospheric pollution of the host white dwarfs. Thus, the observation of gaseous white dwarf debris discs is a rapidly evolving and expanding field. I now turn our attention towards understanding how these observed dust and gas discs are formed.

Debris Disc Models and Formation Theories

The observed IR excesses have often been modelled as an opaque, flat disc of material (analogous to the rings of Saturn) formed following the tidal disruption of a planetary body and was first described in Jura [2003]. Such a flat ring of debris is characterized by the stellar radius R and effective temperature T_{eff}, the distance at which the disc orbits d and three free parameters which describe the geometry of the disc: the inner and outer disc radii r_{in} and r_{out} respectively, and the inclination i. The flux from the ring can then be described by the following

$$F = \frac{2\pi \cos i}{d^2} \int_{r_{\text{in}}}^{r_{\text{out}}} B_\nu(T) r dr, \tag{1.15}$$

where $B_\nu(T)$ is Planck's function. Calculating a range of flux profiles predicted from the equation above, and comparing them to the shape of observed IR excess allows us to place constraints on the geometry of the discs. Early studies which modelled IR excesses with this model found that discs could spatially extend from around $0.1R_{\odot}$ to $\sim 0.4R_{\odot}$, complimentary with the idea of formation through tidal disruptions at the Roche radius [Jura et al., 2007; Farihi et al., 2008].

A star's Roche radius, R_{Roche}, describes the orbital distance at which its gravitational forces are able to overcome the forces holding together an object orbiting it. As such, the Roche radius can be a complex function of the orbiting body's shape, spin state, composition and how exactly disruption is defined. Consequently, there have been a number of analytical descriptions of the Roche radius presented in the literature. One particular form which takes into account the assumed rubble pile nature of a minor body is presented in Bear and Soker

[2013] as

$$
\begin{aligned}
R_{\text{Roche}} &\approx C R_{\text{WD}} \left(\frac{\rho_{\text{WD}}}{\rho_{\text{ast}}}\right)^{1/3} \\
&\approx 1.3 \left(\frac{C}{2}\right) \left(\frac{M_{\text{WD}}}{0.6 M_{\odot}}\right)^{1/3} \left(\frac{\rho_{\text{ast}}}{3\text{g cm}^{-}3}\right)^{-1/3} R_{\odot},
\end{aligned}
\tag{1.16}
$$

where R_{WD}, M_{WD} and ρ_{WD} are the radius, mass and density of the white dwarf respectively and ρ_{ast} is the density of the rubble pile. The coefficient C aims to encompass other physical parameters of the body and its value is in the range $1.3 - 2.9$ [Davidsson 1999; Jura 2003; see Table 1 of Veras et al. 2017 for C values for specific body assumptions]. Under the assumption of a solid, spinning rubble pile asteroid with a fiducial density of 3 g cm^{-3} (roughly indicative of a body composed of solid ices and dust) the Roche radius around a $0.6M_{\odot}$ white dwarf resides at approximately $0.94R_{\odot} \sim 0.004$ au.

Thus, if an object reaches a distance towards the white dwarf that is smaller than R_{Roche}, the object will be shredded down to its smallest constituent particles whose internal strength is able to dominate over the gravitational forces. These smaller, constituent components then go on to form the debris discs we observe around the white dwarfs.

A number of numerical simulations have directly modelled how a planetesimal reacts during the tidal disruption process [e.g. Debes et al., 2012; Veras et al., 2014b, 2017; Malamud and Perets, 2020a,b; Li et al., 2021]. The simulations typically find that a body will take a number of pericentre passes to disrupt completely, with the resultant debris spreading out in streams before filling an annulus around the white dwarf. Figure 1.14 shows the tidal disruption process from one simulation presented in Veras et al. [2017]. In just a few orbits, the outer material of the body is stripped away and within four orbits the body has completely tidally disrupted and formed a stream of debris orbiting the white dwarf.

Veras et al. [2014b] presents a closed-form expression to estimate the amount of time it would take for the debris formed from a tidal disruption event to completely fill a ring of material,

$$
\begin{aligned}
\frac{t_{\text{fill}}}{P} = r_b^{3/2} \Bigg[&\left\{ \frac{r_b^2 + 2aR - r_b R}{r_b - R} \right\}^{3/2} \\
&- \left\{ \frac{r_b^2 - 2a \times \min(r_{\text{crit}} - r_b, R) + r_b \min(r_{\text{crit}} - r_b, R)}{r_b + \min(r_{\text{crit}} - r_b, R)} \right\}^{3/2} \Bigg]^{-1},
\end{aligned}
\tag{1.17}
$$

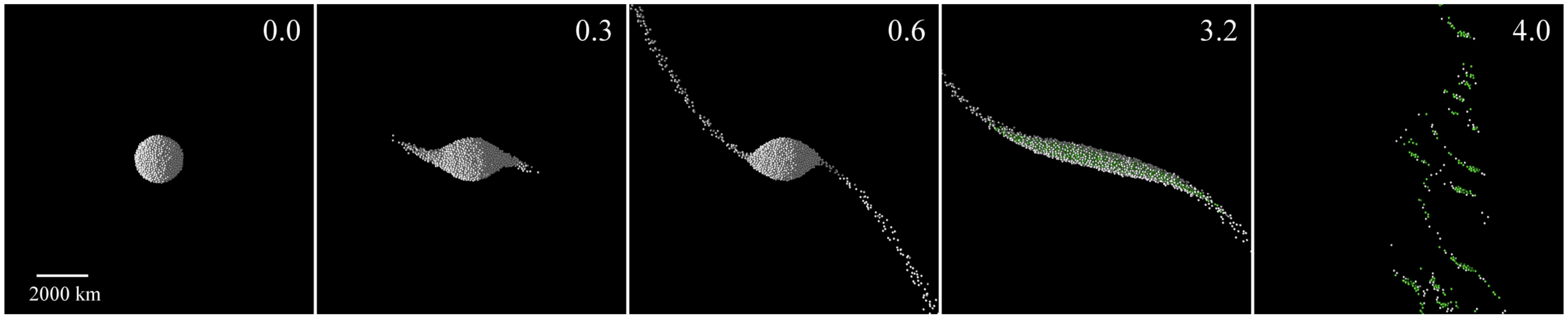

Figure 1.14: The tidal disruption process for a differentiated synchronously-spinning rubble pile asteroid orbiting a $0.6M_{\odot}$ white dwarf with $e = 0.1$. The simulation snapshots are shown in the rotating frame with the white dwarf to the left and the asteroid moving upwards. The number in the top right corner indicate the number of orbits the body has undergone at the particular snapshot. The differentiation is indicated by white particles representing the mantle and green particles the core. The mantle particles are stripped very quickly and then the core is able to disrupt with a stream of debris forming after just three orbits. Figures from Veras et al. [2017].

with

$$
\begin{aligned}
r_{\text{crit}} &= \frac{2ar_b}{\left(1+\frac{M}{M_{\text{WD}}}\right)(2a-r_b)}, \\
&\approx \frac{2ar_b}{2a-r_b}.
\end{aligned}
\tag{1.18}
$$

r_b is the distance at which the instantaneous disruption happens, R is the radius of the disrupting planetesimal and a is the semi-major axis of the body's orbit. The distance at which the orbit of a particle liberated during a tidal disruption event becomes parabolic is described by the variable r_{crit} as in Equation 1.18. If the distance of the debris particle r_{p} is less than r_{crit}, the debris remains in an elliptical bound orbit, and if $r_{\text{p}} > r_{\text{crit}}$, the debris is ejected on a hyperbolic orbit. Thus, r_{crit} determines the amount of disrupted material which remains bound to the host star.

Assuming that the body disrupts at the pericentre of its orbit, $r_b = a(1-e)$, Veras et al. [2017] find that the filling time for the debris observed around WD 1145+017 can further be approximated as

$$
t_{\text{fill}} \approx 250\,\text{days}\left(\frac{a}{0.00535\text{au}}\right)\left(\frac{R}{100\text{km}}\right)^{-1}(1-e)^2, \tag{1.19}
$$

and suggest that depending on the mass of the progenitor a complete ring of debris could be filled in 10 – 100 days.

The progenitor body by necessity has to enter the region close to the white dwarf at high eccentricity. This requirement is driven by the understanding already explored in Section 1.2 that planets and planetesimals are unlikely to survive the violent giant branch phases of evolution within a few au of the central star. A planetesimal which has a semi-major axis of 7 au (the survival limit for minor bodies due to giant branch radiation) would require an eccentricity > 0.99 in order to have a pericentre at the fiducial Roche radius calculated above.

The debris discs we observe around white dwarfs appear to be on compact, circular orbits, thus a number of processes have been suggested to reduce the eccentricity of the debris. Veras et al. [2015b] find that the Yarkovsky and Poynting-Robertson (PR) effects (futher discussed in the next section) are capable of shrinking and circularizing the orbits of small dust on timescales which are orders of magnitude smaller than the cooling age of the white dwarf.

As the tidal disruption fragments will vary in size, they will undergo circularization at different timescales. The orbits begin to precess due to general relativity, which makes collisions between fragments more common and drives the size distribution of the the debris down. Kenyon and Bromley [2017a] discuss how collisional cascades are able to reduce tidal disruption fragments with initial sizes in the range 1 – 100 km to μm dust in $10^2 - 10^6$ yrs.

Observed evolution in the light curve of debris around WD 0145+234 has been attributed to collisional evolution in the disc producing both gas and dust [Swan et al., 2021]. Stone et al. [2015] discuss the role that gas drag plays in circularizing debris. Finally, Malamud et al. [2021] note that if an incoming tidally disrupted body interacts with an extant debris disc, then the resulting debris can rapidly circularize through dissipative forces.

As the outer edge of the disc is governed roughly by the Roche radius where bodies are tidally disrupted and then ground down to dust, the inner edge is controlled by the stellar radiation through the sublimation front. As the dusty material is pulled onto tighter orbits through effects such as PR drag, it may eventually reach a radial distance where the temperature due to the stellar radiation is large enough that the dust can sublimate.

Steckloff et al. [2021] define the sublimation radius as the point where radiative and sublimative heat loss mechanisms are equal and so material interior to this radius will sublimate. This occurs at temperatures in the range 1540 – 2560 K for a range of chemical species commonly found in Solar System bodies [Steckloff et al., 2015]. This leads to an inner disc edge at distances around $0.1 - 0.5 R_\odot$, although this is heavily dependent on the effective temperature of the white dwarf and the dominant chemical species in the debris. The inner edge of debris discs being driven by sublimation naturally explains why debris discs around extremely young and hot white dwarfs are poorly observed. As the sublimation radius is so strongly dependent on the temperature of the white dwarf and it migrates inwards as the white dwarf ages and cools, the sublimation radius for extremely hot white dwarfs may be outside of the Roche radius, which directly precludes the formation of dusty debris discs.

The region between the inner edge of the white dwarf's debris disc and the surface of the star itself is then thought to be filled with the gaseous products of sublimation at the disc edge.

Disc Accretion

Observations of continuous accretion onto white dwarfs requires that material is continuously being delivered to the inner edge of the debris discs where they can sublimate and subsequently be accreted.

Poynting-Robertson (PR) drag has long been evoked as an effective mechanism for replenishing inner disc material. Stellar radiation incident on small dust grains can act to remove angular momentum and cause the particles to spiral inwards towards the star [Poynting, 1904; Robertson, 1937]. The mass delivery rate to the sublimation radius due to PR drag can be expressed as

$$\begin{aligned} \dot{M}_{\rm PR}(r) &= \frac{4\phi_r}{3\pi} \frac{R_*}{r} \frac{L_*}{c^2} \\ &\approx 10^8 \mathrm{g\,s^{-1}} \phi_r \frac{L_*}{10^{-3} L_\odot} \frac{20 R_*}{r}, \end{aligned} \tag{1.20}$$

where L_*, R_* are the luminosity and radius of the star, r is the radial distance from the star, c is the speed of light and ϕ_r characterizes the efficiency of the radiative momentum absorption at the disc surface [Rafikov, 2011a]. By assuming that the size of the particles is much larger than the characteristic wavelength of the stellar radiation, it can be defined as $\phi_r \approx 1 - e^{-\tau_{\|}}$, where $\tau_{\|}$ is the optical depth at the full disc thickness.

This mass delivery rate estimate is of a similar order of magnitude to the observed accretion rates at white dwarfs [Rafikov, 2011a,b]. Thus, although the inwards migration will have to compete with outward migration mechanisms driven by stellar radiation, such as radiation pressure and the Yarkovsky effect, PR drag has been widely invoked as a mechanism for replenishing the dusty material at the sublimation front.

The gaseous component interior to the sublimation front can then viscously spread down to the surface of the white dwarf where the accretion actually takes place. Rafikov [2011a] discusses that by assuming the typical α parameterisation of disc viscosity [Shakura and Sunyaev, 1973], the viscous time for this gaseous component can be given by

$$\begin{aligned} t_v &\sim \frac{R_s^2}{\nu} \\ &\approx 10\mathrm{yr}\,\frac{\mu_{28}}{\alpha}\,\frac{1500\mathrm{k}}{T}\left(M_{*,1}\frac{R_s}{0.2R_\odot}\right)^{1/2}, \end{aligned} \tag{1.21}$$

where R_s is the sublimation radius, $M_{*,1} \equiv M_*/M_\odot$, μ_{28} is the mean molecular weight of the metallic gas normalised to pure Si, T is the temperature and α is dependent on the particular modelled viscosity. Thus, material can be delivered to the white dwarf fast enough to explain observed accretion rates as long as it is delivered to the sublimation radius at sufficient rates.

With an understanding of how debris discs evolve and form around white dwarfs, below I look to describe the processes that deliver planetesimals to the Roche radius in the first place.

Planetary Systems

Although observational evidence for planetary systems around white dwarfs has existed since the 1920s, the first detection of a (relatively) intact planetesimal took almost another century. In 2015, the first detection of a planetesimal around a white dwarf was made by Vanderburg et al. [2015], and since then the population of known planetary bodies around white dwarfs has increased exponentially. Below is a summary of some of the most important of these discoveries.

Minor bodies

In 2015, Vanderburg et al. [2015] reported the discovery of deep and irregular transits around WD 1145+017 in data from the *K2* mission. Six significant periodicities in the light curves were identified with periods in the range 4.5 – 4.9 hours, indicative of orbiting

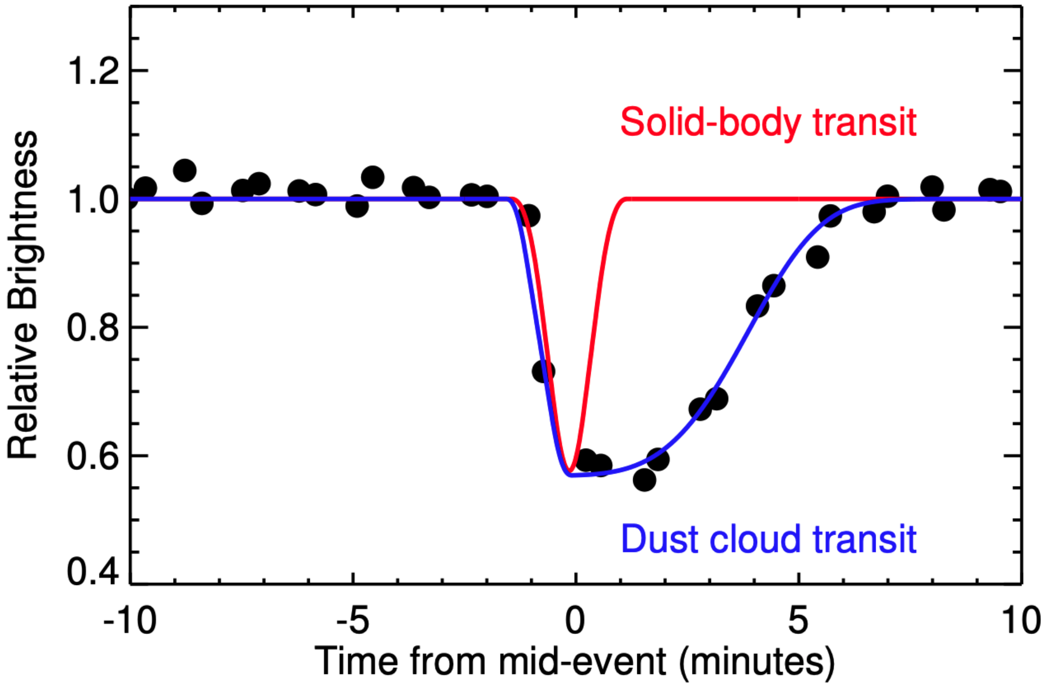

Figure 1.15: Light curve for the strongest transit signature observed around WD 1145+017 by the Fred L. Whipple Observatory (FLWO). The observed photometry is shown in black dots, a transit model for a sub-Earth sized planet orbiting the white dwarf is shown in red and the model in blue shows shows the expected transit for a solid body with a trailing dust cloud. The observed transit strongly agrees with the model for a dust cloud transiting the white dwarf. Figure taken from Vanderburg et al. [2015].

objects with semi-major axes $a \sim 0.005$ au. The light curves themselves did not show the usual u-shape displayed by solid planetary body transits as discussed in Section 1.1.2, and instead showed deep, irregular and asymmetric shapes as shown in Figure 1.15. The shape of these transits strongly agrees with a model for a disrupting solid body with a trailing dust cloud. It is thought that the orbiting planetesimals are approximately at the Roche radius and sporadically launch plumes of gas which condense into the trailing dust clouds [Vanderburg et al., 2015]. Thus, the first detection of (relatively) intact planetary bodies around a white dwarf seemingly confirm the previously discussed theories of debris disc formation.

As this discovery represented a landmark for the field of post-main-sequence planetary systems, it has become one of the most well observed and modelled systems. Dedicated observation campaigns were able to further characterize the transiting debris. Croll et al. [2017] proposed that phase shifts in the transits detected by Vanderburg et al. [2015] were caused by a number of different discrete bodies all orbiting in near identical 4.5 hour orbits. Rappaport et al. [2016] and Gary et al. [2017] carried out long-term monitoring campaigns of the system and identified significant evolution and variability, sometimes on a night-by-night basis. A large number of other dedicated observational studies have all contributed a wealth of information to inform theoretical studies [e.g. Gänsicke et al. 2016; Zhou et al. 2016; Izquierdo et al. 2018; and Vanderburg and Rappaport 2018 for a pre-2018 review of WD 1145+017].

Subsequent theoretical studies have produced a number of explanations for observed features, a few of which are summarised below. Rappaport et al. [2016] suggest drifting features are caused by fragments which are broken off from the main body and subsequently orbit at slightly smaller distances. Farihi et al. [2017] argue that the transit shapes can be caused by dust clouds trapped by the stellar magnetosphere. Gurri et al. [2017] use N-body simulations to find that body masses larger than $\simeq 10^{20}$ kg, or on non-circular orbits ($e > 10^{-3}$), would become unstable on timescales shorter than the length of time the debris system around WD 1145+017 has been observed. Duvvuri et al. [2020] use N-body simulations to investigate how different internal structures affects the shape of a transit light curve and suggest that the observations may be best explained by the tidal disruption of an object with low core fraction and low mantle-to-core density ratio.

The next white dwarf transit signatures were reported around ZTF J0139+5245 in 2019 [Vanderbosch et al., 2020] and like those in the WD 1145+017 system, the transits are very deep and irregular, implying a disintegrating debris system. However, these signatures recur on a period of ≈ 107.2 days and last between $15 - 25$ days, which suggests a vastly different geometry compared to the WD 1145+017 system. For a planetesimal with the observed semi-major axis of 0.36 au to cross the Roche radius and tidally disrupt, it requires an extremely high eccentricity ($e > 0.97$). Vanderbosch et al. [2020] suggest that this high eccentricity could show the system is in the first stages of tidal disruption before the ensuing disc of debris is shrunk and circularized (as in Section 1.3.2). Alternatively, Veras et al. [2020a] find that the extremely high eccentricity constraint can be relaxed if the body is an elongated ellipsoid as rubble pile bodies can rotationally fission due to the chaotic exchange of orbital and rotational energy at pericentre.

In the three years since the detection of ZTF J0139+5245, even more transiting debris systems have been found [e.g. Vanderbosch et al., 2021; Farihi et al., 2022] and a large number of candidate systems have been identified and are shown in Figure 1.16 [Guidry et al., 2021].

One final white dwarf minor planet to note is that orbiting around SDSS J1228+1040 which was not detected through transit signatures. With a long period observational baseline, Manser et al. [2016] identified a low-amplitude variability in the Ca II emission lines from the associated gaseous debris disc with a period of 123.4 ± 0.3 minutes. The authors attribute this variation to an intact planetesimal orbiting within the dust disc actively producing gas. In order for such a planetesimal to resist tidal disruption at its orbit within the white dwarf's Roche radius, the object requires a high internal strength and likely a density > 7.7 g cm^{-3}. This extreme density could imply the body is a differentiated iron-rich core of a larger body which crossed the Roche radius and had its outer layers stripped which subsequently formed

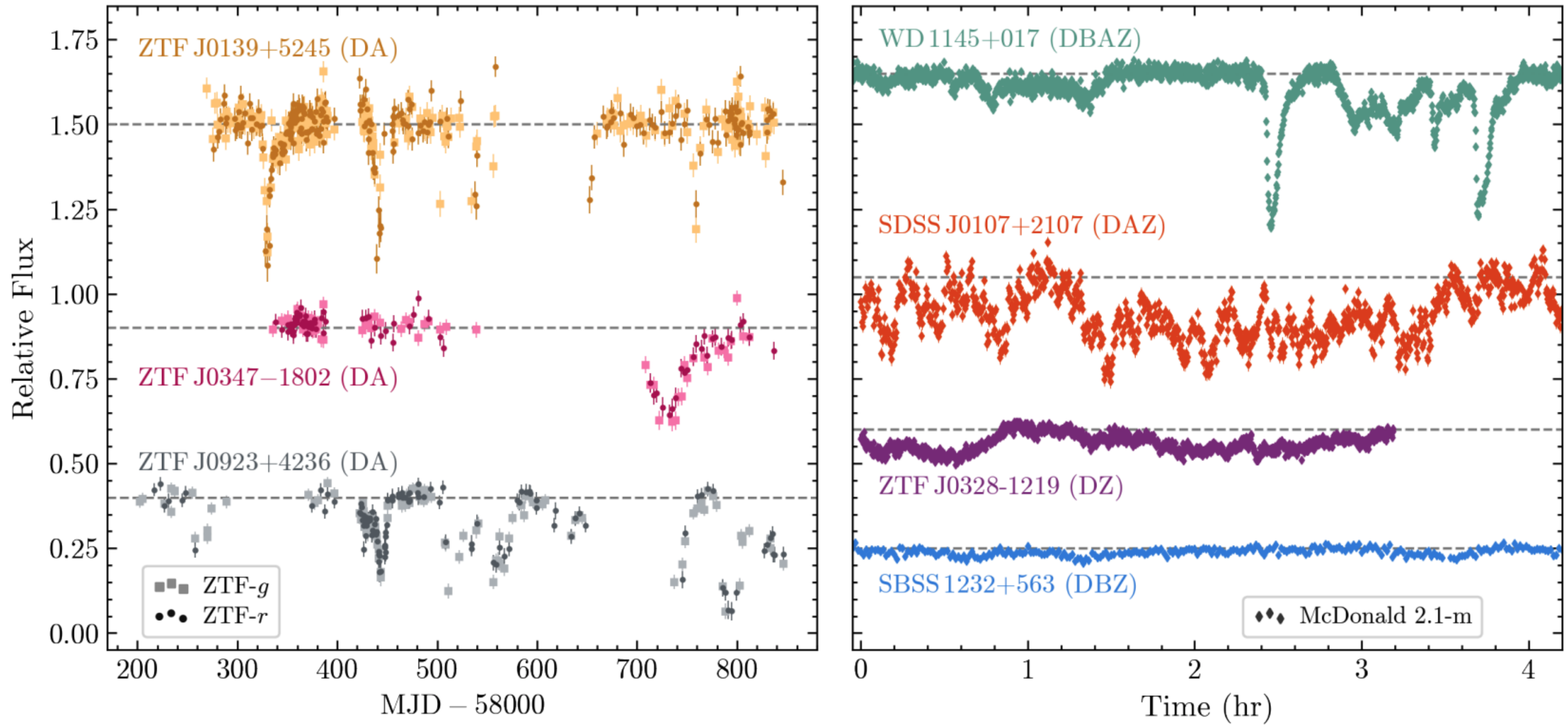

Figure 1.16: Light curves for the confirmed white dwarf debris transit systems and a number of candidate systems observed by the Zwicky Transient Facility (ZTF) and McDonald observatory. The left panel shows systems where the transit periods are on the order of days and the transits displayed in the right panel have hour long periods. The spectral type for each host white dwarf is shown in brackets after the source name. Figure taken from Guidry et al. [2021].

the debris disc.

The growing diversity of planetesimal-sized objects around white dwarfs highlights the variety of delivery methods required to explain observations. A large number of theoretical studies have attempted to understand the dynamical processes which drive planetesimals towards the white dwarf, invoking a number of different planetary system architectures including multiple stars, major planets, and even no large bodies at all.

Studies which include no planets invoke other mechanisms for the dynamical evolution of the minor bodies themselves, such as; sublimation driving volatile-rich planetesimals onto closer orbits [Veras et al., 2015a] and the chaotic exchange of orbital and spin energy causing elongated bodies to rotationally fission [Makarov and Veras, 2019; Veras et al., 2020a]. Veras et al. [2022] suggest that planetesimals may be able to pollute white dwarfs with no planetary influence through a mixture of PR drag, and the Yarkovsky and YORP effects.

Forces exterior to the planetary system have also been considered, including; galactic tides, stellar flybys [Veras et al., 2020b], and the effect of stellar mass loss on Oort cloud analogues [Alcock et al., 1986; Parriott and Alcock, 1998; Veras et al., 2014c; Stone et al., 2015]. Further, distant stellar companions can initiate Kozai-Lidov cycles in orbiting bodies which lead to oscillations in both eccentricity and inclination [Kozai, 1962; Lidov, 1962] and can drive bodies to Roche limit crossing orbits [e.g. Hamers and Portegies Zwart, 2016; Stephan et al., 2017].

Including at least one planet increases the dynamical activity of post-main-sequence systems and thus the chances for planetesimal delivery. Increasing the number of planets in a system acts to increase the dynamical activity even further. Largely, less massive planets are more efficient at scattering planetesimals towards the white dwarf across longer timescales [Bonsor et al., 2011; Mustill et al., 2018; Maldonado et al., 2020a] and even a slight planetary eccentricity ($e > 0.02$) increases the rate of planetesimal perturbations [Frewen and Hansen, 2014]. Veras and Rosengren [2023] find that even planetary bodies down to the mass of the Earth's moon are capable of perturbing smaller bodies towards a white dwarf.

The dynamical instabilities between planets which lead to planetesimal scattering can be driven by the giant branch evolutionary changes. In systems with multiple planets, the stability of adjacent orbits is related to the planet-star mass ratio, and thus the mass loss on the giant branches can cause previously stable orbits to destabilise [Debes and Sigurdsson, 2002]. Further, the stellar mass loss can cause chaotic orbital regions to expand in size and instabilities between planets to occur even if their initial orbital separations are large [Caiazzo and Heyl, 2017; Veras et al., 2013b; Voyatzis et al., 2013; Mustill et al., 2014, 2018].

Post-main-sequence stellar evolution can also affect resonances within a planetary system with consequences for planetesimal populations around white dwarfs. Mean motion resonances (MMRs) occur when two orbiting bodies orbit the central star with periods that are an integer (or near) ratio of each other. These resonances can be stable if the bodies' orbits do not lead to close encounters between the bodies, else they are unstable. Due to the stellar mass loss on the giant branches, the width of these resonant regions increases which allows planetesimals on previously stable orbits to become unstable and possibly perturbed towards the central body [Smallwood et al., 2021].

Alternatively, secular resonances which act on much longer timescales occur when the precessional frequencies of two bodies have integer ratios. Planetary engulfment on the giant branches changes the distribution of mass in a system which changes the locations of secular resonances [Smallwood et al., 2018]. This can have a similar effect of perturbing previously stable planetesimal orbits. The role of resonances in perturbing planetesimals onto Roche crossing orbits is being increasingly studied as a mechanism for causing white dwarf pollution.

Thus, although pollution without the presence of planets is possible, planets can act as drivers of dynamical activity which increase the chances of planetesimal delivery. Below I discuss the current evidence for planets in white dwarf systems.

Major bodies

Although there had been observations of giant planets in systems containing white dwarfs since the early 1990s [Thorsett et al., 1993; Sigurdsson et al., 2003; Luhman et al., 2011], evidence for planets around single white dwarfs that could drive planetesimals towards the star proved more elusive [e.g. Hogan et al., 2009; Faedi et al., 2011; Fulton et al., 2014; Xu et al., 2015; Sandhaus et al., 2016].

That is until 2019, when the first giant planet was inferred to be orbiting at very close distances to its host white dwarf [Gänsicke et al., 2019]. The ~ 27 750 K white dwarf WD J0914+1914 is observed accreting material rich in hydrogen, oxygen and sulphur from a gaseous debris disc at $\sim 3.3 \times 10^9$ g s^{-1}. Observed spectra display the classic double-peaked emission lines from a gaseous debris discs, but the omission of the usual Ca II lines and inclusion of a Hα line sets this system apart from other gas discs. The inferred composition of the debris disc is distinct from the usual rocky material observed around white dwarfs. Gänsicke et al. [2019] argue that the most likely explanation for this observation is that the white dwarf is accreting from a purely gaseous debris disc being fed by an evaporating ice giant planet with similar composition to the deep icy layers of the Solar System's ice giants. They find that such a giant planet orbiting at $a \sim 15 R_\odot$ would be sufficiently irradiated by the white dwarf's extreme ultraviolet (EUV) radiation that atmospheric evaporation can produce the observed accretion rate.

Theoretical studies modelling the evolution and inwards migration of the planet suggest that it could be highly inflated [Veras and Fuller, 2020; Zotos et al., 2020]. Stephan et al. [2021] propose that a currently unknown companion to WD J0914+1914 could have

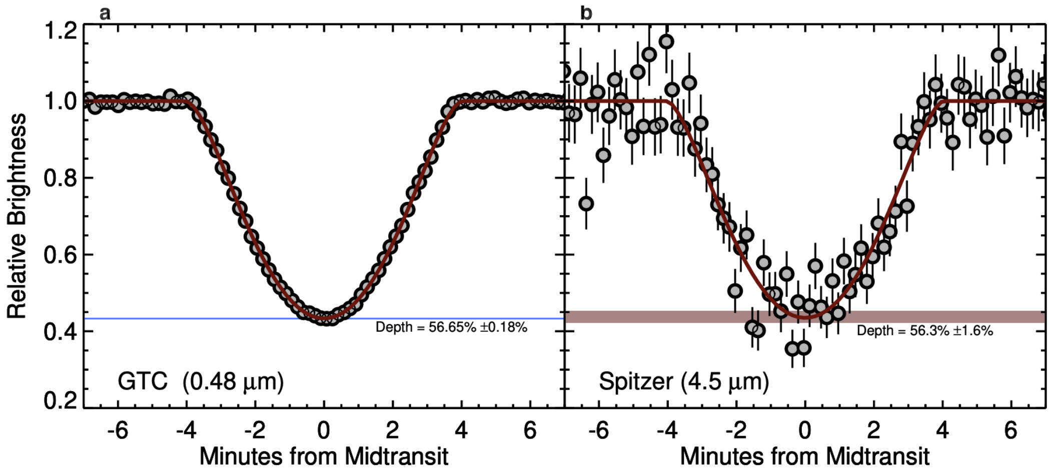

Figure 1.17: Observed transits of WD 1856 b from the Gran Telescopio Canarias (GTC, left panel) and *Spitzer* (right panel). The standard *u*-shape expected for a solid body can clearly be seen and the deep (> 50 per cent) transit suggests a large body. Figure taken from Vanderburg et al. [2020].

perturbed the planet onto its short period orbit through the eccentric Kozai-Lidov mechanism within the stars $\sim$ 13 Myr cooling age. Further, Veras [2020] suggest that the close-in orbit of the planet could act to prevent small bodies from polluting the white dwarf through radiative processes which may explain the lack of observed rocky pollution. Although this discovery again represented the disrupted remains of a planetary body, the first glimpses of an intact planetary body were not far behind.

In 2020, Vanderburg et al. [2020] reported the discovery of a giant planet transiting the DC white dwarf WD 1856+534 using the *TESS* space telescope. The planet (hereafter WD 1856 b) transits in front of the $\sim$ 4710 K WD every 1.4 days which suggests a semi-major axis of $a \sim 0.02$ au. Examples of the transit light curve are shown in Figure 1.17. The extremely clean and deep transits suggest a completely intact body with a mass $< 13.8 M_{\rm J}$ due to the lack of observed IR excess which would indicate a brown dwarf. Thus, this body is almost certainly in the mass range for a giant planet.

The community were quick to model the formation of such a system. Chamandy et al. [2021] found that the planet could not have been at its current location during the GB phases and survived a common envelope event, unless there was a similarly large planet interior to its orbit which was engulfed first. However, Lagos et al. [2021] argued that it could have survived a common envelope event, but only if some other source of energy, such as recombination energy stored in the envelope, contributed to the expelling of the envelope. Alternatively, the Kozai-Lidov mechanism driven by the distant K dwarf binary companion to WD 1856 can form the planet's observed orbit after the white dwarf phase began, assuming it initially orbited at larger distances [Muñoz and Petrovich, 2020; O'Connor et al., 2021; Stephan et al., 2021]. Perhaps one of the most interesting aspects of this system is that the host star is currently unpolluted, thus similarly to WD J0914+1914 it has not accreted any rocky material from planetesimals in its recent history. This adds required complexity to models which try to deliver planetesimals to the Roche radii of white dwarfs under the influence of remnant planets, since two white dwarfs with observed planets have no observed pollution (see Chapter 4 for discussion of such a model).

Turning to planets which do not reside on short period orbits there have been recent exciting hints. Blackman et al. [2021] were unable to detect a main sequence host star to a microlensing event, which suggests a $\sim 1.4M_{\mathrm{J}}$ planet orbiting a $\sim 0.53M_{\odot}$ white dwarf. Although, the nature of microlensing events precludes follow up observations and full characterisation of this planetary system. The exquisitely precise astrometric data becoming available from the *Gaia* mission may be able to detect giant planets orbiting white dwarfs at wide distances. Estimates suggest that future data releases could lead to the detection of at least eight further white dwarf planets [Sanderson et al., 2022].

The rapidly expanding catalogue of remnant planetary systems around white dwarfs necessitates careful theoretical study in order to understand how these systems evolve into their current observed state. Thus, the work presented in this thesis aims to contribute to the expanding theoretical literature surrounding white dwarf planetary systems.

1.4 Thesis Outline

This thesis aims to contribute to the theoretical efforts made to model and understand the evolution of planetesimals in post-main-sequence planetary systems. With the rapidly increasing population of known white dwarf debris systems highlighting the variety of different planetesimal origin locations and delivery mechanisms required, these modelling efforts are of high importance.

In Chapter 2, I discuss the consequences of using a more accurate triaxial ellipsoidal shape model for planetesimals approaching a white dwarf and highlight the effect this has on different disruption mechanisms. Chapter 3 presents the first investigation into the dynamical evolution of white dwarf binary asteroid systems and the role binarity may have on the pollution of white dwarfs. The post-main-sequence migration of giant planets to short-period orbits (such as WD 1856 b) and the subsequent effect on planetesimal populations is considered in Chapter 4. Finally, in Chapter 5, I conclude the work and discuss the prospects for the future of post-main-sequence planetary system science.

Chapter 2

White dwarf planetary debris dependence on physical structure distributions within asteroid belts

White dwarfs which exhibit transit signatures of planetary debris and accreted planetary material provide exceptional opportunities to probe the material composition and dynamical structure of planetary systems. Although previous theoretical work investigating the role of minor body disruption around white dwarfs has focussed on spherical bodies, Solar System asteroids can be more accurately modelled as triaxial ellipsoids. Here we present an analytical framework to identify the type of disruption (tidal fragmentation, total sublimation or direct impact) experienced by triaxial asteroids approaching white dwarfs on extremely eccentric ($e \sim 1$) orbits. This framework is then used to identify the outcomes for simplified Main Belt analogues of 100 bodies across five different white dwarf temperatures. We also present an empirical relationship between cooling age and effective temperature for both DA and DB white dwarfs to identify the age of the white dwarfs considered here. We find that using a purely spherical shape model can underestimate the physical size and radial distance at which an asteroid is subjected to complete sublimation, and these differences increase with greater elongation of the body. Contrastingly, fragmentation always occurs in the largest semi-axis of a body and so can be modelled by a sphere of that radius. Both fragmentation and sublimation are greatly affected by the body's material composition, and hence by the composition of their progenitor asteroid belts. The white dwarf temperature, and hence cooling age, can affect the expected debris distribution: higher temperatures sublimate large elongated asteroids, and cooler temperatures accommodate more direct impacts.

2.1 Introduction

White dwarfs provide a unique opportunity to investigate the composition of exoplanetary bodies. The extreme surface gravities of white dwarfs cause elements heavier than hydrogen or helium to rapidly sink and not be visible in spectra [Paquette et al. 1986b; Wyatt et al. 2014; see Chapter 1.3.2 for more details]. However, observations indicate that between a quarter and half of all white dwarfs have evidence of metals in their atmospheres [Zuckerman et al., 2010; Koester et al., 2014], with the most commonly visible elements being closely aligned with the composition of the Solar System terrestrial planets [Jura and Young, 2014; Hollands et al., 2018; Doyle et al., 2019]. The consistent visibility of these metals suggest ongoing accretion of planetary material.

Recent observations have found evidence of planetary bodies which could lead to this accretion (Chapter 1.3.2). Vanderburg et al. [2015] identifies at least one, but most likely at least six, rocky planetesimals with densities $> 2\ \mathrm{g\,cm^{-3}}$, actively disrupting around the white dwarf WD 1145+017. Figure 1.15 shows an example light curve recorded for the strongest transit signature observed around WD 1145+017 [Vanderburg et al., 2015]. These planetesimals orbit on short periods ($\sim 4.5 - 4.9$h) near the Roche limit of the star, causing them to be frequently releasing material which forms a dust cloud, observed in asymmetric transit curves of up to 60 per cent in depth[1] [See also Gänsicke et al., 2016; Rappaport et al., 2016; Zhou et al., 2016; Croll et al., 2017; Gary et al., 2017; Izquierdo et al., 2018; Vanderburg and Rappaport, 2018].

Vanderbosch et al. [2020] report the observation of a planetesimal on a highly eccentric ($e > 0.97$) orbit around the white dwarf ZTF J0139+5245 producing transit depths of up to 45 per cent. The observations indicate that the object is in an early stage of disruption. However, its large 110-day period could be indicative of an orbital pericentre outside of the star's Roche limit. The planetesimal's disruption could therefore originate from an alternative mechanism to the canonical Roche limit disruption, which doesn't involve tidal forces from the star. Veras et al. [2020a] show that chaotic exchange of orbital and spin angular momentum can lead to an ellipsoidal planetesimal achieving a spin rate higher than the cohesionless spin barrier [see Figure 1.5 or figure 1 of Warner et al. 2009] and disrupting.

Most recently Vanderbosch et al. [2021] reported a third transiting minor body around the white dwarf ZTF J0328-1219, exhibiting two significant periods at 9.937 hours and 11.2 hours. The shorter period is roughly twice that of the debris orbiting WD 1145+017 and much less than that around ZTF J0139+5245. These transits show much shallower depths of 10 per cent and exhibit variability across the entire phase of the orbit, which suggests this object is in a different stage of disruption compared to the two previously discovered objects.

[1]See http://www.brucegary.net/1145/ for detailed observations of the debris around WD 1145+017 between 2015-19.

These three minor bodies actively disrupting in different orbital configurations raise questions about the circumstances that lead to planestesimal disruption around white dwarfs, and the object around ZTF J0139+5245 showcases the importance of adopting aspherical asteroid models. Further, Guidry et al. [2021] reported an additional two candidates exhibiting variation on long timescales similar to ZTF J0139+5245 and two more with shorter variations akin to WD 1145+017 (see Figure 1.16), highlighting an urgent need to increase our understanding of the disruption process.

During the giant branch phases of a star's evolution, 0.1-10 km bodies within ~ 7 au of the star will be broken down to their strongest components by the YORP effect [Veras et al., 2014a]. It is likely that bodies at larger distances or with high internal strengths [Veras and Scheeres, 2020] will remain intact despite both luminosity variations and the dynamical instability of the remnant planetary system after the giant branch mass loss phases [Debes and Sigurdsson, 2002; Veras and Gänsicke, 2015; Veras et al., 2016; Mustill et al., 2018; Maldonado et al., 2020a,b,c]. Minor bodies can then be vulnerable to perturbations from major bodies like more distant analogues of the gas giants recently discovered by Gänsicke et al. [2019] and Vanderburg et al. [2020] and approach the white dwarf on eccentric orbits.

A further $1-3$ per cent of white dwarfs display infrared excesses indicative of dusty debris discs [Rebassa-Mansergas et al., 2019], with $0.04-0.1$ per cent also having an observed gaseous component [Gänsicke et al., 2006; Manser et al., 2020]. Although it should be noted that discs, or narrower rings of debris, should exist around most polluted white dwarfs, with an estimated 90 per cent of all such discs being currently unobservable [Rocchetto et al., 2015]. It is generally thought that the perturbed minor bodies come within the star's Roche limit and are tidally disrupted, forming the observed debris discs [Debes et al. 2012; Veras et al. 2014b; Malamud and Perets 2020a; further discussion on debris disc formation is available in Chapter 1.3.2].

Numerical simulations of debris disc formation suggest a minimum disc mass of $\sim 10^{23}$ g to agree with observations [Kenyon and Bromley, 2017a; van Lieshout et al., 2018; Farihi et al., 2018], which is comparable to the mass of the largest Main Belt asteroid Ceres and the theoretically constrained mass of the asteroid disrupting around WD 1145+017 [Rappaport et al., 2016; Gurri et al., 2017]. The first white dwarf observed with an infrared excess caused by a dusty debris disc, G29-38 [Zuckerman and Becklin, 1987], is estimated to have accreted $\sim 4 \times 10^{24}$ g of material, about the total mass of the asteroids in the Solar System [Jura, 2003].

The observational mass and chemical abundance constraints, alongside the abundance and dynamical availability of asteroids, have led to these minor bodies being the preferred cause of white dwarf pollution. The observed accreted material is largely terrestrial in composition (Figure 1.11), which suggests the polluting bodies will have formed within the snow line of their planetary system [Martin et al., 2020]. A typical $0.6M_{\odot}$ white dwarf would have a $1.39 \pm 0.44M_{\odot}$ main sequence progenitor [see equation 4 of Cummings et al. 2018 and Chapter 1.3.1], with a water ice line at ~ 2 au [Adams and Shu, 1986; Kenyon and Hartmann, 1987; Chiang and Goldreich, 1997; Kennedy and Kenyon, 2008]. Although, it should be noted that a small number of white dwarf systems show evidence for the accretion of more icy, Kuiper Belt like bodies [Farihi et al., 2013; Raddi et al., 2015; Gentile Fusillo et al., 2017; Xu et al., 2017; Hoskin et al., 2020]. Further, dynamical mixing between the terrestrial Main Belt and volatile Kuiper Belt in the Solar System should populate the Main Belt region with both rocky and icy bodies. Thus, pollutant asteroids could have either a rocky terrestrial composition or a volatile rich icy composition.

Solar System asteroids have been well observed and studied, revealing a wide range of shapes, sizes and characteristics [Warner et al., 2009; Ďurech et al., 2018]. Observed orbital and physical parameters of these bodies have been successfully reproduced using ellipsoidal rather than spherical models [Carbognani et al., 2012; Dobrovolskis, 2019]. Using this knowledge, this chapter aims to expand on the work presented in Brown et al. [2017] (hereafter BVG17), which investigates the destruction of quasi-spherical bodies approaching a white dwarf on a parabolic trajectory. BVG17 formed a basic first step in understanding the role of asteroids in white dwarf pollution, but their results may not be suitably accurate for comparison to observations, or with other theory [e.g. Wyatt et al., 2014]. The following work (i) considers the effect of imposing asphericity on the asteroid treatment presented in BVG17, and (ii) applies the formalism to Main Belt analogue reservoirs of white dwarf pollutants.

In Section 2.2 we introduce the properties of the white dwarfs considered in this chapter (Section 2.2.1), the shape and material properties of asteroids (Section 2.2.2) and the properties of asteroid Main Belt analogues (Section 2.2.3). In Section 2.3 we introduce the conditions for the three different disruption regimes (i) *sublimation*, (ii) *fragmentation* and (iii) *impact* and the analytical formalism used to identify which form of disruption will befall a particular asteroid. We then apply this formalism to a Main Belt analogue of 100 asteroids in Section 2.4 and further investigate the role of triaxiality in the disruption regime an asteroid befalls. Section 2.5 briefly considers what happens to the asteroidal material after the initial disruption process identified in Section 2.4. We conclude in Section 2.6.

2.2 Properties

We begin by characterizing the physical and orbital properties separately of white dwarfs (Section 2.2.1), asteroids (Section 2.2.2) and asteroid belts (Section 2.2.3).

2.2.1 White Dwarfs

Although the majority of stars in the Milky Way will become white dwarfs [Koester, 2013], white dwarf masses are restricted to a very small range, typically between $0.4 - 0.8 M_{\odot}$, although the most massive white dwarfs can have $M_{\mathrm{WD}} \approx 1.4 M_{\odot}$. In the following, a white dwarf mass of $0.6M_\odot$ is used, which corresponds to the peak of the white dwarf mass distribution [Althaus et al. 2010; Kleinman et al. 2013; Tremblay et al. 2016; McCleery et al. 2020; see Figure 1.6].

Radii

White dwarf radii are closely related to their masses through a mass-radius relationship [Hamada and Salpeter, 1961]. BVG17 utilised a basic mass-radius relationship, which exploited the fact the relation is approximately independent of temperature as follows

$$R_{\rm WD} = \gamma R_\odot \left(\frac{M_{\rm WD}}{M_\odot}\right)^{-1/3}, \tag{2.1}$$

with $\gamma \simeq 10^{-2}$.

Here, we use a more precise form of the mass-radius relationship [eqs 27-28 of Nauenberg, 1972]

$$\frac{R_{\rm WD}}{R_\odot} \approx 0.0127 \left(\frac{M_{\rm WD}}{M_\odot}\right)^{-1/3} \sqrt{1 - 0.607\left(\frac{M_{\rm WD}}{M_\odot}\right)^{4/3}}, \tag{2.2}$$

by assuming a mean molecular weight per electron of 2 from Hamada and Salpeter [1961]. See Chapter 1.3.1 for an alternative mass-radius relationship and further discussion.

Temperature and cooling age

During the white dwarf phase, nuclear burning no longer proceeds, so although white dwarfs can start off at very high temperatures, they then monotonically cool for the rest of their lifetimes (Chapter 1.3.1). How long a star has been in the white dwarf phase is known as the cooling age, $\tau_{\rm WD_{cool}}$, and is a function of the temperature and mass of the white dwarf.

Here we derive an empirical relation between a white dwarf's cooling age and effective temperature $T_{\rm eff}$. This algebraic relation may potentially be useful for and facilitate future studies. We present both a long-form relation for $\tau_{\rm WD_{cool}}$ as a function of both $M_{\rm WD}$ and $T_{\rm eff}$ and a more compact relation (useful for analytical manipulations) as a function of just $T_{\rm eff}$ for a $0.6M_\odot$ white dwarf.

Our formulae attempt to match the cooling models of *both* DA and DB white dwarfs (with the same relation) from Fontaine et al. [2001]. These models can be downloaded [2] and should be used for higher precision work; here we seek just a rough estimate with an analytic formula. Our long-form relation is

[2] http://www.astro.umontreal.ca/~bergeron/CoolingModels

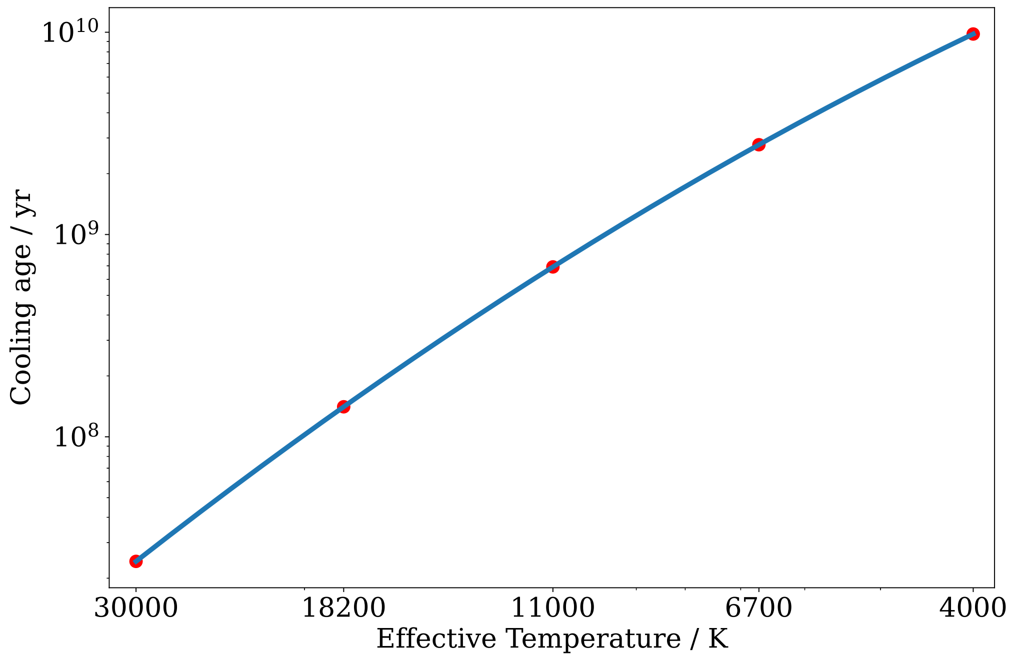

Figure 2.1: Empirical formula relating white dwarf cooling age to effective temperature for a $0.6M_\odot$ white dwarf. The red circles indicate the five equally log-spaced temperatures chosen for analysis in this work. From largest temperature to smallest the cooling ages are $\tau_{\mathrm{WD_{cool}}} = [0.02, 0.14, 0.69, 2.78, 9.8]$Gyr.

$$\log\left[\frac{\tau_{\mathrm{WD_{cool}}}}{yr}\right] = C_1 + C_2\log\left[\frac{T_{\mathrm{eff}}}{\mathrm{K}}\right] + C_3\left(\log\left[\frac{T_{\mathrm{eff}}}{\mathrm{K}}\right]\right)^2$$
$$+ C_4\exp\left[\frac{-\left(\frac{T_{\mathrm{eff}}}{K}\right)^3 - \left(10^4 - \frac{T_{\mathrm{eff}}}{K}\right)^3}{5500^3}\right]\cos\left[\frac{2\pi}{4700}\frac{T_{\mathrm{eff}}}{K}\right] \tag{2.3}$$
$$+ C_5\exp\left[\frac{-\left(\frac{T_{\mathrm{eff}}}{K}\right)^3 - \left(61000 - \frac{T_{\mathrm{eff}}}{K}\right)^3}{20000^3}\right]\sin\left[\frac{2\pi}{38000}\frac{T_{\mathrm{eff}}}{K}\right]$$

such that

$$C_1 = 8.62 - 6.49\left(\frac{M_{\mathrm{WD}}}{M_\odot}\right) + 13.58\left(\frac{M_{\mathrm{WD}}}{M_\odot}\right)^2 - 10\left(\frac{M_{\mathrm{WD}}}{M_\odot}\right)^3, \tag{2.4}$$

$$C_2 = 3.09 + 2.766\left(\frac{M_{\mathrm{WD}}}{M_\odot}\right) - 5\left(\frac{M_{\mathrm{WD}}}{M_\odot}\right)^2 + 3.33\left(\frac{M_{\mathrm{WD}}}{M_\odot}\right)^3, \tag{2.5}$$

$$C_3 = -0.839 - 0.014\left(\frac{M_{\mathrm{WD}}}{M_\odot}\right) + 0.039\left(\frac{M_{\mathrm{WD}}}{M_\odot}\right)^2, \tag{2.6}$$

$$C_4 = 0.7 - 2\left|\left(\frac{M_{\mathrm{WD}}}{M_\odot}\right) - 0.6\right|, \tag{2.7}$$

$$\begin{aligned} C_5 = 250\mathcal{H}&\left[\left(\frac{M_{\mathrm{WD}}}{M_\odot}\right) - 0.6\right] + \mathcal{H}\left[0.6 - \left(\frac{M_{\mathrm{WD}}}{M_\odot}\right)\right] \\ &\times\left[-1910 + 6000\left(\frac{M_{\mathrm{WD}}}{M_\odot}\right) - 4000\left(\frac{M_{\mathrm{WD}}}{M_\odot}\right)^2\right], \end{aligned} \tag{2.8}$$

where $\mathcal{H}$ is the Heaviside step function and, as is standard, log refers to $\log_{10}$. This long-form relation was derived for the ranges $0.4M_\odot \leq M_{\mathrm{WD}} \leq 0.8M_\odot$ and $4000 \leq T_{\mathrm{eff}} \leq 30,000$K. Within these ranges, the maximum per cent error with the Fontaine et al. [2001] models is 157 per cent.

For specifically the $M_{\mathrm{WD}} = 0.6M_\odot$ case, we obtain our compact relation by setting $C_4 = C_5 = 0$ such that

$$\log\left[\frac{\tau_{\mathrm{WD_{cool}}}}{yr}\right] \sim 7.45 + 3.67\log\left[\frac{T_{\mathrm{eff}}}{K}\right] - 0.83\left(\log\left[\frac{T_{\mathrm{eff}}}{K}\right]\right)^2. \tag{2.9}$$

This compact relationship differs from the Fontaine et al. [2001] models with a maximum per cent error of just 25 per cent. We plot the relationship in Figure 2.1, where five temperatures equidistant in log-space are shown as red circles. The points marked relate to the following effective temperatures and cooling ages $T_{\rm eff} = [30\,000, 18\,200, 11\,000, 6700, 4000]$ K and $\tau_{\rm WD_{cool}} = [0.02, 0.15, 0.69, 2.78, 9.8]$ Gyr.

Because $\tau_{\rm WD_{cool}} \sim 0$ yr relates to an effective temperature of $\sim 10^5$ K, the destructive forces of the stellar radiation will have its maximum reach at this time. Polluted white dwarfs have been observed with temperatures up to 27, 000 K [Koester et al., 2014]. Simulations have shown that disrupted material shouldn't make its way to the surface of the white dwarf until cooling ages of at least 10s of Myr [Mustill et al., 2018]. The young white dwarf WD J0914+1914, with $\tau_{\rm WD_{cool}} \sim 13.3$ Myr, does not yet contain rocky pollutants despite it hosting a planetary system [Gänsicke et al., 2019]. Thus it is important to consider a wide range of white dwarf temperatures and cooling ages when looking at pollution pathways.

2.2.2 Asteroid properties

Shape models

The predecessor to this work, BVG17, used a quasi-spherical shape model characterised by a single mean dimension a and an approximate volume of a^3. However, given that Solar System asteroids have been observed with a large variety of shapes [Warner et al., 2009; Ďurech et al., 2018], it is likely that using such a simplified shape model affects the reliability of the results.

Here, we introduce an ellipsoidal shape model characterised by the lengths of the semi-major, -intermediate and -minor axes denoted as a, b and c respectively. We further introduce the following aspect ratios

$$\mathfrak{b} \equiv \frac{b}{a}, \tag{2.10}$$

$$\mathfrak{c} \equiv \frac{c}{a}, \tag{2.11}$$

which allow us to focus on the shape of the ellipsoid. Typically, asteroids are defined as oblate when the major and intermediate axes are equal ($\mathfrak{b} = 1 \neq \mathfrak{c}$), and prolate when the intermediate and minor axes are equal ($\mathfrak{b} = \mathfrak{c}$) [Holsapple, 2001]. Observations of Solar System asteroids allow us to place constraints on the possible values of the aspect ratios. Oblate asteroids have only been observed with $\mathfrak{c} > 0.4$, but prolate asteroids have been observed with $\mathfrak{c}$ values as small as 0.2 [Zhang and Lin, 2020]. We consider a range of shape models which are detailed in Table 2.1 and graphically represented in Figure 2.2.

Density, porosity and mass

For simplicity we assume that the asteroids have a uniform density throughout their bodies.

Estimates of the density of Solar System bodies derived via direct and indirect observational methods range from $\rho < 1$ g cm^{-3} for icy cometary bodies to $\rho \sim 11$ g cm^{-3}

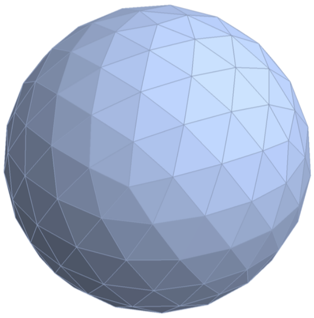

(a) Spherical

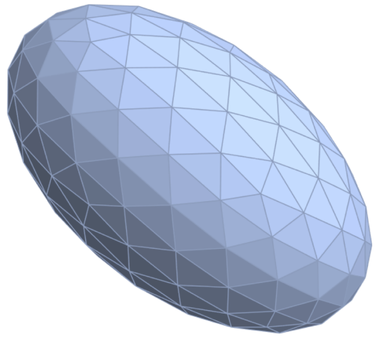

(b) Prolate

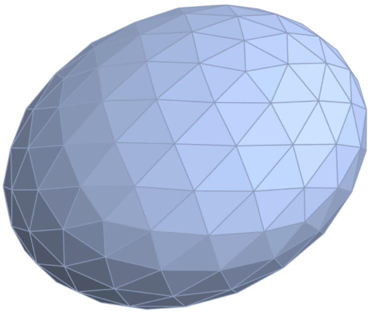

(c) Oblate

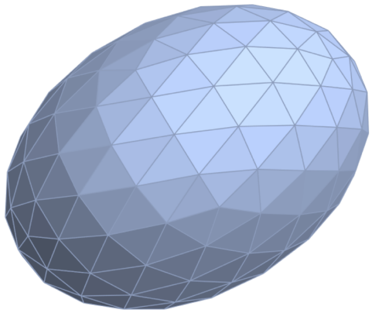

(d) Generic

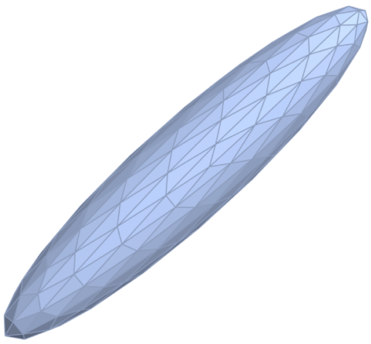

(e) Extreme Prolate

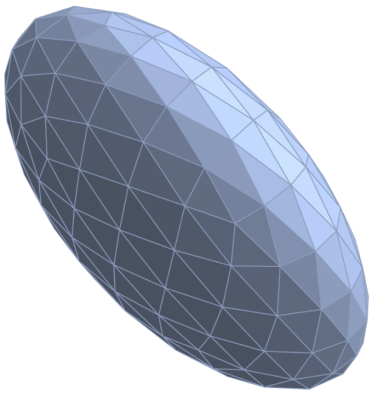

(f) Extreme Oblate

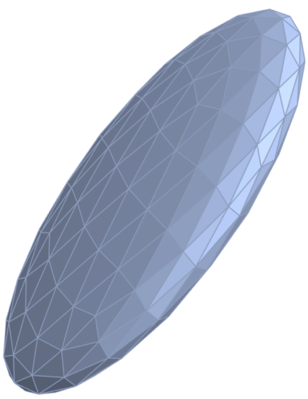

(g) Extreme Generic

Figure 2.2: Graphical examples of the triaxial shape models detailed in Table 2.1.

Table 2.1: Aspect ratios, $\mathfrak{b}$, $\mathfrak{c}$ for the individual shape models used in this chapter.

	$\mathfrak{b}$	$\mathfrak{c}$	Figure
Spherical	1.0	1.0	2.2(a)
Prolate	0.6	0.6	2.2(b)
Oblate	0.6	1	2.2(c)
Generic	0.6	0.8	2.2(d)
Extreme Prolate	0.2	0.2	2.2(e)
Extreme Oblate	0.4	1	2.2(f)
Extreme Generic	0.2	0.8	2.2(g)

for rocky-iron bodies, although these extreme values are likely unphysical and have large associated uncertainties [Carry, 2012]. To take into account this wide range of possible densities, we loosely define three material types, compared to the two used in BVG17:

1. *Snowy bodies:* bodies comprised of a mixture of ices and dust with a given density of $\rho_{\text{Snow}} = 0.5\ \text{g cm}^{-3}$.
2. *Rocky bodies:* more solidified bodies made of solid ices or dust, with a given fiducial density of $\rho_{\text{Rock}} = 3\ \text{g cm}^{-3}$.
3. *Iron bodies:* solid bodies rich in iron, with a given density of $\rho_{\text{Iron}} = 8\ \text{g cm}^{-3}$.

Porosity is related to the number of voids in a body that are larger than a typical micrometer crack size for meteorites [Carry, 2012]. Very massive, monolithic asteroids seem to have no porosity. Rubble pile asteroids, which are common in the Solar System, have up to 20 per cent porosity, with icier bodies exceeding this percentage. Constraining porosity values from observations is very difficult, and estimates for Solar System asteroids can vary by up to 30-40 per cent depending on the model used. Further, objects exist which go against the broad trends mentioned above and the specific evolutionary history of a body can affect its porosity. Thus, the possible range of porosity values and hence density values is very large and in order to not overcomplicate our study, we elect to not consider porosity in the model presented here.

Assuming an ellipsoidal shape and a uniform density allows us to write the mass of an asteroid in terms of its aspect ratios as

$$M = \frac{4}{3}\pi a^3 \mathfrak{b}\mathfrak{c}\rho. \tag{2.12}$$

Latent heat

As a body approaches the strong radiative influence of a star, sublimation becomes an important process. The mass loss per unit area of an asteroidal body for a particular stellar flux depends strongly on the latent heat of sublimation, $\mathcal{L}$. Although constituent materials of an asteroid will have different values of latent heat, Brown et al. [2011] define the relevant

Table 2.2: Summary of material properties for the three types of asteroids considered here.

Type	Density ρ $\mathrm{g\,cm^{-3}}$	Latent heat $\mathcal{L}$ erg g^{-1}	Tensile strength S dyne cm^{-2}
Snow	0.5	2.6×10^{10}	10^4
Rock	3	8×10^{10}	10^7
Iron	8	10^{11}	10^9

value as the weighted mean of all mass components. For the snowy bodies considered here this gives a value of $\mathcal{L}_{\text{Snow}} = 2.6 \times 10^{10}$ erg g^{-1} . The values for solid bodies are higher: $\mathcal{L}_{\text{Rock}} = 8 \times 10^{10}$ erg g^{-1} and $\mathcal{L}_{\text{Iron}} = 10^{11}$ erg g^{-1} [Chyba et al., 1993].

Internal strength

Asteroids approaching a white dwarf are also subjected to forces additional to sublimative mass loss. The effect of these forces depend on the body's ability to resist them, or how materially strong the body is. There are multiple strengths which help to hold a body together, including: tensile, shear and compressive strengths. Following the argument presented in BVG17, the variation between different strengths for a single material is less than the variation of specific strengths between materials and so only the tensile strength S is considered in the following.

Studies of the break up of Shoemaker-Levy 9 and the surface morphology of 67P/Churyumov-Gerasimenko suggest a tensile strength as low as 10^3 dyne cm^{-2} for cometary material [Greenberg et al., 1995; Groussin et al., 2015]. Laboratory experiments on Earth have been used to identify tensile strengths for various meteorite types which can be used in this study. Measurements of tensile strength for carbonaceous chondrite meteorites give a value of $\sim 4 \times 10^7$ dyne cm^{-2} [Pohl and Britt, 2020]. C-type asteroids are the most common rocky asteroid type in the Solar System and provide the reservoir for C chondrites and so their measured tensile strengths are used in this study as a proxy for our model of a more general rocky asteroid.

Here we adopt the following strength values, $S_{\text{Snow}} = 10^4$ dyne cm^{-2} , $S_{\text{Rock}} = 10^7$ dyne cm^{-2} and $S_{\text{Iron}} = 10^9$ dyne cm^{-2} .

A summary of all material properties considered here can be seen in Table 2.2.

Orbital properties

Here we consider the situation where an individual asteroid is subject to an external perturbation, such as from a giant planet in the outer system, and approaches the white dwarf on a highly eccentric orbit with pericentre inside the photosphere of the white dwarf. This case is particularly interesting in light of the observations of the highly eccentric ($e \sim 0.97$) disrupting asteroid around the white dwarf ZTF J0139+5145 [Vanderbosch et al., 2020].

As discussed in BVG17, during most of the asteroid's approach to the white dwarf, the orbit behaves as a linear parabolic orbit. Under this assumption, the velocity is only comprised of the radial speed, which can be written in the following form

$$\begin{aligned} v(r) &= \left(\frac{2GM_{\rm WD}}{r}\right)^{1/2} \\ &= v_* \left(\frac{R_{\rm WD}}{r}\right)^{1/2} \\ &= v_* x^{-1/2}, \end{aligned} \tag{2.13}$$

where v_* is the stellar escape speed and r is the distance between the centre of the white dwarf and the centre of the asteroid. Here we introduce x as the relative astrocentric distance as

$$x = \frac{r}{R_{\rm WD}}, \tag{2.14}$$

to maintain notational consistency with BVG17.

2.2.3 Asteroid belts

Asteroid belts which survive giant branch evolution may be enriched by more distant icy objects via the giant branch Yarkovksy effects [Veras et al., 2019b] and persist as reservoirs for white dwarf pollution. A large portion of this matter reservoir could then be nonuniformly perturbed towards the white dwarf over a period of time ranging from orbital to Gyr timescales by post-mass-loss planetary system instability [Mustill et al., 2018].

Here we construct a simplified Main Belt analogue of 100 bodies. Each body's shape and material is randomly chosen from those presented in Tables 2.1 and 2.2. Although there are almost certainly some preferences for shape and material within the Solar System's Main Belt, we make the assumption here that there will be an approximate equal split between these properties. It is important to note here that considering only 100 asteroids and randomly sampling sizes, shapes, and materials means that all of the results presented in the following chapter are subject to small number statistics. Although we can begin to draw some conclusions from the data, much larger sample sizes would be required to come to statistically significant conclusions.

Much of the accreted material measured in white dwarfs appear to be from rocky, terrestrial asteroids. However, a small number of white dwarfs have been observed with volatile and excess hydrogen pollution [Farihi et al., 2013; Raddi et al., 2015; Gentile Fusillo et al., 2017; Xu et al., 2017; Hoskin et al., 2020], which points to the progenitor material being water-enriched. Observations of the Main Belt dwarf planet Ceres indicate a high polar concentration of water ice and a subsurface water ocean [Prettyman et al., 2019]. Such water-rich bodies can persist throughout the giant branch phases of stellar evolution. Malamud and Perets [2017] find that larger bodies ($a > 25$ km) around $0.6M_\odot$ white dwarfs can retain around 50 per cent of their water content at distances of $\sim$ 100 au. Additionally, bodies can be dynamically exchanged between the icy outer reaches of the Solar System's Kuiper Belt and Oort Cloud and the rockier, terrestrial Main Belt [Weissman and Levison, 1997; Shannon et al., 2015]. Therefore, using a mixture of rocky and snowy bodies in our analogue Main Belt is realistic.

For a planetesimal reservoir in collisional equilibrium (as expected for the Main Belt), the size distribution of bodies can be described by a power law of the form $N(D) \propto D^{-q}$ [Dohnanyi, 1969]. Numerous estimates for this power law exponent q have been made throughout the literature, and a significant break in the distribution around 8 km in size has been noted [Jedicke and Metcalfe, 1998; Ivezić et al., 2001; Ryan et al., 2015].

Thus to take this break into account, here we adopt $q \approx 1.29$ for sub-kilometre bodies from the Subaru Main Belt Asteroid Survey (SMBAS) [Yoshida and Nakamura, 2007] and $q \approx 4.4$ for bodies > 1 km determined from the High Cadence Transient Survey (HiTS) [Peña et al., 2020]. We force 90 per cent of the 100 asteroids to be smaller than 1 km and the remaining 10 per cent to be larger. Thus, our sample sizes are artificially designed so that we can sample a reasonable number of larger asteroids.

All sizes are then randomly chosen from the respective power law distribution. Figure 2.3 shows an example histogram of asteroid sizes randomly chosen to follow the above power law distributions. The distribution for asteroids smaller than a kilometre (with $q \approx 1.29$) is shown in blue and for asteroids larger than a kilometre (with $q \approx 4.4$ in pink).

Helium dominated DB white dwarfs have much longer diffusion timescales ($\sim$ Myr) than hydrogen dominated DAs (days to weeks), thus the level of accreted material visible in their convective zones can act as a tracer to the total amount of accreted material across the last $\sim$Myr of the planetary systems evolution and a proxy for the average across all white dwarf types (see Chapter 1.3.2 for more details). Most polluted DB white dwarfs are estimated to have accreted $10^{21} - 10^{23}$ g of planetary material [Farihi et al., 2010; Xu and Jura, 2012; Girven et al., 2012; Veras, 2016] in the last Myr, comparable with the mass of the Solar System's Main Belt.

A number of studies which utilised numerical simulations to identify how often minor bodies in white dwarf planetary systems are tidally disrupted and should contribute to the accreted material, find that in order for the fraction of their belts which accrete onto the star to match the observed totals, the overall disc mass must be several times greater than the mass of our own Main Belt [Debes et al., 2012; Frewen and Hansen, 2014]. However, the polluted white dwarfs we currently observe largely have main sequence progenitors which were more massive than our Sun [Tremblay et al., 2016; Cummings et al., 2018; El-Badry et al., 2018; McCleery et al., 2020; Barrientos and Chanamé, 2021] and so persisted on the main sequence for less time, both of which could correspond with more massive belts. While the specific dynamical evolution of the Solar System could have depleted the reservoir of asteroids in the Main Belt [Walsh et al., 2011], and thus may not represent the mass of a

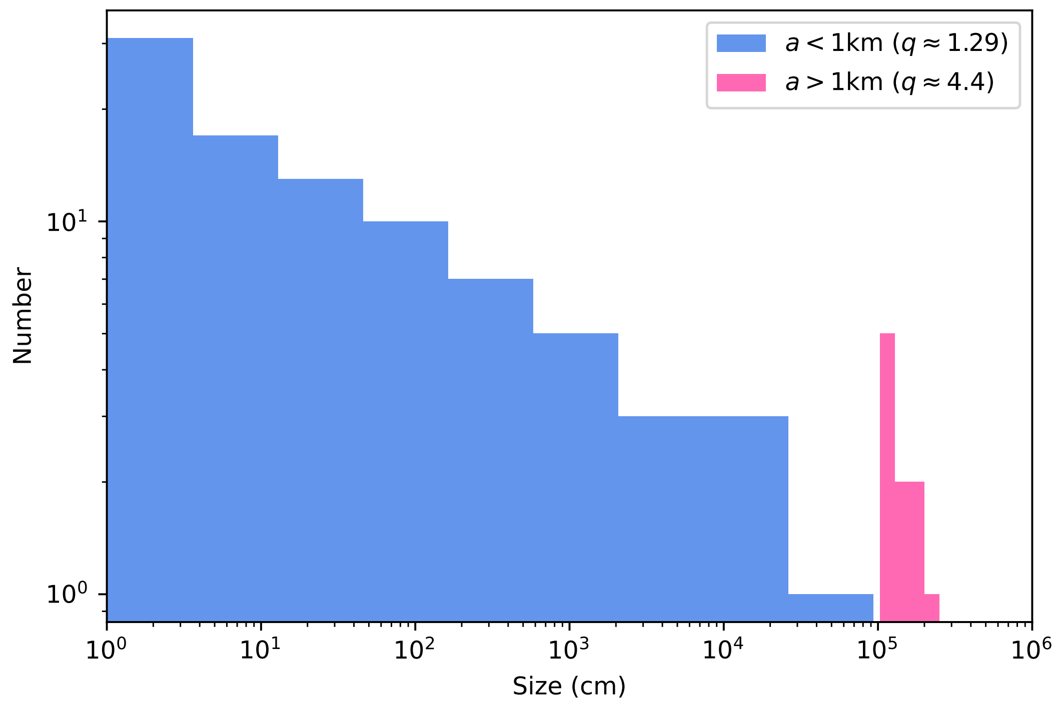

Figure 2.3: An example random size distribution for asteroids as used in this work. Sizes randomly chosen from the power law distribution for sizes smaller than a kilometre with $q \approx 1.29$ [Yoshida and Nakamura, 2007] is shown in blue and for sizes larger than a kilometre with $q \approx 4.4$ [Peña et al., 2020] is shown in pink.

'typical' asteroid belt. Although the mass of the belts is undoubtedly important, and each individual asteroid has a mass, we do not ensure that the total mass in the Main Belt analogue is equivalent across our simulations.

2.3 Asteroids approaching the white dwarf

Having laid out the physical and orbital properties of white dwarfs and asteroids, we now proceed to consider possible destruction regimes for an ellipsoidal body approaching a white dwarf on a linear trajectory. We assume that the scatterer is the only or innermost major planet in the system, such that nothing generates deviations in this trajectory.

We consider three possible regimes: *i) sublimation* where the bodies total mass is lost due to the incident energy flux; *ii) fragmentation* where tidal forces from the star overcome the body's own internal tensile strength and gravitational forces; and *iii) impact* where the body enters the white dwarf photosphere and undergoes frictional ablative mass loss and/or ram-pressure pancaking and deceleration effects.

Much of the following analysis in this chapter proceeds in the same way as presented in BVG17, however with the introduction of considering the three principle directions of the three dimensional ellipsoidal model separately.

In the following we consider the cartesian basis $\{\hat{\imath}, \hat{\jmath}, \hat{k}\}$ to be aligned with the ellipsoid's semi-axes such that $\hat{\imath}$ and $\hat{\jmath}$ are aligned with the largest and intermediate semi-axes. This allows us to define the cross-sectional areas of the asteroids in the three principal directions in terms of the largest semi-axis a and the aspect ratios $\mathfrak{b}$ and $\mathfrak{c}$ as

$$\text{cross-sectional area} = \left\{\pi a^2 \mathfrak{b}\mathfrak{c}\hat{\imath},\ \pi a^2 \mathfrak{c}\hat{\jmath},\ \pi a^2 \mathfrak{b}\hat{k}\right\}. \tag{2.15}$$

2.3.1 Sublimation

Outside the Roche limit of the white dwarf, sublimation should dominate the disruption of infalling planetesimals and is governed by the incident flux of starlight on a body. The radiation flux at an astrocentric distance r (with $x = r/R_*$ as in equation 2.14) is

$$\begin{aligned} F_{\text{rad}}(r) &= \frac{L_{\text{WD}}}{4\pi r^2} \\ &= \left[\frac{R_{\text{WD}}}{r}\right]^2 \sigma T_{\text{eff}}^4 \\ &= \frac{F_{\text{WD}}}{x^2}, \end{aligned} \tag{2.16}$$

where L_{WD} is the bolometric luminosity of the white dwarf, R_{WD} is the radius of the white dwarf, T_{eff} is the white dwarf effective temperature, F_{WD} is the bolometric radiation flux at the surface of the star and σ is the Stefan-Boltzmann constant.

Assuming the incoming asteroid has near-zero albedo the incident power of the starlight $\boldsymbol{P}_*$ is

$$\boldsymbol{P}_* = \frac{a^2 \pi \sigma T_*^4}{x^2} \left[\mathfrak{b}\mathfrak{c}\hat{\imath} + \mathfrak{c}\hat{\jmath} + \mathfrak{b}\hat{k} \right]. \tag{2.17}$$

A simple expression for the mass loss per unit radial distance, which assumes that sublimation occurs at its maximum rate and does not take into account the intrinsic vapour pressure, interactions with an extant accretion disk or other effects which might alter the sublimation process, can be found as follows

$$\begin{aligned} \frac{\mathrm{d}\boldsymbol{M}}{\mathrm{d}r} &= \frac{1}{v(r)} \frac{\mathrm{d}\boldsymbol{M}}{\mathrm{d}t} = \frac{1}{v(r)} \frac{\boldsymbol{P}_*}{\mathcal{L}} \\ &= \frac{1}{v(r)} \frac{a^2 \pi T_{\mathrm{eff}}^4 \sigma}{\mathcal{L} x^2} \left[\mathfrak{b}\mathfrak{c}\hat{\imath} + \mathfrak{c}\hat{\jmath} + \mathfrak{b}\hat{k} \right]. \end{aligned} \tag{2.18}$$

Using the definitions of the orbital velocity (equation 2.13) and the ellipsoidal mass (equation 2.12) to rewrite equation 2.18, we can find the mass loss per astrocentric distance ($x = r/R_*$ equation 2.14) as follows

$$\begin{aligned} \frac{\mathrm{d}\boldsymbol{M}}{\mathrm{d}x} &= \frac{\mathrm{d}\boldsymbol{M}}{\mathrm{d}r} \frac{\mathrm{d}r}{\mathrm{d}x} \\ &= \frac{\pi \sigma T_{\mathrm{eff}}^4 R_{\mathrm{WD}}}{\mathcal{L} v_* x^{3/2}} a^2 \left[\mathfrak{b}\mathfrak{c}\hat{\imath} + \mathfrak{c}\hat{\jmath} + \mathfrak{b}\hat{k} \right]. \end{aligned} \tag{2.19}$$

Finally we can write the change in largest semi-axis a per astrocentric distance x due to sublimative forces on the three principal axes,

$$\begin{aligned} \frac{\mathrm{d}a}{\mathrm{d}x} &= \frac{\mathrm{d}a}{\mathrm{d}\boldsymbol{M}} \frac{\mathrm{d}\boldsymbol{M}}{\mathrm{d}x} \\ &= \frac{R_{\mathrm{WD}}^{3/2} T_{\mathrm{eff}}^4 \sigma}{2^{5/2} (G M_{\mathrm{WD}})^{1/2} \mathcal{L} \rho x^{3/2}} \left[\hat{\imath} + \frac{1}{\mathfrak{b}} \hat{\jmath} + \frac{1}{\mathfrak{c}} \hat{k} \right]. \end{aligned} \tag{2.20}$$

By considering the mass loss from the body due to this incident starlight, in the same way as in BVG17, we can find an expression for how the largest semi-axis varies as a function of astrocentric distance due to sublimative effects

$$a_{\mathrm{sub}}(x) = a_0 - \frac{A_x}{x^{1/2}}. \tag{2.21}$$

$\boldsymbol{A}$ is the *sublimation parameter,*

$$\boldsymbol{A} = \frac{R_{\mathrm{WD}}^{3/2} T_{\mathrm{eff}}^4 \sigma}{2\sqrt{2 G M_{\mathrm{WD}}} \mathcal{L} \rho} \left[\hat{\imath} + \frac{1}{\mathfrak{b}} \hat{\jmath} + \frac{1}{\mathfrak{c}} \hat{k} \right], \tag{2.22}$$

and represents the minimum value of the largest semi-axis size scaled by the relative astrocentric distance which allows an asteroid to withstand sublimative forces alone until it reaches the white dwarf photosphere. a_0 is the initial size of the asteroid. This value differs from that presented in BVG17 by a numerical factor in the x-direction and additional factors of the aspect ratios in the y and z-directions.

This sublimation model neglects cooling effects and assumes that the sublimation occurs much more quickly than radiative energy is otherwise lost. See Steckloff et al. [2015] for a more complete treatment of the sublimation process and Steckloff et al. [2021] for said treatment applied around white dwarfs.

2.3.2 Fragmentation

A minor body will fragment into smaller child bodies when the tidal forces from the white dwarf overcome the body's own internal forces. Here we will simply consider the body's self-gravitational and tensile strength forces as interior forces. While this approach is similar to the process in BVG17, we again introduce three dimensional ellipsoidal forces.

The tidal force on an ellipsoidal body due to a large central body is

$$\boldsymbol{F_T} = \frac{GMM_{\mathrm{WD}}a}{x^3 R_{\mathrm{WD}}^3}\left[2\hat{\imath} - \mathfrak{b}\hat{\jmath} - \mathfrak{c}\hat{k}\right]. \tag{2.23}$$

This form assumes that the body rotates about the z-axis – which has the greatest inertia – and that the x-axis, with the least inertia, always points towards the central body. This form also assumes that librations about this orientation can be neglected [Dobrovolskis, 2019]. This assumption is further discussed in Section 2.5.4.

The force due to the internal tensile strength is the cross-sectional area (equation 2.15) multiplied by the material's tensile strength [Davidsson, 2001],

$$\boldsymbol{F_S} = -\pi a^2 S\left[\mathfrak{c}\mathfrak{b}\hat{\imath} + \mathfrak{c}\hat{\jmath} + \mathfrak{b}\hat{k}\right]. \tag{2.24}$$

For a homogeneous ellipsoid, such as considered here, the self-gravitational force depends only on the shape of the asteroid through the aspect ratios and can be written as follows [Holsapple, 2004; Holsapple and Michel, 2006],

$$\boldsymbol{F_G} = -2\pi GM\rho a\left[U_x\hat{\imath} + U_y\mathfrak{b}\hat{\jmath} + U_z\mathfrak{c}\hat{k}\right], \tag{2.25}$$

with

$$U_x = \mathfrak{b}\mathfrak{c}\int_0^\infty \frac{du}{(u+1)^{3/2}\left(u+\mathfrak{b}^2\right)^{1/2}\left(u+\mathfrak{c}^2\right)^{1/2}}, \tag{2.26}$$

$$U_y = \mathfrak{b}\mathfrak{c}\int_0^\infty \frac{du}{(u+1)^{1/2}\left(u+\mathfrak{b}^2\right)^{3/2}\left(u+\mathfrak{c}^2\right)^{1/2}}, \tag{2.27}$$

$$U_z = \mathfrak{b}\mathfrak{c}\int_0^\infty \frac{du}{(u+1)^{1/2}\left(u+\mathfrak{b}^2\right)^{1/2}\left(u+\mathfrak{c}^2\right)^{3/2}}. \tag{2.28}$$

The strength and gravitational forces together resist the influence of the tidal force.

The net force acting on the triaxial body is then

$$\boldsymbol{F}_{\text{tot}} = +|\boldsymbol{F}_T| - |\boldsymbol{F}_S| - |\boldsymbol{F}_G| \tag{2.29}$$

and the condition for a body to resist the tidal forces of the central star is

$$\frac{|\boldsymbol{F}_S + \boldsymbol{F}_G|}{\boldsymbol{F}_T} \gtrsim 1. \tag{2.30}$$

In this chapter, we want to focus on the case where internal strength dominates over the self-gravity of the body, which is likely to be the case for many of the smaller bodies assumed here. Although 'rubble pile' asteroids dominated by self-gravity are expected to be common in the Solar System (see Figure 1.5), they are likely to break into constituent particles through tidal disruption or rotational fission. The result would be a large collection of smaller bodies with much higher internal integrity than the parent body, dominated by internal strength.

The size where a body's internal strength dominates over self-gravity, occurs when the ratio between the internal strength force (equation 2.24) and self-gravitational force (equation 2.25) is greater than 1 as follows,

$$\frac{\boldsymbol{F}_S}{\boldsymbol{F}_G} > 1. \tag{2.31}$$

To quantify the boundary where the internal strength dominates, and thus where we can neglect self gravity, we calculate the ratio in equation (2.31) and present an order of magnitude result for the x-component of the ratio in Table 2.3. As is discussed further in Section 2.3.4, fragmentation always occurs in the x-direction of the body and thus here we only consider the ratio of the x-components of the forces. The largest asteroid size considered in our study is 10^8cm, since the assumption that the internal strength dominates over self-gravity begins to break down for the weakest comet-like bodies at 10^6cm and the strongest iron bodies at 10^8cm as shown in Table 2.3. The extremely strong iron planetesimal inferred to be orbiting inside the Roche limit of the white dwarf SDSS J122859.93+104032.9 (hereafter SDSS J1228+1040; further discussed in Chapter 1.3.2) is assumed to be between $2 \times 10^5 - 2 \times 10^7$cm in size [Manser et al., 2019], which puts this object firmly in the regime where internal strength dominates over self-gravitation as defined in this chapter.

A further way to examine the body size at which internal strength dominates is to look at a graph of frequency against period and diameter, such as Figure 1.5 or figure 1 of Hestroffer et al. [2019]. In such a graph, the spin barrier (the rotational velocity at which a rubble pile asteroid will undergo rotational fission) is clearly visible. The location of the spin barrier implies that rubble pile asteroids begin to dominate the asteroid population between $10^4 - 10^5$cm in size. Although this estimate is below the minimum size for a rubble pile body 10^6 cm found from Table 2.3, fast monolithic rotators have been observed [Polishook

Table 2.3: The ratio of internal strength to self gravitation forces (equation 2.31) for all of the shape models and compositions considered in this work. The values where the assumption that internal strength dominates over self-gravity breaks down are highlighted in red.

Size	Generic			Extreme Generic			Prolate			Extreme Prolate			Oblate			Extreme Oblate		
(cm)	Snow	Rock	Iron	Snow	Rock	Iron	Snow	Rock	Iron	Snow	Rock	Iron	Snow	Rock	Iron	Snow	Rock	Iron
10^3	10^5	10^6	10^7	10^5	10^6	10^8	10^5	10^6	10^7	10^5	10^7	10^8	10^5	10^6	10^7	10^5	10^6	10^7
10^4	10^3	10^4	10^5	10^3	10^4	10^6	10^3	10^4	10^5	10^3	10^5	10^6	10^3	10^4	10^5	10^3	10^4	10^5
10^5	10^1	10^2	10^3	10^1	10^2	10^4	10^1	10^2	10^3	10^1	10^3	10^4	10^1	10^2	10^3	10^1	10^2	10^3
10^6	10^{-1}	10^0	10^1	10^{-1}	10^0	10^2	10^{-1}	10^0	10^1	10^{-1}	10^1	10^2	10^{-1}	10^0	10^1	10^{-1}	10^0	10^1
10^7	10^{-3}	10^{-2}	10^{-1}	10^{-3}	10^{-2}	10^0	10^{-3}	10^{-2}	10^{-1}	10^{-3}	10^{-1}	10^0	10^{-3}	10^{-2}	10^{-1}	10^{-3}	10^{-2}	10^{-1}
10^8	10^{-5}	10^{-4}	10^{-3}	10^{-5}	10^{-4}	10^{-2}	10^{-5}	10^{-4}	10^{-3}	10^{-5}	10^{-3}	10^{-2}	10^{-5}	10^{-4}	10^{-3}	10^{-5}	10^{-4}	10^{-3}

et al., 2016; Chang et al., 2022] and thus our slightly larger estimate is not unreasonable.

In this case, we can neglect self-gravity. As discussed in BVG17, unless a body is particularly large the tensile strength is much more important in resisting tidal forces than the body's self-gravitation. When solely considering tensile strength as a resistive force, the condition for fragmentation becomes

$$a(x) < a_{\text{frag}}(x) = \boldsymbol{B}x^{3/2} \tag{2.32}$$

where $x = r/R_*$ is the dimensionless relative astrocentric distance and

$$\boldsymbol{B} = \sqrt{\frac{3R_{\text{WD}}^3 S}{4GM_{\text{WD}}\rho}} \left[\frac{\hat{i}}{\sqrt{2}} + \frac{\hat{j}}{\mathfrak{b}} + \frac{\hat{k}}{\mathfrak{c}}\right] \tag{2.33}$$

is the *binding size parameter* and represents the size that must be exceeded for a body to fragment and is equivalent to the minimum body size which would fragment at $x = 1$. Again, this only differs from the BVG17 result by a numerical factor and the aspect ratios in the semi-intermediate and -minor axes.

2.3.3 Impact

If the body is not completely destroyed by sublimation, and it never meets the criteria to fragment, then we assume that the body enters the photosphere of the white dwarf. In this subsection, we discuss qualitatively what happens to the body during impact. For a quantitative discussion see Section 6 of Brown et al. [2017], or, for the analogous Sun-comet case, see Brown et al. [2015].

As discussed in Section 2.2.2, the bodies considered here propagate along orbits with orbital pericentres inside of the photosphere of the white dwarf and with periastron distance $q = 0$. Once the body enters the photosphere of the white dwarf, it encounters a very different environment. The white dwarf's very high gravity and temperature restricts the atmosphere to have a very small density scale height. Due to this scale height, in the photosphere the atmospheric frictional heating very quickly overcomes the effect of any further sublimation, and ablation becomes dominant.

The ablation also has to battle with the deceleration effects felt by the body. The majority of the incident atmospheric bombardment flux felt by the body as it moves through the photosphere does not reach the nucleus to ablate it, but instead heats up the surrounding atmosphere through a bow shock, decelerating the body and ablating the nucleus through heat transfer. Under these intense forces, the body can only survive passage through a few vertical scale heights of the atmosphere.

2.3.4 Outcomes

As a body moves towards the white dwarf, its instantaneous size at any astrocentric distance x is described by the sublimation size, $a_{\rm sub}(x)$, as in equation (2.21). For fragmentation to occur, this instantaneous size must coincide with the fragmentation condition, $a_{\rm frag}(x)$ (equation 2.32) at the particular distance. Again, we only consider the x components of the sublimation and binding parameters, A_x and B_x respectively as fragmentation only occurs in the x-direction. This coincidence requires the two functions to touch at $a_{\rm sub}(x) = a_{\rm frag}(x)$.

The two functions are plotted in Figure 2.4. The grey dashed lines show the sublimation size for different initial asteroid sizes. At large asteroid sizes ($a > 10^4$cm), only a small amount of the bodies total mass is lost due to sublimation, regardless of the body's material. The instantaneous size of the body is largely independent of material and, only the weakest (snowy), smallest bodies lose mass due to sublimation. Thus only the instantaneous size for a snowy body is shown.

The lines for an equal sized body of rock or iron would follow the same straight trajectory as the dashed grey lines visible in Figure 2.4. The coloured lines indicate the required size for fragmentation to occur for each material described in Table 2.2. The points where the grey and coloured lines intersect identify the positions where fragmentation will occur. If the condition for fragmentation is not met, the body will continue to lose mass through sublimation until there is no more mass to be lost, or the body impacts directly onto the white dwarf.

Here, we would like to visibly track the size changes of the asteroid as it approaches the white dwarf and pinpoint the moment, and mode of disruption. Thus, we calculate the sublimation size (equation 2.21) in each semi-axis across a fine grid of astrocentric distance values until one of the destruction criterion is reached in any of the body's three principal directions.

Figure 2.5 shows an example of this process, where the asteroid moves from right to left. The figure shows how the size of each ellipsoidal semi-axis varies due to sublimation as the asteroid approaches the white dwarf, compared to the same size variation presented in BVG17. In all cases where fragmentation occurs, it is always the x-direction (largest semi-axis) that fragments first. As the body's least stable part is at the end of its longest axis [Harris, 1996], fragmentation occurring in the x-direction is not unexpected. It should also be noted, that considering just the x-direction would be the same as considering the bodies as purely spherical with the semi-intermediate and -minor axes the same length as the semi-major axis. For the bodies which sublimate completely ($a < 1$cm) in Figure 2.5, the smallest semi-axis (z-direction) consistently completely sublimates first. Although this failure in the z-direction (dot-dash line) occurs further away from the white dwarf than the case presented in BVG17 (solid line) and the equivalent purely spherical case (dotted line), this increased distance of sublimation is not large enough to drastically change the expected debris distribution from such an asteroid sublimating. A further discussion on the effect of

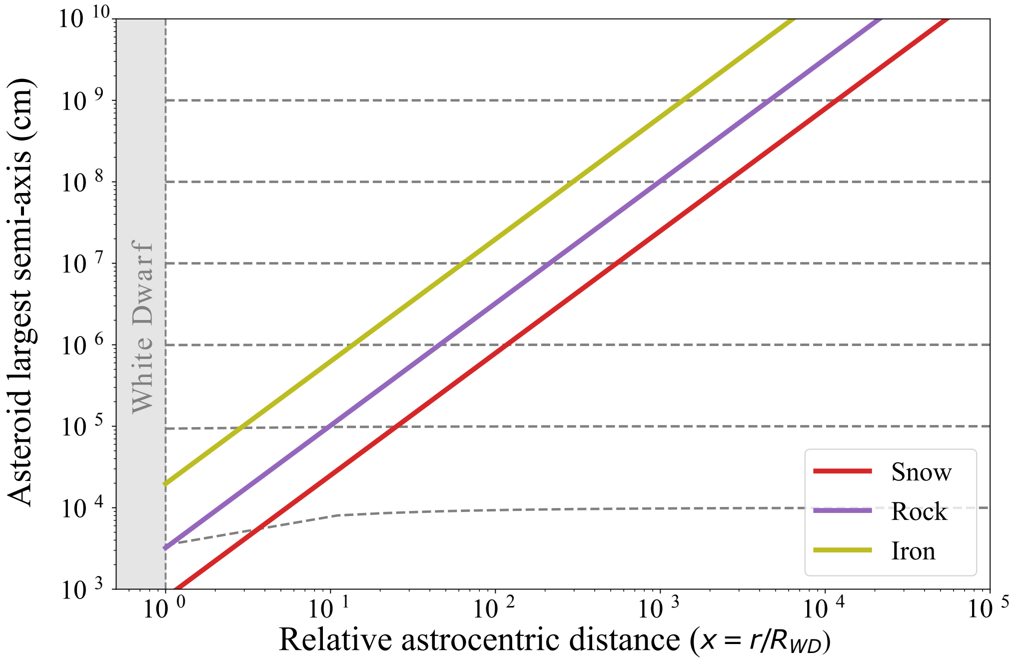

Figure 2.4: Asteroid fragmentation will occur when the instantaneous size of the body due to sublimation (dashed lines) coincides with the size and location condition for the body to fragment (solid coloured lines). The instantaneous size due to sublimation shown is for a body with snowy composition which shows the greatest amount of change compared to a rocky or iron composition. The large size of these bodies resist large amounts of size changes due to sublimation and so these lines are effectively straight, even for a snowy composition. The less tensile strength and density a body has, the further away from the white dwarf fragmentation can occur. As fragmentation always occurs in the x-direction, and the x-components of both the sublimation and binding size parameters are independent of shape model, this graphical representation of the fragmentation condition is valid for all shape models presented in this work.

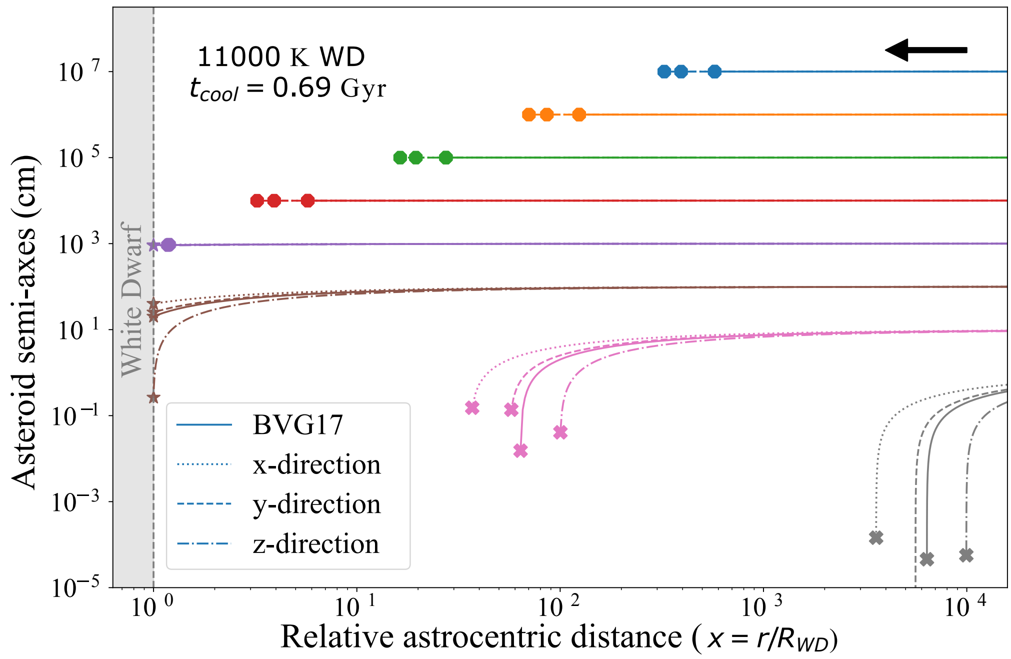

Figure 2.5: An example of following the body's change in size during approach and identifying destruction. Here, the astrocentric distance is on the x-axis, with the asteroid moving from right to left. The body's semi-axes sizes are plotted on the y-axis, and the line styles indicate the different axes as described in the legend. The white dwarf temperature is chosen at 11000K and initial sizes in the range $10^0 - 10^7$cm are considered. The body is assumed to be of snowy composition, and the generic shape model described in Table 2.1 is used. A circle marker indicates that the body ultimately fragments, a star indicates impact and the cross indicates that the body completely sublimates. Fragmentation always occurs in the x-direction of the triaxial model and at the same locations as fragmentation in the BVG17 model. Sublimation occurs in the smallest, z-direction, first. Hence, the BVG17 model consistently underestimates the distance from the white dwarf where complete sublimation occurs.

chosen triaxial shape model on the process of sublimation can be found in Section 2.4.1.

Although the further analysis in this chapter will track the asteroid's size across a fine grid of astrocentric values, there is another method to determine which destruction regime is relevant. It is possible to identify where and how a particular asteroid will undergo destruction using only the sublimation (equation 2.22) and binding size (equation 2.33) parameters. Both of these parameters can be converted into a dimensionless form by dividing by the body's initial largest semi-axis a_0

$$\alpha = \frac{A}{a_0}, \tag{2.34}$$

$$\beta = \frac{B}{a_0}. \tag{2.35}$$

These dimensionless quantities allow us to further examine the conditions for fragmentation, sublimation and impact. If we remember that the condition for fragmentation to occur is that the fragmentation and sublimation sizes are equal $a_{\rm frag}(x) = a_{\rm sub}(x)$, we can write the intersection of the two functions as

$$f_{\rm cross}(x) = \frac{A_x}{x^{1/2}} + B_x x^{3/2} = a_0. \tag{2.36}$$

This function is U-shaped, with a minimum, $a_{\rm crit}$, that occurs when $f'_{\rm cross}(x) = 0$ at the following points

$$x_{\rm crit} = \left(\frac{A_x}{3B_x}\right)^{1/2} \tag{2.37}$$

and

$$a_{\rm crit} = \Gamma A_x^{3/4} B_x^{1/4} = \Gamma a_0 \alpha_x^{3/4} \beta_x^{1/4}, \tag{2.38}$$

where

$$\Gamma = \left[3^{1/4} + 3^{-3/4}\right] \simeq 1.75. \tag{2.39}$$

There are two possible solutions to equation (2.36), with the larger solution, x_2, representing the location of the onset of fragmentation, since the asteroid reaches that point before x_1. Thus, the first condition that must be met for fragmentation to occur is $a_0 > a_{\rm crit}$.

The second, more stringent, fragmentation condition is that fragmentation occurs outside of the white dwarf photosphere, with $x_2 > 1$. Thus fragmentation can only occur if both of the following conditions are satisfied

$$\begin{aligned} A_x + B_x &< a_0, \\ \alpha_x + \beta_x &< 1. \end{aligned} \tag{2.40}$$

The remainder of the α-β domain is simply divided into impact or sublimation along the line $\alpha = 1$, where the objects with $\alpha < 1$ can survive sublimation. The individual destruction regimes in α-β space are shown in Figure 2.6.

Alternatively, once the values of α and β have been found, then a logical process as described in Figure 2.7 can be carried out in each principal direction to identify which form of disruption occurs. Whichever principal axis disrupts at the largest relative astrocentric distance, x, will be the ultimate disruption mode. If the outcome is fragmentation, the position x_2 can be found from a look-up resource. Such a resource could either take the form of a table of values such as presented in BVG17, or a plot of different x_2 values for pairs α and β values as can be seen in Figure 2.8.

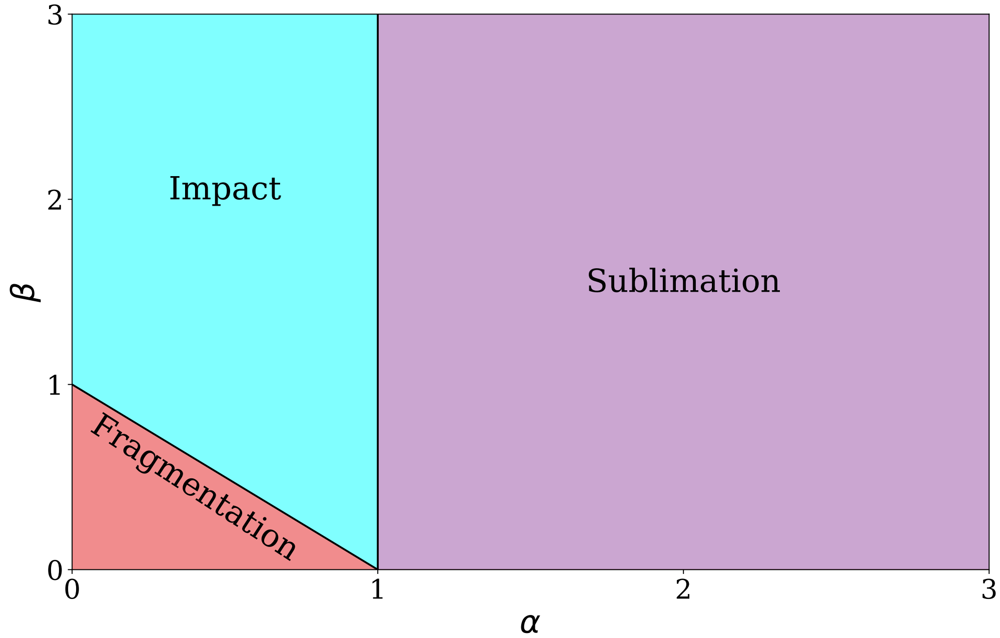

Figure 2.6: The possible destruction outcomes in the $\alpha - \beta$ plane: total sublimation, fragmentation and direct impact. Fragmentation is restricted to the lower left hand corner of the phase space where both α and β are less than 1. Sublimation occurs whenever α is larger than one and impact occurs when neither of these two conditions are met.

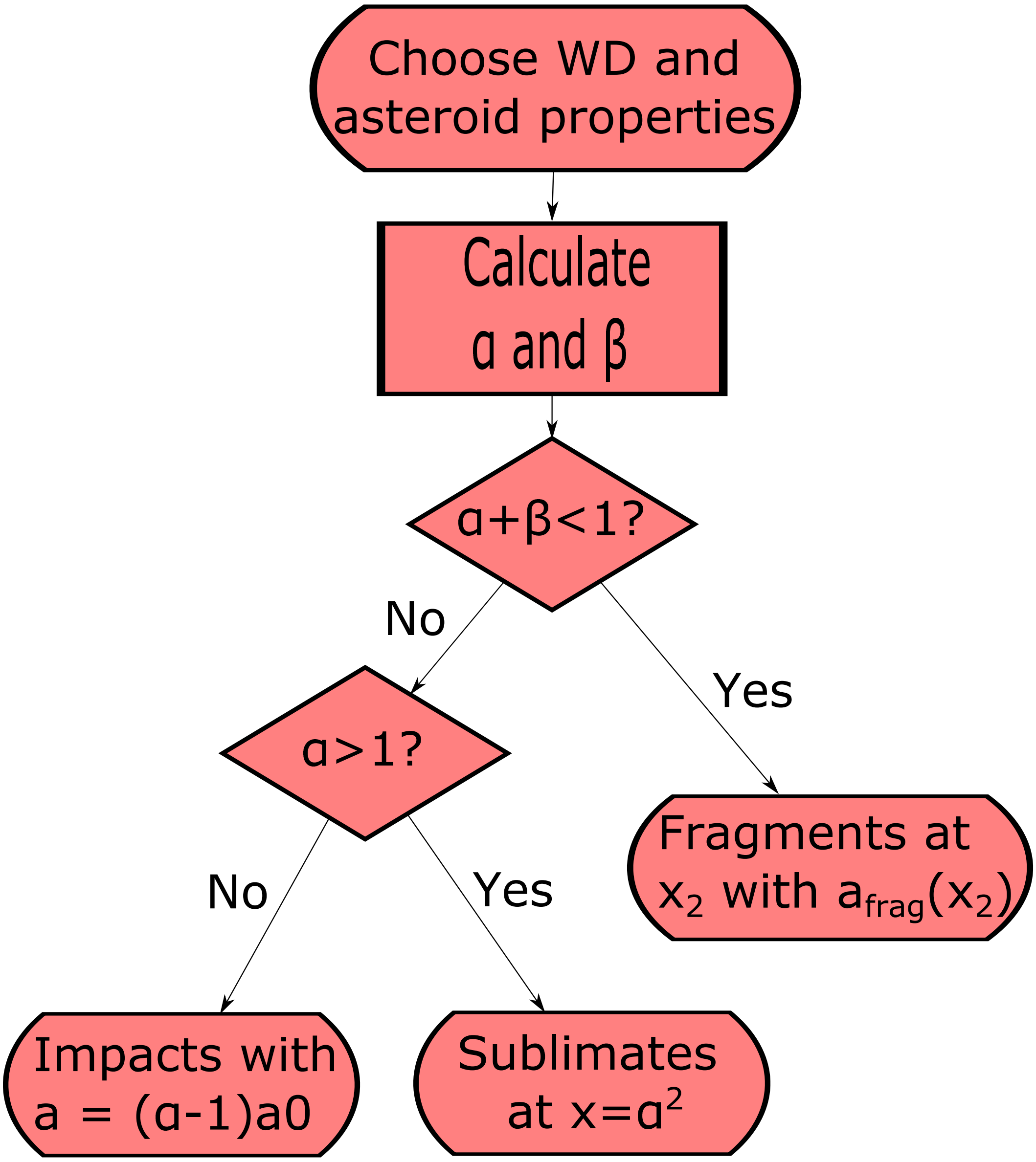

Figure 2.7: A flowchart which shows how to find the destruction regime, size and position of the failure for any arbitrary selection of white dwarf and asteroid properties. The shape of the asteroid is embedded within the values of α and β.

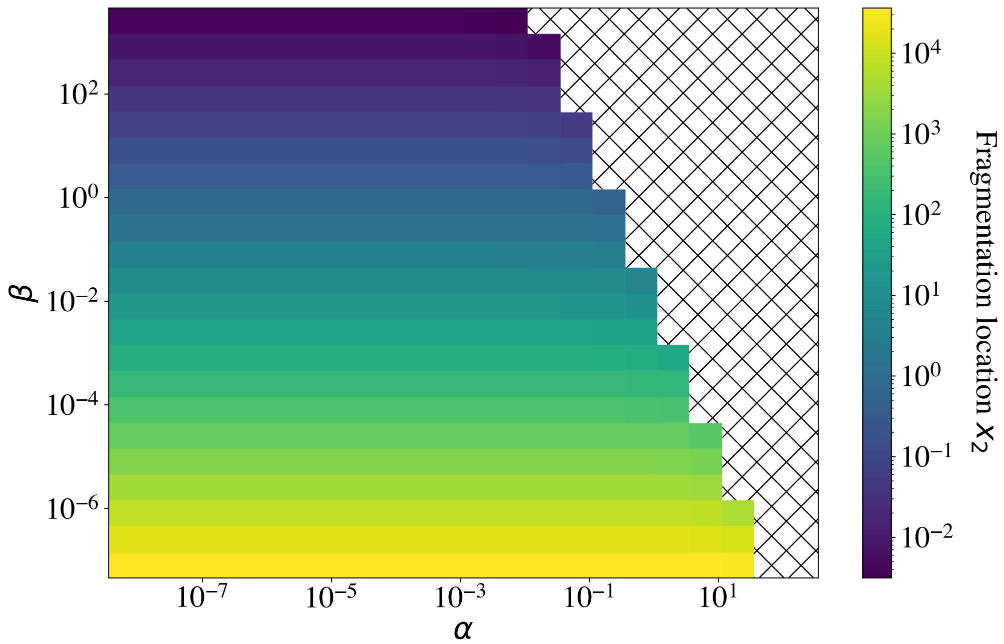

Figure 2.8: x_2 values for a range of α and β values. The x_2 values are indicated by the colour, which is described in the colour bar on the right hand side of the plot. The hatched area with the white background indicates that there is no fragmentation solution for that particular pair of α and β values. Smaller values of both α and β trigger the fragmentation of the asteroid at greater x_2 values further from the white dwarf.

2.4 A Main Belt Analogue

By using the structure and properties of a Main Belt analogue discussed in Section 2.2.3, here we aim to identify the fates of the bodies in such a belt if each asteroid was perturbed onto an extremely eccentric ($e \sim 1$), effectively linear, parabolic orbit.

Figure 2.9 shows the outcomes for such belts around five white dwarfs with $T_{\rm eff}$ = [30, 000 K, 18, 200 K, 11, 000 K, 6700 K, 4000 K] as described in Section 2.2.1. The asteroids enter at the right-hand edge of the plots and move to the left (as indicated by the black arrows), towards the white dwarf which is shown by the grey shaded region at the y-axis. The line colour indicates the shape model from the possibilities detailed in Table 2.1 and Figure 2.2. A solid line shows the fiducial shape model has been used, while the dashed line indicates the extreme model. The shape marker at the point of disruption illustrates which destruction regime is active: octagons indicate that the body fragments, crosses are the locations of complete sublimation, and stars at the edge of the white dwarf zone show that the body impacts onto the white dwarf. Finally, the fill attribute of these markers demonstrates the material makeup of the bodies: empty is snowy material, transparent is rocky and solid fill is iron material. On the right-hand side of each plot some relevant Solar System asteroid sizes are shown[3].

Generally it can be seen that regardless of white dwarf temperature and body material, the largest asteroids are likely to fragment across the entire astrocentric distance considered. The diagonal lines formed by the fragmentation locations that can be seen in Figure 2.9 are caused by the fragmentation conditions we impose, and can also be visualized in the coloured lines in Figure 2.4. By recalling that when considering fragmentation we only need to consider the x-components of the binding size parameter (equation 2.33), we remove any dependence on the specific shape model used and are left with a relationship for each material, independent of white dwarf temperature. The weaker the internal strength of the body's material, the further away from the white dwarf the body will fragment. The size of the body will also affect the distance of fragmentation, with larger bodies fragmenting further from the central star.

Although the smallest bodies consistently sublimate completely across all white dwarf temperatures, higher white dwarf temperatures can cause larger bodies to sublimate. The two coolest (4000 K and 6700 K) white dwarfs considered here sublimate 4 ± 2 and 17 ± 4 per cent of asteroids respectively, this increases to 46 ± 7 per cent of asteroids sublimated for the 11, 000 K white dwarf, where Poissonian errors are presented to account for small number statistics. The simulations for the two hottest white dwarf temperatures featured in Figure 2.9 show significantly more sublimation with 61 ± 8 (18, 200 K) and 77 ± 9 (30, 000 K) per cent of the total belt being completely sublimated. Thus, although the errors on these percentages are large, the increase in sublimation with increasing temperature is robust.

[3]Sizes for the three largest asteroids are taken from the NASA JPL Small Body Database https://ssd.jpl.nasa.gov/sbdb.cgi. 2015 TC5 is the smallest named Near-Earth Asteroid [Reddy et al., 2016].

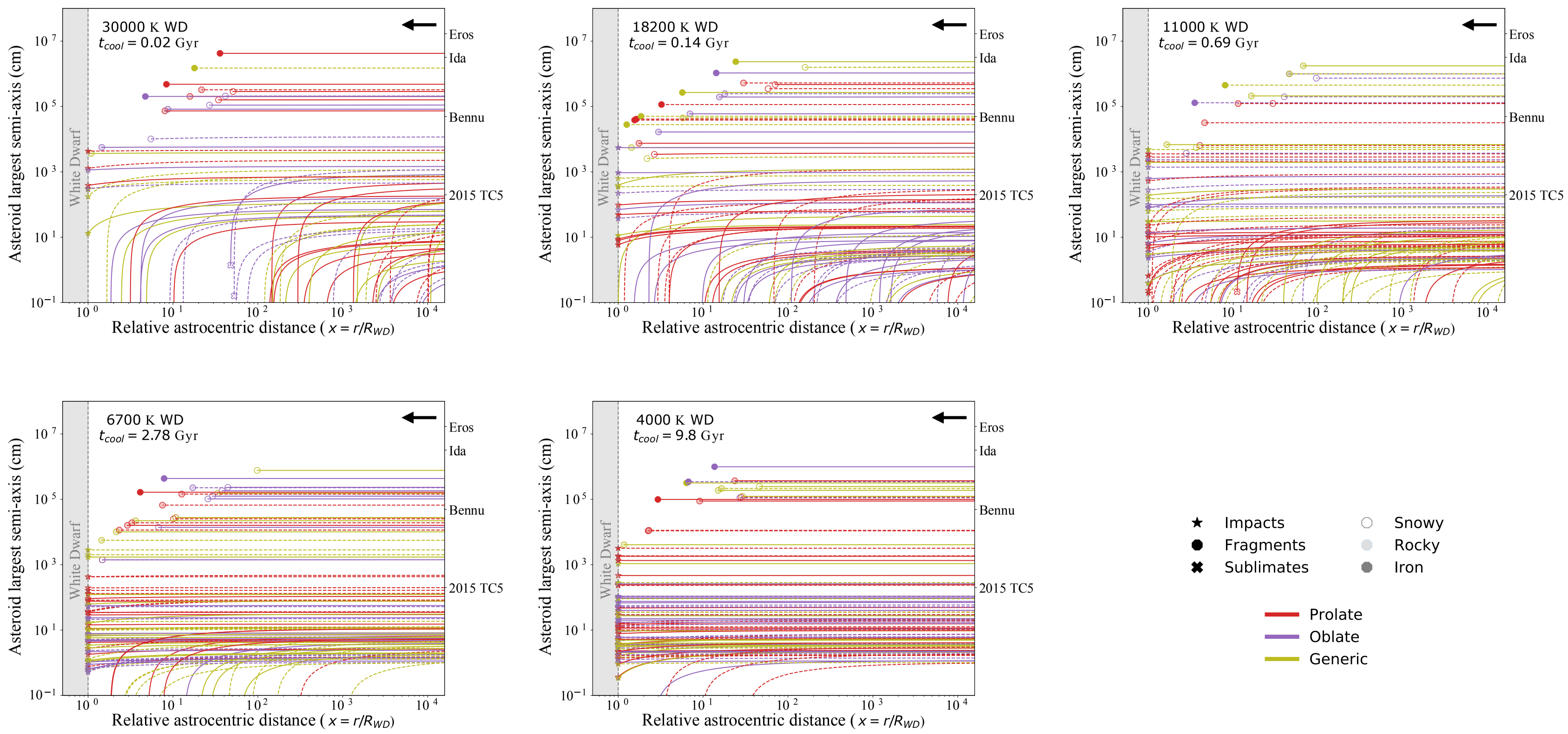

Figure 2.9: The fate of exo-asteroid belts perturbed towards white dwarfs. Each panel shows the entire belt of 100 asteroids with randomly chosen initial largest semi-axis (physical) size, shape and material, for different white dwarf temperatures and cooling ages as stated in the top left hand corner of each panel. The colour of the individual asteroid tracks highlights which shape model has been used, where a solid line indicates the fiducial model, and the dashed line the extreme version. The marker at the end of the tracks show the ultimate fate of the body, and the fill of this marker shows the asteroid's material properties. The right-hand axis of each plot shows some example sizes of named Solar System asteroids. Across all white dwarf temperatures, asteroids above $\sim 10^3$cm in semi-major axis fragment. Hotter white dwarfs are able to sublimate larger bodies up to 10^3cm. Cooler white dwarfs are more vulnerable to direct impacts in the size range $10^0 - 10^4$cm.

This increased level of sublimation also occurs at an increased distance from the white dwarf. 13 ± 4 per cent of the asteroids which sublimate around the $18,200$ K white dwarf do so beyond the maximum relative astrocentric distances displayed in Figure 2.9. For the $30,000$ K white dwarf, 32 ± 6 per cent of total sublimations occur beyond 10^4 relative astrocentric distances.

Thus, an additional simulation is carried out for the two hottest white dwarf temperatures with relative astrocentric distance range extended to 10^9. These extended simulations, which can be seen in Figure 2.10, show that for hot white dwarfs, small asteroids can sublimate up to 10^8 relative astrocentric distances from the white dwarf, four orders of magnitude larger than for the coolest white dwarf considered here. The physical extent at which asteroids can sublimate around a hot white dwarf is particularly interesting when compared to the tidal boundary for canonical rubble pile asteroids.

In Section 2.3.2, we used the assumption that internal strength dominates over self-gravitation and that bodies are closer to monoliths than rubble piles. If we instead adopt the assumption that $\boldsymbol{F}_S/\boldsymbol{F}_G << 1$ then the condition derived by solving equation (2.30), provides us with the location of tidal disruption for a rubble pile body,

$$x_{\rm Roche} = \left(\frac{M_{\rm WD}a}{\pi\rho U_x R_{\rm WD}^3}\right), \tag{2.41}$$

where again we are only considering the x-direction. Using equation (2.41), the material properties given in Table 2.2 and the shapes in Table 2.1, we find that $x_{\rm Roche} \sim 10^2 - 10^4$. The smaller constituent particles of a rubble pile asteroid are then susceptible to sublimation before they are even tidally disrupted from their parent body, and thus are unlikely to persist for long after an initial disruption event.

Figure 2.9 also shows that there are very few cases where a body will undergo partial sublimation before impacting directly onto the white dwarf, and no cases where a partially sublimated body fragments, although again here we note the small number of bodies we sample in this work. Two clear examples of partial sublimation can be seen in the top left hand panel of Figure 2.9 with the two smallest generic shaped asteroids that impact. These two specific cases begin to lose mass at about 10 relative astrocentric distances from the star and their semi-major axes only decrease by a small amount before they are directly accreted. Further investigations with larger sample sizes may exhibit more partial sublimation events.

For the two hottest white dwarfs considered, the largest body which undergoes partial sublimation is $\sim 10^3$ cm, whereas only the smallest $a < 10^1$ cm bodies partially sublimate around the cooler white dwarfs. Since our model assumes that the body has a uniform composition, the asteroids here represent a maximal level of sublimation for a particular material, and thus the small amount of objects which partially sublimate could imply a small range of asteroid sizes per white dwarf temperature where volatile elements are preferentially lost compared to more refractory elements.

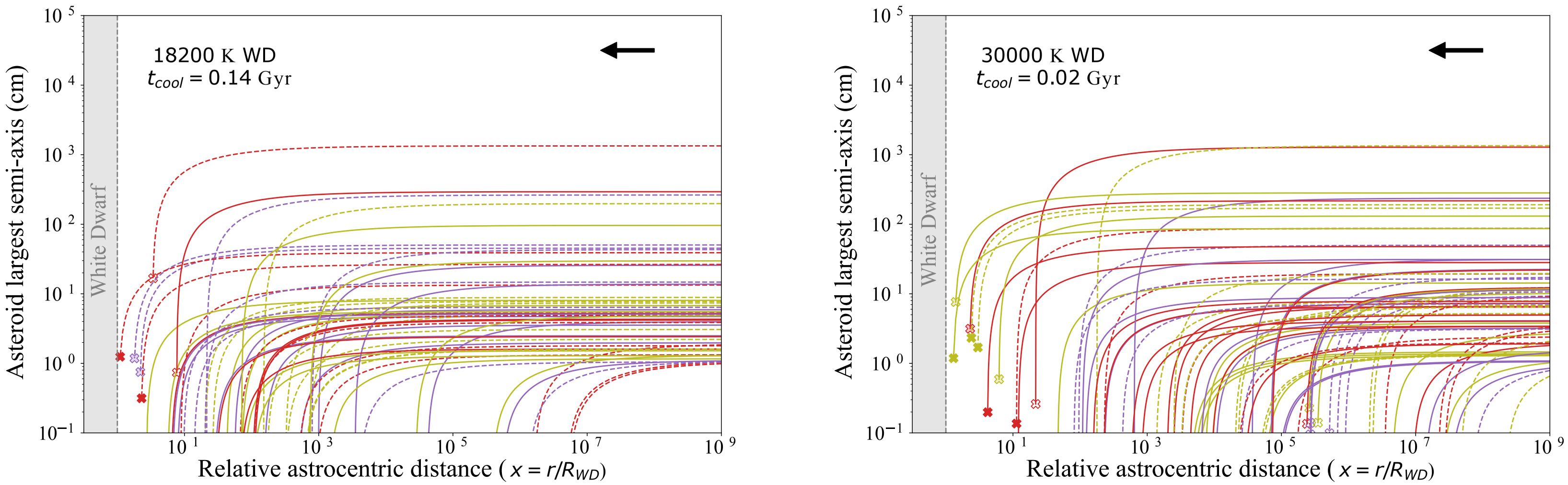

Figure 2.10: The fate of sublimated Main Belt analogue asteroids approaching a white dwarf on an extremely eccentric orbit. Here as in Figure 2.9, the line colours and line styles indicate the shape model, the marker fill shows the material properties of the specific body. Only sublimated asteroids are shown in these panels, and hence all end points have the same cross-shaped marker. The x-axis showing the relative astrocentric distance from the white dwarf is extended to 10^9 ($\sim 10^4$ au)

, as compared to 10^4 in Figure 2.9. The hottest white dwarfs considered in this work can completely sublimate small asteroids up to $\sim 10^8$ relative astrocentric distances away from the central star, seven orders of magnitude further out than for the coolest white dwarf considered in this work.

Table 2.4: Minimum, median and maximum impactor sizes across the range of white dwarf temperatures.

T_{WD}	Minimum (cm)	Median (cm)	Maximum (cm)
30 000 K	97.9	839	11400
18 200 K	6.72	107	2290
11 000 K	0.14	12.8	10600
6 700 K	0.24	12.8	10600
4 000 K	0.84	11.7	19300

Although direct impacts occur across all white dwarf temperatures considered, the range of sizes which impact increases as the white dwarf cools. Table 2.4 gives the minimum, median and maximum asteroid sizes at moment of impact across all five white dwarf temperatures in the simulations presented in Figure 2.9. The minimum and median impactor sizes generally decrease as the white dwarf cools. This can be explained by the fact that at higher white dwarf temperatures, these smaller bodies will be sublimated completely. The maximum impact sizes range between the order of 10^3 – 10^4 cm, with all of these bodies being made from iron. The smaller maximum impactor size recorded for the 18, 200 K white dwarf simulation is due to the random nature of size and material selection and small sample sizes used in the simulations. As each simulation has a different selection of size and asteroid properties, the 18, 200 K simulation simply did not contain an iron asteroid with a similar size to the largest impactors in the other simulations.

To confirm the random selection and small sample number is the cause of the different maximum sizes, a dedicated study with a fixed material and size distribution was carried out. The maximum impactor size for iron asteroids is always of the order 10^4 cm. For rocky asteroids the maximum is 10^3 cm, and for snowy asteroids it is 10^2 cm. Although it should be noted that for snowy asteroids, no impacts are expected for the hottest white dwarf temperature due to the increased rate of sublimation. Thus, the largest asteroid that could directly impact on a white dwarf's photosphere has $a \sim 10^4$ cm = 0.1 km, a value that is similar in size to the Solar System asteroid Bennu[4].

The maximum asteroid size for direct impact is determined by the specific material properties of the body itself, while the minimum impact size is dictated by the sublimation limit due to the stellar radiation from the white dwarf. A direct asteroid impact could be inferred from a short term increase in calculated accretion rates.

2.4.1 The effect of shape

To investigate the role of triaxiality on the destruction regime of a body approaching a white dwarf, we first compare the triaxial model to a spherical model (Section 2.4.1), then we look at the specific impact on sublimation (Section 2.4.1).

[4]Bennu has a radius of 0.246 km taken from the NASA JPL Small Body Database https://ssd.jpl.nasa.gov/sbdb.cgi.

Shape model comparison

To further motivate the future use of triaxial shape models, we now directly compare the forces and binding and sublimation parameters introduced in Sections 2.3.1-2.3.2 to the equivalent spherical forms.

The following spherical forces are similar in form to those presented in BVG17 and Bear and Soker [2015],

$$F_{T_{\text{spher}}} = \frac{2GM_{\text{WD}}Ma}{x^3 R_{\text{WD}}^3}, \tag{2.42}$$

$$F_{S_{\text{spher}}} = -\pi a^2 S, \tag{2.43}$$

$$F_{G_{\text{spher}}} = -\frac{GM}{a^2}. \tag{2.44}$$

Using the above forces, we can find the sublimation and binding size parameters (equations 2.22 and 2.33) for a purely spherical shape model

$$A_{\text{spher}} = \frac{R_{\text{WD}}^{3/2} T_{\text{eff}}^4 \sigma}{2\mathcal{L}\rho\sqrt{2GM_{\text{WD}}}}, \tag{2.45}$$

$$B_{\text{spher}} = \sqrt{\frac{3R_{\text{WD}}^3 S}{8GM_{\text{WD}}\rho}}, \tag{2.46}$$

where these differ from the BVG17 results only by a numerical factor. Remembering that the binding size parameter dictates the fragmentation of an object, that it involves the tidal and strength forces, and that fragmentation always occurs in the x-direction of the ellipsoidal body, we can compare the forces in the following ratios

$$\frac{F_{T_x}}{F_{T_{\text{spher}}}} = 1, \tag{2.47}$$

$$\frac{F_{S_x}}{F_{S_{\text{spher}}}} = \mathfrak{c}\mathfrak{b}. \tag{2.48}$$

Thus, the tidal force on the longest (x) axis of a triaxial body is identical to the spherical body case. However, the tensile strength on the longest axis of a triaxial body is reduced by a factor equal to the product of the body's two aspect ratios $\mathfrak{b}$ and $\mathfrak{c}$. Using these two results and following the procedure from Section 2.3.2 we can compare the x component of the triaxial binding size parameter to the spherical parameter

$$\frac{B_x}{B_{\text{spher}}} = 1. \tag{2.49}$$

The above result confirms that the condition for fragmentation is independent of an individual shape model and can be approximated using a spherical model.

As discussed in Section 2.3.4, total sublimation always occurs in the semi-minor axis (z-direction) first. Using this fact, we can compare A_z from the triaxial model to the spherical sublimation parameter from equation (2.45) to identify the effect of shape on sublimation

$$\frac{A_z}{A_{\mathrm{spher}}} = \frac{1}{\mathfrak{c}}. \tag{2.50}$$

The result in equation (2.50) shows that when using a triaxial shape model, the minimum size a body must be to withstand sublimation all the way to the photosphere of the white dwarf, is increased by a factor of the aspect ratio $\mathfrak{c}$ between the semi-minor and semi-major axes. As total sublimation occurs in the semi-minor axes, the $\mathfrak{b}$ aspect ratio between the semi-intermediate and semi-major axes does not affect the level of sublimation in a triaxial asteroid compared to a spherical model. Thus, triaxial asteroids are more vulnerable to complete sublimation than a spherical asteroid.

The effect of shape on sublimation

Figures 2.9 and 2.10 show that sublimation is most prevalent around hot white dwarfs, where bodies up to 10^4 cm in size can sublimate completely. To further investigate the role of triaxiality on sublimation, a larger sample size of 1000 asteroids with semi-major axes evenly spaced in log space in the range $10^0 - 10^4$ cm were run through the analytical process discussed in Section 2.3.4, except with fixed shape models and materials for a $18,200$ K and $30,000$ K white dwarf.

Figure 2.11 shows the fraction of these 1000 asteroids which sublimate for each possible combination of material and shape. The fiducial (prolate, oblate and generic) shape columns show the total percentage of bodies which sublimate, while the extreme shape model columns show the percentage increase in sublimation compared to the fiducial models. As an example, for the $18,200$ K white dwarf and iron bodies, 28 ± 2 per cent of prolate bodies sublimated, whereas 40 ± 2 per cent of extreme prolate asteroids sublimated. Again, the errors presented above are calculated assuming Poisson statistics and show that increasing the sample size by one order of magnitude decreases the errors compared to those previously discussed in Section 2.4.

These graphics show that amongst the fiducial shape models, there is no dependence on shape on the percentage of bodies which sublimate. However, all of the extreme shape models show an increased level of sublimation compared to their fiducial counterparts. The extreme prolate and generic models show the same increase in sublimation, while the extreme oblate models shows less, which can be explained by examining equation (2.50) and the shape parameters defined in Table 2.1. The fiducial models all share a common aspect ratio $\mathfrak{b} = 0.6$, the extreme oblate model has $\mathfrak{b} = 0.4$, whereas both the extreme generic and extreme prolate models have $\mathfrak{b} = 0.2$. The levels of sublimation increases as the $\mathfrak{b}$ aspect ratio decreases according to equation (2.50).

2.5 Further considerations

This work takes an overall simple approach to solving the problem of asteroid disruption around a white dwarf. The analytical model described here only records the initial disruption process and does not consider what happens to the products of the disruption process. The possible subsequent processes which affect the initial disruption products are now briefly considered.

2.5.1 Sublimated material

The sublimated material from an asteroid approaching a white dwarf on an extremely eccentric orbit could quickly accrete onto the white dwarf, or form part of a gaseous debris disc [Trevascus et al., 2021]. The white dwarf SDSS J1228+1040 is observed with an extremely dense planetesimal orbiting inside a debris disc with a gaseous component expanding out to $\sim 1.2R_{\odot}$ [Gänsicke et al. 2006; Manser et al. 2019; further discussed in Chapter 1.3.2]. In order to compare both the level of sublimation and the physical extent of a gas disc which could be produced by the process discussed in this chapter, 1000 asteroids are passed through the process described in Section 2.3.4. In this case, we adjust the fiducial white dwarf properties previously used in this work and adopt the measured SDSS J1228+1040 properties; $M_{\mathrm{WD}} = 0.77M_{\odot}$ and $T_{\mathrm{eff}} = 22020$ K [Gänsicke et al., 2006]. Figure 2.12 shows a histogram of the relative astrocentric distances at which the bodies sublimate. The black, dashed, vertical line indicates the outer radius of the SDSS J1228+1040 gas disc. This figure shows that sublimated gaseous materials can easily form within the radial extent of the SDSS J1228+1040 debris disc. Further, gaseous materials could be produced beyond this limit, but with decreasing amounts as the astrocentric distances increases.

This work focusses on sublimation as the origin of gaseous debris around white dwarfs, however this is not the only avenue for gas production.

Collisional cascades of fragmented material will likely produce gas, both during and immediately after a fragmentation event [Kenyon and Bromley, 2017a]. However, Metzger, Rafikov, and Bochkarev [2012] argue that long-lived observations of infrared excesses around white dwarfs preclude collisions being the main source of gaseous debris, as collisions would convert all disc material into gas on the order of days. Thus sublimation is expected to play a large role in the production of gaseous debris. The interaction of planetesimals with existing gaseous debris can further produce gas as discussed in Section 2.5.3.

Further, the process of sublimation is complicated if there is a pre-existing debris disc around the white dwarf. If an incoming body can be captured and embedded into the debris disc [Grishin and Veras, 2019; O'Connor and Lai, 2020; Malamud et al., 2021] it can be shielded from sublimative effects. Since the disc will not be isothermal, the optical depth

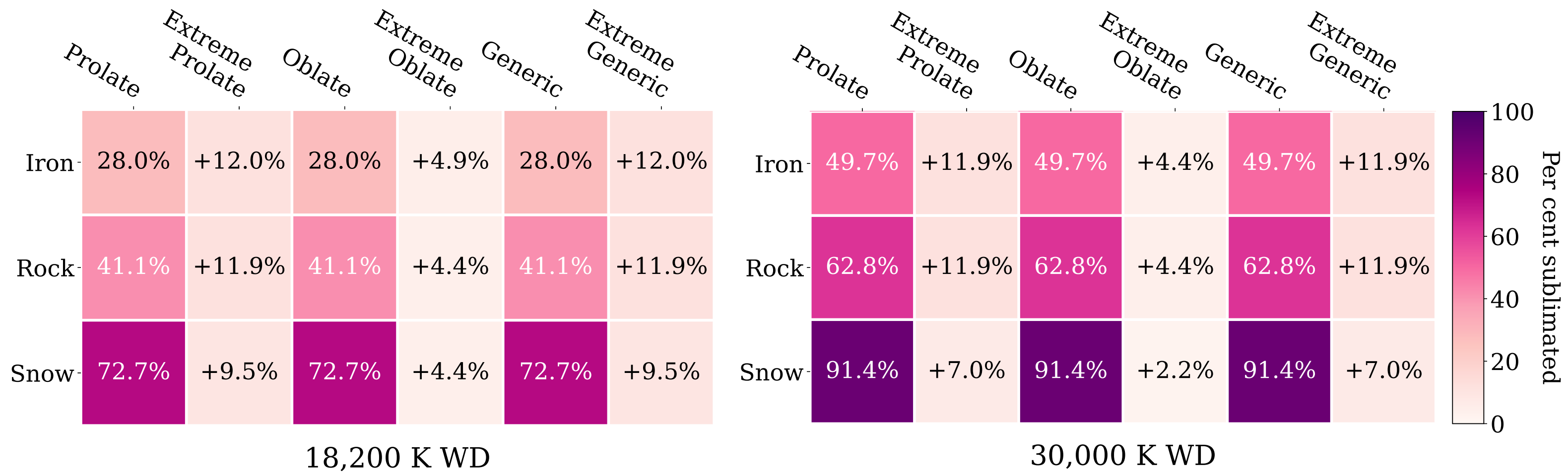

Figure 2.11: The effect of a triaxial shape model and material on the amount of sublimation an analogue Main Belt perturbed towards the white dwarf will undergo. The fiducial shape model (prolate, oblate and generic) columns display the percentage of 1000 asteroids in the size range $10^0 - 10^4$cm which sublimate completely. The extreme shape model columns show the percentage increase in asteroids which sublimate completely compared to their respective fiducial shape models. The colour of each box illustrates the percentage as described by the colour bar along the right hand side. The fiducial shape models show identical levels of sublimation for each material, all extreme models show even more increased sublimation. The extreme prolate and generic shape models show the same increase in sublimation, although the extreme oblate model exhibits a smaller increase.

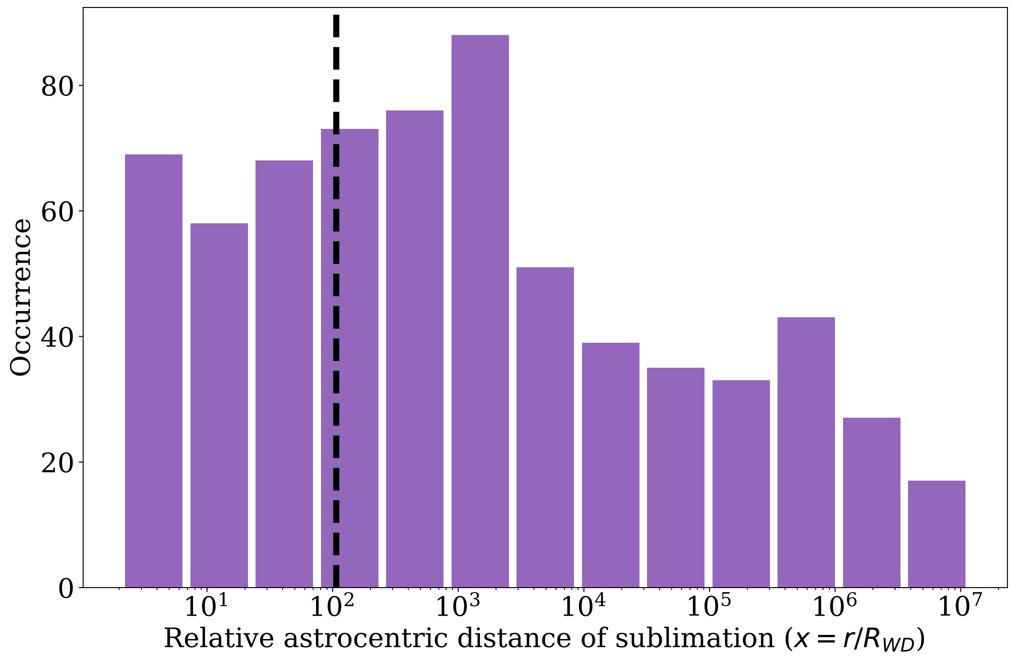

Figure 2.12: A histogram showing the number of bodies which sublimate at different astrocentric distances from a white dwarf with the same properties as SDSS J1228+1040. The dashed black line at $\sim 10^2$ indicates the estimated outer radius of the gas disc around SDSS J1228+1040. This outer radius is similar to those of other gas discs with well-constrained geometries. Small bodies $< 10^4$cm can sublimate far beyond the radial extent of this observed gaseous disc.

will vary throughout the disc. Rafikov and Garmilla [2012] give the following expressions for the equilibrium temperature of dust particles within an optically thin part of the disc ($T_{\rm thin}$) and an optically thick part of the disc ($T_{\rm thick}$)

$$
\begin{aligned}
T_{\rm thin} &= T_{\rm WD}\left(\frac{1}{2}\right)^{1/2}\left(\frac{R_{\rm WD}}{r}\right)^{1/2} \\
&= T_{\rm WD}\left(\frac{1}{2}\right)^{1/2} x^{-1/2},
\end{aligned}
\tag{2.51}
$$

$$
\begin{aligned}
T_{\rm thick} &= T_{\rm WD}\left(\frac{2}{3\pi}\right)^{1/4}\left(\frac{R_{\rm WD}}{r}\right)^{3/4} \\
&= T_{\rm WD}\left(\frac{2}{3\pi}\right)^{1/4} x^{-3/4},
\end{aligned}
\tag{2.52}
$$

where $x = r/R_{\rm WD}$ is the relative astrocentric distance as before. $T_{\rm thin}$ approximates the temperature of dust particles at the very inner edge of a debris disc which are directly illuminated by the central star.

The canonical model for a white dwarf planetary debris disc is one similar to Saturn's rings; geometrically thin and optically thick (see Chapter 1.3.2 for more details about the disc model). Thus, $T_{\rm thick}$ likely approximates the dust particle temperatures throughout the rest of the disc. If we take the outer edge of the SDSS J1228+1040 gas disc at $R \sim 1.2R_{\odot}$ which gives $x \sim 107$ as the outer edge of an optically thick disc, the equilibrium temperature of dust particles around a $T_{\rm WD} = 22020$ K white dwarf is $T_{\rm thick} \sim 450$ K. However, the equilibrium temperature in an optically thin disc at the same location is $T_{\rm thin} \sim 1505$ K. Thus, in the presence of a pre-existing debris disc the efficiency of sublimation for infalling bodies is largely dependent on the optical depth of the surrounding material. The shielding effects of optically thick material may allow infalling material to come closer to the white dwarf before undergoing sublimation as temperatures rise in the inner disc.

The effect of interactions with an extant debris disc on infalling material which are expected to impact on the white dwarf in this model are further discussed in Section 2.5.3.

2.5.2 Fragmented material

The products of the fragmentation process will likely continue fragmenting until the products reach a size where the internal strength of the body will exceed the tidal force acting upon it regardless of how far away it is from the star. This resultant distribution of dusty debris will form a ring on short time scales depending on the initial size of the asteroid. Asteroids which approach the white dwarf from the location of an exo-Main Belt at ≈ 5 au and tidally disrupt, will completely fill a ring with debris within 100 yr [Chapter 1.3.2; Veras et al. 2014b].

We can provide very rough estimates for the lifetime of a disc of fragments after they have circularized enough [Veras et al., 2015b; Malamud et al., 2021] such that their eccentricity and inclination dispersions are less than about 0.1 rad. In this case, if the fragments are assumed to be equal rocky spheres, then we can read off the disc lifetimes from the appropriate figures in Veras and Heng [2020].

Consider fragmentation at two different locations from a white dwarf: $0.5R_{\odot}$ and $3.0R_{\odot}$, values which are deliberately chosen to straddle the often-used rubble pile Roche limit and to correspond to Figures 5 and 7 of Veras and Heng [2020]. According to our Figure 2.4, rocky asteroids with $a \approx 10^{5.8}$ cm and $a \approx 10^{7.0}$ cm will respectively fragment at these distances when $x \approx 40$ and $x \approx 240$, assuming that $R_{\rm WD} \approx 9 \times 10^3$ km. These asteroids will form discs of mass $\approx 3 \times 10^{15}$ kg and $\approx 1 \times 10^{19}$ kg, respectively.

Their lifetimes are then determined by the size of the fragments. If $\mathcal{N}$ fragments are formed, then $a_{\rm frag} = \mathcal{N}^{-1/3}a$. Suppose $\mathcal{N} = 10^3$. Then, the disc lifetime for the $a \approx 10^{5.8}$ cm progenitor is 10^{4-5} yr. For the $a \approx 10^{7.0}$ cm progenitor, the lifetime depends more strongly on the eccentricity and inclination dispersion of the fragments. When these dispersions are on the order of 10^{-1}, then the lifetime is 10^{3-5} yr. However, for dispersions on the order of 10^{-4}, the disc lifetime may be comparable to the white dwarf's cooling age.

These disc lifetimes then allow us to provide estimates for the rate material is accreted onto the central white dwarf. The less massive $\approx 3 \times 10^{15}$ kg debris disc developing from an $a \approx 10^{5.8}$ cm progenitor can thus have accretion rates on the order of $10^5 - 10^6$ g s^{-1} . However, the larger $a \approx 10^{7.0}$ cm progenitor which leads to a more massive 1×10^{19} kg debris disc can have accretion rates varying from 10^9 g s^{-1} to 10^{11} g s^{-1} . Inferred accretion rates for observed white dwarfs lie in the range $10^5 - 10^{10}$ g s^{-1} , with older, colder white dwarfs having lower rates [e.g. Wyatt et al., 2014; Koester et al., 2014; Farihi, 2016]. Therefore, our calculated discs can plausibly recreate observed accretion rates.

2.5.3 Impactors

As discussed in Section 2.3.3 the bodies that enter directly into the white dwarf's photosphere will not be able to survive this encounter and continue on their orbits. It is thought that such large-scale accretion could be observed in the form of surface abundance variations for warm white dwarfs. DA white dwarfs with $T_{\rm eff} > 13,000$K are inefficient at homogenising material accreted onto the surface of the white dwarf and hence one large impact accretion event could be observable in surface abundance variations, whereas DB white dwarfs can homogenise accreted material within a diffusion timescale [Cunningham et al., 2021]. At lower white dwarf temperatures, the homogenisation process becomes more efficient and thus abundance variations from impact events will be unobservable.

An inherent assumption in our study is that an incoming asteroid does not first impact an extant disc. This important scenario has been considered in several contexts and different regions of parameter space [Grishin and Veras, 2019; O'Connor and Lai, 2020;

Malamud et al., 2021], and may help to explain the origin of the planetesimal orbiting SDSS J1228+1040.

Further, the interaction of an incoming asteroid with an existing debris disc can further produce gaseous material [Malamud et al., 2021]. Smaller dust grains entering into a disc can collide with other dust grains resulting in compression shock vaporisation. Dust grains colliding with a larger incoming planetesimal can cause dusty material to be ejected from the surface of the body and then go on to vaporise through collisions. Finally, energetic gas ions colliding with solid material can cause collisional cascades between the material's lattice atoms. If the cascade reaches the surface of the material with an energy that exceeds the surface binding energy, then atoms can be ejected from the surface in a process known as sputtering [Behrisch and Eckstein, 2007].

The gaseous material produced through direct sublimation, as in the focus of this work, or by the interaction between an incoming body and an extant debris disc as discussed above, can have a further erosive effect on a planetesimal moving within it. Bodies which move within a gas disc are subject to a gas drag dependent on the relative velocity of the object and the gas. This gas drag can cause outer layers of the body to be lost analagous to aeolian erosive winds [Rozner et al., 2021].

2.5.4 Rotation

In this work we do not consider the effect of rotation because the tidal potential model used here and in Dobrovolskis [2019] assumes that the minor body is tidally locked to the star and the body's semi-major axis is always pointing towards the central body. This assumption has a physical basis because a body's least stable and most vulnerable point to tidal forces is at the end of the longest axis [Harris, 1996]. Thus, tidal disruption will always occur in the x-direction first, which is seen in Figure 2.5 and discussed in Section 2.3.4. Since the tidal force on the x-axis will always be strongest when pointing directly towards the central body, our results represent the distance furthest from the white dwarf where fragmentation can occur.

Although in this chapter we do not consider the effect of asteroid rotation, it is known that if a rubble pile asteroid acquires a sufficient spin rate, it can no longer support itself and undergoes disruption at the so-called 'spin barrier' [see Figure 1.5 or figure 1 of Hestroffer et al. 2019]. While YORP based spin up is expected to destroy a large number of small bodies during the giant branch phases, it has also been shown that extremely eccentric asteroids can chaotically increase their rotational speed through the exchange of orbital and angular momentum at repeated pericentre passages [Makarov and Veras, 2019; Veras et al., 2020a]. Rotation thus provides a whole new avenue to destruction for eccentric, triaxial asteroids that is not considered here.

2.6 Conclusions

Increasing observations of minor bodies being disrupted around white dwarfs provide motivation for increasing our understanding of the processes which lead to these bodies being destroyed. Most previous theoretical work on this topic has used spherical shape models to approximate asteroids. However, Solar System studies show that asteroids can be well-approximated by triaxial ellipsoids. In this work, we expand on the work of Brown et al. [2017] studying steeply infalling debris around a white dwarf by considering the effects of a triaxial shape model on the destruction mode of an asteroid approaching a white dwarf on an extremely eccentric orbit using analytical methods and considering an ensemble of asteroids from simplified Main Belt analogues. To consider the effect of a white dwarf's temperature on the type of disruption, we first provide an empirical relation between the white dwarf cooling age and effective temperature which encompasses both DA and DB cooling models in equation 2.9.

By considering the individual forces acting on each individual principal direction of the body, we define the binding size parameter (equation 2.33) as the size a body must exceed to fragment and the sublimation parameter (equation 2.22) as the minimum size a body must be to survive sublimation to the white dwarf photosphere. These two parameters allow us to outline an analytical framework to quickly identify how and where an asteroid with specific properties will disrupt around a white dwarf, this framework is shown graphically in Figure 2.7.

Using this analytical model, we identified that tidal fragmentation principally occurs in the largest semi-axis for bodies larger than $\sim$ 100m (Figure 2.5). As considering the semi-major axis, x-direction, for a triaxial shape model is equivalent to considering a spherical model with radius the same size as the semi-major axis, using a spherical shape model is adequate to investigate tidal disruption.

On the other hand, total sublimation will occur first in the smallest semi-axis (Figure 2.5), and thus in order to not underestimate the distance from the white dwarf where sublimation occurs, an ellipsoidal shape model should be used. Hot white dwarfs can sublimate bodies up to $\sim 10^3$cm at large distances from the white dwarf (Figure 2.10), beyond the estimated extent of the gaseous debris disc around the white dwarf SDSS J1228+1040 (Figure 2.12). Cooler white dwarfs are only efficient at sublimating extremely small bodies ($a < 10^1$cm) at distances relatively close to the white dwarf (Figure 2.9). Snowy, cometary, bodies are more susceptible to sublimation than rock or iron bodies which have higher values of latent heat. The fiducial triaxial shape models used in this work have little affect on the amount of sublimation. However, the extreme shape models with a greater degree of elongation show increased levels of sublimation (Figure 2.11). The increased level of sublimation is caused by the minimum size a body must be to withstand sublimation increasing by a factor of $\mathfrak{c}$, the ratio between the longest and shortest semi-axes, for triaxial models compared to spherical as in equation 2.50.

Bodies which neither fragment nor sublimate can directly impact the white dwarf's photosphere. The minimum impactor size is governed by the maximum size body that the white dwarf can sublimate, and hence the temperature of the white dwarf. The maximum impactor size depends on the minimum body size which will fragment while approaching the white dwarf as seen in Table 2.4. Thus the maximum impactor size is independent of the white dwarf temperature and the minimum size increases as the white dwarf cools.

To investigate how the planetary debris around a white dwarf would change as the star cools and ages, we simulated simplified Main Belt analogues of 100 bodies with randomised shape, materials and sizes drawn randomly between $10^0 - 10^9$cm and assumed all the bodies were randomly perturbed towards the white dwarf without further dynamical interactions (Figure 2.9). The material properties of the bodies were chosen to broadly align with three different planetary materials; snowy-cometary bodies, rocky bodies similar to meteorites and solid iron bodies and largely affect the destruction outcomes. The small sample sizes considered in this work, which are exacerbated by randomising asteroid properties, subject the results to small number statistics, and more statistically significant conclusions could be drawn with increased sample sizes in future investigations.

It was found that early in a white dwarf's lifetime, while it still has a relatively large effective temperature, bodies of 10s of metres can sublimate completely at distances quite far from the white dwarf. The condition for a body to fragment is affected by the size of the white dwarf, but not by its temperature (equation 2.33). Therefore, across all ages, bodies larger than $\sim$ 100m can fragment. The bodies that survive either of these conditions will enter directly into the white dwarf's photosphere.

Ultimately, the cooling age, and hence effective temperature, of the white dwarf can have a large effect on the distribution of any disrupted material. While white dwarfs are young and hot, a broader ring of gaseous sublimated material out to large distances (10^9 relative astrocentric distances) could be expected (Figure 2.10). The physical extent of solid, tidal fragments would not be different between white dwarf cooling ages. The size range of bodies which directly impact onto the white dwarf grows as the white dwarf cools, however, the possibility of observing such direct impacts from variations in surface abundances decreases as the white dwarf cools.

Chapter 3

Binary asteroid scattering around white dwarfs

Increasing observations of white dwarf atmospheric pollution and disrupting planetesimals is driving increased studies into the fate of exo-asteroids around post-main-sequence stars. Planetesimal populations in the Solar System which are most likely to survive the violent post-main-sequence evolution, such as the Kuiper Belt, display a large binary fraction with a propensity for near equal-mass components and provide a previously unexplored population of planetesimals which are likely to exist around white dwarfs. Here we simulate the dynamical evolution of equal-mass binary asteroid systems around white dwarfs using the N-body integrator `REBOUND` for 1 Gyr. We confirm that giant planets are efficient at dissociating and ejecting binary asteroid systems on eccentric orbits, while Earth-mass planets are better at keeping planetesimals in their planetary systems. We find binary systems can be dissociated and ejected from their systems across Myr timescales, producing interstellar objects. We do not expect a population of free-floating binary asteroid systems as all ejected planetesimals are gravitationally unbound from each other. Further, we discuss the influence of asteroid binarity on the white dwarf pollution process and find there is little to no impact on how close a body can get to a star. However, the orbital evolution of binary asteroids changes the distribution of planetesimals available in a white dwarf planetary system to be further scattered onto white dwarf polluting orbits.

3.1 Introduction

White dwarfs provide a unique opportunity to understand the composition of planets and planetesimals in exoplanetary systems, as white dwarfs have such intense surface gravities that elements heavier than hydrogen and helium should quickly sink to the cores and hence no longer be visible in spectroscopic observations [Paquette et al. 1986b; Wyatt et al. 2014; Chapter 1.3.2]. However, between a quarter and half of all white dwarfs are observed with metals in their atmospheres [Zuckerman et al., 2010; Koester et al., 2014; Kepler et al., 2015, 2016; Coutu et al., 2019] which could only be present if they had recently been deposited on the surface.

A large proportion of this accreted material appears to be aligned with the composition of terrestrial planetesimals [Zuckerman et al. 2010; Jura and Young 2014; Hollands et al. 2018; Doyle et al. 2019; see Figure 1.11] and a much smaller proportion with more volatile rich bodies [Farihi et al., 2013; Raddi et al., 2015; Gentile Fusillo et al., 2017; Xu et al., 2017; Hoskin et al., 2020]. It is believed that this material originates in asteroidal bodies which have been perturbed onto orbits which cross the Roche limit of the white dwarf and hence are tidally disrupted. The subsequent material likely forms a disc of dust and/or gas orbiting around the white dwarf. Such dusty debris discs are observed in the form of infrared excesses around $1-3$ per cent of white dwarfs [Rebassa-Mansergas et al., 2019] and gaseous discs are observed around $0.04-0.1$ per cent of white dwarfs [Manser et al., 2020]. But it is expected that most white dwarfs which exhibit metallic pollution should also be host to debris discs (see section 4 and figure 9 of Bonsor et al. [2017]) with up to 90 per cent of those discs being currently unobservable [Rocchetto et al., 2015].

As a star leaves the main sequence, its increased luminosity and physical size will have a considerable effect on the planetary system that might reside around it. See Chapter 1.2 for a full discussion of the evolution of planetary systems during the giant branch evolutionary phases. Close in planets will be engulfed by the expanding stellar envelope, and planets which escape this fate will be pushed out onto orbits $2-3\times$ larger than their main sequence distances [Veras, 2016]. A significant proportion of minor bodies within ~ 7 au of the host star will be broken down to their strongest components through the increased YORP effect during the giant branch phases of stellar evolution [Veras et al., 2014a]. At larger distances, Veras and Scheeres [2020] find that asteroids with $a \gtrsim 50$ au will almost always avoid rotational fission due to the YORP effect. Further, planetesimals at these distances, such as in an exo-Kuiper Belt, will likely remain intact through the post-main-sequence increased luminosity and dynamical instabilities [Debes and Sigurdsson, 2002; Veras and Gänsicke, 2015; Veras et al., 2016; Mustill et al., 2018; Maldonado et al., 2020a,b,c].

The increasing number of observations showing planetesimals in various stages of disruption transiting white dwarfs [Vanderburg et al. 2015; Vanderbosch et al. 2020, 2021; Guidry et al. 2021; Farihi et al. 2022; Chapter 1.3.2], are presenting new challenges to our understanding of remnant planetary systems around white dwarfs. Thus using our knowledge of Solar System asteroids, which remain the most well studied population of planetesimals, could provide the key to improving our efforts to model white dwarf debris systems.

In the Solar System a significant proportion of planetesimals exist in binary, or higher multiplicity, systems. This proportion has been shown observationally to vary from several per cent to several tens of per cent depending on both location and planetesimal size, and theorised to be as high as 100 per cent at formation [Fraser et al., 2017].

In particular, photometric studies of the Main Belt suggest that 6 ± 3 per cent of asteroids with radius larger than 10 km should be binaries with comparable sized components [Behrend et al., 2006]. The Near-Earth asteroid (NEA) population appears to host $15 - 17$ per cent of bodies larger than 0.3 km in diameter as binaries [Margot et al., 2002; Pravec et al., 2006] and a further ~ 10 per cent of NEA bodies exist as contact binaries [Benner et al., 2006]. The prevalence of multiple asteroid systems persists throughout the outer regions of the Solar System with $6 - 10$ per cent of Trojan asteroids existing as contact binaries [Mann et al., 2007] and three Trojans containing their own satellites [Merline et al., 2002; Marchis et al., 2014; Noll et al., 2020].

Out to even further orbital distances, the Trans-Neptunian Objects (TNOs) in the Kuiper Belt are estimated to have a $10 - 20$ per cent binary fraction [Stephens and Noll, 2006; Noll et al., 2008]. The cold classical Kuiper Belt objects (CCKBOs) are a population of planetesimals harbouring low inclinations and eccentricities alongside red colours and high albedos [Nesvorný and Vokrouhlicky, 2019] and are thought to be a primordial reservoir of planetesimals which formed at their current location. The binary fraction for the CCKBOs is thought to be higher than the TNO region as a whole at $\sim 20 - 30$ per cent [Benecchi et al., 2019].

It has been suggested that binarity is a natural consequence of planetesimal formation and thus populations such as the CCKBOs could have had a near 100 per cent binary fraction at formation [Fraser et al., 2017]. Thus these bodies perhaps provide a unique opportunity to look at the relatively unprocessed results of planetesimal formation, without the influence of the Solar System's particular dynamical history.

The planetesimals which are most likely to survive post-main-sequence evolution are those in the outer regions of planetary systems where binarity is high in the Solar System. However, this potentially significant population has been almost completely ignored in previous post-main-sequence investigations. Thus, in this chapter we investigate the dynamical evolution of binary asteroids in white dwarf planetary systems, and characterise their influence on observable pollution, transiting debris and the population of interstellar free-floaters (of which 1I/2017 U1 'Oumuamua is an example).

In Section 3.2 we outline the set up of our simulations and the conditions for asteroid tidal disruption, system ejection and binary dissociation. We apply these simulations to a

Solar System analogue including the four giant planets, as well as systems where the binary asteroids are interior and exterior to an Earth-mass planet's orbit, in Section 3.3. In Section 3.4 we discuss some of the implications of asteroid binarity on the prospects for white dwarf debris systems and the production of interstellar objects. Finally, we conclude in Section 3.5.

3.2 REBOUND simulations

To investigate the fate of binary asteroids in a post-main-sequence planetary system, we carry out N-body simulations using the REBOUND package [Rein and Liu, 2012].

We utilise the WHFast integrator module within REBOUND [Rein and Tamayo, 2015] which is an implementation of the symplectic Wisdom-Holman integrator [Wisdom and Holman, 1991]. We chose to use WHFast instead of an adaptive timestep integrator such as IAS15 [Rein and Spiegel, 2015] as in order to capture the dynamics of the binary orbit alongside the circumstellar orbit the integration timestep needed to be small and we found a significant speed advantage in using WHFast over IAS15 without loss of information.

Although the use of a Wisdom Holman integration scheme such as WHFast is most accurate for systems where motion is dominated by a central potential and other perturbations are small [Rein and Liu, 2012], we carried out a number of tests to ensure that our numerical simulations are sufficient and provide valid results.

Firstly, we confirm that the relative error on energy and angular momentum of the majority of our simulations are of the order $\times 10^{-10}$, and never larger than $\times 10^{-7}$, ensuring a reasonable accuracy for our numerical simulations. As the majority of the energy and angular momentum in our simulations is held by the planets, we also considered the binary asteroid systems in the absence of planets. As before, the relative error on energy and angular momentum of the binary asteroid systems is also on the order of $\times 10^{-10}$ or smaller.

Secondly, we carried out a small number of test simulations with varying timestep values to check our results converge. For a total of 12 asteroid systems in each planetary architecture considered in this work, we carried out additional simulations with identical initial conditions and timesteps either a factor of three larger or one third smaller than $dt \sim 0.006$ yr. We find that for the Solar System analogue simulations (Section 3.3.1) and those containing planetesimals exterior to an Earth-mass planet (Section 3.3.2), only a single binary asteroid system has a different fate dependent on the simulation timestep used. The simulations with planetesimals interior to an Earth mass planet (Section 3.3.3) had no divergent results with differing timesteps. As there is only a small change in results dependent on the timestep used, and using a timestep a factor of three smaller increases the computation time by a factor of five, we find that the simulation procedure outlined above is sufficient for this general study.

Finally, we compared the performance of the WHFast integrator to the standard

Leapfrog scheme also provided in Rebound [Rein and Liu, 2012]. We again ran a small number of simulations for each planetary architecture using the Leapfrog integrator and examined the relative energy and angular momentum errors and the convergence of the results.

This integrator showed a similar outcome in terms of energy and angular momentum, with relative errors on the order of $\times 10^{-10}$. However, this integrator also produced significantly more divergent results than with WHFast. While considering the Solar System analogue architecture, 5 out of 12 simulations ran with the Leapfrog integrator produced divergent results dependent on the timestep chosen, compared to the single divergent result using WHFast.

Thus, we consider our choice of WHFast to be robust and sufficient for the aims of this study.

The outputs of each of the simulations carried out in this study were stored using the SimulationArchive format available in REBOUND which stores the state of the simulation regularly allowing for exact reproducibility [Rein and Tamayo, 2017].

Modelling binary asteroids orbiting a star is computationally demanding due to the difference in timescales for the two orbits. Thus we sought to find the combination of integration timestep and SimulationArchive output which would allow reasonable integration times. In order to preserve the information provided by the binary orbit, the integration timestep was set at ~ 0.006 yr, the same order of magnitude as the period of the tightest binaries we consider and three orders of magnitude smaller than the period of the widest. A snapshot was saved to the SimulationArchive every 10^5 yrs. As the binary systems are not expected to interact with each other significantly, we chose to simulate 100 binary asteroid systems across 25 simulations each containing four binaries. This provided a speed advantage over simulating 100 systems individually. With this configuration simulating the evolution of 100 binary asteroids in a planetary system took ~ 5200 hrs.

The planet and planetesimal architectures used in the simulations in this chapter are now explained.

3.2.1 Simulation set up

All of the simulations in this study began with the same basic set up. A central white dwarf was initialized with $M_{\mathrm{WD}} = 0.6\,\mathrm{M}_{\odot}$, which corresponds to the peak of the white dwarf mass distribution [Althaus et al. 2010; Kleinman et al. 2013; Tremblay et al. 2016; McCleery et al. 2020; see Figure 1.6].

We then added a number of binary asteroid systems orbiting around the central star. Each binary system is comprised of two equal size components with a mass of $m_{\mathrm{a}} = 2.5 \times 10^{19}$ kg, calculated assuming that each component has a radius of $r_{\mathrm{a}} = 125$ km and a fiducial density of 3 $\mathrm{g\,cm^{-3}}$. These values were motivated by the observation that 100 km class CCKBOs have a large percentage of resolved binaries with near equal-sized components [Parker and Kavelaars, 2010; de la Fuente Marcos et al., 2017; Nesvorný and Vokrouhlicky, 2019] and that TNOs in the mass range $10^{17} - 10^{22}$ kg are observed with calculated densities up to 4 g cm^{-3} [Carry, 2012].

A number of circumstellar semi-major axis ranges were considered based on the particular planetary system architectures which are described in Section 3.3. The circumstellar orbit was further initiated with a random eccentricity between $0 - 1$ (unless otherwise specified) and random inclination between $0 - 1°$. The initial mean anomaly of the circumstellar orbit was randomly chosen between $0 - 2\pi$ radians. The initial longitudes of ascending node and pericentre are set as zero. In order to implement our binary asteroid systems in `REBOUND` and correctly determine orbits, we set the primary of the system within the code as one of the binary asteroid components. The other binary component is then designated as the secondary.

A large range of initial circumstellar eccentricity values are chosen to cover the possibility that dynamical interactions with remnant planets may have already excited the circumstellar planetesimal orbit to higher eccentricities through a number of mechanisms [e.g. Wyatt et al., 2017; Pichierri et al., 2017], including eccentricity excitation without destructive instabilities [O'Connor et al., 2022].

The range of possible binary primary-secondary semi-major axes values were again motivated by observations. Nesvorný and Vokrouhlicky [2019] define the separation of a binary asteroid system as the ratio of the binary semi-major axis to the combined size of the binary components $a_{\mathrm{B}}/R_{\mathrm{B}}$, where $R_{\mathrm{B}}^3 = R_1^3 + R_2^3$, such that R_1, R_2 are the radii of the primary and secondary, respectively, and a_{B} is the semi-major axis of the primary-secondary orbit. Figure 2 of Nesvorný and Vokrouhlicky [2019] shows the distribution of binary separations for different dynamical classes of KBO using the catalogue of physical and orbital properties of binary asteroids maintained by W. R. Johnston on the NASA Planetary Data System (PDS) node [Johnston, 2019]. From this figure, it can be identified that binary CCKBOs have a binary separation in the range $10 < a_{\mathrm{B}}/R_{\mathrm{B}} < 1000$. Using the previously described asteroid properties chosen, we can thus find an approximate range of a_{B} for our binary asteroid systems; $1500 < a_{\mathrm{B}} < 1.5 \times 10^5$ km.

Finally we add planets to the simulations based on the planetary architecture of interest as discussed in Section 3.3. We now discuss the different outcomes for the binary asteroids in our simulations.

3.2.2 Encounters with the white dwarf

We remove a body if it approaches within the white dwarf's Roche limit, at which point it would undergo tidal disruption, as described in Chapter 1.3.2.

Here, we adopt the Roche radius expression assuming a solid, spinning rubble pile as in Veras et al. [2017],

$$r_{\rm Roche} = 0.89 \left(\frac{M_{\rm WD}}{\rho_{\rm a}} \right)^{1/3}, \tag{3.1}$$

where $M_{\rm WD}$ is the mass of the white dwarf and $\rho_{\rm a}$ is the bulk density of the orbiting body. We adopt a body density of $3\,{\rm g\,cm^{-3}}$ to represent a body largely consisting of solid ices and dust and use a fiducial white dwarf mass of $M_{\rm WD} = 0.6 M_{\odot}$, which results in $r_{\rm Roche} = 0.94\ {\rm R}_{\odot} \sim 0.004$ au.

Due to the computational timestep limitations of these simulations and the high velocity of bodies on orbits with small pericentres, we also take into account the possibility that the bodies in our simulations could cross the Roche radius between timesteps.

For each recorded simulation snapshot we calculate the expected pericentre distance for each asteroid using the osculating circumstellar orbital elements and identify if this is within 5 per cent of the white dwarf's Roche radius. When this occurs, we then return to the previous simulation archive step ($\sim 6 \times 10^5$ yrs before) and proceed to carry out a further simulation with a reduced timestep of $dt \sim 6 \times 10^{-6}$ yrs, three orders of magnitude smaller than that used in the original simulations. At this resolution, even the fastest moving asteroid travels a fraction of a Roche radius in a single timestep and thus a Roche radius crossing is resolvable. We carry out an integration with this smaller timestep for ~ 2 Myr and remove any bodies which cross the Roche radius from the simulation.

3.2.3 Ejections from the system

We consider a body to truly have been ejected from the planetary system if it reaches a distance from the central star which exceeds the Hill surface of the system in the Galactic tidal field. Veras and Evans [2013] show that this Hill surface is an ellipsoid defined by the following

$$r_{\rm Hill,\,sys} = \left(\frac{G M_{\rm WD}}{\alpha} \right)^{1/3} \boldsymbol{k}, \tag{3.2}$$

with

$$\boldsymbol{k} = \left(1, \frac{2}{3}, \frac{\left[Q(1+\sqrt{1+Q}\right]^{2/3} - Q}{\left[Q(1+\sqrt{1+Q}\right]^{1/3}} \right) \tag{3.3}$$

and

$$Q \equiv -\frac{\alpha}{\Upsilon_{\rm zz}}. \tag{3.4}$$

The parameter $\alpha \equiv 4A(A-B)$ relies on the Oort constants whose values at the solar radius are $A = 14.5\ {\rm km\,s^{-1}\,kpc^{-1}}$ and $B = -12.9\ {\rm km\,s^{-1}\,kpc^{-1}}$. The contribution from the disc to the perturbation due to the Galactic tide is represented by $\Upsilon_{\rm zz}$ and given by

$$\Upsilon_{\rm zz} = -\left[4\pi G \rho_{\rm tot} - 2\delta\Omega_{\rm G}^2 \right], \tag{3.5}$$

where ρ_{tot} is the total Galactic density, Ω_{G} is the circular frequency of the star around the Galactic centre and $\delta \equiv -(A-B)/(A+B)$ is the logarithmic gradient of the Galactic rotation curve in terms of the Oort constants.

Veras et al. [2014b] notes that the third term in equation 3.3 is always in the range $0-2/3$. Thus, if we take its maximal value and assume our simulated planetary systems are hosted by a 0.6 $\mathrm{M}_{\odot}$ white dwarf at the solar location in the galaxy, then the system's Hill ellipsoid has dimensions of $r_{\mathrm{Hill,\,sys}} \sim (240000, 160000, 160000)$ au. Thus we consider a body to be truly ejected from their planetary system if they exceed an instantaneous distance from the central white dwarf of 240000 au.

3.2.4 Binary Dissociation

The Hill radius for a binary asteroid system can describe the region around a primary asteroid within which a secondary asteroid would orbit the primary despite the gravitational influence of a central star and is given by

$$r_{\mathrm{H}} = a_{\mathrm{a}} \left(\frac{2M_{\mathrm{a}}}{3M_{\mathrm{WD}}} \right)^{1/3}, \tag{3.6}$$

where a_{a} is the circumstellar semi-major axis and M_{a}, M_{WD} are the masses of the individual binary components and white dwarf respectively [Donnison, 2011]. Thus if the distance between the binary component exceeds r_{H}, the secondary should only move under the influence of the central star.

An alternative condition for a binary system to be considered unbound is if the total energy of the system is greater than 0 [Parker and Kavelaars, 2010; de la Fuente Marcos et al., 2017]. The total energy of a binary asteroid system using a two body approximation can be given by

$$E = -\left(\frac{2GM_{\mathrm{a}}}{2a_{\mathrm{B}}} + \frac{GM_{\mathrm{WD}}\mu}{2a_{\mathrm{a}}} \right), \tag{3.7}$$

where $\mu = 2m_{\mathrm{a}}$ and a_{B} is the binary semi-major axis [Donnison, 2011].

In this work we consider a binary to be dissociated if the instantaneous distance between the binary components exceeds r_{H}, and confirm that in all such cases $E > 0$.

3.3 Results

3.3.1 A Solar System Analogue

The first planetary system architecture we consider is a Solar System analogue which contains the four giant planets: Jupiter, Saturn, Uranus and Neptune. We doubled the semi-major axes of the giant planets to mimic the expected ≈ 50 per cent mass loss for a solar analogue host star [Veras et al., 2020b]. We gave the giant planets zero initial eccentricity and a small random inclination between $0-1^{\circ}$.

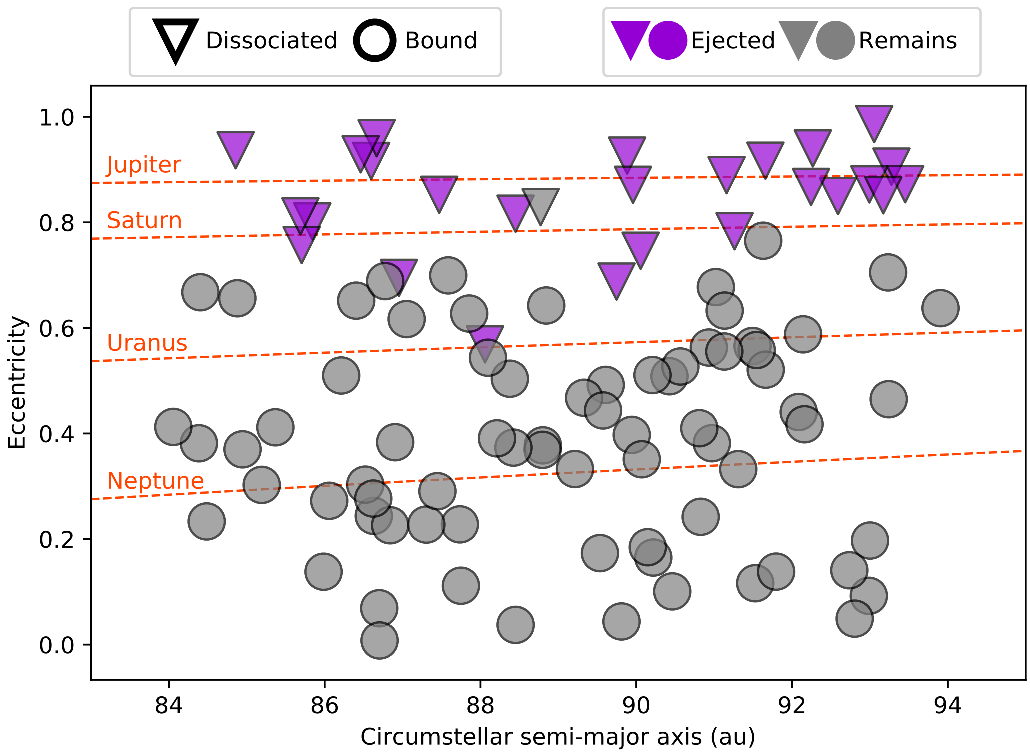

Figure 3.1: The initial semi-major axis and eccentricity values for the 100 simulated binary asteroid systems in our Solar System analogue. The marker design highlights the final state of the binary; a triangle indicates that the binary dissociates, while a circle shows the binary remains gravitationally bound. Further, the colour of the marker shows the end location of the binary; purple indicates at least one of the components is ejected from the system while grey shows that the binary remains in a stable orbit around the white dwarf. The one grey triangle at about 89 au indicates the only dissociated binary which has remained bound to the white dwarf. The dashed orange lines indicate the eccentricity required for a planetesimal to reach a pericentre at the orbital location of the included giant planets as indicated by the annotations above each line.

The Solar System CCKBO region extends between 42 and 47 au [Nesvorný and Vokrouhlicky, 2019] and is expected to remain stable at least until the end of the main sequence as seen in figure 3 of Bonsor et al. [2011]. Thus we populated the expanded, post-main-sequence CCKBO region of 84 – 94 au with 100 binary asteroid systems as described in Section 3.2.1.

We then integrate the motion of the white dwarf Solar System analogue for 10^9 yrs, removing the bodies from the simulation if they either enter the white dwarf Roche limit and tidally disrupt or if they exceed the limits of the system's Hill ellipsoid and are hence ejected.

Figure 3.1 shows the initial semi-major axis and eccentricity values for the 100 binaries considered in our Solar System analogue. In this figure, the marker shape identifies the fate of the binary as a whole: triangles indicate that at some point during the Gyr simulation, the binary dissociates as the separation between the bodies is greater than the Hill radius as in equation 3.6, whereas a circle indicates that the binary remains bound. Further, the colour indicates the final outcome for at least one of the components: purple shows that at least one of the binary components is ejected, while grey shows that both components remain in the planetary system.

From Figure 3.1 it can broadly be seen that higher eccentricity binaries across all semi-major axes are nearly always dissociated and both components are ejected from the system; this appears to hold true regardless of the initial separation of the binary, as is further discussed in Section 3.3.1. There is one case where the binary dissociates according to our Hill radius condition and energy conditions (but does not gain a binary eccentricity larger than unity) and remains within the extent of the white dwarf's Hills ellipsoid at the end of the 1 Gyr simulation time. However, by examining the trajectory of the body across the simulation (see Section 3.3.1), the bodies are clearly undergoing a process whereby their semi-major axes and eccentricities are gradually being increased by successive pericentre passes, and the binary would likely be fully ejected soon after the end of the simulated time.

The dashed orange lines in Figure 3.1 show the eccentricity values required for bodies across the included semi-major axis range to reach a pericentre value at the indicated giant planet's semi-major axis, thus highlighting which bodies are expected to undergo orbit crossings based on their initial orbits. It can be seen that all binary systems that cross Jupiter's orbit are both dissociated and ejected from the planetary system. All bar one system which crosses Saturn's orbit (see Section 3.3.1) are again dissociated and ejected. Although there are a few systems which are dissociated and ejected after crossing Uranus' orbit, largely the ice giants are much less efficient at dissociating and ejecting binary asteroid systems.

Evolution of binary separation

To further investigate the effect of the initial separation of the binary components on the probability for the binary to dissociate, we plot a histogram showing dissociations as a function of initial separation in Figure 3.2 for all of the simulation architectures considered in this work. As can be seen in this figure, for the Solar System analogue (labelled as JSUN in the figure legend) binary dissociations occur across the entire range of initial separation values, with 27/100 binaries in total dissociating. When considering all architectures, there is a slight preference for wider binaries to be dissociated, but dissociations occur regardless of the tightness of the binary.

As discussed in Section 3.2.4, we define a binary as having been dissociated if the instantaneous distance between the binary components exceeds the Hill radius of the binary system. A binary will be gravitationally unbound by a close encounter with a planet if it approaches at a distance q close enough such that the binary separation is approximately its

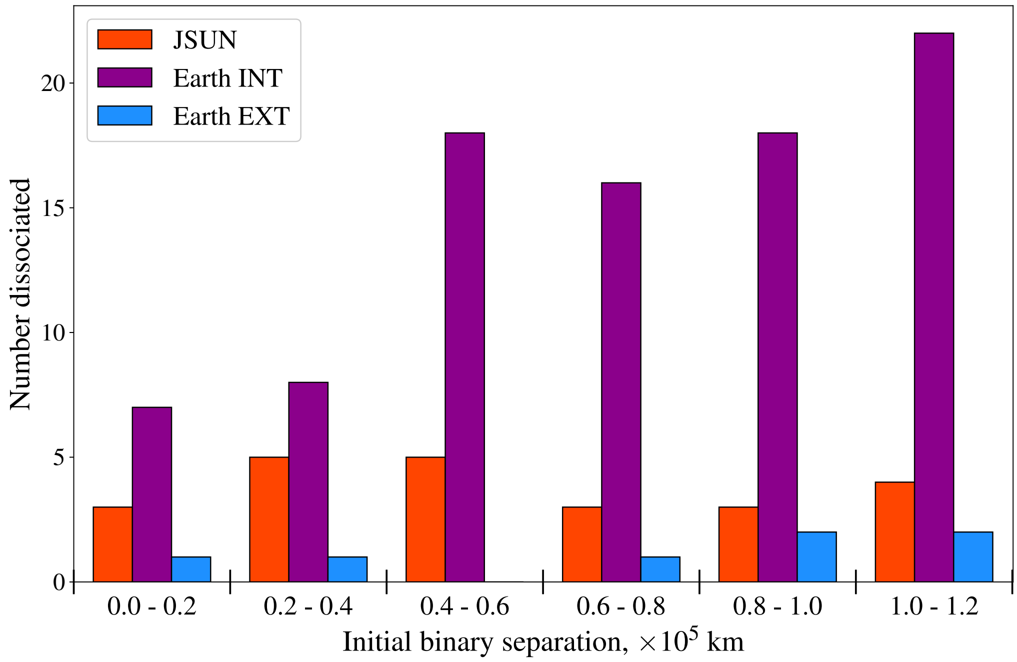

Figure 3.2: A histogram showing the number of binary systems which dissociate as a function of initial binary separation for all planetary system architectures considered in this work, where the colours indicate the architecture as described in the legend. Here, JSUN refers to our Solar System analogue simulations (Section 3.3.1), Earth INT, a system with a single Earth mass planet with binary asteroids on interior orbits, (Section 3.3.3) and Earth EXT, a single Earth mass planet with binary asteroids exterior to its orbit (Section 3.3.2). Each architecture's distributions have the same histogram bins, whose widths are identified by the ranges between the large tick marks on the x-axis.

Hill sphere,

$$q \lesssim a_B \left(\frac{3M_\mathrm{p}}{M_\mathrm{B}}\right)^{1/3}, \tag{3.8}$$

where a_B is the semi-major axis of the binary orbit, M_p is the mass of the planet and M_B is the combined mass of the binary system [Agnor and Hamilton, 2006]. Araujo et al. [2018] suggest that encounters within 3× and 10× this closest approach distance are still significant encounters which can impart some change onto the binary orbit.

To further investigate if any of our dissociated binaries have a close planetary encounter prior to dissociation, we utilise the `REBOUND` Simulation Archive and and carry out higher resolution simulations focussing on the time when the binary dissociates. Of all the binaries which dissociate, only seven have some kind of significant encounter with one of the giant planets, and in only one of these cases is an encounter within 3× Neptune's closest approach distance immediately followed by a dissociation event. Thus planetary encounters does not appear to be the main driver of binary dissociation in this work.

Most of the binaries which do not dissociate remain on relatively stable binary and circumstellar orbits. However, a small number which undergo circumstellar orbit changes, such as orbit crossings, also undergo a corresponding binary orbit change, largely by the binary orbit widening. Further, twelve systems which remain gravitationally bound to each other appear to be captured into an orbit at, or close to, the semi-major axis of one of the planets. These systems spend an average of ∼ 0.2 Gyr at, or close to, the semi-major axis of the the planet often before moving back on to wider orbits. In all but one case this occurs around Neptune's orbit, in the other the system bypasses Neptune's orbit and gets temporarily captured by Uranus.

Ejections from the system

We now investigate specific scenarios which lead to planetesimal ejection.

The Safronov number [Safronov, 1972] for a planet can provide an indication of how efficient it will be at causing other bodies to be scattered and can be described in terms of the planet's properties as follows

$$\Theta = \frac{a_p}{R_p}\frac{M_p}{M_\mathrm{WD}}, \tag{3.9}$$

where a_p is the semi-major axis of the planet, R_p is the radius of the planet and M_p, M_WD are the mass of the planet and white dwarf respectively.

We calculate the Safronov number for each planet included in all simulations discussed in this chapter and present the values in Table 3.1. A Safronov number larger than unity indicates that a planet will be efficient at scattering bodies out of their planetary system, and larger numbers indicate greater efficiency. The calculated values in Table 3.1 confirm that more massive planets are more likely to cause planetesimals to be ejected from the

Table 3.1: Semi-major axis values and calculated Safronov numbers, Θ, for the Solar System planet analogues considered in this work.

Planet	a au	Θ
Jupiter	10.4	35.5
Saturn	19.2	23.5
Uranus	38.4	16.5
Neptune	60.1	31.5
Earth	60.1	7.1

system rather than scattered inwards.

Thus in our Solar System analogue simulations, Jupiter is the most efficient at ejecting planetesimals from the system, although Neptune's Safronov number is similar. The main sequence Safronov number's for the same planets are all significantly lower; for Jupiter around the Sun $\Theta = 10.6$. Although this value is still significantly larger than unity, it is only ~ 30 per cent of its post-main-sequence counterpart, highlighting the increased dynamical instability present in white dwarf planetary systems.

Just over a quarter of the binaries simulated in our Solar System analogue (26/100) are ejected fully from the system, with both components reaching a distance larger than 2.4×10^5 au from the central white dwarf. We find that 16 of these binaries reach a minimum circumstellar distance either inside or very close to Jupiter's semi-major axis, with 9 of these binaries subsequently being ejected separately. A further 9 ejected binaries cross or approach Saturn's orbit and the final binary reaches a minimum distance of ~ 30 au, crossing Uranus' orbit. This can also be seen in Figure 3.1 with all purple triangles existing above the dashed orange line denoting the required orbital elements to have a pericentre within Uranus' orbit. All of which confirms that the more massive and close-in a planet is, the more likely it is to eject a planetesimal from its planetary system.

Figure 3.3 shows the process of ejection for one particular binary system in our Solar System analogue simulations. The plot shows that the evolution of the distance between the binary components and the central star, with the solid and dashed lines representing the arbitrarily chosen primary and secondary respectively. The binary dissociates ~ 1.6 Myr after the beginning of the simulation, and the arbitrarily chosen primary is ejected from the system at ~ 54.6 Myr. However, the secondary remains in the system for a further ~ 661.7 Myr, gradually having its semi-major axis and eccentricity pumped up at repeated pericentre passes before finally being ejected from the system. 10 of the 26 binaries which are ejected here showcase a similar long-term ejection process, seemingly 'bouncing' out of the system.

Such increases in semi-major axis and eccentricity are analogous to the processes which populate the Solar System Oort Cloud with comets from the inner planetary system. Under the gravitational influence of a planet, a comet with semi-major axis much larger than its pericentre will receive an effective kick in energy at pericentre which leads to increases

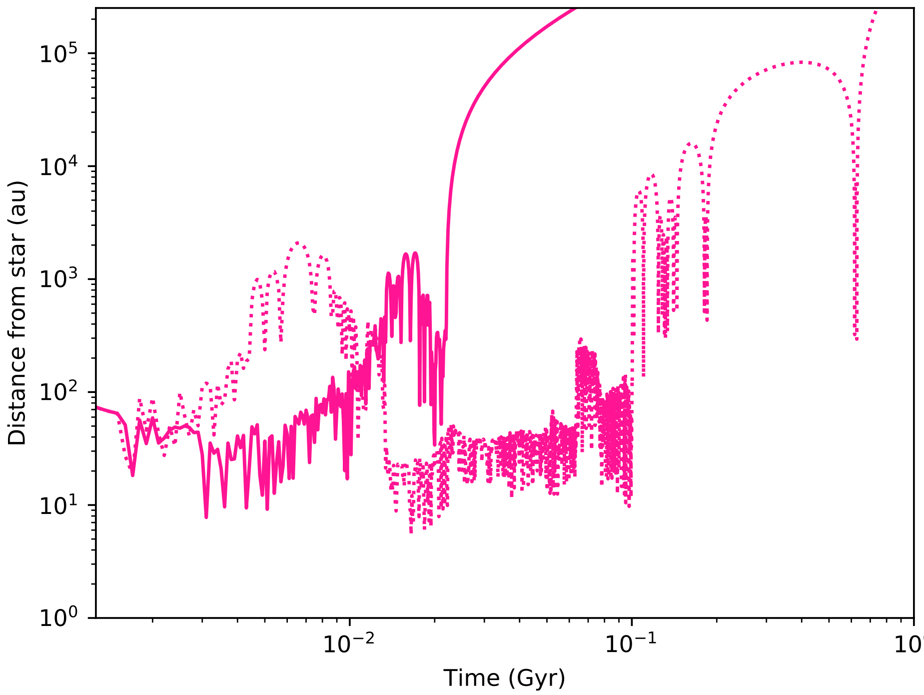

Figure 3.3: The ejection process for a single binary asteroid system in the Solar System analogue simulations. The plot shows the distance from the central star for the binary primary (solid line) and secondary (dashed line) for the 1 Gyr simulation time. The binary dissociates at 1.6 Myr, and the primary is ejected at 54.6 Myr. However, the secondary remains in the system for a further ~ 660 Myr, gradually increasing its semi-major axis and eccentricity at successive pericentre passes before finally being ejected from the system.

in semi-major axis and eccentricity with fixed pericentre. This process leads to a random walk in orbital evolution which has been investigated by many authors [eg Duncan et al., 1987; Brasser et al., 2006, and others]. Without the influence of galactic tides or stellar flybys to raise the pericentre values of the 'comets' outside of the inner planetary system in our simulation, the bodies are ejected.

A similar process for planet mass objects has also been seen in simulations before: the left hand panel of figure 2 of Veras et al. [2009] also shows wide orbits induced by scattering persisting in their planetary systems for hundreds of Myr before being ejected.

Four of these binary systems dissociate according to the condition that the distance between the components exceeds the Hill radius of the binary (equation 3.6). However, their components maintain similar orbits and hence are ejected simultaneously from the system. As discussed in Section 3.3.1, one binary system which is dissociated per the Hill radius condition but is not ejected from the system undergoes a similar 'bouncing' trajectory to that shown Figure 3.3, where it expected the binary components would be ejected after the end of the simulated time.

Close approaches to the white dwarf

Directly from our simulation results, we find no instances where a binary component directly crosses the Roche radius of the white dwarf. By following the procedure outlined in Section 3.2.2, we identify three binary systems which have a component with an expected pericentre below the white dwarf's Roche radius. Of those, two are components which are ejected from the system and hence have eccentricities exceeding unity. The third is not ejected during the course of our original simulations but does undergo a trajectory similar to that displayed in Figure 3.3 and hence is expected to be ejected. We find that no binary component physically reaches the white dwarf Roche radius across the three deeper simulations and hence we find no tidal disruption events across our Solar System analogue simulations.

Although no binary components directly reach the Roche radius of the white dwarf in these simulations, 15 binaries cross Jupiter's orbit and travel further into the inner system. Of these 15 binaries, nine had initial circumstellar eccentricities $e_{\mathrm{i}} > 0.9$, five had $0.8 < e_{\mathrm{i}} < 0.9$ and one had $0.7 < e_{\mathrm{i}} < 0.8$ implying that an intense dynamical perturbation which can push the body onto a large eccentricity orbit is required for forays into the inner planetary system.

Figure 3.4 shows a histogram of the minimum distance that each binary asteroid component makes to the white dwarf (orange for the primary and purple for the secondary) with overlaid Poissonian error bars. In this work, as we neglect the presence of any remnant planets, asteroids which cross Jupiter's orbit and enter the inner planetary system ($a \leq 10$ au) may encounter smaller surviving terrestrial planets which could further scatter the planetesimals onto Roche limit crossing orbits. Overall, three of our binaries approach

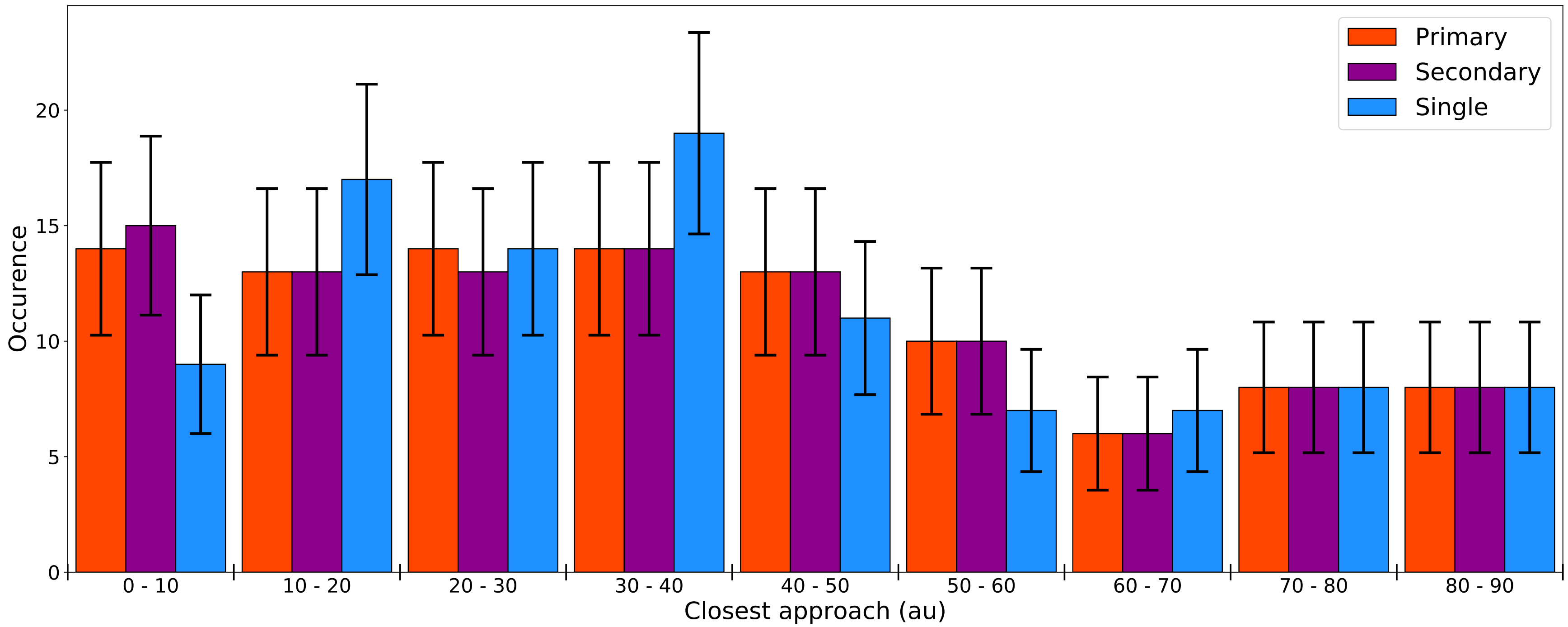

Figure 3.4: Histogram of the closest approach distance for each binary component in our simulations; the primary is denoted with orange and the secondary by purple, as indicated in the legend. Broadly the distribution for primary and secondaries are very similar and only diverge at the closest approaches. In blue we show the closest approach distance for additional simulations which were run with identical clones of the primary binary component but with the secondary removed. In all cases a significant fraction of bodies cross Jupiter's orbit where they may then be further perturbed by remnant terrestrial planets. Each distribution has the same histogram bins, whose widths are identified by the ranges between the large tick marks on the x-axis. The overlaid Poissonian error bars show the expected variance of these distributions due to the small occurrence rates in each bin. As the errors for the binary components and single counterparts in each bin all overlap, this implies that the distributions are similar and there is little statistical difference in how close a binary asteroid system or single-body counterpart can approach a central white dwarf.

the white dwarf within 5 au and a further twelve within 10 au where they may be more likely to encounter further planets and undergo more perturbations.

Comparison with single-body evolution

To further understand if the binarity of these systems has any impact on the evolution of the asteroids, we carried out additional simulations where the secondary component has been removed. These simulations are begun with otherwise identical initial conditions to the binary simulations through utilising the `REBOUND` SimulationArchive [Rein and Tamayo, 2017]. Here we discuss some of the results comparing the evolution of a binary asteroid system to its single-body counterpart.

Firstly, we consider the ultimate fate of the binary and single body counterpart systems. Often, when both components of the binary are ejected from the planetary system, the corresponding single body is also ejected, which suggests the ejection process is tied more to the initial orbital configuration of the system than the binarity. However, there are four occurrences where the binary system is ejected but the single body is not, and another four where the single body is ejected and the binary is not. Where both the binary and the single body counterpart are ejected, the timescales for these ejections can differ.

Alongside cases where the single body is ejected either before or after the binary components, there are four cases where the binary components are ejected separately and the single body is ejected at a time between the two binary components ejection events. For the specific binary asteroid shown in Figure 3.3, the binary primary and secondary are ejected at ~ 55 and ~ 716 Myr respectively, while the single body counterpart is ejected at ~ 90 Myr. Thus, largely there are very little differences in the final fates of binary asteroid systems compared to their single body counterparts. Although we only consider a small number of systems in this work ($N = 100$), we do not expect these results to drastically change with additional simulations as Poisson statistics suggest only single digit errors for the occurrences of ejections discussed above.

Next, we look at the prospects for white dwarf pollution by considering the closest distance to the white dwarf reached by the binary systems and single body counterparts. Figure 3.4 shows a histogram of the closest approach for both the binary and single body simulations. The distributions of closest approaches into the inner system the binary components reach are shown by orange and purple bars, while the single body counterpart is shown in blue. The Poisson errors for the occurrence rates are overlaid on each bar in black. Although there are histogram bins where the differences between binaries and single bodies are large (such as $0 - 10$ au and $30 - 40$ au), the overlaid error bars suggest that this is due to small number statistics, and further simulations may drive the distributions to equality.

For 40 per cent of the simulated systems the difference in closest approach values is less than 1 au, while another 26 differ in closest approach value by up to 40 au. In 54 of our systems, the binary approaches closer to the WD than the single body, in 45 cases the single body makes a deeper entrance to the inner system, and in two cases, the single body arrives between the two binary components. Although the difference in closest approach can be large for a single binary asteroid system and single body counterpart, on a population (albeit small $N = 100$) level these differences are less pronounced.

Thus, we find that binarity has little effect on the rates of system ejection or the closest approach an asteroid can make towards the central white dwarf compared to a single body counterpart.

3.3.2 A single Earth-mass planet with exterior planetesimals

It has been shown that lower mass planets are more efficient at delivering planetesimals into the inner regions of white dwarf planetary systems where they can undergo further encounters which lead to tidal disruption and eventual accretion [see left hand panel of figure 6 of Bonsor et al., 2011]. Since our Solar System analogue simulations include the influence of giant planets and show a number of ejected and stable binaries, but no planetesimals on orbits which would suggest eventual accretion, we now change our attention to lower mass planets. Figure 6 of Bonsor et al. [2011] shows that in their numerical simulations, the highest number of planetesimals are scattered inwards under the influence of a 1 $M_\oplus$ planet compared to higher masses ($10 - 100$ $M_\oplus$). In their work, a planetesimal is considered to be scattered inwards if its semi-major axis is less than $a_{\rm in}$, taken to be $a_{\rm in} = a_{\rm p} - 7r_{\rm H}$, where $r_{\rm H} = a_{\rm p}\left(M_{\rm p}/3M_{\rm WD}\right)^{1/3}$.

This value is chosen in their work under the assumption that the planetesimals could then be scattered by remnant planets within the inner system. Thus, in the context of our work $a_{\rm in} = 55.17$ au.

Thus we place a 1 $M_\oplus$ planet at the WD semi-major axis of Neptune in the previous Solar System analogue ($a = 60.1$ au), again with zero initial eccentricity and a random inclination between $0 - 1°$. Then following the procedure set out in Bonsor et al. [2011], and ignoring the effect of post-main-sequence mass loss on mean motion resonances (MMRs) [Debes et al., 2012; Voyatzis et al., 2013; Li et al., 2021], we place our binary asteroids from the post-main-sequence orbital location of the planet to the location of the outer 2:1 MMR (60.1 au $< a_{\rm a} <$ 95.4 au). This 2:1 MMR with Neptune is also the approximate edge of the Solar System's Kuiper Belt [Allen et al., 2001; Trujillo and Brown, 2001] and the location of the resonance is defined as

$$a_{\rm 21MMR} = \left(\frac{2}{1}\right)^{2/3} a_{\rm p}, \tag{3.10}$$

where $a_{\rm p}$ is the semi-major axis of the planet [Murray and Dermott, 1999].

The 100 binary asteroid systems were again initialised using the same orbital elements as discussed in Section 3.2.1, and then the system was integrated for 1 Gyr.

Figure 3.5 shows the initial semi-major axes and eccentricities of the binary asteroids

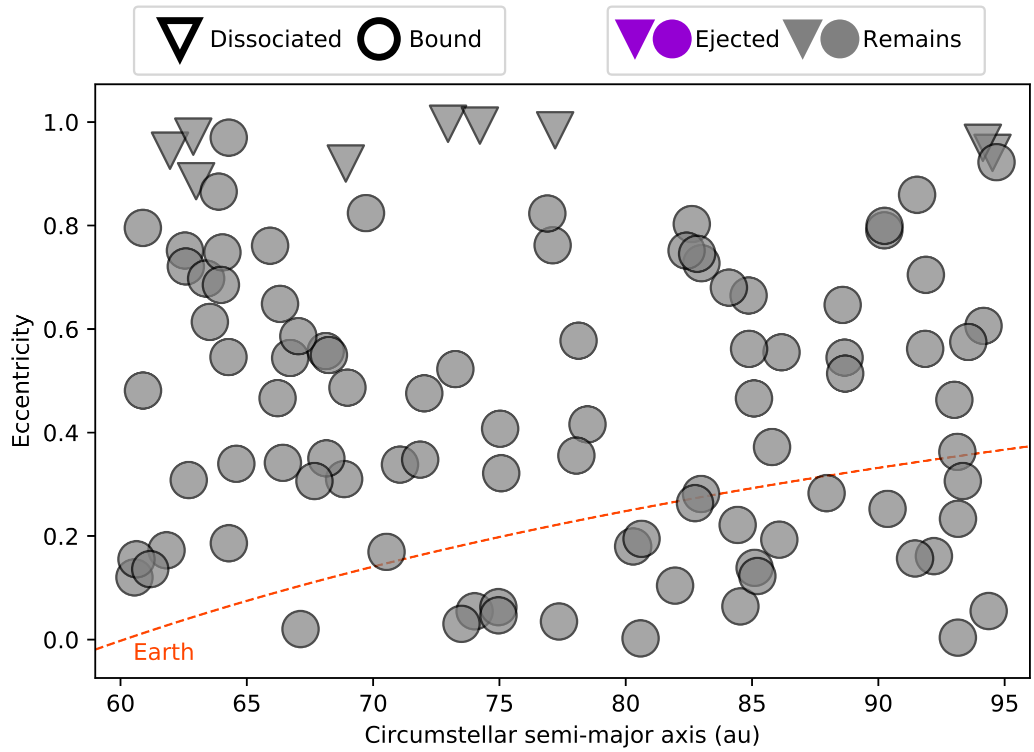

Figure 3.5: The initial semi-major axis and eccentricity values for 100 binary asteroids on orbits exterior to a single Earth-mass planet. As in Figure 3.1 and as in the legend, the marker shape highlights the outcome for the binary orbit and the marker colour indicates the final state of the stellar orbit. In this case, only binaries with stellar eccentricity $e > 0.9$ dissociate and no binary components are ejected from the planetary system.

considered in these simulations. The shape markers and colours are indicators of the same as in Figure 3.1 and are described in the figure legend. From this figure it is clear that all of the binaries remained in the system during the course of the 1 Gyr integration, with no ejections or bodies being directly scattered to the Roche limit of the star. Due to the lower value of the Safronov number for the Earth-mass planet considered here (see Table 3.1) it is not unsurprising that there are no ejections in these simulations.

Using the definition of the inner planetary system of $a_{\rm in}$ = 55.17 au from Bonsor et al. [2011], a quarter of the binaries in our simulation including an Earth-mass planet and a quarter from the Solar System analogue encroach in the inner system, seemingly in contrast with the results of Bonsor et al. [2011]. At closer distances, only two binaries in the Earth-mass simulations had a closest approach towards the white dwarf within 1 au and only another ten binaries approached within 10 au. We find no binary components come within 5 per cent of the white dwarf's Roche radius.

The number of bodies which enter into the deeper regions of the planetary system (< 10 au) is less when the binaries start exterior to an Earth-mass planet (10 binaries) compared to in the Solar System analogue simulations (12 binaries). However, all of the binaries in the Solar System analogue simulations which approach within approximately 10 au of the white dwarf are subsequently ejected from the system. Thus, lower mass planets are more efficient at scattering bodies to closer pericentres without ejecting them, so they can stay in the inner system and be perturbed by further remnant planets for longer timescales.

When comparing the closest approaches for the binary systems and their single body counterparts, there is again less difference than for the Solar System analogue, with only 13 systems having a change in closest approach larger than 1 au and a single single body simulation whose closest approach was $\sim$ 11 au closer than the counterpart binary components.

In these simulations a very small number of binary systems (9/100), all of which start out with very high eccentricities ($e > 0.8$), are dissociated, such that the remaining 91 systems stay bound. The binaries which remain bound do not show as much binary orbital evolution as those in the Solar System analogues, and the few that do undergo widening exhibit the same corresponding change in circumstellar semi-major axis. These features can be explained due to the smaller gravitational perturbations from a single-Earth like planet than from multiple giant planets.

3.3.3 A single Earth-mass planet with interior planetesimals

Having found no tidal disruption events caused by giant planet scattering, we now focus on a particular region of phase space where previous studies have found asteroids to be particularly vulnerable to being scattered onto orbits which lead to tidal disruptions.

Antoniadou and Veras [2019] provide scale-free analytical estimates for the outcomes of planetesimals on planar, elliptic periodic orbits near, or inside, the 2:1 MMR under the influence of one exterior planet. Motion near unstable periodic orbits is driven by chaos which leads to instabilities such as collisions or system escape. Antoniadou and Veras [2019] produce dynamical stability maps around periodic orbits by calculating the detrended fast Lyapunov indicator (DFLI, see Froeschlé et al. [1997a] and Froeschlé et al. [1997b] for more details about FLIs). The DFLI provides a measure for chaos; when a orbit is regular its DFLI remains approximately constant, but when the orbit is chaotic then the DFLI increases exponentially. The middle panel of their figure 7 shows such a dynamical stability map with the shaded grey region highlighting chaotic orbits (DFLI > 15). The overlaid points display the fate of asteroids from N-body simulations and confirm that the DFLI chaos indicator is efficient at identifying orbits which will lead to instabilities. From this figure, we identified a particular region of a-e space that is predicted to cause asteroids to be perturbed into the inner planetary system and subsequently collide with the white dwarf.

This region led us to model binary asteroids with parameters distributed in the ranges $0.9 < e < 1$ and $0.61 < a_{\mathrm{a}}/a_{\mathrm{p}} < 0.64$ where a_{a} and a_{p} are the circumstellar semi-major axes of the binary system and the planet respectively. These values give 36.7 au $\lesssim a_{\mathrm{a}} \lesssim$ 38.5 au assuming the Earth-mass planet is again placed at $\sim$ 60 au ($\times 2$ Neptune's current semi-major axis).

Once again, the binaries were initiated with the same orbital elements as previously discussed and then their motion was integrated for 1 Gyr.

Figure 3.6 shows the initial semi-major axes and eccentricities of the circumstellar orbits of the binary asteroid systems. The marker styles and colours remain the same as in Figures 3.1 and 3.5 and as described in the figure legend, but note here the scale on the y-axis which ranges between $0.9 < e < 1.0$ as opposed to $0.0 < e < 1.0$ as before.

As can be seen on this figure, the binaries in this simulation largely have a very different outcome to those planetary system architectures already discussed, with all but eight binaries dissociating before the end of the simulation. Further analysis of these dissociation events shows that only 15/92 of the binaries which did dissociate did so after the first 0.5 Myr of the simulation and none did so after a close encounter with the planet, which may suggest that this region of phase space is mostly inhospitable to binary stability in the first place.

These features are supported by the fact that the binaries which remained bound all had initial separations smaller than 3.5×10^4 km, which are some of the tightest binaries we consider in this work. Thus, the wider binaries which are typically found in the Solar System Kuiper Belt may not be able to exist as binaries at these locations. The binaries which remained gravitationally bound in this architecture largely also underwent changes in the circumstellar semi-major axis, albeit smaller in magnitude than in the Solar System analogue simulations. The corresponding changes in binary semi-major axis were similar in size to those in the Solar System analogue simulations for a similar sized increase in

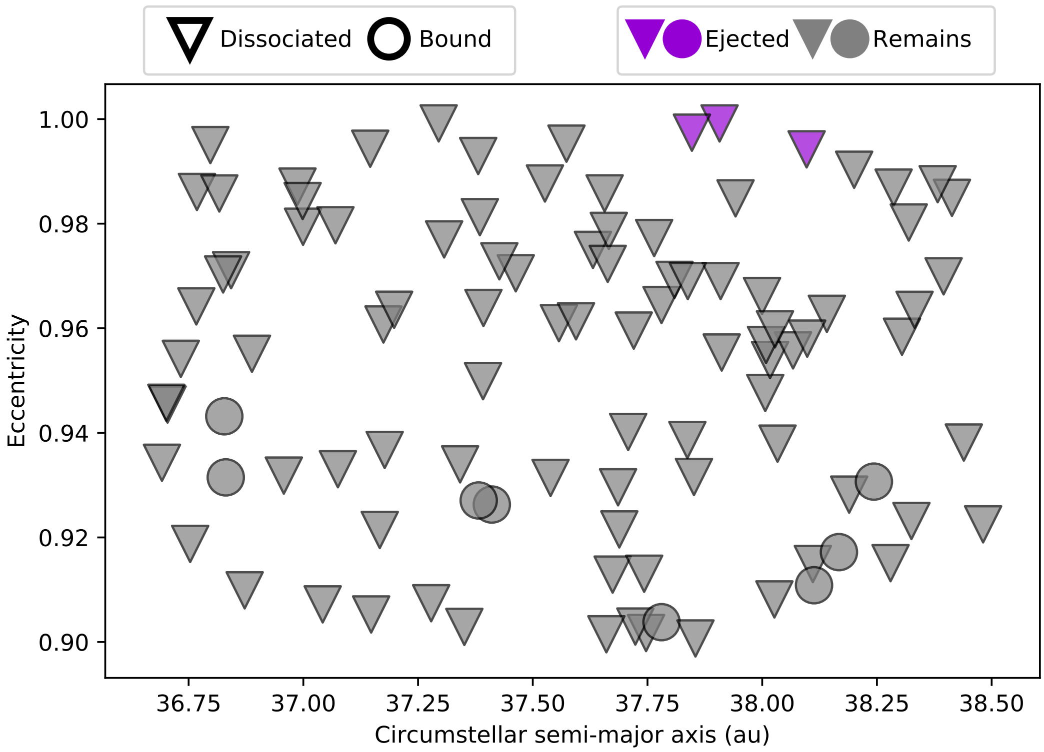

Figure 3.6: The initial semi-major axis and eccentricity values for 100 binary asteroids interior to an Earth-mass planet chosen to have orbits likely to lead to the planetesimals being accreted onto the white dwarf. As before and the legend, the marker shape highlights the stellar orbit outcome and colour shows the binary orbit end state. In contrast to the previous planetary system architectures, here only 8 binaries do not dissociate, all with $e < 0.95$. For three separate binaries with $e > 0.99$ and 37.75 au $< a <$ 38.25 au, they are dissociated and a single binary component is ejected from the system.

circumstellar semi-major axis.

As in these simulations we used the same planet mass and semi-major axis as when targetting the exterior 2:1 MMR. The Sarfronov number is again as given in the last row of Table 3.1 (equalling 7.1), which is a sufficiently low value that we should not expect many ejections. Indeed, we find only three ejection events, which represents a significant reduction of the level of planetesimals which are scattered to ejection compared to those from the Solar System analogue simulations.

The ejected planetesimals are clustered in the semi-major axis - eccentricity phase space with $37.75 < a_{\rm a} < 38.25$ and $e > 0.99$. In contrast to the ejection events in our Solar System analogue simulations, in these three cases only the arbitrarily chosen secondary of the binary is ejected, with both the primaries and their single body counterparts remaining in the planetary system. Further, the ejections all occur early in the Gyr simulation at $\sim 1.7, 4.8$ and 22.6 Myr, which means that none of the ejections show the same 'bouncing' trajectories across hundreds of Myrs as discussed in Section 3.3.1.

The binaries in these simulations were all initiated with smaller semi-major axes and higher initial eccentricities than in the previously discussed architectures, thus the bodies here make much closer approaches towards the white dwarf. 31/100 of the binaries reach within 1 au of the central star, and the closest distance to the star that any body achieved was ~ 0.03 au, which is still an order of magnitude larger than the Roche radius of the star (see Section 3.2.2). We again find three binary asteroid systems which have a predicted osculating pericentre within 5 per cent of the white dwarf's Roche radius. These three systems are those highlighted in Figure 3.6 as being ejected during the course of the simulation and hence with an eccentricity larger than unity. As outlined in Section 3.2.2, we carry out simulations with a smaller timestep centred on the time of the predicted Roche crossing from the osculating orbital elements. Subsequently we find that no binary component crosses the white dwarf's Roche radius. There is also less variation in the closest approach distances between the binary and the single body counterparts with only one system where the difference was just larger than 1 au.

Thus, although we chose to specifically target areas of parameter space which have previously been identified as potential drivers of white dwarf pollution, here we find that further interactions with other planets would be required to cause both binary and single asteroids to reach the white dwarf Roche radius.

3.4 Discussion

Although our simulations have not highlighted a particular tendency for binary asteroids reaching orbits which would allow them to be disrupted and then accreted onto the white dwarf over single body counterparts, there are a few particularly interesting consequences of considering binary asteroid evolution.

3.4.1 Implications for white dwarf pollution

The process of binary dissociation can affect the orbits of the binary components which remain in the system. All of the binaries which dissociate are ejected in our Solar System analogue simulations, or at least follow trajectories which would lead to them subsequently being ejected. Thus, we turn our attention to the effect of binary dissociation on the white dwarf pollution process in our system architectures including Earth-mass planets.

For the case where the planetesimals begin the simulations exterior to the Earth-mass planet, the final circumstellar semi-major axes of the dissociated primary and secondary can differ by up to 3 au, while the circumstellar eccentricity differs by only up to 0.01. Figure 3.7 shows the circumstellar semi-major axis, eccentricity and inclination evolution for a binary which dissociates from an initial location exterior to an Earth-mass planet and where both components remain in the system for the duration of the simulation. In Figure 3.7, the coloured lines show the orbital elements of the binary components, as indicated in the legend, calculated assuming they are on Keplerian orbits around the white dwarf and undergoing small perturbations due to the presence of the binary companion. The vertical grey dashed line shows the time at which the binary is dissociated according to the condition that the instantaneous distance exceeds the system's Hill radius. In the specific example shown, the binary remains bound for just over 0.5 Gyr of simulation time, after which there is a gradual increase in eccentricity and decrease in inclination towards the point of dissociation, which occurs at just under 0.6 Gyr.

After the dissociation point, the binary primary settles onto an orbit with a semi-major axis $\sim$ 64.6 au, while the secondary sits at $a \sim 62.2$ au. Thus, the dissociated binary components have a maximum difference in apocentre of $\sim$ 4.8 au and $\sim$ 0.06 au at pericentre. The circumstellar eccentricity of the components appear to diverge from each other slightly while still following the same trajectory. By the end of the simulation, the circumstellar eccentricity values had been steadily decreasing for $\sim$ 0.2 Gyr. Further simulation time, may highlight that the circumstellar eccentricity decreases even further. The circumstellar inclinations continue the steady decrease in value that preceded the dissociation event, with both components acquiring $\sim 0^\circ$ by the end of the simulation time.

Thus, the dissociation process can significantly alter the subsequent orbital evolution of the binary components. We can examine this effect further by looking at the distribution of binary components both at the beginning and end of our simulations to see how it changes as in Figures 3.8-3.10.

Each figure shows the initial and final position distributions for the simulated planetesimals in our simulated system architectures. In the left hand panels we show the initial location of the binaries as coloured markers and the following 10^4 yrs of their orbital evolution as grey lines, while in the right hand panels we show the final location of the binary components and their preceding 10^4 yrs of evolution.

Figure 3.8 shows the initial and final distributions of the 100 binary asteroids in

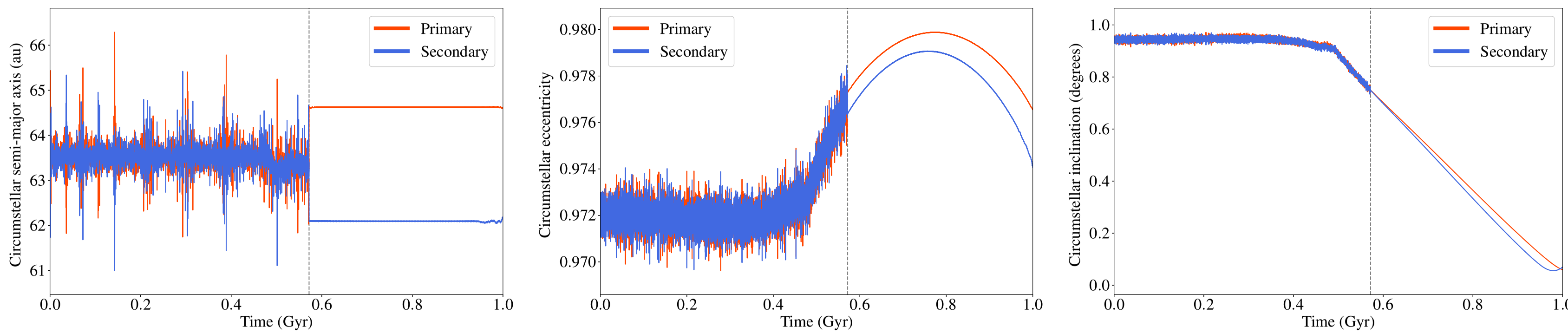

Figure 3.7: The evolution of circumstellar semi-major axis (leftmost panel), circumstellar eccentricity (centre panel) and circumstellar inclination (rightmost panel) for the two components of a particular binary which dissociates but is not ejected from an initial orbit exterior to an Earth-mass planet. In each panel, the primary is shown by an orange line, the secondary by a blue line and the vertical dashed grey line pinpoints the time when the binary dissociates. After the point of dissociation the semi-major axes of the components orbits differ by ~ 2.4 au. The circumstellar eccentricity values continue a slow increase that began before the dissociation event, albeit separated by ~ 0.001, for ~ 1 Gyr before both begin to decline with an increasing separation. Finally, the inclination values again follow a similar pattern to their pre-dissociation evolution by continuing to decrease from almost 1° to $\sim 0^{\circ}$ by the end of the simulation, with the values for the two components diverging slightly as more time passed from their dissociation. Thus, the dissociation process can affect the subsequent orbital evolution of the components.

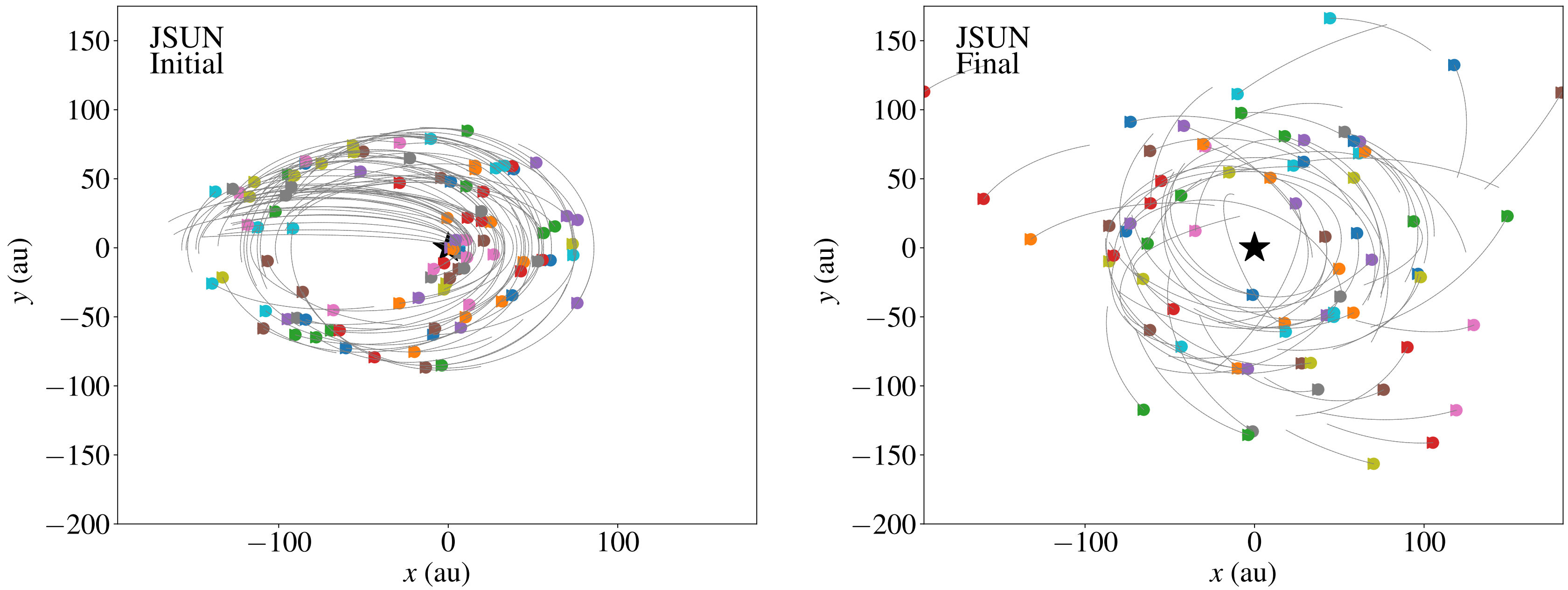

Figure 3.8: The distribution in x-y space of binary components at the beginning of the simulation time (left panels) and then at the end of the 1 Gyr simulation time (right panels) for the Solar System analogue planetary system considered here (Section 3.3.1). The grey lines show the orbital path of the objects for either the following 10^4 yr (left panels) or the preceding 10^4 yr (right panels), where the positions have been calculated at higher resolution than in our full simulations, with positions recorded every 100 years. The central white dwarf is located at $(0, 0)$ and is denoted by a black star which is hard to distinguish in some panels due to the density of orbit visualisations. The binary primaries are identified by circle markers and triangles of the same colours show the secondaries. By comparing the left and right panels, it is possible to identify how the distribution of planetesimals changes over the course of a Gyr. It is clear that for the Solar System analogue simulations, a number of binary systems have been ejected and those that remain have diffused in the system.

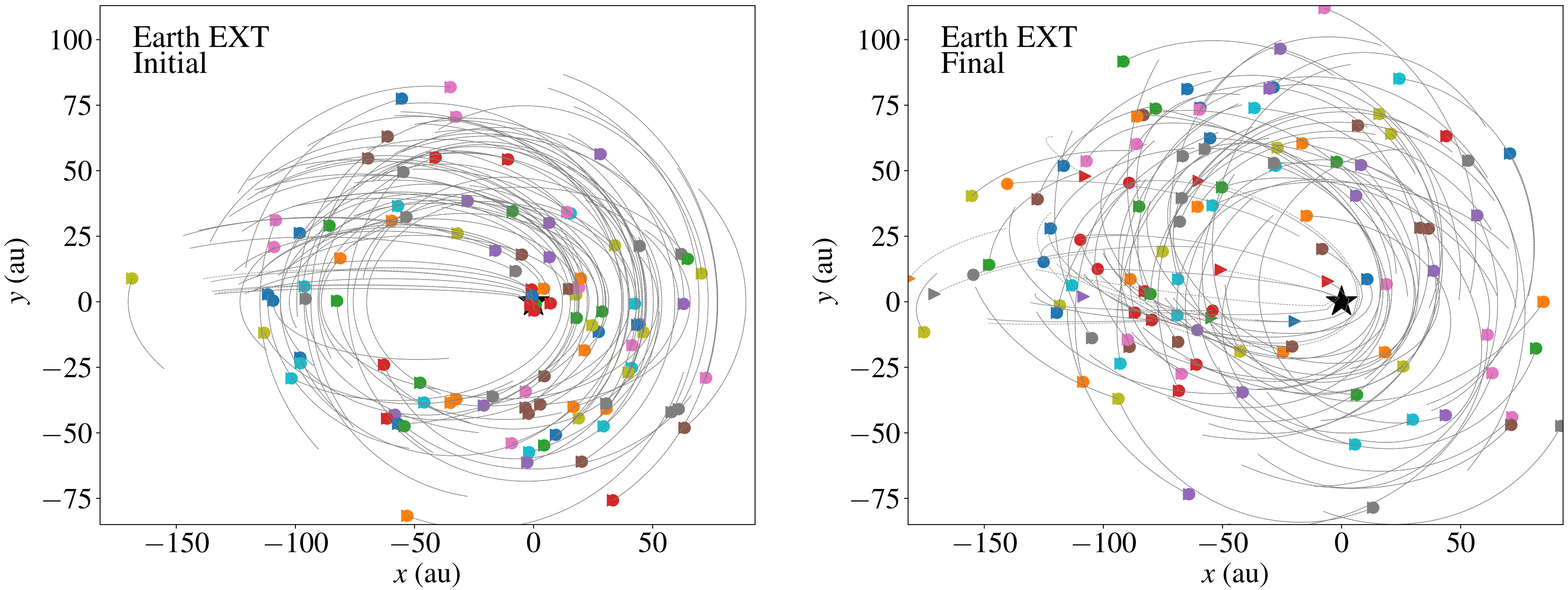

Figure 3.9: This figure is the same as Figure 3.8, but instead displays the orbital distribution evolution for the binary asteroid systems simulated exterior to an Earth-mass planet (Section 3.3.2) In these simulations, dissociated binary components can be distinguished by lone triangle and circle markers in the right-hand panel. No planetesimals are ejected in these simulations, but the orbits do become more diffuse by the end of the simulation.

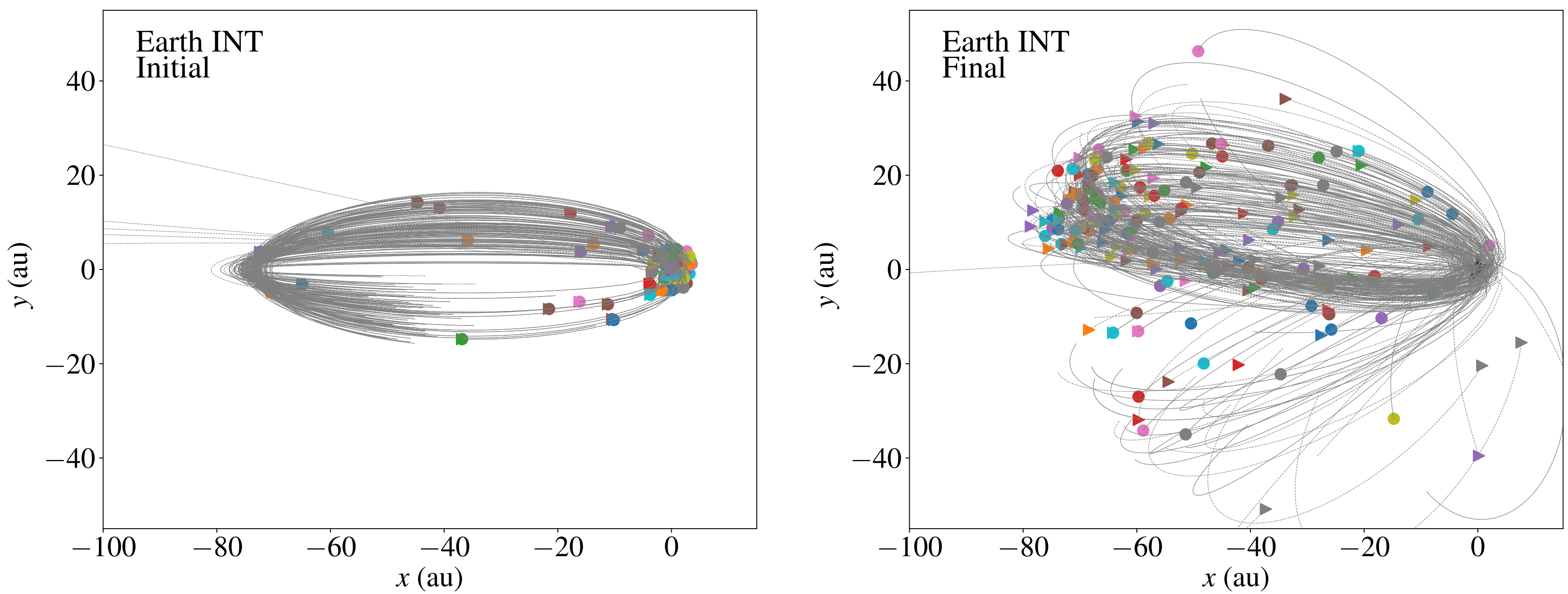

Figure 3.10: Again, this figure is the same as in Figure 3.8, but this time displays the orbital evolution for binary asteroids interior to an Earth-mass planet. In this figure, the most evident feature is the significant evolution of the argument of pericentre which has led to the orbits precessing around the central star.

our Solar System analogue simulations introduced in Section 3.3.1. The reduction in planetesimal density highlights the ~ 25 per cent of planetesimals which are ejected from the planetary system. The orbital paths of the binary asteroids appear to have diffused around the star, with a number of bodies being pushed out onto wider orbits.

The initial and final position distributions for binary asteroids on orbits exterior to an Earth-mass planet are shown in Figure 3.9. In this planetary architecture, none of the binaries are ejected from the planetary system and very few are dissociated, but one example can be seen in the lone grey triangle towards the left hand side of the right hand panel. The orbital distribution as a whole has also become more diffuse across the simulation time in both the x and y directions.

Finally, Figure 3.10 shows the position distributions for binaries interior to an Earth-mass planet on orbits expected to cause tidal disruption events. By comparing the two panels, it is clear that the orbital distribution of the asteroids changes significantly during the course of the simulation. Not only can individual dissociated binary components be distinguished, but a number of objects have undergone significant argument of pericentre evolution.

Since these simulations only explicitly considered the gravitational interaction between the planets and the planetesimals, this observed precession is likely to be caused by these gravitational interactions.

Veras [2014] presents equations of motion for the restricted many body problem, which can help us determine the level of gravitational precession expected in our simulations. These equations use the orbital plane of the planet around the star as the fixed reference plane and an arbitrary but fixed reference direction within that plane from which to measure the orbital angles. Their equation 176 describes the time evolution of the argument of pericentre in the reference direction for a planetesimal in the coplanar case averaged over the orbit of both the planet and the planetesimal as below

$$\frac{d\omega}{dt} \approx \left(\frac{1}{a_{\mathrm{p}}^3}\right) \frac{3GM_{\mathrm{p}}\sqrt{1-e_{\mathrm{a}}^2}}{4n_{\mathrm{a}}(1-e_{\mathrm{p}}^2)^{3/2}}, \tag{3.11}$$

where G is the universal gravitational constant, M_{p} is the mass of the planet, n is the mean motion, a is the circumstellar semi-major axis, e is the eccentricity and the subscripts a and p refer to the asteroid system and planet respectively. In Equation 3.11, we only present the first of four terms presented in Veras [2014] as the higher order terms are negligible and to leading order the argument of pericentre evolution can be solved exactly. Averaged quantities such as that in Equation 3.11 are particularly useful for determining the long-term secular evolution of systems, such as studied in our Gyr long simulations.

While applying Equation 3.11 for our approximate calculation, we consider the binary asteroid system as a single object whose orbit is approximated by the orbital elements of the primary. Taking the range of initial circumstellar semi-major axis and eccentricity values for our simulated binary asteroid systems interior to an Earth-mass planet (36.7 au $\lesssim$ $a_{\mathrm{a}} \lesssim$ 38.5 au and $0.9 < e < 1.0$), we find an expected rate of change of argument of pericentre of $d\omega/dt \sim 0 - 9^{\circ}$ Gyr^{-1}. Indeed, we find that a large number of binary systems in our simulations which start with a circumstellar argument of pericentre of 0°, end the 1 Gyr simulation with $\omega \sim 0 - 7^{\circ}$. Thus, the observed argument of pericentre evolution is broadly in line with being caused by gravitational interactions with the perturbing planet. The small level of scatter observed in Figure 3.10 can be explained by the stochastic nature of the three body problem and excitation due to encounters with resonances or other longer term secular interactions.

Although we did not explicitly include general relativistic effects in our simulations, these would provide an additional mechanism to induce argument of pericentre evolution. Veras et al. [2014a] present the averaged rate of change for the argument of pericentre due to the effects of general relativity as

$$\frac{d\omega}{dt} = \frac{3\left[G\left(M_{\mathrm{WD}} + M_{\mathrm{a}}\right)\right]^{3/2}}{a_{a}^{5/2} c^{2}\left(1 - e^{2}\right)}, \tag{3.12}$$

where G is the universal gravitational constant, a is the semi-major axis of the circumstellar orbit, c is the speed of light and e is the orbit's eccentricity. For the objects in our simulations with binaries interior to an Earth-mass planet, bodies with an initial eccentricity $e = 0.9$ can achieve $d\omega/dt$ on the order of 0.05° Gyr^{-1}. But for the very highest eccentricities considered in this work, on the order of $e = 0.999$, $d\omega/dt \sim 5^{\circ}$ Gyr^{-1}. Considering the argument of pericentre precession due to general relativistic effects would then add an additional rotation to that observed in our simulations due to purely gravitational effects.

Binaries which do not dissociate and continue to have pericentre passes close to the white dwarf could have interesting consequences for the disruption/accretion processes. Although as is seen in Section 3.3.3 it can be difficult to have binaries survive on close in orbits, especially if there are large planets in the system, binaries which initially exist exterior to a low mass planet can make close approaches into a planetary system without dissociating. How the tidal disruption process might differ if a gravitationally bound binary asteroid system were to cross the Roche limit of their white dwarf is beyond the scope of this chapter, but may lead to an interesting distribution of orbiting debris which might be observable through transits.

3.4.2 Implications for interstellar asteroid populations

The discovery of interstellar objects (ISOs) with the detection of 1I/'Oumuamua in 2017 [Meech et al., 2017] and 2I/Borisov in 2019 [Guzik et al., 2020] motivated studies into the dynamical processes which lead to planetesimal ejections. Alongside ejection during the protoplanetary disk phase [Moro-Martín, 2018], ejection from a remnant planetesimal reservoir during the post-main-sequence phases of stellar evolution has also been proposed as a mechanism [Rafikov, 2018; Moro-Martín, 2019; Malamud and Perets, 2020b]. Although the estimated number density of ISOs originating from post-main-sequence systems is not sufficient to explain the estimated ISO number density from the observation of 'Oumuamua, they should still contribute to ISO population.

Hansen and Zuckerman [2017] predict that as much as $0.1 - 1.0\mathrm{M}_{\oplus}$ of material can be ejected from a white dwarf planetary system hosting Saturn-Jupiter mass planets by considering the average accretion rates for polluted white dwarfs and the fraction of material expected to be accreted versus ejected. Veras et al. [2020b] simulated the dynamical evolution of Solar System analogue exo-Kuiper belts consisting of large planetesimals across a star's entire lifetime from stellar cluster birth to the white dwarf phase. They find that planetesimals are most vulnerable to system ejections during the stellar cluster phase of evolution, while in the white dwarf phase it is negligible with only a few per cent of planetesimals being ejected (see their figures 4-7). This predicted lower level of ejections could be due to the planetesimals in their simulations largely remaining on near circular, co-planar orbits, while increasing eccentricities is favourable for ejections in our work. The result that there is a negligible difference between the ejections of binary and single component systems in our simulations (Section 3.3.1) highlights that differences in our orbital distributions is the likely cause for the discrepancies between our results.

In this work we similarly find that giant planets are efficient at scattering material out of their planetary systems and into free floating populations. In our Solar System analogue simulations, approximately a quarter of all binary asteroid systems we consider are ejected from their planetary systems when their distance from the central star exceeds the extent of the systems Hills ellipsoid. The new aspect that our work provides is then not only that there are two bodies to be ejected at every event, but that in ~ 40 per cent of our ejection events, the binary components are not ejected simultaneously as discussed in Section 3.3.1. Thus, ejection of a binary asteroid system via planet perturbations around a white dwarf could inject rocky material into interstellar regions across Myrs.

Further, none of our ejected systems are ejected while they remain gravitationally bound as a binary, thus we may not expect a population of free-floating binary asteroids. Here we aim to expand on this possibility and identify any regions of orbital space where a bound binary may be ejected. Jackson et al. [2014] present an analytic formalism which relates the motion of escaping material to the orbit of its progenitor, assuming the escaping material receives an impulsive 'kick' in velocity. Although their work focussed on direct impacts between planetary embryos and the resulting debris, the formalism is also applicable to planetesimals being scattered by planets, if we assume the interaction is impulsive.

In this formalism, the minimum velocity kick required to cause a body to be ejected from the system is

$$\Delta v_{\mathrm{min}} = v_{\mathrm{k}} \left[\sqrt{2} \left(\frac{1 + e\cos f}{1 - e^2} \right)^{1/2} - \left(\frac{1 + 2e\cos f + e^2}{1 - e^2} \right)^{1/2} \right], \tag{3.13}$$

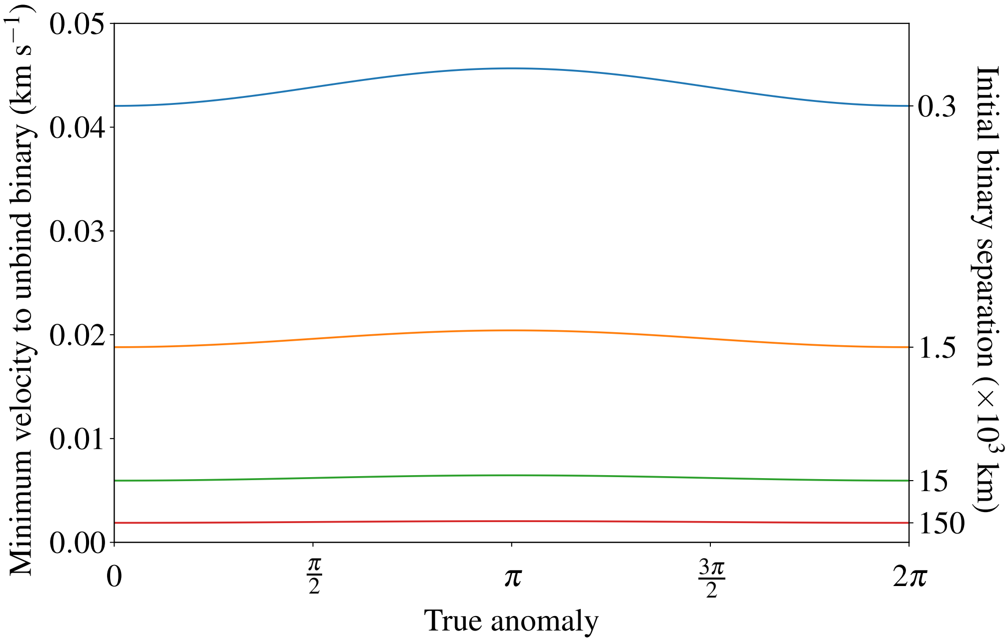

Figure 3.11: Minimum velocity impulse required to unbind a binary asteroid system as a function of the binary's true anomaly. A range of initial binary semi-major axes are considered and highlighted by labels on the right hand y-axis and the different colour curves. The highest required velocity kick and hence the most resilient binary occurs for the tightest binary with a separation of just 300 km. The minimum velocity required peaks at $f = \pi$, but largely does not vary across the orbit.

where e is the eccentricity, f the true anomaly and $v_{\mathrm{k}} = \sqrt{G\,(M+m)\,/a}$ is the circular orbital speed. The true anomaly dependence of Δv_{min} is due to the orbital velocity of the body varying during the course of the orbit, travelling fastest at pericentre and slowest at apocentre. Therefore, the additional velocity required for the body to reach escape speed also varies across the orbit, with the largest additional kick being required when the body is moving slowest, i.e. at apocentre. The velocity kick required for ejection is minimised when the impulsive kick occurs in the same direction as the orbital motion and so entirely goes towards increasing the orbital energy. We can use Equation 3.13 to calculate the minimum velocity kick required to unbind the binary and the circumstellar orbit and consider if it is possible to eject a gravitationally bound binary asteroid system from its planetary system assuming the ejecting interaction is impulsive.

First, we turn our attention to identifying how the velocity kick required to unbind the binary changes with the separation between the binary components. Figure 3.11 plots the minimum kick velocity required to unbind the binary as a function of the true anomaly assuming that the binary orbit has a near-zero initial eccentricity as in our simulations. We plot the distribution of velocity kicks required for initial binary semi-major axis values in the range 300 km < a_B < 1.5×10^5 km as indicated on the right-hand side of Figure 3.11. This binary semi-major axis range extends to lower values than those introduced in Section 3.2.1 as we aim to identify the tightest binary which might survive, thus we include the semi-major axis of the tightest TNO (a Plutino) identified in figure 2 of Nesvorný and Vokrouhlicky [2019].

The blue line at 300 km separation in Figure 3.11 is the tightest binary and requires the largest velocity kick to unbind, with the wider binary orbits typical of the CCKBO region needing a much smaller velocity kick. Although the top-most line does show a slight peak at $f = \pi$, the distributions are relatively flat due to the near circular orbit, especially as the binary separation increases. The peak velocity can thus be approximately taken as constant across the orbit. For the purpose of identifying if it is possible for a binary asteroid system to be ejected while bound, we focus on the most resilient and tight binaries which require $\Delta v_{\mathrm{min,\,B}} \sim 0.046$ kms^{-1} in order to be unbound.

For a gravitationally bound binary asteroid system to be ejected from its planetary system, the binary must receive an impulsive kick small enough to not unbind the binary but sufficient to unbind the system from the central star, or $\Delta v_{\mathrm{min,\,B}} > \Delta v_{\mathrm{min,\,*}}$. To begin to assess when the above inequality is satisfied, we now turn our attention to the circumstellar orbit.

The range of circumstellar semi-major axis values considered in our Solar System analogue simulations (84 au < a < 94 au, see Section 3.3.1) display a narrow range of $\Delta v_{\mathrm{min,\,*}}$ for any given eccentricity which all vary by less than 3 per cent from the average value across that range. Thus, in the following calculations we use $a_* = 94$ au as a proxy for the entire semi-major axis range.

Figure 3.12 shows the minimum velocity kick required to eject a binary asteroid system from the planetary system as a function of circumstellar true anomaly. The coloured, solid lines show the velocity impulse required for different circumstellar eccentricity values as shown in the legend. We only show circumstellar eccentricities in the range $0.5 < e < 1.0$, as only binary asteroid systems in this range are dissociated and ejected in our Solar System analogue simulations as shown in Figure 3.1 and we restrict the figure to positive $\Delta v_{\mathrm{min,\,*}}$ values. As the circumstellar eccentricity increases, the velocity distribution narrows and reaches a higher peak velocity. This is caused by the apocentre distance and orbital velocities varying with eccentricity, and contrasts the essentially flat distributions seen for the minimally eccentric binary orbits in Figure 3.11. As opposing sides of an eccentric orbit have the same orbital velocity, but in opposing directions, the distributions are symmetric about apocentre.

The dashed, grey, horizontal line at $\Delta v_{\mathrm{min}} \sim 0.046$ kms $^{-1}$ shows the minimum velocity kick required to unbind the tightest binary orbit seen in Figure 3.11, which we take as the most likely binary to survive the ejection process. As bound binary asteroid systems can only be ejected when $\Delta v_{\mathrm{min,\,B}} > \Delta v_{\mathrm{min,\,*}}$, only velocity kicks below the dashed grey line

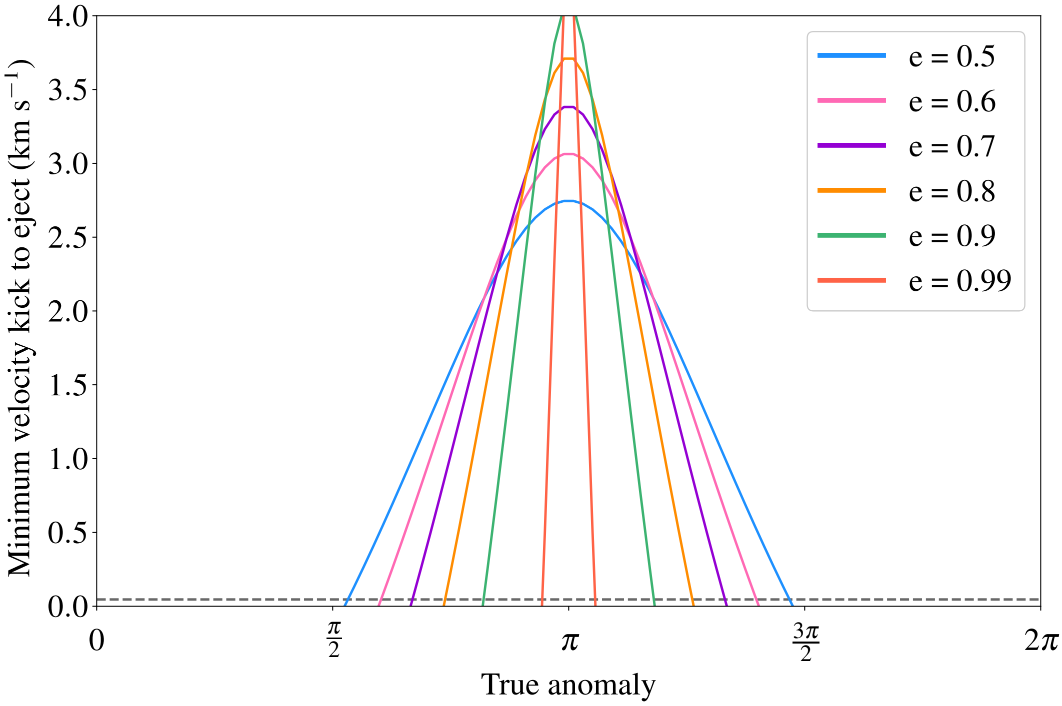

Figure 3.12: Minimum velocity impulse required to eject a binary asteroid system from its planetary system as a function of the circumstellar true anomaly. The minimum kick velocity required for a number of different circumstellar eccentricity values are shown in solid lines whose colours are described in the legend, with higher eccentricity values requiring higher peak velocity kicks. The velocity kick required to dissociate the binary orbit, $\Delta v_{\rm min,\,B} \sim 0.046$ kms^{-1} as in Figure 3.11, is shown by the dashed, grey horizontal line. Only when the coloured lines are beneath the grey, dashed line can a bound binary asteroid system be ejected from the planetary system.

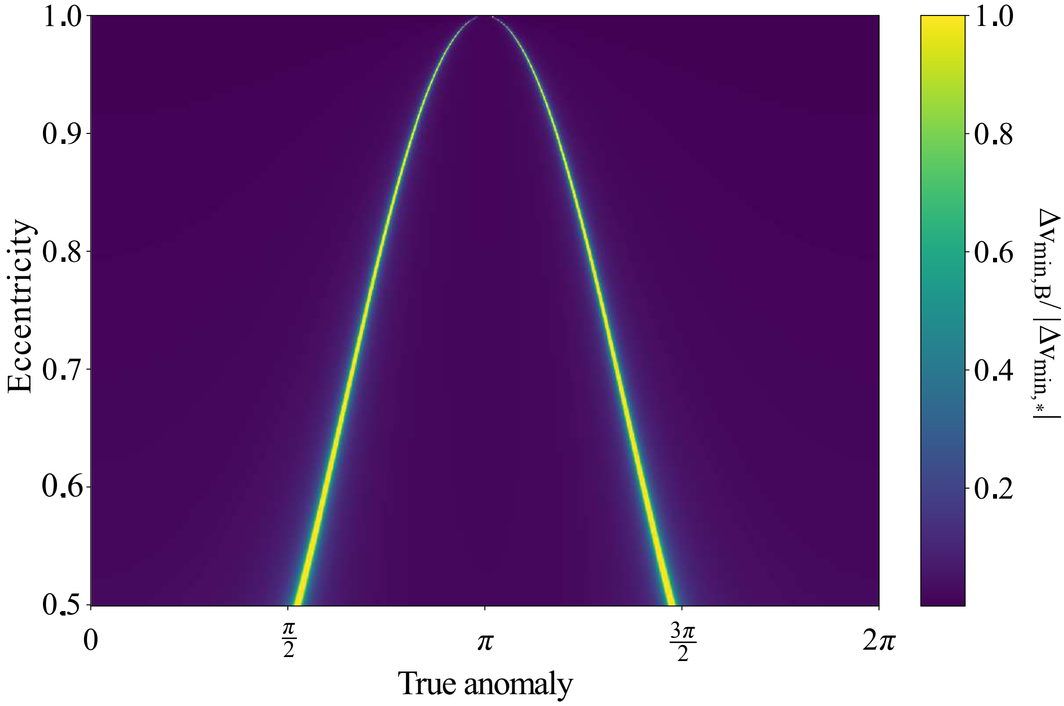

Figure 3.13: The ratio $\Delta v_{\rm min,\,B}/|\Delta v_{\rm min,\,*}|$ for a range of circumstellar eccentricity and true anomaly values. Yellow regions indicate regions of phase space where the above ratio exceeds unity, as demonstrated by the colour bar, and a bound binary could be ejected from its planetary system. Across the whole range of eccentricity values sampled, there is at least one location along the orbit where a bound binary could be ejected, although these regions are very narrow. Thus, a bound binary could only be ejected if it received a small velocity kick at one of the highlighted regions of it's orbit.

are capable of ejecting a bound binary asteroid system. Figure 3.12 thus begins to highlight the difficulties in producing interstellar binary asteroid systems, with the majority of the circumstellar orbit requiring much higher velocity impulses to eject the circumstellar orbit than the binary orbit.

To further consider the problem, we now calculate the ratio $\Delta v_{\rm min,B}/|\Delta v_{\rm min,*}|$, assuming a fixed $\Delta v_{\rm min,B} = 0.046$ kms $^{-1}$, across a larger range of circumstellar eccentricity and true anomaly values and identify regions where the ratio exceeds unity and hence the binary could be ejected while still bound. Figure 3.13 identifies where the inequality $\Delta v_{\rm min,\,B}/|\Delta v_{\rm min,\,*}| > 1$ is true across a range of circumstellar eccentricity and true anomaly values. As described by the colour bar, yellow regions indicate where the above inequality is true and thus where it could be possible to eject a bound binary. As in Figure 3.12 there are two locations in each orbit where $\Delta v_{\rm min,\,*}$ is below the velocity required to unbind the binary and the inequality is satisfied. The range of true anomaly values where a bound binary asteroid system can be ejected decreases as the circumstellar eccentricity increases as evidenced by the yellow region narrowing at high eccentricities and the two solutions converging towards apocentre.

Thus, the circumstances required for a binary asteroid system to be ejected from its circumstellar orbit by a single impulsive perturbation are substantially restricted to particular circumstellar orbital velocities. Equation 3.13 and Figures 3.11-3.13 consider only the maximal case where the impulsive perturbation occurs in the same direction as the orbital motion and thus will have its strongest effect. The likelihood of bound binary ejection thus reduces even further when considering that the perturbation could be oriented away from the direction of orbital motion. Additionally, Figures 3.12 and 3.13 only consider the most resilient and tightly bound binary asteroid systems from Figure 3.11, and thus more typical wider binary systems will be even easier to dissociate through impulsive kicks.

Further, although Figure 3.13 highlights two locations where such an ejection is possible, we reiterate that a very small impulsive kick ($\Delta v_{\rm min} \leq 0.046$ km s^{-1}) is required to keep the binary gravitationally bound. Previous studies looking at planetary encounters with binary asteroid systems consider hyperbolic encounter velocities on the order of $\sim$ 10 km s^{-1}[Fang and Margot, 2012; Meyer and Scheeres, 2021], much larger than that required here. Thus, the coincidence of the small impulsive kick required and the limited region of orbital space for this kick to occur makes the ejection of a bound binary asteroid system unlikely, as seen in the results of our simulations.

As binary asteroids are thought to be a primordial consequence of planetesimal formation and thus should be present in exoplanetary systems, the impact of binarity on ISO production channels could be important to consider in future work.

3.5 Conclusions

Understanding how we can form the observed debris systems and polluted atmospheres of some white dwarfs is an important aspect of our knowledge of the future evolution of currently observed main-sequence planetary systems as well as the fate of our own Solar System. While our current knowledge of planetesimal populations around other stars is limited due to observational difficulties, we can use our much better understanding of the Solar System minor bodies to improve our extra-Solar modelling attempts.

In this work we considered how binary asteroids would evolve during the white dwarf phase of stellar evolution under the presence of different planetary architectures. This is an important area to study as binary asteroids are so prevalent in the Solar System and likely as prevalent in extrasolar systems, thus they could play an integral role in the evolution of white dwarf planetary systems. We carried out computationally demanding N-body simulations using `REBOUND` to follow the evolution of multiple sets of 100 equal-mass asteroid binaries embedded within different planetary architectures: within a Solar System analogue containing the four giant planets (Section 3.3.1), and located interior and exterior to a single Earth-mass planet (Sections 3.3.3 and 3.3.2) respectively. We also performed comparable simulations with a single binary component removed, and targeted instability in some simulations by appealing to known periodic orbits.

The first result from our simulations is that higher mass planets are more efficient at ejecting binary planetesimal systems from their planetary systems than lower mass planets, a result already well known for single component systems. Around a quarter of the binary systems in our Solar System analogue simulations with giant planets are ejected, but only 1.0 per cent of binaries are ejected with Earth-mass planets present. The processes which lead to the ultimate ejection of bodies differ with planet mass, as both binary components are consistently ejected in the Solar System analogue case, while only a single component is ejected by Earth-mass planets.

We find across all our numerical simulations that no binary asteroid systems are ejected while gravitationally bound. A further analytic investigation finds that an extremely low velocity impulse from a planetary encounter is required in order to eject a bound binary asteroid system. Thus, we do not expect a population of free-floating binary asteroids.

Lower mass planets are less efficient at dissociating binary systems, unless they are in a region of phase space where single body asteroids are expected to be unstable. Binaries which are unbound but not subsequently ejected from their planetary systems evolve to have a broader semi-major axis distribution and also undergo changes in eccentricity and inclination, all of which changes the distribution of objects available to form white dwarf debris systems.

Thus, while asteroid binarity may not directly affect the production of white dwarf debris, it can help shape the population of planetesimals available to be disrupted. Further work into the prospects of binary asteroid survival throughout stellar evolution in the lead up to the white dwarf phase could help further elucidate the role that asteroid binarity has in post-main-sequence planetary systems.

Chapter 4

The effect of planetary tidal migration on planetesimal populations

The discovery of the first transiting white dwarf giant planet around the unpolluted star WD 1856+534 introduces interesting questions about the fate of planetesimals in planetary systems. The orbital similarities between this system and observed main sequence hot Jupiters may indicate a common migration process through high-eccentricty migration. In this work we present preliminary numerical simulations modelling the tidal migration of giant mass planets around both white dwarf and main sequence host stars alongside a population of planetesimals. We find that $80-90$ per cent of planetesimals in the region around the migrating planet's orbit are ejected from the system within the first 0.2 Gyr of migration, contributing to the population of interstellar objects. Planetesimals which avoid ejection are either left at orbital distances far from the planet, or migrated inwards alongside the planet while captured in mean motion resonances. This provides a mechanism for populating the inner regions of a planetary system with a small number of planetesimals which may be able to pollute the white dwarf under further perturbations. Main sequence hot Jupiter hosts may be expected to have under-massive inner debris discs due to the effects of high-eccentricity migration. However, we find that planetesimal clearing during planetary migration may provide a natural explanation for the unpolluted nature of WD 1856+534.

4.1 Introduction

The evolution of giant planets in planetary systems have been of interest to the astrophysics community since the discovery of the first exoplanet around a Sun-like star, 51 Peg, in 1995 [Mayor and Queloz 1995; see Chapter 1.1.2.] With $M_\mathrm{p}\sin i \sim 0.464 M_\mathrm{J}$ and $a \sim 0.05$ au, 51 Peg b became the prototype hot Jupiter (hereafter HJ) and lead to a rich and diverse literature surrounding the formation and evolution of HJs.

Although a large number of HJs have been found as the catalogue of known exoplanets has expanded to 5338[1] (see Figure 1.3), their occurrence rate throughout the Milky Way is low compared to other planet types, with just $0.4 - 0.57$ per cent of main sequence stars hosting a HJ [eg. Howard et al., 2012; Petigura et al., 2018; Zhou et al., 2019]. Data from *Kepler* DR25 suggests that the most frequently occurring planets have $1R_\oplus < \mathrm{R} < 3R_\oplus$ and 4 days $< P <$ 500 days with occurrence rates in the range $2 - 17$ per cent [see figure 2 of Hsu et al., 2019]. Planet population synthesis models agree with observational trends of close-in planets being dominated by lower mass planets [Mordasini, 2018].

The existence of large Jupiter-sized planets at HJ distances is contrary to planet formation theories which predict gas giant planets should form at several au, beyond the ice lines of their host stars [Pollack et al., 1996]. Thus, it is believed that HJs migrate to their observed locations after formation. A number of mechanisms are theorised to drive these planets to small stellar distances and are further discussed in Section 4.2.

Alongside exoplanets, we also detect exo-planetesimal belts similar to the Solar System's Kuiper Belt, more details about debris discs are given in Chapter 1.2.2. Observations of FGK solar-like stars find an occurrence rate for massive debris discs of 17.1 ± 2.4 per cent [Sibthorpe et al., 2018], with no known significant correlation between debris disc occurrence and the detection of planets via radial velocity [Yelverton et al., 2020]. However, as planetesimal discs are predicted to be the remnant reservoirs of planet formation, the co-existence of planets and planetesimals is expected. Thus, the question of how a population of planetesimals may evolve alongside a planet migrating to HJ distances is of importance to the wider picture of planetary systems.

The interplay between a planet's migration and planetesimals is of particular importance in the light of growing evidence for planetary systems around white dwarfs.

White dwarfs are the evolutionary end point for approximately 97 per cent of stars in the Milky Way [Fontaine et al., 2001]. Their extreme densities and surface gravities should allow the white dwarfs to maintain pristine hydrogen or helium atmospheres, since heavier elements will be quickly sunk to the stellar core [e.g. Paquette et al. 1986b; Wyatt et al. 2014; and further discussed in Chapter 1.3.2]. Then the observation of $25 - 50$ per cent of all white dwarfs having heavy elements in their atmosphere[2] [Zuckerman et al., 2010;

[1] As of 27$^{\mathrm{th}}$ April 2023; https://exoplanetarchive.ipac.caltech.edu/

[2] O'Brien et al. [2023] find a lower occurrence rate of metal polluted white dwarfs at 15 per cent for hydrogen dominated DA white dwarfs within a local 40 pc sample, but suggest this may be due to the faintness of their

Koester et al., 2014] implies the material was recently accreted.

To date a large number of chemical elements have been observed within the atmospheres of polluted white dwarfs (see Table 1.2 for a historical picture of observed elements; Klein et al. 2021). Largely the observed abundances are indicative of a terrestrial chondritic-like compositions [e.g. Jura and Young 2014; Hollands et al. 2018; Doyle et al. 2019; see Figure 1.11], although a small number of white dwarfs have been observed with volatile-rich pollution [e.g. Farihi et al., 2013; Raddi et al., 2015; Gentile Fusillo et al., 2017; Xu et al., 2017; Hoskin et al., 2020; Johnson et al., 2022]. The chondritic-like nature of white dwarf pollution implies that white dwarfs may be accreting material from an exo-asteroid belt.

The violent giant branch phases of stellar evolution will effectively clear out the inner few au of a planetary system through planetary engulfment [Mustill and Villaver, 2012; Villaver et al., 2014], mass loss driven orbital expansion [Veras, 2016] and luminosity driven YORP destruction of minor bodies out to $\sim$ 7 au [Veras et al., 2014a]. The YORP effect is further discussed in Chapter 1.2.2. Thus, the accreted planetary material requires a dynamic delivery from the outer planetary system after the star has become a white dwarf.

The canonical idea is that remnant planetesimals are perturbed onto highly eccentric orbits which cross the Roche radius of the white dwarf and are subsequently tidally disrupted (this process is further discussed in Chapter 1.3.2 and an overview is given in Brouwers et al. 2022). The resultant debris goes on to form debris discs which are predicted to exist around all polluted white dwarfs [Rocchetto et al., 2015; Bonsor et al., 2017], although they are currently only observed around 1 – 3 per cent of white dwarfs [Rebassa-Mansergas et al., 2019]. The material then accretes onto the white dwarf from the disc.

Recent observations of disrupting planetesimals transiting white dwarfs [Vanderburg et al. 2015; Vanderbosch et al. 2020, 2021; Guidry et al. 2021; Farihi et al. 2022; see Figure 1.16] bolster this canonical theory, and observed giant planets [Gänsicke et al., 2019; Vanderburg et al., 2020; Blackman et al., 2021] provide a viable mechanism to deliver planetesimals to white dwarfs. The current known planetesimal and planet populations around white dwarfs are further discussed in Chapter 1.3.2.

Of particular interest to the work here is WD 1856+534 b (hereafter WD 1856 b), a giant planet candidate with $M < 11.7\ \mathrm{M}_{\mathrm{J}}$ on a $\sim$ 1.4 day orbit around a white dwarf [Vanderburg et al., 2020]. Figure 1.17 shows the observed transit signature from WD 1856 b, the deep u-shape of the transit suggests it is a large, solid body. As discussed above, such a planet could not have resided at its current orbital distance ($a \sim 0.0204$ au) during the giant branch phases of stellar evolution and so must have migrated to its current location after the onset of the white dwarf phase. The fact that the 5.85 Gyr old WD 1856 displays a DC spectrum with no observed metallic lines implies there has been no accretion in the star's recent history. This then raises questions about how a migrating planet affects planetesimal populations and the prospects for delivering planetesimals to white dwarfs.

sample and the use of medium-resolution spectroscopy leading to fewer line detections.

The following study investigates how reservoirs of planetesimals react to the process of a giant planet migrating through the system. In Section 4.2 we discuss how planets with HJ-like orbits may be formed through high eccentricity migration. Section 4.3 outlines preliminary numerical simulations combining both a migrating planet and planetesimals. The results of these simulations are discussed in Section 4.4 and further complications to our simple model and directions of future work are explored in Section 4.5. Finally, we conclude the work in Section 4.6.

4.2 Hot Jupiter Production

Since the discovery of 51 Peg b, the formation of HJs has been widely studied, both in the context of main sequence stars and in post-main-sequence systems. Although the definition of a HJ can vary throughout the literature, here we adopt that of Dawson and Johnson [2018] as a gas giant planet with $m_{\mathrm{p}} \geqslant 0.25M_{\mathrm{J}}$ and orbital period $P < 10$ days to aid with discussion.

Firstly, studies have shown that in situ formation at their observed orbital locations in the protoplanetary disc is unlikely. Gravitational instabilities would require impossibly high temperatures and gas densities such that the gaseous disc would unbind from the central star [Rafikov, 2005, 2006] and theories of core accretion formation struggle to grow sufficiently massive cores before the gas disc dissipates [Dawson and Johnson, 2018].

However, if the planet formed further out in the protoplanetary disc, interactions between the planet and the gaseous disc through a combination of corotation and Linblad torques could drive the planetary orbit to HJ distances [e.g. Goldreich and Tremaine, 1980; Lin and Papaloizou, 1986; Lin et al., 1996; Baruteau et al., 2014]. Although the contribution of disc migration to the observed population of HJs is unclear as the sign and magnitude of the migration is highly sensitive to the disc conditions [Dawson and Johnson, 2018]. Further, if the disc migration timescale is smaller than the disc lifetime, the planet can migrate all the way into the star itself.

Once the protoplanetary gas disc has dispersed, it is still possible for giant planets to migrate inwards through interactions with remnant planetesimals. The interactions can remove angular momentum from the planetesimals, scattering them outwards which acts to reduce the semi-major axis of the planet [e.g. Malhotra, 1995; Murray et al., 1998; Davies et al., 2014].

The discs we observe around white dwarfs are vastly different from protoplanetary discs and are typically thought to be more like planetary rings [Jura 2003; the canonical white dwarf debris disc model is further discussed in Chapter 1.3.2]. Thus instead, we focus on high eccentricity migration - where a perturbation drives a planet to high eccentricities then tidal interactions with the central star act to shrink and circularize the orbit.

There are a number of processes which have been suggested to excite planets onto high eccentricity orbits. Firstly, dynamic interactions with other planets in the system can increase eccentricities through a series of close encounters [e.g. Rasio and Ford, 1996; Weidenschilling and Marzari, 1996; Ford and Rasio, 2006; Chatterjee et al., 2008]. Such planet-planet scattering is particularly prevalent in tightly packed planetary systems [Jurić and Tremaine, 2008] or stellar cluster environments [Shara, Hurley, and Mardling, 2016]. Next, both periodic [Petrovich, 2015] and chaotic [Wu and Lithwick, 2011; Hamers et al., 2017] secular interactions in systems containing two or more bodies can drive planets to high eccentricities.

One particular form of secular excitation that is frequently invoked to induce high eccentricities is the Kozai-Lidov mechanism (Kozai 1962; Lidov 1962; see Naoz 2016 for a recent review), where exchanges of angular momentum leads to cycles of eccentricity and inclination. Kozai-Lidov cycles can be driven by both stars [Naoz et al., 2012] or planets [e.g. Naoz et al., 2011] and is capable of explaining a large fraction of observed HJs.

As there are a plethora of ways to excite the eccentricities of proto-HJs after the protoplanetary disc has dissipated, here we focus on the next stage of high eccentricity migration; tidal dissipation.

Once the planet's orbit has achieved sufficient eccentricity, it approaches close enough to the central star for tidal interactions to begin. During the process of tidal dissipation, both orbital and rotational energy decrease, while orbital and rotational angular momentum are exchanged, conserving the total angular momentum of the system [Hut, 1981]. Thus, the semi-major axis of a tidally migrating planet approximately evolves as follows

$$a_\mathrm{f} = a_\mathrm{i}(1 - e_\mathrm{i}^2), \tag{4.1}$$

where e_i is the initial high eccentricity, a is the semi-major axis and the i, f subscripts refer to initial and final values respectively [Dawson and Johnson, 2018]. Thus, if we assume that WD 1856 b began at $a_\mathrm{i} = 1.5$ au before migrating to $a_\mathrm{f} = 0.0204$ au this implies it gained an eccentricity of 0.993.

Here, we consider only the equilibrium tide model first described by Darwin [1879] and later expanded to the constant time lag weak friction model in Alexander [1973] and Hut [1981]. In this model, bodies are composed of a weakly viscous fluid which assumes its hydrostatic equilibrium shape with the time-varying gravitational potential of the system [Bolmont et al., 2015; Lu et al., 2023]. As the body deforms under the tidal torque, energy is lost due to friction and the tidal 'bulge' is misaligned with the line between the centers of the two objects [Hut, 1981]. In other words, the tidal deformation will lag behind the gravitational potential by a fixed time lag τ [Alexander, 1973; Hut, 1981; Baronett et al., 2022; Lu et al., 2023].

The leading contribution to the tidal perturbation force is given in Hut [1981] as

$$F = -G\frac{Mm}{r^2}\left\{\hat{r} + 3q\left(\frac{R}{r}\right)^5 k_2\left[\left(1 + 3\tau\frac{\dot{r}}{r}\right)\hat{r} - \left(\Omega - \dot{\theta}\right)\tau\hat{\theta}\right]\right\}, \tag{4.2}$$

where G is the gravitational constant, M and m are the mass of the tidally deformed body and perturber respectively, r is the radial distance between the two bodies if they were point masses, $q = m/M$ is the mass ratio, R is the radius of the perturbed body, and Ω and $\hat{\theta}$ are the rotational and instantaneous orbital angular velocities of the perturbed body and the perturber. The perturbed body's tidal Love number k_2 is dependent on the interior structure of the body and can be described by

$$k_2 = \frac{3 - \eta_2}{2 + \eta_2}, \tag{4.3}$$

where η_2 is the solution of Radau's equation for $j = 2$ at the body's surface [Becker and Batygin, 2013; Csizmadia et al., 2018].

The evolution of the orbiting body's semi-major axis and eccentricity can then be described by the following differential equations

$$\frac{da}{dt} = -6\frac{k_2}{T}q\left(1+q\right)\left(\frac{R}{a}\right)^8 \frac{a}{\left(1-e^2\right)^{15/2}} \cdot \left\{f_1(e^2) - \left(1-e^2\right)^{3/2} f_2(e^2)\frac{\Omega}{n}\right\}, \tag{4.4}$$

$$\frac{de}{dt} = -27\frac{k_2}{T}q\left(1+q\right)\left(\frac{R}{a}\right)^8 \frac{e}{\left(1-e^2\right)^{13/2}} \cdot \left\{f_3(e^2) - \frac{11}{18}\left(1-e^2\right)^{3/2} f_4(e^2)\frac{\Omega}{n}\right\} \tag{4.5}$$

where

$$f_1(e^2) = 1 + \frac{31}{2}e^2 + \frac{255}{8}e^4 + \frac{185}{16}e^6 + \frac{25}{64}e^8, \tag{4.6}$$

$$f_2(e^2) = 1 + \frac{15}{2}e^2 + \frac{45}{8}e^4 + \frac{5}{16}e^6, \tag{4.7}$$

$$f_3(e^2) = 1 + \frac{15}{4}e^2 + \frac{15}{8}e^4 + \frac{5}{64}e^6, \tag{4.8}$$

$$f_4(e^2) = 1 + \frac{3}{2}e^2 + \frac{1}{8}e^4, \tag{4.9}$$

$n = G^{1/2}(M+m)^{1/2}a^{-3/2}$ is the mean orbital angular velocity and $T = R^3/(GM\tau)$ gives an indicative timescale over which significant tidal evolution occurs [Hut, 1981; Baronett et al., 2022].

The above described constant time lag model has been implemented in a number of computational modelling codes which have been widely used to investigate planetary system

Table 4.1: Stellar properties for the main sequence and white dwarf stars modelled in our simulations.

	Mass ($M_\odot$)	Radius (au)	k_2	τ (yr)
Main Sequence	1	4.65×10^{-3}	0.03	2.12×10^{-9}
White Dwarf	0.6	3.92×10^{-5}	0.03	1.2×10^{-16}

evolution [e.g. Bolmont et al., 2015; Baronett et al., 2022]. Previous studies considering the tidal interaction between white dwarfs and planets have either focussed on solid bodies [Veras et al., 2019a; Veras and Wolszczan, 2019] or the chaotic tidal regime for gas giants at high eccentricities [Veras and Fuller, 2019]. However, in the following work we neglect the influence of chaotic tides and focus on the above described equilibrium tides which act over longer timescales.

4.3 `REBOUND` Simulations

To investigate the response of planetesimal populations under the influence of a migrating planet, we carried out a number of numerical simulations using the N-body integrator `REBOUND` [Rein and Liu, 2012] coupled with its library of additional forces `REBOUNDx` [Tamayo et al., 2020].

We utilise the `MERCURIUS` integrator, a hybrid symplectic integrator which ensures high accuracy and speed by using the high order integration scheme `IAS15` to resolve close encounters and otherwise switches to the standard 2nd order Wisdom-Holman scheme `WHFast` [Rein et al., 2019]. We set the standard timestep used in `WHFast` as 0.001 yr and the minimum adaptive timestep used by `IAS15` as 1×10^{-7} yr to prevent simulation stalling.

To ensure accuracy, we confirm that the relative total angular momentum error for our simulations around white dwarfs are always on the order of $\times 10^{-10}$ or smaller, and $\times 10^{-6}$ or smaller for the simulations around a Solar-like star, all of which are reasonable values. We believe the orders of magnitude difference in relative errors between stellar types in our work is driven by our choice of computational tidal model and related parameters, as discussed further in the following section.

To model the tidal interaction between the star and planet and hence the planet's subsequent migration, we utilise the `REBOUNDX` additional effect 'tidal constant time lag' (`TCTL`) introduced by Baronett et al. [2022]. `TCTL` implements a general form of the weak friction tidal model discussed in Section 4.2, which is parameterised by k_2, τ and Ω.

In order to examine the effect of planetary migration in systems around main sequence and white dwarf stars, we model systems around both a Solar-like star and a typical white dwarf, the parameters used to model these stars are listed in Table 4.1.

The chosen white dwarf mass of $M_{\rm WD} = 0.6 M_\odot$ represents the peak of the observed white dwarf mass distribution [McCleery et al. 2020; O'Brien et al. 2023; Figure 1.6]. We adopt $k_2 = 0.03$ for both stars to represent a fully convective stellar atmosphere (which is valid for cooler white dwarfs where convection dominates over radiation) [Schröder and Smith, 2008; Baronett et al., 2022].

Baronett et al. [2022] present an expression for the constant tidal time lag τ by equating the expression for the tidal torque from Equation 11 of [Zahn, 1989] to the azimuthal component of the tidal perturbing force (Equation 4.2), leading to the following

$$\tau = \frac{2R^3}{GMt_f}, \tag{4.10}$$

where the convective friction time t_f is given as

$$t_f = \left[\frac{MR^2}{L}\right]^{1/3}. \tag{4.11}$$

The τ values shown in Table 4.1 and used in the presented simulations were calculated according to Equations 4.10 and 4.11, with the main sequence value being calculated assuming standard Solar parameters. The white dwarf τ value was chosen as the approximate median for a range of values encompassing different stellar luminosities calculated from Equation 2.5 of Veras [2016], stellar metallicities from Romero et al. [2015] and white dwarf cooling ages. However, we note that the values presented in Table 4.1, and used in the simulations presented in this Chapter, are incorrect due to a calculation error. We choose to still present the simulations and their results, to highlight the analysis that could be carried out and conclusions we may be able to draw from future simulations with corrected constant tidal time lag values.

We now discuss the correct calculation of τ. Assuming solar values as before, a constant time lag value of $\tau_{\mathrm{MS}} \sim 1.18 \times 10^{-8}$ yr ~ 0.62 s is expected. The picture is more complicated for white dwarfs, where the stellar luminosity is dependent on the cooling age of the star. Using the white dwarf luminosity range $10^{-5} L_\odot$ - $10^3 L_\odot$ from Veras [2016], assuming $M_{\mathrm{WD}} = 0.6 M_\odot$ and estimating R_{WD} from Equation 2.1, we find the range 1.6×10^{-14} yr $< \tau_{\mathrm{WD}} < 7.5 \times 10^{-12}$ yr (5.1×10^{-7} s $< \tau_{\mathrm{WD}} < 2.0 \times 10^{-4}$ s). The lower constant tidal time lag value for white dwarfs compared to main sequence stars is a consequence of their smaller radii and masses combined with the range of possible stellar luminosities through Equation 4.11. Both τ_{MS} and τ_{WD} are consistent with constant time lag values presented in other tidal migration studies [e.g. Fellay et al., 2023; Lu et al., 2023]. Future simulations will utilise these values to provide more accurate results.

In advance of these new simulations, we can begin to consider how the updated τ values will affect the results presented in this chapter. Returning to Chapter 4.2, equations 4.4-4.5 describe the semi-major axis and eccentricity evolution caused by tidal evolution in the constant tidal time lag model. Both of these equations are dependent on τ via T, an indicative timescale over which significant tidal evolution can occur [Hut, 1981; Baronett et al., 2022]. As $T = R^3/(GM\tau)$, changing τ by an order of magnitude (as is the case for the updated τ_{MS}) also changes T by an order of magnitude. Although, the variable that has the largest effect on the determination of T is still the stellar radius, which goes someway to explaining the differences in our results for a main sequence or white dwarf star. Thus, the larger τ values we find from our corrected calculations suggest that we may expect to observe faster rates of tidal evolution in the upcoming improved simulations. The increased tidal evolutionary rate may reduce the amount of time available to perturb planetesimals in the system, lowering the rate of system ejections and coincident inwards migration seen in the results discussed in Chapter 4.4.1-4.4.2.

In order to investigate how changing τ might affect the angular momentum conservation in our simulations, we carried out a small number of short duration simulations containing only the central star and migrating planet with both the original and updated τ values. These simulations ran for 1 Myr, a small fraction of the full simulations duration, which is insufficient to observe significant tidal evolution, but could highlight the beginnings of divergent angular momentum conservation. We find that the relative total angular momentum errors measured for simulations with the original and corrected τ values are of the same order of magnitude for the same stellar type and do not show significant differences. Thus, although additional simulation time could cause differences in angular momentum conservation to become clearer, this suggests that the updated τ values may have only a small impact on the relative total angular momentum errors measured for our future simulations. The anomalous differences in relative errors measured for the different stellar types previously noted, then likely have another cause which is further discussed in the next section.

Next, we place a Jupiter mass, and sized, planet around the star at varying semi-major axis values (between $1-2$ au), initialised with an extremely high eccentricity ($e = 0.955$). This eccentricity value was chosen from a number of initial tests to maximise the amount of time the planet spends migrating, while ensuring that a significant semi-major axis change occurs within 1 Gyr of simulation time. The rotation of the bodies Ω is initially set to 0 as in Baronett et al. [2022].

Finally, we add 50 planetesimals as semi-active test particles which can influence the planet, while not influencing other test particles. These bodies are all given a small mass of $\sim 10^{13}$ kg which approximately corresponds with a planetesimal with $\rho = 3\ \mathrm{g\,cm^{-3}}$ and $R \sim 1$ km.

The test particles are placed between the location of the planets 2:1 mean motion resonance (MMR) which is given by $a_{\mathrm{MMR}} = (2/1)^{2/3} a_p$ [Murray and Dermott, 1999], and the apocentre of the planet's orbit. This orbital region was chosen as preliminary simulations suggested that this region would be most influenced by the planets migration and hence of most interest to us. The planetesimal's orbits were given zero initial eccentricity and their true anomaly is randomly chosen between $(0, 2\pi)$ to distribute the bodies around their orbits. Although exact coplanarity can artificially increase the rate of collisions in N body simulations, the inclination of the planetesimals in these simulations is initially set to zero. Further investigations of how our simulation results would change if the planetesimals are initialised with a small random inclination would help further validate the results presented in this Chapter.

Then the simulation is set to evolve the system for a maximum of 1 Gyr. Bodies within the simulation are removed if one of two conditions is reached. Firstly, if the particle crosses the Roche radius of the white dwarf we assume that the body will be tidally disrupted and hence is removed from the simulation. Here we define the Roche radius for a solid, spinning rubble pile asteroid with density $\rho_a = 3\ \mathrm{g\,cm^{-3}}$ (roughly indicative of a body consisting of solid ices and dust while neglecting effects of porosity) as in Veras et al. [2017]

$$r_{\mathrm{Roche}} = 0.89 \left(\frac{M_{\mathrm{WD}}}{\rho_a} \right)^{1/3}, \tag{4.12}$$

which puts the Roche radius at $r_{\mathrm{Roche}} = 0.94 R_{\odot} \sim 0.004$ au.

Secondly, if the particle exceeds an instantaneous circumstellar distance of 2000 au, we consider the body to have left the inner planetary system and no longer be of interest. Although in reality, bodies can remain bound to planetary systems until they exceed the system's Hills Ellipsoid which can extend to over 100000 au [Veras and Evans 2013; Veras 2014; see Chapter 3.2.3], here we consider a smaller ejection distance to reduce computational strain.

Now we move on to discuss the preliminary results from these simulations.

4.4 Results

4.4.1 White Dwarf Migration

First, we look at the results of simulating a migrating Jupiter analogue around a $0.6 M_{\odot}$ white dwarf, with initial planetary semi-major axes, $a_p = [1\mathrm{au}, 1.5\mathrm{au}, 2\mathrm{au}]$. Although these orbital distances are closer than expected to be able to survive engulfment on the giant branch phases [Villaver et al. 2014; Chapter 1.2.2], we assume that these planets have already migrated to our initial distances prior to the beginning of the simulations in order to improve computational speed.

Figure 4.1 shows the semi-major axis evolution of the planet, planetesimals and a number of first order MMRs for the simulation where the planet started with $a = 1.5$ au. As expected from the constant time lag tidal prescription discussed in Section 4.2, the planet largely migrates inwards as the simulation progresses, as shown by the solid orange line in the figure. However, we should draw attention to the small period of seeming outward migration that begins around 0.025 Gyr.

In the constant tidal time lag model utilised in this work [Baronett et al., 2022], a

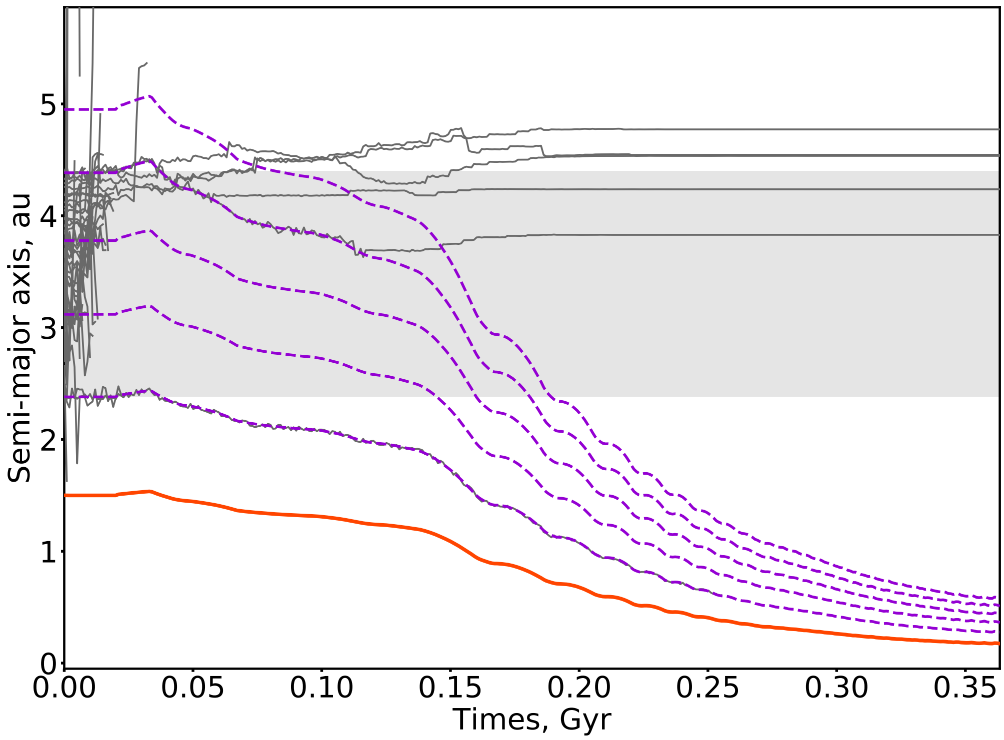

Figure 4.1: Semi-major axis evolution of a Jupiter-mass planet tidally migrating towards a white dwarf and influencing a number of planetesimals exterior to its orbit. The planet starts at a_i = 1.5 au and reaches a_f ~ 0.17 au after ~ 0.35 Gyr, its evolution is shown by the thick, solid orange line. The location of a number of MMRs (2:1, 3:1, 4:1, 5:1, 6:1, bottom to top) are shown in thick purple dashed lines. The semi-major axis evolution of the planetesimals are shown in thin grey lines until either they achieve $e > 1$, or they are removed from the simulation as discussed in the text. The horizontal shaded region between the 2:1 MMR and the apocentre of the planet's orbit shows the region initially occupied by the planetesimals. A small number of planetesimals are able to persist at wider orbital distances even after migrating inwards within MMRs. A single planetesimal initialised near the 2:1 MMR migrates inwards with the planet for ~ 0.25 Gyr and comes within 1 au of the central star before it is subsequently ejected.

non-zero τ causes bodies to be driven either radially inwards or outwards dependent on if they orbit faster, or slower, than the spin of the tidally deformed body. As the spin of the central star in our simulations is set to zero, then we should only expect to see inwards migration, contrary to what is seen in Figure 4.1. In an attempt to reconcile these two facts, we carried out a number of investigations. Firstly, we check that the anomalous migration is not introduced by transformations between Jacobi and heliocentric coordinate systems, but find the outwards migration is present in both coordinate systems. Secondly, we confirm that the outwards migration is not influenced by planetesimals in the system by identifying the same outwards migration in an identical simulation with no planetesimals. Thus, we believe that this outwards migration is due to a numerical issue with our simulations.

This numerical effect is likely due to the `REBOUNDX` implementation of `TCTL` not evolving the spins during the simulation and thus anomalous results could be introduced in systems where the angular momentum exchange non-negligibly influences the spins. This is likely one of the main drivers behind the large differences in relative angular momentum errors between our stellar types. We find the relative angular momentum error in the main sequence systems increases as the planetary semi-major axis decreases. For the main sequence systems with the widest planetary orbits, the relative error is the same as the smallest white dwarf system relative error. Thus, we believe the anomalous relative angular momentum errors are caused by the lack of consistent spin evolution in the `TCTL` model.

Since the simulations presented in this Chapter were produced, an additional tidal effect `tides_spins` as described in Lu et al. [2023] has been introduced to `REBOUNDX`. This new implementation includes the self-consistent spin, tidal and dynamical equations of motion first introduced in Eggleton et al. [1998], and will likely provide an improvement in applicability and accuracy to our simulations compared to the results presented in this Chapter. Thus, although the simulations in this Chapter are subject to numerical effects driven by the lack of self-consistent spin evolution, we still present their results in the following sections to highlight the analyses to be carried out and results we may expect to find from further simulations using `tides_spins`.

Returning to Figure 4.1, the locations of the 2:1, 3:1, 4:1, 5:1 and 6:1 MMRs (bottom to top) are shown by purple dashed lines, the resonances move inwards with the planet and the spacing between them reduces.

The horizontal shaded region in the figure shows the original orbital region occupied by the 50 planetesimals included in the simulations, and the thin grey lines show the subsequent semi-major axis evolution of the planetesimals. From the figure it is immediately clear that a large number of planetesimals are ejected very soon after the simulation begins. This is a feature seen across all simulations with varying initial planetary semi-major axis as can be seen in the purple lines in Figure 4.2, which shows the number of planetesimals ejected across the first 0.1 Gyr of simulation. From Figure 4.2 it can be seen that the majority of planetesimals are ejected within the first 0.02 Gyr of simulation.

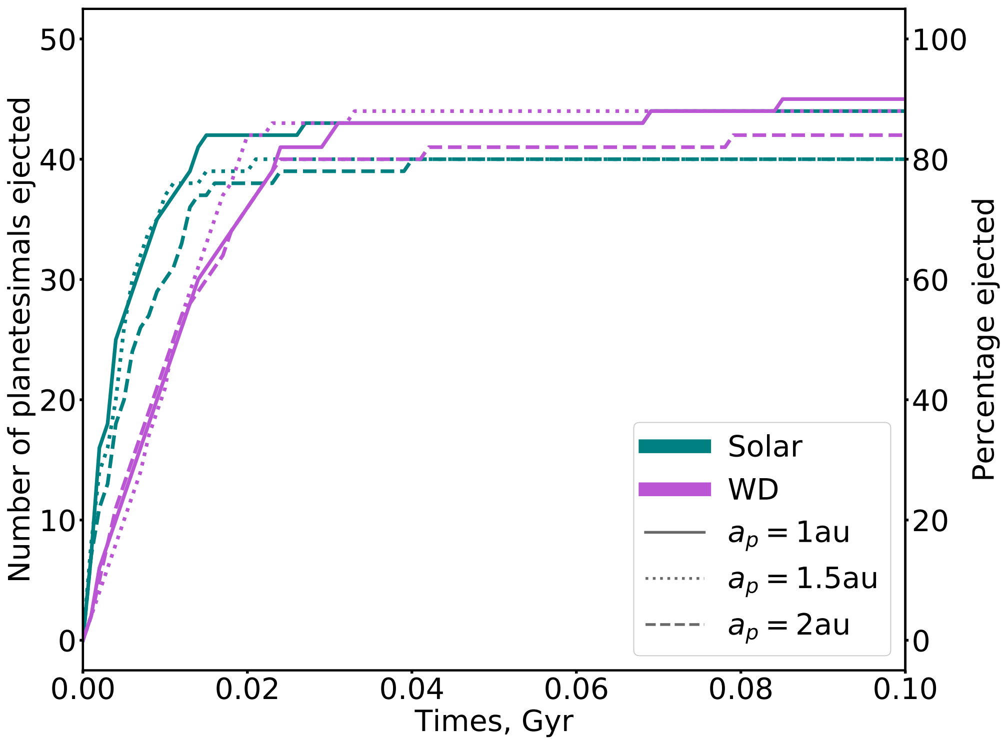

Figure 4.2: The number of planetesimals ejected from the simulations of Jupiter-mass planet tidally migrating around both a white dwarf (purple) and a Solar-like star (green). The results for simulations with different initial planet semi-major axes are highlighted by different line styles as shown in the legend. Across all simulations the majority of planetesimals are ejected from the simulation within ~ 0.02 Gyr.

Table 4.2: Final semi-major axis (a_{f}) achieved by Jupiter-mass planets tidally migrating around a white dwarf from initial semi-major axis a_{i} and the number of 50 planetesimals remaining at the end of the simulation time, N_{pl}.

	a_{i} (au)	a_{f} (au)	N_{pl}
White Dwarf	1	0.11	3/50
	1.5	0.17	5/50
	2	0.79	4/50
Solar	1	0.11	6/50
	1.5	0.20	0/50
	2	0.28	9/50

Table 4.2 summarises the results of the simulations around a white dwarf with varying initial planet semi-major axis a_i, a_f gives the final semi-major axis reached by the planet while migrating and N_pl gives the number of 50 planetesimals which are remaining at the end of the simulation. For all three white dwarf simulations, less than 10 per cent of the planetesimals included are remaining at the end of the simulation. Previous studies have suggested that planetesimal ejections during the white dwarf phase may contribute to the population of interstellar objects (ISOs) [Hansen and Zuckerman 2017; Rafikov 2018; Moro-Martín 2019; Malamud and Perets 2020b; McDonald and Veras 2023; Chapter 3.4.2], and here we find that a migrating planet may also directly contribute planetesimals to interstellar space. Although none of the simulated planets reach an orbit analogous to that of WD 1856 b, it should be noted that these simulations have not run for the full 1 Gyr intended and thus it is possible that they would reach HJ distances if integrated for longer and with more accurate tidal models.

We verify the fate of the planetesimals which are removed from the simulations by utilising the `REBOUND` SimulationArchive to identify the timestep at which they are removed [Rein and Tamayo, 2017]. We then access the simulation snapshot before removal and reintegrate with a smaller timestep to more finely resolve the ejection. Through this we are able to confirm that all planetesimals are removed when they reach the outer edge of our simulations at 2000 au and that they all have either eccentricities greater than unity or close to, suggesting that they have been unbound from the planetary system.

We further take into account the possibility that we are unable to resolve Roche crossings due to the limited time step duration of our simulations, by calculating the osculating pericentre at each SimulationArchive snapshot. If this pericentre distance is within 5 per cent of the white dwarf's Roche radius, we again use the SimulationArchive to carry out finer resolution simulations around any potential Roche crossings. This allows us to confirm that no planetesimals in our simulations cross the white dwarf's Roche radius and are expected to tidally disrupt.

Previous work by Veras [2020] investigated the prospects for rocky pollution of the white dwarf WD J0914+1914, which is inferred to be accreting the evaporated atmosphere of an ice giant planet on a short period orbit [Gänsicke et al., 2019]. Their work finds that polluting the white dwarf through radiative effects on planetesimals is only possible for a narrow range of planetesimal sizes, thus suggesting it is even harder to pollute white dwarfs with close-in planets than our simulations suggest alone.

Turning our attention back to Figure 4.1 we also see a number of planetesimals which survive to the end of the simulation. First, there are a number of planetesimals which begin far from the planet which are able to survive, a number of these planetesimals actually migrate outwards during the simulation, highlighted by the fact their final semi-major axes are above the shaded region. Their evolution remaining stable after ~ 0.2 Gyr suggests that their motion has completely decoupled from the migrating planet.

Resonant Planetesimal Migration

Also evident in Figure 4.1 are planetesimals which begin the simulations close to the locations of MMRs simultaneously migrating inwards with the planet. At least two planetesimals which are in the 5:1 MMR are migrated inwards until they are able to escape the resonance and continue their stable evolution.

We now discuss the prospects for capturing planetesimals into MMRs while a planet is migrating, although we note that resonant capture is not possible for diverging orbits (where the ratio between the orbital periods diverges away from unity) as is the case for the majority of the planetesimals in this study [Sinclair, 1972; Yu and Tremaine, 2001; Chiang et al., 2002].

Both Quillen [2006] and Mustill and Wyatt [2011] present general models that describe the probability for planetesimals to be captured in a resonance while migrating in the low eccentricity limit. Although neither model is directly applicable to our work due to the high eccentricities of the migrating planets in our simulations, general conclusions from their work may be relevant. Figure 2 of Mustill and Wyatt [2011] shows the capture probabilities for a range of eccentricity values and migration rates (there described by dimensionless and scaled eccentricity J_0 and migration rate $\dot{\beta}$). The bodies in our simulations are outside the bounds of this plot, but it can be seen that largely, resonant capture is more likely for small eccentricities and slow migration rates. Capture at higher eccentricities is more probable under faster migration rates than for lower eccentricities, thus suggesting the capture observed in our simulations may not be unreasonable [Mustill and Wyatt, 2011]. Similarly, Quillen [2006] find that captures can still occur at high migration rates.

Wang and Malhotra [2017] present an investigation into the higher eccentricity regime of MMRs and find that in contrast to previous assumptions, resonances at higher eccentricites can have libration zones comparable to those at lower eccentricites strengthening our findings of resonant capture at high eccentricities. Although again we must note that the analysis presented in Wang and Malhotra [2017] is not directly applicable to our results as they only consider interior resonances, it again shows positive prospects for resonant capture during high eccentricity migration.

Finally, one planetesimal in Figure 4.1, which is initialised around the location of the 2:1 MMR is strongly embedded into the resonance and migrated inwards with the planet for ~ 0.25 Gyr. Figure 4.3 examines this particular planetesimal's evolution in more detail, the bottom panel is the same as in Figure 4.1, but only shows the evolution of the planetesimal in question. The top panel shows the eccentricity evolution of the planetesimal, where it can be seen that the eccentricity oscillates between an approximately circular orbit and $e \sim 0.5$. The end of the green line in the top panel indicates the time at which the planetesimal is removed from the simulation. From our finer follow up integration, we find the eccentricity of the planetesimal very quickly increases and the planetesimal's eccentricity exceeds unity and is ejected from the simulation.

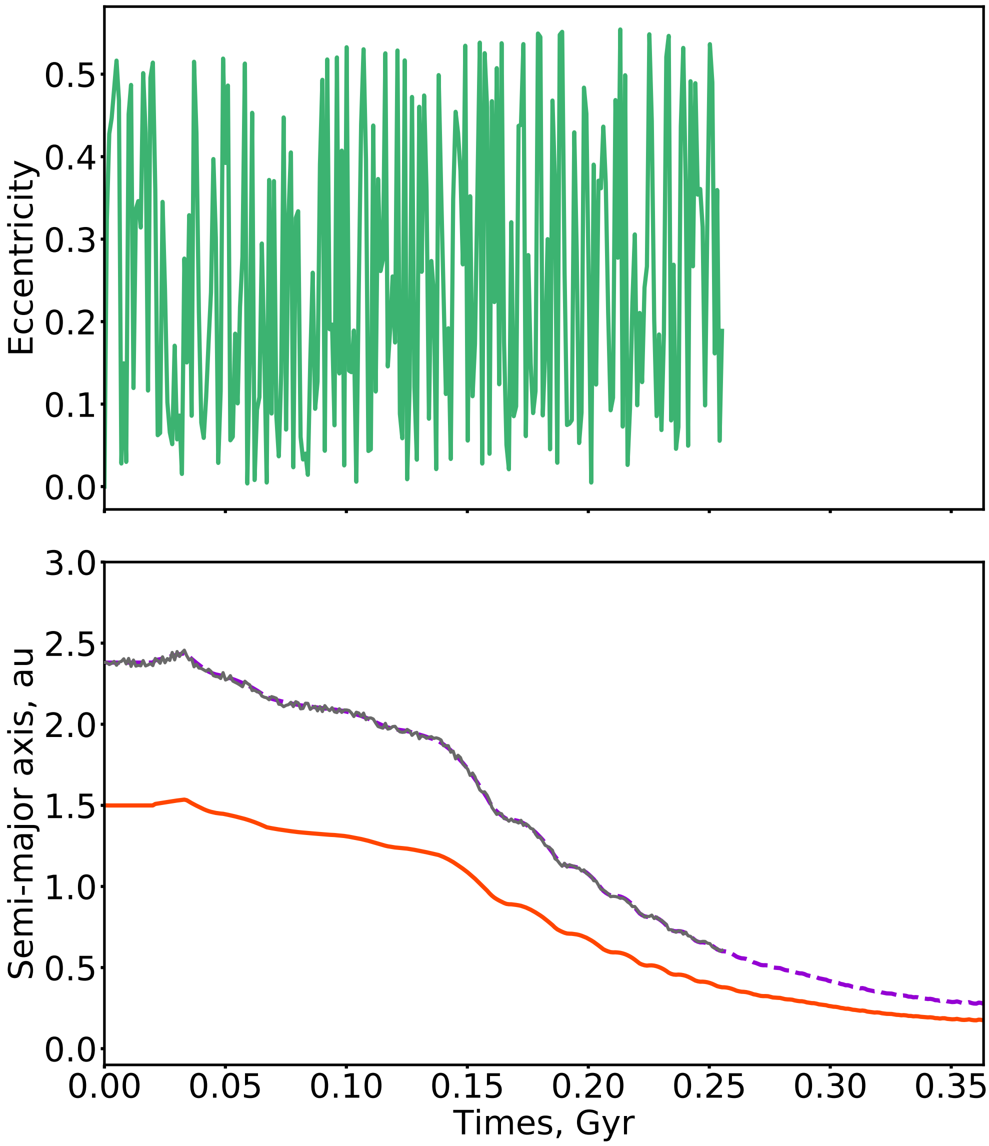

Figure 4.3: Specific evolution of a planetesimal captured in the 2:1 MMR of a migrating Jupiter analogue around a white dwarf. The bottom panel shows the semi-major axis evolution of the planet in thick, solid orange, the MMR in thick, purple dashed and the planetesimal in a thin, grey line. The planetesimal traces the path of the 2:1 MMR for ~ 0.25 Gyr. The top panel highlights the eccentricity evolution of the planetesimal while it is captured in the resonance, where it oscillates between approximately circular and $e = 0.5$ until it is ejected from the resonance and the simulation.

The evolution of small bodies while captured within resonances has been previously studied, although not in the high-eccentricity context considered in this work. Resonances in the Solar System's Main Belt can explain the formation of the Kirkwood gaps through inclination and eccentricity excitations when asteroids fall into chaotic zones [e.g. Wisdom, 1982, 1985, 1987a,b]. Such chaos could be expected in regions where resonances overlap, which can be defined as where the separation between two resonances are smaller than the sum of their half-widths [Chirikov, 1979]. Studies focussed on the tidal evolution of the Uranian satellites similarly find that the effects of nearby resonances can drag satellites into chaotic zones where they may then be ejected [Tittemore and Wisdom, 1990; Dermott et al., 1988].

While in an MMR, the eccentricity of a planetesimal can increase to a sufficient value for the body to enter into a nearby inclination type resonance which causes a rapid increase in inclination and escape from the resonance [Lee and Peale, 2002; Thommes and Lissauer, 2003; Libert and Tsiganis, 2011]. The particular planetesimal displayed in Figure 4.3 however, does not show a corresponding inclination evolution which would suggest this mechanism causes the following ejection.

As planetesimals in our simulations appear to be able to survive for relatively long periods of time inside MMRs, and be dragged closer towards the white dwarf, we then carried out a number of simulations specifically focussed on the 2:1 MMR. Gallardo [2020] and Gallardo et al. [2021] present a semi-analytical model for describing planetary MMRs. The model allows the locations and widths of MMRs to be calculated by evaluating the resonant disturbing function numerically as opposed to using expansions. Using the Gallardo model, we calculated the location and width of the 2:1 resonance and linearly spaced 50 planetesimals across this region.

Figure 4.4 shows the results of such a simulation where the planet was initialised with $a = 2$ au. As before, the solid orange line shows the semi-major axis evolution of the planet and the evolution of the planetesimals is shown in grey. The horizontal shaded region shows the original region populated by planetesimals and the purple region covers the width of the resonance as the planet migrates inwards. Again, the majority of planetesimals are ejected very quickly after the beginning of the simulation. However, two planetesimals located near the centre of the resonance are able to migrate inwards with the planet for at least 0.5 Gyr.

Veras et al. [2023] present detailed resonant stability portraits for asteroids in a single-planet white dwarf system. Their results find that asteroids which are close to the centre of the 2:1 resonance region can spend enough time in the resonance for secular evolution to drive their eccentricities to near-unity while keeping their semi-major axes near constant. This could drive asteroids to Roche crossing orbits and facilitate the delivery of pollutants to the central white dwarf and may highlight the fate of the captured asteroids in our simulations given more simulation time.

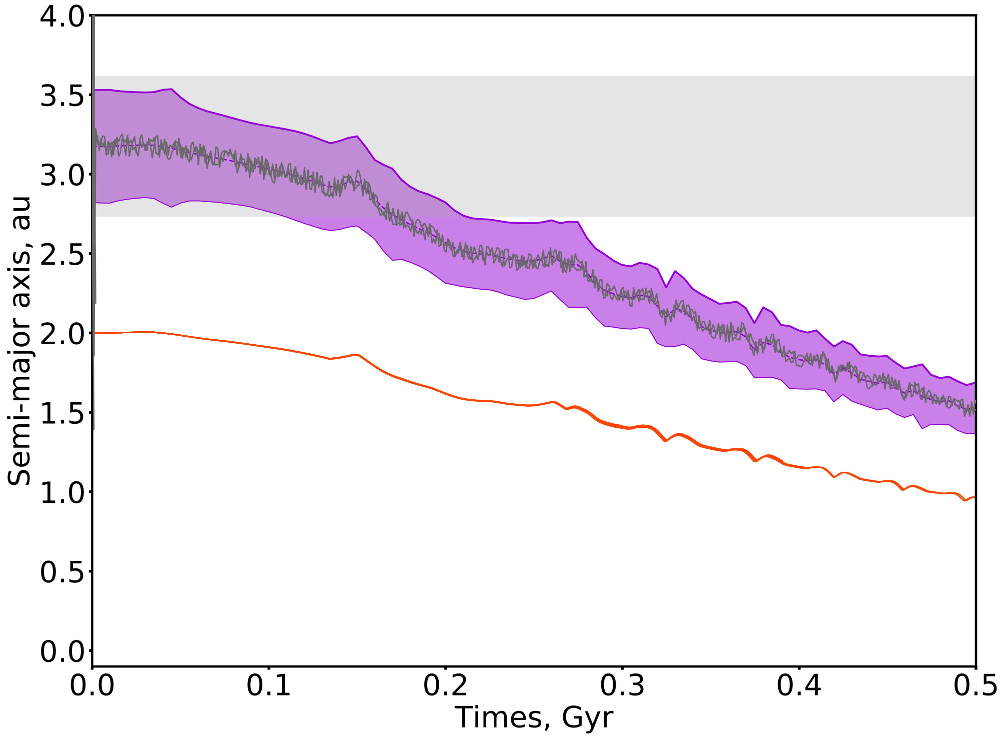

Figure 4.4: Semi-major axis evolution of 50 planetesimal placed across the width of the 2:1 MMR. As before, the planet's semi-major axis is shown by the solid orange line and the planetesimals by the grey lines. The horizontal shaded region shows the original semi-major axis distribution of the planetesimals. The purple shaded region shows how the width and location of the 2:1 MMR evolves as the planet migrates inwards. There are two planetesimals remaining in the 2:1 MMR at the end of the simulated time.

Thus, our simulated planetary systems around white dwarfs suggest that the process of tidal circularisation in post-main-sequence systems efficiently clears out planetesimal reservoirs close to the planet's initial orbit unless the planetesimals are strongly embedded in mean motion resonances. Resonant planetesimals can migrate inwards with the planet and may be more likely to pollute the white dwarf due to secular eccentricity increases. Coupled, these two effects may then explain the unpolluted status of WD 1856 b.

However, it is important to reiterate here that the initial conditions for our simulations are contrived to investigate the effect of planetary migration on planetesimal populations. At the onset of the white dwarf phase of stellar evolution, the planet and planetesimals in our simulations could not be in their starting locations, as they would have undergone dynamical evolution and thermal destruction during the giant branch phases of evolution (Chapter 1.2). We further note that we impose the initial system architecture without taking into account the effect of the initial perturbation that caused the high eccentricity orbit of the giant planet.

Thus, our results are likely not entirely physical and may instead represent the maximal case where planetesimals remain close to the planet's orbit during the white dwarf phase and hence are most drastically affected by the planet's migration. Some further implications for the assumptions we made in the set-up of our simulations are discussed in Section 4.5.

4.4.2 Main Sequence Migration

Given the similarities between main sequence HJs and WD 1856 b, we also investigate the fate of planetesimals alongside a main sequence migrating proto-HJ. These simulations are nearly identical to those discussed in Section 4.4.1, except with changed stellar parameters as described in Table 4.1. Figure 4.5 shows the system's evolution for a Jupiter-mass planet originally at 2 au. The semi-major axis evolution of the Jupiter-mass planet is shown in solid orange, the planetesimals in thin grey, and first order MMRs in dashed purple. Again, the shaded region covers the planetesimals' orbital region between the 2:1 MMR and the planet's apocentre.

As in the white dwarf simulations, the majority of planetesimals are ejected soon after the simulation begins, but here we see a larger number of planetesimals surviving. Again similarly to the white dwarf simulations, a number of planetesimals which begin at the outer edges of the included region migrate outwards and others are temporarily migrated inwards while in resonances. One planetesimal which is initialised near the 3:1 resonance escapes this resonance just before 0.1 Gyr and is then seemingly recaptured by the 4:1 resonance as that resonant width migrates across the planetesimal's location. This planetesimal's semi-major axis jumps upwards slightly due to the passing through of the 5:1 and 6:1 resonances, as is expected for resonant encounters, and briefly migrates inwards one last time with the 7:1 MMR (not shown in the figure), before it finally settles at the approximate initial location of the 2:1 MMR.

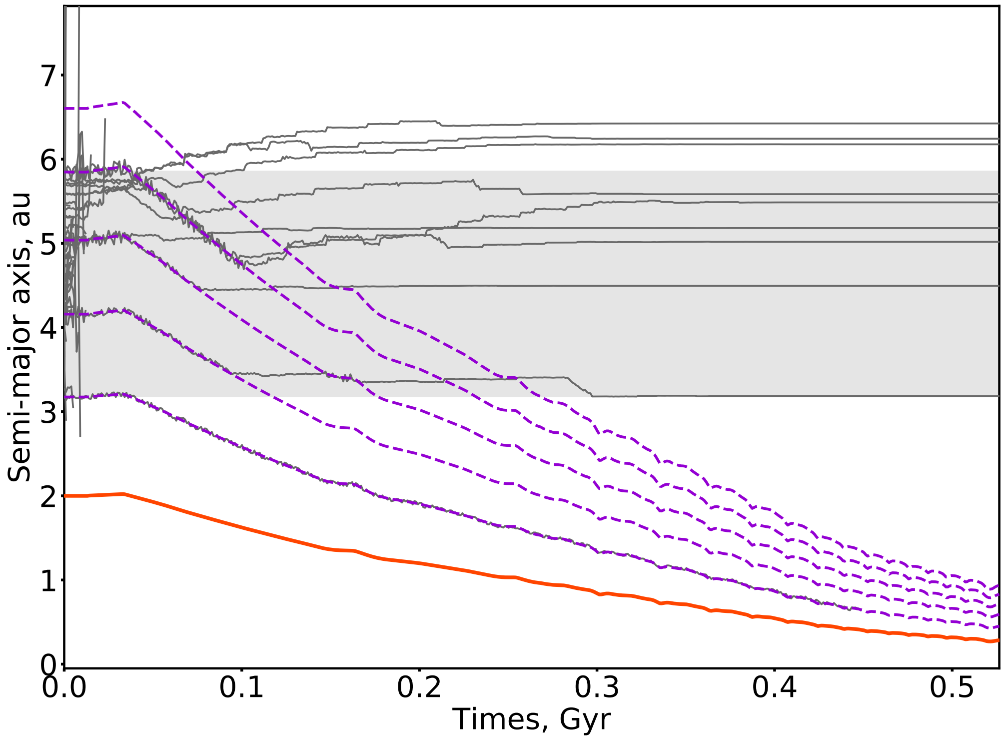

Figure 4.5: Semi-major axis evolution of a Jupiter-mass planet and planetesimals tidally migrating around a Solar-like star. As before, the planet's evolution is shown by a solid orange line, it begins the simulation with a_i = 2 au and reaches a final semi-major axis of a_f = 0.28 au. The location of a number of first order mean motion resonances are shown by dashed purple lines and the planetesimals by thin, grey lines. The horizontal shaded region shows the original semi-major axis distribution of the 50 simulated planetesimals. Again, a number of planetesimals are temporarily captured into MMRs and one can be seen to be caught in multiple resonances as they migrate past the planetesimal.

Figure 4.2 shows the number of planetesimals ejected from all simulations around the Solar-like main sequence star in green, where the different line styles described in the legend represent simulations with varying initial planet semi-major axis. This figure highlights that the majority of planetesimals around main sequence stars are ejected within the first 0.1 Gyr, slightly faster than in white dwarf systems which are shown by the purple lines.

These results suggest that debris discs should be able to persist in main sequence planetary systems with a HJ, although with a depleted mass compared to prior to migration.

4.5 Discussion

Although this work shows promising prospects for explaining the unpolluted nature of WD 1856, there are a number of additional complications and neglected effects which we do not consider.

The first is that our work neglects to consider the initial perturbation that drives the planet to high eccentricities prior to tidal migration. This was chosen, as discussed in Section 4.2, as there are a number of processes which can initially excite the planet's orbit and it is hard to discern which method may have been at play in the WD 1856 system with current observations. Thus, we focussed on the final stage of the process which is less degenerate. However, this means that we assume the planetesimals in our simulations were able to survive the initial perturbation.

We have shown in our simulations that it is possible for planetesimals to survive on orbits which cross the eccentric orbit of the planet, thus it could be possible for planetesimals to survive the initial perturbation too. This would perhaps suggest that the planetesimal reservoirs undergo a two-step clearing process that may deplete them even more than suggested by our simulations. Thus, future work further investigating the effect of the excitation mechanisms on planetesimal reservoirs would help bolster our results.

Our study only consider stars which have convective envelopes, which may not be a valid assumption for extremely hot white dwarfs with small convective zones. Figure 2 of Batygin and Adams [2013] shows that the k_2 value for a fully radiative star can be an order of magnitude smaller than for a convective star, thus the timescales for planet migration will differ around radiative stars. Further, Fuller and Lai [2012] discuss white dwarf dynamical tides in the context of white dwarf binaries and note that the strength of the tides heavily depends on the internal structure of the white dwarf itself. Thus, it is likely that our simulations do not completely cover the possible tidal evolutionary pathways for planets around white dwarfs, which could be further investigated in future work.

Finally, a natural extension of the work presented here would be considering how a migrating giant planet would affect other planet-mass bodies in the system. As the migrating planet may create a gap in the system which is devoid of bodies, this could act as a barrier to allowing planetesimals from the outer system to approach the white dwarf. If the migrating giant planet is also able to drag other planets inwards even on short lifetimes, this may facilitate planetesimal accretion at white dwarfs. Planetesimals are more likely to achieve Roche crossing orbits through multiple encounters with lower mass planets [e.g. Bonsor et al., 2011]. Thus, simultaneously migrating a lower mass planet inwards may act to bridge the dynamical gap which would otherwise form.

Mustill et al. [2015] carry out a number of numerical simulations modelling the tidal migration of a main sequence hot Jupiter with interior terrestrial mass planets. Their results find that the process ends in one of two ways; *i)* all inner planets are ejected from the system or destroyed, or *ii)* the giant planet is ejected and 1-3 inner planets remain. A number of their simulations result in the inner planets colliding with the star, or collisions between the planets producing debris. This may provide an additional possible mechanism for generating white dwarf debris. Thus, further investigating the migration of multiple planets may be of great interest.

Finally, we reiterate that the simulations presented in this Chapter are likely unphysical due to incorrect stellar parameters and overly simplistic tidal migration models used. Thus, before embarking on further avenues of research, more accurate and reasonable simulations will be carried out first.

4.6 Conclusions

Increasing observations of white dwarf systems displaying evidence for planetary material within their atmospheres is driving theoretical work to model dynamical processes to deliver the material. The observation of WD 1856 b as the first intact planet around an unpolluted white dwarf then raises questions about the link between planets and pollution.

In this work, we model the tidal migration of a giant planet around both a main sequence and post-main-sequence star using `REBOUND` N-body simulations to mimic the formation of the WD 1856 b system. We include a number of planetesimals in these simulations to further understand how likely planetesimal reservoirs are to survive the migration process and thus be available to pollute the white dwarf through further dynamical excitation.

Our preliminary results indicate that the migration process is able to largely clear planetesimals, regardless of the planet's initial semi-major axis. The ejected planetesimals contribute to the population of ISOs. A small number of bodies are able to migrate inwards with the planet while in MMRs. This migration can last for fairly long timescales, up to 0.25 Myr for the particular planetesimal in the 2:1 MMR shown in Figure 4.3. As the planetesimals migrate inwards with the resonances, their eccentricities are increased until they are able to escape the resonance and can subsequently be ejected from the planetary system. Planetesimals which are securely embedded in the centre of resonances can migrate inwards alongside the planet for more than 0.5 Gyr as seen in Figure 4.4.

We find that a small number of planetesimals which begin the simulations at the outer edge of the planet's orbit can remain stably in the planetary system, suggesting that planetesimal reservoirs can survive. Although this may open up a dynamical gap in the system which is devoid of bodies and may further prohibit the delivery of planetesimals from the outer system to the white dwarf.

Migrating planets around a Solar-like star may be more efficient at clearing their nearby systems quicker than around a white dwarf, but ultimately they achieve similar levels of clearing. This suggests that HJ main sequence systems may show a lack of observed debris discs.

Carrying out more accurate simulations with self-consistent spin evolution will allow us to make more significant and substantial steps towards considering this important problem. Expanding this work to consider more initial planetesimal belt locations and the effect of a radiative stellar envelope on the tidal process and hence expanding the study to more white dwarfs may help further elucidate the connection between planets and planetesimal pollution at white dwarfs.

Chapter 5

Conclusions

5.1 Thesis Summary

The work presented in this thesis aims to explore the problem of forming white dwarf debris systems through the evolution of planetesimals. Each chapter presents an analytic or numerical study into different aspects of planetesimal system evolution and below I summarise the conclusions of the work.

5.1.1 Reservoirs of Triaxial Planetesimals

Chapter 2 aimed to complement previous theoretical studies of planetesimals in white dwarf systems which have focussed on spherical shape models, by considering the effects of triaxial shape models.

The chapter expands on work originally presented in Brown et al. [2017] which analytically determined the fate of quasi-spherical asteroids approaching a white dwarf on an essentially parabolic orbit. The model considers the mass loss due to sublimation, the tidal forces from the central star and the self-gravitational and strength forces of the planetesimal itself across a grid of circumstellar distances. This allows the precise location of, and type of, destruction (total sublimation, tidal fragmentation or direct impact) faced by the body. The model is presented in a way that an interested reader would be able to determine the exact disruption expected to befall a body of any shape, size and composition.

If purely considering the tidal disruption of a body analytically, then a spherical shape model should be sufficient as all tidal disruption failures occur in the body's largest semi-axis. The more elongated and extended a shape is, the more susceptible the body is to sublimation, due to the extreme ratios between the shape's largest and smallest semi-axes.

The work is further extended to consider the disruption of entire belts of planetesimals to predict the distribution of debris expected around a white dwarf across its lifetime. Across all white dwarf cooling ages, and hence temperatures, the largest bodies are tidally disrupted out to several stellar radii depending on the body's size and material composition.

The produced fragments will continue to disrupt until they reach sizes where the internal strength is sufficient to resist the gravitational forces from the star. This will populate the region interior to the Roche radius with small fragments of planetary material.

Around the hottest white dwarfs, bodies up to 10 m in size can sublimate completely due to stellar radiation. Sublimation reduces in efficiency around cooler stars, where only the smallest cm scale dust grains can sublimate completely. Across all white dwarf temperatures, there is a range of planetesimal sizes which can escape both tidal fragmentation and total sublimation and may impact the atmosphere of the white dwarf directly. The model then predicts that at least initially, a white dwarf debris system will consist of extended gaseous debris discs out to many stellar radii, with a smaller dusty component formed from small rocky fragments of high internal strength at closer orbital distances.

This work motivates future studies to consider the importance of using more realistic shape models. The predicted initial distribution of debris in a white dwarf system presented can also provide needed context to studies which model the further evolution of such systems.

5.1.2 The Role of Binary Planetesimals

Chapter 3 further applies observational knowledge of Solar System planetesimal populations to the problem of white dwarf planetary systems. It is well known that a large number of planetesimals in the Solar System across all populations exist in binary (or higher multiplicity) systems. In particular, the cold classical Kuiper Belt shows a preponderance of near equal-mass binaries, which have likely remained as such since formation. As this orbital region is expected to remain stable and relatively dynamically untouched by the post-main-sequence stages of Solar evolution, the presented study investigates the evolution of equal mass binaries in exo-Kuiper Belts around white dwarfs.

The study presents N-body simulations which model binary asteroid systems being gravitationally scattered by planets. The results suggest that asteroid binarity may not have a direct effect on the delivery rate of planetesimals to white dwarfs, as the majority of planetesimals in systems with giant planets are ejected. For systems with Earth-mass planets, less planetesimals are ejected, but binarity still has little impact on possible accretion events.

The high level of planetesimal ejections suggest that asteroid binarity could have an effect on the production rate of interstellar asteroids, thus contributing to the population of ’Oumuamua-like objects. All planetesimals which are ejected are gravitationally unbound, thus a population of interstellar binary asteroids is not expected.

Once the binary systems are unbound, it is possible for the components’ orbits to become so dissociated that their evolution diverges across large timescales. Dissociated components can be ejected from the system separately across Myr. Thus, binary planetesimals can persist in the system for much longer then single body counterparts, increasing the chances for further perturbations and subsequent accretion.

In simulations containing lower mass planets, binaries which are dissociated and not ejected from the system change the orbital distribution throughout the system. This can populate new regions of the system with planetesimals which may then undergo further perturbations driving them towards the white dwarf.

A very recent study which investigated the effects of secular resonances on binary asteroids around white dwarfs similarly found that binaries have a negligible effect on the accretion rate of white dwarfs [Jin et al., 2023]. Two studies on the effect of asteroid binarity in short succession highlight the need for further work in this area. Of particular importance is studies investigating the effect of giant branch stellar evolution on binary asteroids. The increase in luminosity on the giant branches could cause the orbit of the binary to change drastically due to the binary YORP effect. Thus understanding how the distribution of binaries may change across the giant branches will help improve further studies of them in white dwarf systems.

5.1.3 Planetesimals Under Migration

Chapter 4 investigates how planetesimals react when they are close to a planet which is tidally migrating. This was motivated by the discovery of WD 1856 b, a giant planet orbiting around an unpolluted white dwarf with an orbit similar to main sequence hot Jupiters. The fact that WD 1856 b likely migrated to its close-in orbit after the star became a white dwarf, suggests that the system has undergone an intense dynamical instability. As we typically think that planetesimals are perturbed towards white dwarfs through interactions with planets, the question is then why WD 1856 is not polluted with asteroidal material.

Thus, the chapter presents preliminary results from N-body simulations tidally migrating a giant planet towards a hot Jupiter-like orbit alongside a population of planetesimals exterior to the planet. The goal was to determine if planetesimals are able to survive the planet's dynamical evolution and hence still be able to pollute the white dwarf, or if they are effectively cleared from the system.

The results indicate that the tidally migrating planet ejects the majority of planetesimals within the orbital region most influenced by the planet. Across all simulations with varying initial planet semi-major axis, $80-90$ per cent of planetesimals are ejected. A small number of planetesimals are able to be strongly captured in mean motion resonances and migrate inwards with the planet. Planetesimals which escape the resonances subsequently evolve in one of two ways.

The first is that the planetesimal continues evolving at the semi-axis at which it escaped. If the planetesimal then encounters another resonance as it migrates inwards, it has a chance to be captured again and migrated further. This can happen a number of times for a single planetesimal and the process occurs more often with resonances further from the planet. Alternatively, if the planetesimal is captured in the resonance for a long period of time, then the eccentricity of the planetesimal can increase and subsequently cause the planetesimal to be ejected from the simulation. Specific simulations targeting planetesimals in the 2:1 MMR find that planetesimals which are strongly captured in the resonance are able to migrate inwards with the planet for upwards of 0.5 Gyr.

Thus, migrating planetesimals are able to move into regions which have already been cleared by the migrating planet. This can act to dynamically bridge the gap between the inner planetary regions and more distance planetesimal populations. If resonant capture migration is also efficient for low-mass planets, this could improve the prospects for planetesimal pollution. Secondly, if planetesimals are able to be dragged very far towards the star while trapped in resonances, then the inner system will be directly populated with planetesimals which may make pollution more likely through additional perturbations.

The simulations suggest that it is unlikely for white dwarfs to be polluted with planetesimals through interactions with a migrating planet directly. Further, simulations which consider a process forming a main sequence hot Jupiter system find a similar level of planetesimal clearing, albeit on slightly faster timescales.

This work will be supplemented by more accurate simulations computed using the `REBOUNDx` module `tides_spin` [Lu et al., 2023], which self-consistently considers spin, tidal and dynamical evolution and so should provide a substantial improvement over the preliminary results presented in Chapter 4. The work could be expanded further by considering stars with radiative envelopes as opposed to convective as discussed in Chapter 4, sampling a greater range of initial planetesimal belt locations and considering the effect on other planetary bodies.

5.2 Future Prospects

Although the work presented in this thesis has added to the theoretical literature examining the delivery of planetary material to white dwarfs, there are still many open questions and areas to advance the study of post-main-sequence planetary system science. In the following section I outline some of the advancements expected, or needed, in the field in the coming years.

5.2.1 Observational Advances

At the beginning of my PhD studies, there was only one confirmed transiting white dwarf debris system. Just four years later, there is now two intact giant planets, one evaporating ice giant, four confirmed transiting planetary debris systems and initial observations hinting at four more (Chapter 1.3.2). Similarly, the known populations of dusty and gaseous debris discs around white dwarfs have massively increased in the last few years [e.g. Melis et al., 2020; Dennihy et al., 2020; Gentile Fusillo et al., 2021]. The number of known white dwarfs themselves has increased by a factor of eight thanks to *Gaia* DR2 [Gentile Fusillo et al., 2019]. Upcoming data releases from large surveys such as *Gaia*, SDSS, DESI and LSST will increase these numbers even further. At least 8 upcoming programs with the James Webb Space Telescope (JWST) will target white dwarf planetary systems and provide previously unknown details which will allow us to characterize these systems further.

Fantin et al. [2020] predict the total population of galactic white dwarfs will increase by 150 million in the first ten years of the Legacy Survey of Space and Time (LSST) and combining this data with observations from space telescopes such as Euclid or the Roman Space Telescope will allow the detection of many more debris disc systems. Additionally, Cortés and Kipping [2019] predict that between $50-4000$ transit signatures detected at white dwarfs will be found for orbiting bodies in the size range of Ceres to Earth with LSST.

Future data releases from the *Gaia* mission are expected to contain astrometric data so precise that we will be able to detect tens of planets on wider orbits around white dwarfs [Perryman et al., 2014; Sanderson et al., 2022]. Finally, the Laser Interferometer Space Antenna (LISA) may be able to detect planets around double white dwarf binaries [Danielski et al., 2019; Tamanini and Danielski, 2019].

These huge expected increases in the number of observed white dwarf planetary systems, will no doubt provide a wealth of interesting systems requiring dedicated dynamical modelling.

5.2.2 Theoretical Advances

Alongside the specific advancements to the work presented in Chapters 2-4, there are a number of other avenues for future exploration. Below, I non-exhaustively outline a few areas of interest.

The majority of white dwarfs we currently observe formed from main sequence stars more massive than the main sequence exoplanetary hosts we observe. Due to this observational limit, theoretical work modelling planet formation has primarily considered lower-mass main sequence stars. Understanding how planet formation might differ around higher mass stars is vital to understanding white dwarf planetary systems. The processes of planet formation around high mass stars was investigated by Veras et al. [2020c], but more dedicated studies will allow us to improve our understanding of initial conditions for white dwarf planetary systems.

Advancements in the understanding of planetary atmospheres being driven by high resolution transmission spectroscopy and upcoming science from JWST may allow us to more precisely identify accreted planetary material as in Gänsicke et al. [2019]. Similarly, increased efforts to model the interiors of planets and planetesimals as they form will allow improved characterization of pollution progenitors. This may elucidate differences in chemistry between the Solar System and exoplanetary systems.

Increased dynamical modelling may be able to answer outstanding questions related to specific debris systems such as that around WD 1054-226 which shows near continuous debris transits [Farihi et al., 2022]. The predominant 25.02 hour period is accompanied by a secondary periodicity occurring every 23.1 minutes. Current theories struggle to explain the coexistence of these two periods but future work may be able to accurately model and explain the system.

Finally, a number of recent studies have begun to examine the possibility of habitable planets around white dwarfs. Investigations into the location of the habitable zone (HZ) around white dwarfs suggest that it is very close to the star and may potentially be in the orbital range where planets could be observed through transits with LSST [Agol, 2011]. The HZ is expected to vary for planets which are subjected to tidal heating from the central star and so may be affected by properties outside of the stellar radiation alone [Becker et al., 2023]. Kozakis et al. [2018] discuss the atmospheric conditions of Earth-like planets orbiting in the white dwarf HZ and further discuss the prospects of characterizing such atmospheres with high resolution transmission spectroscopy in Kozakis et al. [2020]. Future observations of such HZ planets may directly test these predictions and drive further studies.

The rapidly expanding and diversifying field of post-main-sequence planetary system science will continue to elucidate the future fate of the Solar System and other more distant worlds.

Bibliography

Adamów, M., Niedzielski, A., Villaver, E., Nowak, G., and Wolszczan, A. *ApJL*, 754:L15, 2012.

Adams, F. C. and Shu, F. *ApJ*, 308:836–853, 1986.

Agnor, C. B. and Hamilton, D. P. *Nature*, 441(7090):192–194, 2006.

Agol, E. *ApJL*, 731:L31, 2011.

Alcock, C., Fristrom, C. C., and Siegelman, R. *ApJ*, 302:462, 1986.

Alexander, M. E. *Astrophys. Space Sci.*, 23:459–510, 1973.

Allen, R. L., Bernstein, G. M., and Malhotra, R. *ApJ*, 549:L241–L244, 2001.

Althaus, L. G., Córsico, A. H., Isern, J., and Gardía-Berro, E. *A&ARv*, 18:471–566, 2010.

Antoniadou, K. I. and Veras, D. *A&A*, 629:A126, 2019.

Araujo, R. A. N., Galiazzo, M. A., Winter, O. C., and Sfair, R. *MNRAS*, 476:5323–5331, 2018.

Baronett, S. A., Ferich, N., Tamayo, D., and Steffen, J. H. *MNRAS*, 510:6001–6009, 2022.

Barrientos, M. and Chanamé, J. *ApJ*, 923:181, 2021.

Baruteau, C., Crida, A., Paardekopoper, S. J., Masset, F., Guilet, J., Bitsch, B., Nelson, R., Kley, W., and Papaloizou, J. Planet-Disk Interactions and Early Evolution of Planetary Systems. In Beuther, H., Klessan, R. S., Dullemond, C. P., and Henning, T., editors, *Protostars and Planets VI*, pages 667–689, 2014.

Batygin, K. and Adams, F. C. *ApJ*, 778:169, 2013.

Bauer, E. B. and Bildsten, L. *ApJL*, 859:L19, 2018.

Bauer, E. B. and Bildsten, L. *ApJ*, 872:96, 2019.

Bear, E. and Soker, N. *New Astron.*, 19:56–61, 2013.

Bear, E. and Soker, N. *MNRAS*, 450:4233–4239, 2015.

Becker, J., Seligman, D. Z., Adams, F. C., and Styczinski, M. J. *ApJL*, 945:L24, 2023.

Becker, J. C. and Batygin, K. *ApJ*, 778:100, 2013.

Becklin, E. E., Farihi, J., Jura, M., Song, I., Weinberger, A. J., and Zuckerman, B. *ApJL*, 632:L119–L122, 2005.

Behrend, R., Bernasconi, L., Roy, R., Klotz, A., Colas, F., Antonini, P., Aoun, R., Augustesen, K., Barbotin, E., Berger, N., Berrouachdi, H., Brochard, E., Cazenave, A., Cavadore, C., Coloma, J., Cotrez, V., Deconihout, S., Demeautis, C., Dorseuil, J., Dubos, G., Durkee, R., Frappa, E., Hormuth, F., Itkonen, T., Jacques, C., Kurtze, L., Laffont, A., Lavayssière, M., Lecacheux, J., Leroy, A., Manzini, F., Masi, G., Matter, D., Michelsen, R., Nomen, J., Oksanen, A., Pääkkönen, P., Peyrot, A., Pimentel, E., Pray, D., Rinner, C., Sanchez, S., Sonnenberg, K., Sposetti, S., Starkey, D., Stoss, R., Teng, J. P., Vignand, M., and Waelchli, N. *A&A*, 446:1177–1184, 2006.

Behrisch, R. and Eckstein, W., editors. *Sputtering by Particle Bombardment*, 2007.

Benecchi, S. D., Borncamp, D., Parker, A., Buie, M. W., Noll, K. S., Binzel, R. P., Stern, S. A., Verbiscer, A. J., Kavelaars, J. J., Zangari, A. M., Spencer, J. R., and Weaver, H. A. *Icarus*, 334:22–29, 2019.

Benner, L. A. M., Nolan, M. C., Ostro, S. J., Giorgini, J. D., Pray, D. P., Harris, A. W., Magri, C., and Margot, J.-L. *Icarus*, 182:474–481, 2006.

Blackman, J. W., Beaulieu, J. P., Bennett, D. P., Danielski, C., Alard, C., Cole, A. A., Vandorou, A., Ranc, C., Terry, S. K., Bhattacharya, A., Bond, I., Bachelet, E., Veras, D., Koshimoto, N., Batista, V., and Marquette, J. B. *Nature*, 598:272–275, 2021.

Bolmont, E., Raymond, S. N., Leconte, J., Hersant, F., and Correia, A. C. M. *A&A*, 583: A116, 2015.

Bonsor, A. and Wyatt, M. *MNRAS*, 409:1631–1646, 2010.

Bonsor, A., Mustill, A. J., and Wyatt, M. C. *MNRAS*, 414:930–939, 2011.

Bonsor, A., Kennedy, G. M., Crepp, J. R., Johnson, J. A., Wyatt, M. C., Sibthorpe, B., and Su, K. Y. L. *MNRAS*, 431:3025–3035, 2013.

Bonsor, A., Kennedy, G. M., Wyatt, M. C., Johnson, J. A., and Sibthorpe, B. *MNRAS*, 437: 3288–3297, 2014.

Bonsor, A., Farihi, J., Wyatt, M. C., and van Lieshout, R. *MNRAS*, 468:154–164, 2017.

Bonsor, A., Carter, P. J., Hollands, M., Gänsicke, B. T., Leinhardt, Z., and Harrison, J. H. D. *MNRAS*, 492:2683–2697, 2020.

Bonsor, A., Lichtenberg, T., Drążkowska, J., and Buchan, A. M. *Nature Astron.*, 7:39–48, 2023.

Borucki, W. J., Koch, D., Basri, G., Batalha, N., Brown, T., Caldwell, D., Caldwell, J., Christensen-Dalsgaard, J., Cochran, W. D., DeVore, E., Dunham, E. W., Dupree, A. K., Gautier, T. N., Geary, J. C., Gilliland, R., Gould, A., Howell, S. B., Jenkins, J. M., Kondo, Y., Latham, D. W., Marcy, G. W., Meibom, S., Kjeldsen, H., Lissauer, J. J., Monet, D. G., Morrison, D., Sasselov, D., Tarter, J., Boss, A., Brownlee, D., Owen, T., Buzasi, D., Charbonneau, D., Doyle, L., Fortney, J., Ford, E. B., Holman, M. J., Seager, S., Steffen, J. H., Welsh, W. F., Rowe, J., Anderson, H., Buchhave, L., Ciardi, D., Walkowicz, L., Sherry, W., Horch, E., Isaacson, H., Everett, M. E., Fischer, D., Torres, G., Johnson, J. A., Endl, M., MacQueen, P., Bryson, S. T., Dotson, J., Haas, M., Kolodziejczak, J., Van Cleve, J., Chandrasekaran, H., Twicken, J. D., Quintana, E. V., Clarke, B. D., Allen, C., Li, J., Wu, H., Tenenbaum, P., Verner, E., Bruhweiler, F., Barnes, J., and Prsa, A. *Science*, 327:977, 2010.

Brasser, R., Duncan, M. J., and Levison, H. F. *Icarus*, 184:59–82, 2006.

Brouwers, M. G., Bonsor, A., and Malamud, U. *MNRAS*, 509:2404–2422, 2022.

Brouwers, M. G., Bonsor, A., and Malamud, U. *MNRAS*, 519:2646–2662, 2023a.

Brouwers, M. G., Buchan, A. M., Bonsor, A., Malamud, U., Lynch, E., Rogers, L., and Koester, D. *MNRAS*, 519:2663–2679, 2023b.

Brown, J., Potts, H., Porter, L., and Le Chat, G. *A&A*, 535:1–12, 2011.

Brown, J., Carlson, R., and Toner, M. *ApJ*, 807:165, 2015.

Brown, J. C., Veras, D., and Gänsicke, B. T. *MNRAS*, 468:1575–593, 2017.

Brown, J. M., Garaud, P., and Stellmach, S. *ApJ*, 768:34, 2013.

Buchan, a. M., Bonsor, A., Shorttle, O., Wade, J., Harrison, J., Noack, L., and Koester, D. *MNRAS*, 510:3512–3530, 2022.

Caiazzo, I. and Heyl, J. S. *MNRAS*, 469:2750–2759, 2017.

Carbognani, A., Tanga, P., Cellino, A., Delbo, M., Mottola, S., and Marchese, E. *Planet. Space Sci.*, 73:80–85, 2012.

Carroll, B. W. and Ostlie, D. A. *An Introduction to Modern Astrophysics*. Pearson Education, 2nd edition, 2013.

Carry, B. *Planet. Space Sci.*, 73:98–118, 2012.

Chamandy, L., Blackman, E. G., Frank, A., Carrol-Nellenback, J., and Tu, Y. *MNRAS*, 495: 4028–4039, 2020.

Chamandy, L., Blackman, E. G., Nordhaus, J., and Wilson, E. *MNRAS Lett.*, 502:L110–L114, 2021.

Chang, C. K., Yeh, T. S., Tan, H., Ip, W. H., Kelley, M. S. P., Ye, Q., Lin, Z. Y., Ngeow, C. C., Bolin, B. T., Prince, T. A., Bellm, E. C., Dekany, R., Duev, D. A., Graham, M., and Zwicky Transient Facility Collaboration. *apJL*, 932:L5, 2022.

Chatterjee, S., Ford, E. B., Matsumura, S., and Rasio, F. A. *ApJ*, 686:580–602, 2008.

Chayer, P., Fontaine, G., and Wesemael, F. *ApJS*, 99:189, 1995.

Chiang, E. and Goldreich, P. *ApJ*, 490:368–376, 1997.

Chiang, E. I., Fischer, D., and Thommes, E. *ApJL*, 564:L105–L109, 2002.

Chirikov, B. V. *Phys. Rep.*, 52:263–379, 1979.

Chyba, C. F., Thomas, P. J., and Zahnle, K. J. *Nature*, 361:40–44, 1993.

Cortés, J. and Kipping, D. *MNRAS*, 488:1695–1703, 2019.

Coutu, S., Dufour, P., Bergeron, P., Blouin, S., Loranger, E., Allard, N. F., and H., D. B. *ApJ*, 886, 2019.

Croll, B., Dalba, P. A., Vanderburg, A., Eastman, J., Rappaport, S., DeVore, J., Bieryla, A., Muirhead, P. S., Han, E., Latham, D. W., Beatty, T. G., Wittenmyer, R. A., Wright, J. T., Johnson, J. A., and McCrady, N. *ApJ*, 836:82, 2017.

Csizmadia, S., Hellard, H., and Smith, A. M. S. *A&A*, 623:A45, 2018.

Cummings, J. D., Kalirai, J. S., Tremblay, P.-E., Ramirez-Ruiz, E., and Choi, J. *ApJ*, 866: 21, 2018.

Cunningham, T., Tremblay, P. E., Freytag, B., Ludwig, H. G., and Koester, D. *MNRAS*, 488: 2503–2522, 2019.

Cunningham, T., Tremblay, P.-E., Bauer, E. B., Toloza, O., Cukanovaite, E., Koester, D., Farihi, J., Freytag, B., Gänsicke, B. T., Ludwig, H.-G., and Veras, D. *MNRAS*, 503: 1646–1667, 2021.

Danielski, C., Korol, V., Tamanini, N., and Rossi, E. M. *A&A*, 632:A113, 2019.

Darwin, G. H. *Philos. Trans. R. Soc. Lond.*, 170:1–35, 1879.

Davidsson, B. J. R. *Icarus*, 142:525–535, 1999.

Davidsson, B. J. R. *Icarus*, 149:375–383, 2001.

Davies, M. B., Adams, F. C., Armitage, P., Chambers, J., Ford, E., Morbidelli, A., Raymond, S. N., and Veras, D. The Long-Term Dynamical Evolution of Planetary Systems. In Beuther, H., Klessen, R. S., Dullemond, C. P., and Henning, T., editors, *Protostars and Planets VI*, pages 787–808, 2014.

Dawson, R. I. and Johnson, J. A. *ARA&A*, 56:175–221, 2018.

de la Fuente Marcos, C., de la Fuente Marcos, R., and Aarseth, S. J. *Ap&SS*, 362:198, 2017.

Deal, M., Deheuvels, S., Vauclair, G., Vauclair, S., and Wachlin, F. C. *A&A*, 557:L12, 2013.

Debes, J., Walsh, K., and Stark, C. *ApJ*, 747:9, 2012.

Debes, J. H. and Sigurdsson, S. *ApJ*, 572:556–565, 2002.

Dennihy, E., Xu, S., Lai, S., Bonsor, A., Clemens, J. C., Dufour, P., Gänsicke, B. T., Gentile Fusillo, N. P., Hardy, F., Hegedus, R. J., Hermes, J. J., Kaiser, B. C., Kissler-PAtig, N., Klein, B., Manser, C. J., and Reding, J. S. *ApJ*, 905:5, 2020.

Dermott, S. F., Malhotra, R., and Murray, C. D. *Icarus*, 76:295–334, 1988.

Dobrovolskis, A. R. *Icarus*, 321:891–928, 2019.

Dohnanyi, J. S. *J. Geophys. Res.*, 74:2531–2554, 1969.

Donnison, J. R. *MNRAS*, 415:470–486, 2011.

Doyle, A. E., Young, E. D., Klein, B., Zuckerman, B., and Schlichting, H. E. *Science*, 366: 356–359, 2019.

Doyle, A. E., Desch, S. J., and Young, E. D. *ApJL*, 907:L35, 2021.

Duncan, M., Quinn, T., and Tremaine, S. *AJ*, 94:1330, 1987.

Ďurech, J., Hanuš, J., Brož, M., Lehký, M., Behrend, R., Antonini, P., Charbonnel, S., Crippa, R., Dubreuil, P., Farroni, G., et al. *Icarus*, 304:101–109, 2018.

Duvvuri, G. M., Redfield, S., and Veras, D. *ApJ*, 893:166, 2020.

Eggleton, P. P., Kiseleva, L. G., and Hut, P. *ApJ*, pages 853–870, 1998.

El-Badry, K., Rix, H.-W., and Weisz, D. R. *ApJL*, 860(2):L17, 2018.

Faedi, F., West, R. G., Burleigh, M. R., Goad, M. R., and Hebb, L. Detection Limits for Close Eclipsing and transiting Sub-Stellar and Planetary Companions to White Dwarfs in the WASP Survey. In Schuh, S., Drechsel, H., and Heber, U., editors, *Planetary Systems Beyond the Main Sequence*, volume 1331 of *American Institute of Physics Conference Series*, pages 254–261, 2011.

Fang, J. and Margot, J.-L. *AJ*, 143:25, 2012.

Fantin, N. J., Côté, P., and McConnachie, A. W. *ApJ*, 900:139, 2020.

Farihi, J. *New Astron. Rev.*, 71:9–34, 2016.

Farihi, J., Zuckerman, B., and Becklin, E. E. *ApJ*, 674:431–446, 2008.

Farihi, J., Barstow, M. A., Redfield, S., Dufour, P., and Hambly, N. C. *MNRAS*, 404: 2123–2135, 2010.

Farihi, J., Gänsicke, B., and Koester, D. *Science*, 342:218–220, 2013.

Farihi, J., von Hippel, T., and Pringle, J. E. *MNRAS*, 471:L145–L149, 2017.

Farihi, J., van Lieshout, R., Cauley, P. W., Dennihy, E., Su, K. Y. L., Kenyon, S. J., Wilson, T. G., Toloza, O., Gänsicke, B. T., von Hippel, T., et al. *MNRAS*, 481:2601–2611, 2018.

Farihi, J., Hermes, J. J., Marsh, T. R., Mustill, A. J., Wyatt, M. C., Guidry, J. A., Wilson, T. G., Redfield, S., Izquierdo, P., Toloza, O., Gänsicke, B. T., Aungwerojwit, A., Dhillon, V. S., and Swan, A. *MNRAS*, 511:1647–1666, 2022.

Fellay, L., Pezzotti, C., Buldgen, P., G. and Eddenberger, and Bolmont, E. *A&A*, 669:A2, 2023.

Fontaine, G., Villeneuve, B., Wesemael, F., and Wegner, G. *ApJL*, 277:L61–L64, 1984.

Fontaine, G., Brassard, P., and Bergeron, P. *PASP*, 113:409–435, 2001.

Fontaine, G., Brassard, P., Charpinet, S., Randall, S. K., and Van Grootel, V. White Dwarf Stars: A Brief Overview. In Shibahashi, H. and Lynas-Gray, A. E., editors, *Progress in Physics of the Sun and Stars: A New Era in Helio- and Asteroseismology. Proceedings of a Fujihara Seminar held 25-29 Novemeber, 2012, in Hakone, Japan.*, volume 479 of *ASP Conference Proceedings*, page 211, San Francisco, 2013. Astronomical Society of the Pacific.

Ford, E. B. and Rasio, F. A. *ApJL*, 638:L45–L48, 2006.

Fouchard, M., Rickman, H., Foreschlé, C., and Valsecchi, G. B. *Icarus*, 231:110–121, 2014.

Fraser, W. C., Bannister, M. T., Pike, R. E., Marsset, M., Schwamb, M. E., Kavelaars, J. J., Lacerda, P., Nevorny, D., Volk, K., Delsanti, A., Benecchi, S., Lehner, M. J., Noll, K., Gladman, B., Petit, J.-M., Gwyn, S., Chen, Y.-T., Wang, S.-Y., Alexandersen, M., Burdullis, T., Sheppard, S., and Trujillo, C. *Nature Astron.*, 1, 2017.

Frewen, S. F. N. and Hansen, B. M. S. *MNRAS*, 439:2442–2458, 2014.

Freytag, B., Ludwig, H. G., and Steffen, M. *A&A*, 313:497–516, 1996.

Froeschlé, C., Gonczi, R., and Lega, E. *Planet. Space Sci.*, 45:881–886, 1997a.

Froeschlé, C., Lega, E., and Gonczi, R. *Celest. Mech. Dyn. Astron.*, 67:41–62, 1997b.

Fuller, J. and Lai, D. *MNRAS*, 421:426–445, 2012.

Fulton, B. J., Tonry, J. L., Flewelling, H., Burgett, W. S., Chambers, K. C., Hodapp, K. W., Huber, M. E., Kaiser, N., Wainscoat, R. J., and Waters, C. *ApJ*, 796:114, 2014.

Gallardo, T. *Clest. Mech. Dyn. Astron.*, 132:9, 2020.

Gallardo, T., Beaugè, C., and Giuppone, C. A. *A&A*, 646:A148, 2021.

Gänsicke, B. T., Marsh, T. R., Southworth, J., and Rebassa-Mansergas, A. *Science*, 314: 1908–1910, 2006.

Gänsicke, B. T., Aungwerojwit, A., Marsh, T. R., Dhillon, V. S., Sahman, D. I., Veras, D., Farihi, J., Chote, P., Ashley, R., Arjyotha, S., Rattanasoon, S., Littlefair, S. P., Pollacco, D., and Burleigh, M. R. *ApJ*, 818:L7, 2016.

Gänsicke, B. T., Schreiber, M. R., Toloza, O., Gentile Fusillo, N. P., Koester, D., and Manser, C. J. *Nature*, 576:61–64, 2019.

Gary, B. L., Rappaport, S., Kaye, T. G., Alonso, R., and Hambschs, F. J. *MNRAS*, 465: 3267–3280, 2017.

Gautier, I., T. N., Rieke, G. H., Stansberry, J., Bryden, G. C., Stapelfeldy, K. R., Werner, M. W., Beichman, C. A., Chen, C., Su, K., Trilling, D., Patten, B. M., and Roellig, T. L. *ApJ*, 667:527–536, 2007.

Gentile Fusillo, N. P., Gänsicke, B. T., Farihi, J., Koester, D., Schreiber, M. R., and Pala, A. F. *MNRAS*, 468:971–980, 2017.

Gentile Fusillo, N. P., Tremblay, P. E., Gänsicke, B. T., Manser, C. J., Cunningham, T., Cukanovaite, E., Hollands, M., Marsh, T., Raddi, R., Jordan, S., Toonen, S., Geier, S., Barstow, M., and Cummings, J. D. *MNRAS*, 482:4570–4591, 2019.

Gentile Fusillo, N. P., Manser, C. J., Gänsicke, B. T., Toloza, O., Koester, D., Dennihy, E., Brown, W. R., Farihi, J., Hollands, M. A., Hoskin, M. J., Izquierdo, P., Kinnear, T., Marsh, T. R., Santamaría-Miranda, A., Pala, A. F., Redfield, S., Rodríguez-Gil, P., Schreiber, M. R., Veras, D., and Wilson, D. J. *MNRAS*, 504:2707–2726, 2021.

Gianninas, A., Dufour, P., and Bergeron, P. *ApJL*, 617:L57–L60, 2004.

Girven, J., Brinkworth, C. S., Farihi, J., Gänsicke, B. T., Hoard, D. W., Marsh, T. R., and Koester, D. *ApJ*, 749:154, 2012.

Goldreich, P. and Tremaine, S. *ApJ*, 241:425–441, 1980.

Greenberg, J., Mizuyani, H., and Yamamoto, T. *A&A*, 295:L35–L38, 1995.

Grishin, E. and Veras, D. *MNRAS*, 489:168–175, 2019.

Groussin, O., Jorda, L., Auger, A., Kührt, E., Gaskell, R., Capanna, C., Scholten, F., Preusker, F., and Lamy, P. *A&A*, 583:A32, 2015.

Grunblatt, S. K., Huber, D., Gaidos, E., Lopez, E. D., Barclay, T., Chontos, A., Sinukoff, E., Van Eylen, V., Howard, A. W., and Isaacson, H. T. *ApJL*, 861:L5, 2018.

Grunblatt, S. K., Huber, D., Gaidos, E., Hon, M., Zinn, J. C., and Stello, D. *AJ*, 158:227, 2019.

Grunblatt, S. K., Saunders, N., Chontos, A., Hattori, S., Veras, D., Huber, D., Angus, R., Rice, M., Breivik, K., Blunt, S., Giacalone, S., Lubin, J., Isaacson, H., Howard, A. W., Ciardi, D. R., Safonov, B. S., Strakhov, I. A., Latham, D. W., Bieryla, A., Ricker, G. R., Jenkins, J. M., Tenenbaum, P., Shroper, A., Morgan, E. H., Kostov, V., Osborn, H. P., Dragomir, D., Searger, S., Vanderspek, R. K., and Winn, J. N. *AJ*, 165:44, 2023.

Guidry, J. A., Vanderbosch, Z. P., Hermes, J. J., Barlow, B. N., Lopez, I. D., M., B. T., Corcoran, K. A., Bell, K. J., Montgomery, M. H., Heintz, T. M., Castanheira, B. G., Reding, J. S., Dunlap, B. H., Winget, D. E., Winget, K. I., and Kuehne, J. W. *ApJ*, 912: 125, 2021.

Gurri, P., Veras, D., and Gänsicke, B. *MNRAS*, 464:321–328, 2017.

Guzik, P., Drahus, M., Rusek, K., Waniak, W., Cannizzaro, G., and Pastor-Marazuela, I. *Nature Astron.*, 4:53–57, 2020.

Hamada, T. and Salpeter, E. E. *ApJ*, 134:683, 1961.

Hamers, A. S. and Portegies Zwart, S. F. *MNRAS Lett.*, 462:L84–L87, 2016.

Hamers, A. S., Antonini, F., Lithwick, Y., Perets, H. B., and Portegies Zwart, S. F. *MNRAS*, 464:688–701, 2017.

Hansen, B. and Zuckerman, B. *Res. Notes Am. Astron. Soc.*, 1:55, 2017.

Harris, A. *EM&P*, 72:113–117, 1996.

Harrison, J. H. D., Bonsor, A., and Madhusudhan, N. *MNRAS*, 479:3814–3841, 2018.

Harrison, J. H. D., Bonsor, A., Kama, M., Buchan, A. M., Blouin, S., and Koester, D. *MNRAS*, 504:2853–2867, 2021a.

Harrison, J. H. D., Shorttle, O., and Bonsor, A. *Earth Planet. Sci. Lett.*, 554:116694, 2021b.

Henry, G. W., Marcy, G. W., Butler, R. P., and Vogt, S. S. *ApJL*, 529:L41–L44, 2000.

Hestroffer, D., Sánchez, P., Staron, L., Bagatin, A. C., Eggl, S., Losert, W., Murdoch, N., Opsomer, E., Radjai, F., Richardson, D. C., Salazar, M., Scheeres, D. J., Schwartz, S., Taberlet, N., and Yano, H. *A&ARv*, 27, 2019.

Hogan, E., Burleigh, M. R., and Clarke, F. J. *MNRAS*, 836:2074–2086, 2009.

Hollands, M., Gänsicke, B., and Koester, D. *MNRAS*, 477:93–111, 2018.

Hollands, M. A., Tremblay, P. E., Gänsicke, B. T., Koester, D., and Gentile-Fusillo, N. P. *Nature Astron.*, 5:451–459, 2021.

Holsapple, K. and Michel, P. *Icarus*, 183:331–348, 2006.

Holsapple, K. A. *Icarus*, 154:432–448, 2001.

Holsapple, K. A. *Icarus*, 172:272–303, 2004.

Hoskin, M. J., Toloza, O., Gänsicke, B. T., Raddi, R., Koester, D., Pala, A., Manser, C. J., Farihi, J., Belmonte, M. T., Hollands, M., Gentile Fusillo, N., and Swan, A. *MNRAS*, 449:171–182, 2020.

Howard, A. W., Marcy, G. W., Bryson, S. T., Jenkins, J. M., Rowe, J. F., Batalha, N. M., Borucki, W. J., Koch, D. G., Dunham, E. W., Gautier, I., T. N., et al. *ApJS*, 201, 2012.

Howell, S. B., Sobeck, C., Haas, M., Still, M., Barclay, T., Mullally, F., Troeltzsch, J., Aigrain, S., Bryson, S. T., Caldwell, D., Chaplin, W. J., Cochran, W. D., Huber, D., Marcy, G. W., Miglio, A., Najita, J. R., Smith, M., Twicken, J. D., and Fortney, J. J. *PASP*, 126:398, 2014.

Hsu, D. C., Ford, E. B., Ragozzine, D., and Ashby, K. *AJ*, 158:109, 2019.

Hut, P. *A&A*, 99:126–140, 1981.

Ivezić, v., Tabachnik, S., Rafikov, R., Lupton, R. H., Quinn, T., Hammergren, M., Eyer, L., Chu, J., Armstrong, J. C., Fan, X., Finlator, K., Geballe, T. R., Gunn, J. E., Hennessy, G. S., Knapp, G. R., Legett, S. K., Munn, J. A., Pier, J. R., Rockosi, C. M., Schneider, D. P., Strauss, M. A., Yanny, B., Brinkmann, J., Csabai, I., Hindsley, R. B., Kent, S., Lamb, D. Q., Margon, B., McKay, T. A., Smith, J. A., Waddel, P., York, D. G., and SDSS Collaboration. *AJ*, 122:2749–2784, 2001.

Izquierdo, P., Rodríguez-Gil, P., Gänsicke, B. T., Mustill, A. J., Toloza, O., Tremblay, P. E., Wyatt, M., Chote, P., Eggl, S., Farihi, J., Koester, D., Lyra, W., Manser, C. J., Marsh, T. R., Pallé, E., Raddi, R., Veras, D., Villaver, E., and Zwart, S. P. *MNRAS*, 481:703–714, 2018.

Izquierdo, P., Toloza, O., Gänsicke, B. T., Rodríguez-Gil, P., Farihi, J., Koester, D., Guo, J., and Redield, S. *MNRAS*, 501:4276–4288, 2021.

Jackson, A. P., Wyatt, M. C., Bonsor, A., and Veras, D. *MNRAS*, 440:3757–3777, 2014.

Jedicke, R. and Metcalfe, T. S. *Icarus*, 131:245–260, 1998.

Jin, Z., Li, D., and Zhu, Z. H. *arXiv:2304.05579*, 2023. arXiv:2304.05579.

Johnson, T. M., Klein, B. L., Koester, D., Melis, C., Zuckerman, B., and Jura, M. *ApJ*, 941: 113, 2022.

Johnston, W. R. Binary Minor Planets Compilation V3.0. NASA Planetary Data System, 2019. URL https://doi.org/10.26033/bb68-pw96.

Jura, M. *ApJ*, 584:L91–L94, 2003.

Jura, M. *AJ*, 135:1785–1792, 2008.

Jura, M. and Young, E. *Annu. Rev. Earth Planet. Sci.*, 42:45–67, 2014.

Jura, M., Farihi, J., and Zuckerman, B. *ApJ*, 663:1285–1290, 2007.

Jura, M., Klein, B., Xu, S., and Young, E. D. *ApJL*, 791:L29, 2014.

Jurić, M. and Tremaine, S. *ApJ*, 686:603–620, 2008.

Kennedy, G. and Kenyon, S. *ApJ*, 673:502–512, 2008.

Kennedy, G. M., Wyatt, M. C., Kalas, P., Duchêne, G., Sibthorpe, B., Lestrade, J. F., Matthews, B. C., and Greaves, J. *MNRAS Lett.*, 438:L96–L100, 2014.

Kenyon, S. and Hartmann, L. *ApJ*, 323:714–733, 1987.

Kenyon, S. J. and Bromley, B. C. *ApJ*, 844(2), 2017a.

Kenyon, S. J. and Bromley, B. C. *ApJ*, 850:50, 2017b.

Kepler, S. O., Pelisoli, I., Koester, D., Ourique, G., Kleinman, S. J., Romero, A. D., Nitta, A., Eisenstein, D. J., Costa, J. E. S., Külebi, B., Jordan, S., Dufour, P., Giommi, P., and Rebassa-Mansergas, A. *MNRAS*, 446:4078–4087, 2015.

Kepler, S. O., Pelisoli, I., Koester, D., Ourique, G., Romero, A. D., Reindle, N., Kleinman, S. J., Eisenstein, D. J., Valois, A. D. M., and Amaral, L. A. *MNRAS*, 455:3413–3423, 2016.

Kilic, M., von Hippel, T., Leggett, S. K., and Winget, D. E. *ApJL*, 632:L115–L118, 2005.

Klein, B. L., Doyle, A. E., Zuckerman, B., Dufour, P., Blouin, S., Melis, C., Weinberger, A. J., and Young, E. D. *ApJ*, 914:61, 2021.

Kleinman, S. J., Kepler, S. O., Koester, D., Pelisoli, I., Peçanha, V., Nitta, A., Costa, J. E. S., Krzesinski, J., Dufour, P., Lachapelle, F. R., Bergeron, P., Yip, C. W., Harris, H. C., Eisenstein, D. J., Althaus, L., and Córsico, A. *ApJS*, 204:14pp, 2013.

Koester, D. *A&A*, 498:517–525, 2009.

Koester, D. White Dwarf Stars. In M. A. Barstow, editor, *Planets, Stars and Stellar Systems, Volume 4: Stellar Structure and Evolution*, pages 559–612. Springer, Dordrecht, 2013.

Koester, D., Weidemann, V., and Zeidler, E. M. *A&A*, 116:147–157, 1982.

Koester, D., Gänsicke, B. T., and Farihi, J. *A&A*, 566:A34, 2014.

Kozai, Y. *AJ*, 67:591–598, 1962.

Kozakis, T., Kaltenegger, L., and Hoard, D. W. *ApJ*, 862:69, 2018.

Kozakis, T., Lin, Z., and Kaltenegger, L. *ApJL*, 894:L6, 2020.

Kudritzki, R. P. and Reimers, D. *A&A*, 70:227–239, 1978.

Lagos, F., Schreiber, M. R., Zorotovic, M., Gänsicke, B. T., Ronco, M. P., and Hamers, A. S. *MNRAS*, 501:676–682, 2021.

Lai, S., Dennihy, E., Xu, S., Nitta, A., Kleinman, S., Legget, S. K., Bonsor, A., Hodgkin, S., Rebassa-Mansergas, A., and Rogers, L. K. *ApJ*, 920:156, 2021.

Lee, M. H. and Peale, S. J. *ApJ*, 567:596–609, 2002.

Lestrade, J. F., Matthews, B. C., Sibthorpe, B., Kennedy, G. M., Wyatt, M. C., Bryden, G., Greaves, J. S., Thilliez, E., Moro-Martin, A., Booth, M., Dent, W. R. F., Duchêne, G., Harvey, P. M., Horner, J., Kalas, P., Kavelaars, J. J., Philips, N. M., Rodriguez, D. R., Su, K. Y. L., and Wilner, D. J. *A&A*, 548:A86, 2012.

Li, D., Mustll, A. J., and Davies, M. B. *ApJ*, 924:61, 2021.

Libert, A. S. and Tsiganis, K. *Cel. Mech. Dyn. Astron.*, 111:201–218, 2011.

Lidov, M. L. *Planet. Space Sci.*, 9:719–759, 1962.

Lin, D. N. C. and Papaloizou, J. *ApJ*, 309:846, 1986.

Lin, D. N. C., Bodenheimer, P., and Richardson, D. C. *Nature*, 380:606–607, 1996.

Lovell, J. B., Wyatt, M. C., Kalas, P., Kennedy, G. M., Marino, S., Bonsor, A., Penoyre, Z., Fulton, B. J., and Pawellek, N. *MNRAS*, 517:2546–2566, 2022.

Lu, T., Rein, H., Tamayo, D., Hadden, S., Mardling, R., Milholland, S., and Laughlin, G. *ApJ*, page 41, 2023.

Luhman, K. L., Burgasser, A. J., and Bochanski, J. J. *ApJL*, 730:L9, 2011.

Luyten, W. J. *PASP*, 34(197):54, 1922.

Makarov, V. V. and Veras, D. *ApJ*, 886:127, 2019.

Malamud, U. and Perets, H. B. *ApJ*, 842:67, 2017.

Malamud, U. and Perets, H. B. *MNRAS*, 492:5561–5581, 2020a.

Malamud, U. and Perets, H. B. *MNRAS*, 493:698–712, 2020b.

Malamud, U., Grishin, E., and Brouwers, M. *MNRAS*, 501:3806–3824, 2021.

Maldonado, R. F., Villaver, E., Mustill, A. J., Chàvez, M., and Bertone, E. *MNRAS*, 497: 4091–4106, 2020a.

Maldonado, R. F., Villaver, E., Mustill, A. J., Chàvez, M., and Bertone, E. *MNRAS*, 489: 1854–1869, 2020b.

Maldonado, R. F., Villaver, E., Mustill, A. J., Chàvez, M., and Bertone, E. *MNRAS Lett.*, page slaa193, 2020c.

Malhotra, R. *AJ*, 110:420, 1995.

Mann, R. K., Jewitt, D., and Lacerda, D. *AJ*, 134:1133–1144, 2007.

Manser, C. J., Gänsicke, B. T., Marsh, T. R., Veras, D., Koester, D., Breedt, E., Pala, A. F., Parsons, S. G., and Southworth, J. *MNRAS*, 455:4467–4478, 2016.

Manser, C. J., Gänsicke, B. T., Eggl, S., Hollands, M., Izquierdo, P., Koester, D., Landstreet, J. D., Lyra, W., Marsh, T. R., Meru, F., et al. *Science*, 364(6435):66–69, 2019.

Manser, C. J., Gänsicke, B. T., Gentile Fusillo, N. P., Ashley, R., Breedt, E., Hollands, M., Izquierdo, P., and Pelisoli, I. *MNRAS*, 493:2127–2139, 2020.

Marchis, F., Durech, J., Castillo-Rogez, J., Vachier, F., Cuk, M., Berthier, J., Wong, M. H., Kalas, P., Duchene, G., van Dam, M. A., Hamanowa, H., and Viikinkoski, M. *ApJL*, 783: L37, 2014.

Margot, J. L., Nolan, M. C., Benner, L. A. M., Ostro, S. J., Jurgens, R. F., Giorgini, J. D., Slade, M. A., and Campbell, D. B. *Science*, 296:1445–1448, 2002.

Martin, R. G., Livio, M., Smallwood, J. L., and Chen, C. *MNRAS*, 494:L17–L21, 2020.

Mayor, M. and Queloz, D. *Nature*, 378:355–359, 1995.

McCleery, J., Tremblay, P.-E., Gentile Fusillo, N. P., Hollands, M. A., Gänsicke, B. T., Izquierdo, P., Tooner, S., Cunningham, T., and Rebassa-Mansergas, A. *MNRAS*, 499: 1890–1908, 2020.

McDonald, C. H. and Veras, D. *MNRAS*, 506:4031–4047, 2021.

McDonald, C. H. and Veras, D. *MNRAS*, 520:4009–4022, 2023.

Meech, K. J., Weryk, R., Micheli, M., Kleyna, J. T., Hainaut, O. R., Jedicke, R., Wainscoat, R. J., Chambers, K. C., Keane, J. V., Petric, A., Denneau, L., Magnier, E., Berger, T., Huber, M. E., Flewelling, H., Waters, C., Schunova-Lilly, E., and Chastel, S. *Nature*, 552: 378–381, 2017.

Melis, C., Klein, B., Doyle, A. E., Weinberger, A., Zuckerman, B., and Dufour, P. *ApJ*, 905: 56, 2020.

Merline, W. J., Weidenschilling, S. J., Durda, D. D., Margot, J. L., Pravec, P., and Storrs, A. D. Asteroids Do Have Satellites. In *Asteroids III*, pages 289–312. Univ. of Arizona Press, 2002.

Metzger, B. D., Rafikov, R. R., and Bochkarev, K. V. *MNRAS*, 423:505–528, 2012.

Meyer, A. J. and Scheeres, D. J. *Icarus*, 367:114554, 2021.

Michaud, G., Montmerle, T., N., C. A., Magee, J., N. H., Hodson, S. W., and Martel, A. *ApJ*, 234:206–216, 1979.

Mordasini, C. Planetary Population Synthesis. In Deeg, H. J. and Belmonte, J. A., editors, *Handbook of Exoplanets*, page 143, 2018.

Moro-Martín, A. *ApJ*, 866:131, 2018.

Moro-Martín, A. *AJ*, 157:86, 2019.

Moro-Martín, a., Marshall, J. P., Kennedy, G., Sibthorpe, B., Matthews, B. C., Eiroa, C., Wyatt, M. C., Lestrade, J. F., Maldonado, J., Rodriguez, D., Greaves, J. S., Montesinos, B., Mora, A., Booth, M., Duchêne, G., Wilner, D., and Horner, J. *ApJ*, 801:143, 2015.

Muñoz, D. J. and Petrovich, C. *ApJ*, 904:L3, 2020.

Murray, C. D. and Dermott, S. F. *Solar System Dynamics*. Cambridge University Press, 1999.

Murray, N., Hansen, B., Holman, N., and Tremaine, S. *Science*, 279:69, 1998.

Mustill, A. J. and Villaver, E. *ApJ*, 761(2), 2012.

Mustill, A. J. and Wyatt, M. C. *MNRAS*, 413:554–572, 2011.

Mustill, A. J., Veras, D., and Villaver, E. *MNRAS*, 437:1404–1419, 2014.

Mustill, A. J., Davies, M. B., and Johansen, A. *ApJ*, 808:14, 2015.

Mustill, A. J., Villaver, E., Veras, D., Gänsicke, B. T., and Bonsor, A. *MNRAS*, 476: 3939–3955, 2018.

Naoz, S. *Annu. Rev. Astron. Astropys.*, 54:441–489, 2016.

Naoz, S., Farr, W. M., Lithwick, Y., Rasio, F. A., and Tessandier, J. *Nature*, 473:187–189, 2011.

Naoz, S., Farr, W. M., and Rasio, F. A. *ApJL*, 754:L36, 2012.

Nauenberg, M. *ApJ*, 175:417, 1972.

Nesvorný, D. and Vokrouhlicky, D. *Icarus*, 331:49–61, 2019.

Noll, K. S., Grundy, W. M., Chiang, E. I., Margot, J. L., and Kern, S. D. Binaries in the Kuiper Belt. In Barucci, M. A., Boehnhardt, H., Cruikshank, D. P., Morbidelli, A., and Dotson, R., editors, *The Solar System Beyond Neptune*, page 345. University of Arizona Press, 2008.

Noll, K. S., Brown, M. E., Weaver, H. A., Grundy, W. M., Porter, S. B., Buie, M. W., Levison, H. F., Olkin, C., Spencer, J. R., Marchi, S., and Statler, T. S. *Planet. Sci. J.*, 1: 44, 2020.

O'Brien, M. W., Tremblay, P. E., Gentile Fusillo, N. P., Hollands, M. A., Gänsicke, B. T., Koester, D., Pelisoli, I., Cukanovaite, E., Cunningham, T., Doyle, A. E., Elms, A., Farihi, J., Hermes, J. J., Holberg, J., Jordan, S., Klein, B. L., Kleinman, S. J., Manser, C. J., De Martino, D., Marsh, T. R., McCleery, J., Melis, C., Nitta, A., Parsons, S. G., Raddi, R., Rebassa-Mansergas, A., Schreiber, M. R., Silvotti, R., Steeghs, D., Toloza, O., Toonen, S., Torres, S., Weinberger, A. J., and Zuckerman, B. *MNRAS*, 518:3055–3073, 2023.

O'Connor, C. E. and Lai, D. *MNRAS*, 498:4005–4020, 2020.

O'Connor, C. E., Liu, B., and Lai, D. *MNRAS*, 501:507–514, 2021.

O'Connor, C. E., Teyssandier, J., and Lai, D. *MNRAS*, 513:4178–4195, 2022.

Oort, J. H. *Bull. Astron. Inst. Netherlands*, 11:91–110, 1950.

Paquette, C., Pelletier, C., Fontaine, G., and Michaud, G. *ApJS*, 61:177, 1986a.

Paquette, C., Pelletier, C., Fontaine, G., and Michaud, G. *ApJS*, 61:197–217, 1986b.

Parker, A. H. and Kavelaars, J. J. *ApJL*, 722:L204–208, 2010.

Parriott, J. and Alcock, C. *ApJ*, 501:357–366, 1998.

Peña, J., Fuentes, C., Förster, F., Martínez-Palomera, J., Cabrera-Vives, G., Maureira, J. C., Huijse, P., Estévez, P. A., Galbany, L., and González-Gaitán, S. *AJ*, 159(4):148, 2020.

Pelletier, C., Fontaine, G., Wesemael, F., Michaud, G., and Wegner, G. *ApJ*, 307:242, 1986.

Penny, M. T., Gaudi, B. S., Kerins, E., Rattenbury, N. J., Mao, S., Robin, A. C., and Calchi Novati, S. *ApJS*, 241:3, 2019.

Perryman, M., Hartman, J., Bakos, G. A., and Lindergen, L. *ApJ*, 797:14, 2014.

Petigura, E. A., Marcy, G. W., Winn, J. N., Weiss, L. N., Fulton, B. J., Howard, A. W., Sinukoff, E., Isaacson, H., Morton, T. D., and Johnson, J. A. *AJ*, 155:89, 2018.

Petrovich, C. *ApJ*, 805:75, 2015.

Pichierri, G., Morbidelli, A., and Lai, D. *A&A*, 605:A23, 2017.

Pohl, L. and Britt, D. T. *Meteoritics Planet. Sci.*, 55:962–987, 2020.

Polishook, D., Moskovitz, N., Binzel, R. P., Burt, B., DeMeo, F. E., Hinkle, M. L., Lockhart, M., Mommert, M., Person, M., Thirouin, A., Thomas, C. A., Trilling, D., Willman, M., and Aharonson, O. *Icarus*, pages 243–254, 2016.

Pollacco, D. L., Skillen, I., Collier Cameron, A., Christian, D. J., Hellier, C., Irwin, J., Lister, T. A., Street, R. A., West, R. G., Anderson, D. R., Clarckson, W. I., Deeg, H., Enoch, B., Evans, A., Fitzsimmons, A., Haswell, C. A., Hodgkin, S., Horne, K., Kane, S. R., Keenan, F. P., Maxted, P. F. L., Norton, A. J., Osborne, J., Parley, N. R., Ryans, R. S. I., Smalley, B., Wheatley, P. J., and Wilson, D. M. *PASP*, 118:1407–1418, 2006.

Pollack, J. B., Hubickyj, O., Bodenheimer, P., Lissauer, J. J., Podalak, M., and Greenzweig, Y. *Icarus*, 124:62–85, 1996.

Poynting, J. H. *Philos. Trans. R. Soc. London Series A*, 202:525–552, 1904.

Pravec, P., Scheirich, P., Kušnirák, P., Šarounová, L., Mottola, S., Hahn, G., Brown, P., Esquerdo, G., Kaiser, N., Krzeminski, Z., Pray, D. P., Warner, B. D., Harris, A. W., Nolan, M. C., Howell, E. S., Benner, L. A. M., Margot, J. L., Galád, A., Holliday, W., Hicks, M. D., Krugly, Y. N., Tholen, D., Whiteley, R., Marchis, F., DeGraff, D. R., Grauer, A., Larson, S., Velichko, F. P., Cooney, W. R., Stephens, R., Zhu, J., Kirsch, K., Dyvig, R., Snyder, L., Reddy, V., Moore, S., Gajdoš, Š., Világi, J., Masi, G., Higgins, D., Funkhouser, G., Knight, B., Slivan, S., Behrend, R., Grenon, M., Burki, G., Roy, R., Demeautis, C., Matter, D., Waelchli, N., Revaz, Y., Klotz, A., Rieugné, M., Thierry, P., Cotrez, V., Brunetto, L., and Kober, G. *Icarus*, 181:63–93, 2006.

Prettyman, T. H., Yamashita, N., Ammannito, E., Ehlmann, B. L., McSween, H. Y., Mittlefehldt, D. W., Marchi, S., Schörghofer, N., Toplis, M. J., Li, J. Y., Pieters, C. M., Castillo-Rogez, J. C., Raymond, C. A., and Russell, C. T. *Icarus*, 318:42–55, 2019.

Prialnik, D. *An Introduction to the Theory of Stellar Structure and Evolution*. Cambridge University Press, 2000.

Quillen, A. C. *MNRAS*, 365:1367–1382, 2006.

Raddi, R., Gänsicke, B. T., Koester, D., Farihi, J., Hermes, J. J., Scaringi, S., Breedt, E., and Girven, J. *MNRAS*, 450:2083–2093, 2015.

Raddi, R., Catalán, S., Gänsicke, B. T., Hermes, J. J., Napiwotzki, R., Koester, D., Tremblay, P. E., Barensten, G., Farnhill, H. J., Mohr-Smith, M., E., D. J., Groot, P. J., Guzman-Ramirez, L., Parker, Q. A., Steeghs, D., and Zijlstra, A. *MNRAS*, 457:1988–2004, 2016.

Rafikov, R. R. *ApJ*, 621:L69–L72, 2005.

Rafikov, R. R. *ApJ*, 648:666–682, 2006.

Rafikov, R. R. *ApJL*, 732:L3, 2011a.

Rafikov, R. R. *MNRAS Lett.*, 416:L55–L59, 2011b.

Rafikov, R. R. *ApJ*, 861(1), 2018.

Rafikov, R. R. and Garmilla, J. A. *ApJ*, 760:123, 2012.

Rappaport, S., Gary, B. L., Kaye, T., Vanderburg, A., Croll, B., Benni, P., and Foote, J. *MNRAS*, 458:3904–3917, 2016.

Rasio, F. A. and Ford, E. B. *Science*, 274:954–956, 1996.

Rebassa-Mansergas, A., Solano, E., Xu, S., Rodrigo, C., Jiménez-Esteban, F. M., and Torres, S. *MNRAS*, 489:3990–4000, 2019.

Reddy, V., Sanchez, J. A., Bottke, W. F., Thirouin, A., Rivera-Valentin, E. G., Kelley, M. S., Ryan, W., Cloutis, E. A., Tegler, S. C., Ryan, E. V., Taylor, P. A., Richardson, J. E., Moskovitz, N., and Le Corre, L. *AJ*, 152:162, 2016.

Rein, H. and Liu, S. F. *A&A*, 537:A128, 2012.

Rein, H. and Spiegel, D. S. *MNRAS*, 446:1424–1437, 2015.

Rein, H. and Tamayo, D. *MNRAS*, 452:376–388, 2015.

Rein, H. and Tamayo, D. *MNRAS*, 467:2377–2383, 2017.

Rein, H., Hernandez, D. M., Tamayo, D., Brown, G., Eckels, E., Holmes, E., Lau, M., Leblanc, R., and Silburt, A. *MNRAS*, 485:5490–5497, 2019.

Ricker, G. R., Winn, J. N., Vanderspek, R., Latham, D. W., Bakos, G. Á., Bean, J. L., Berta-Thompson, Z. K., Brown, T. M., Buchhave, L., Butler, N. R., Butler, R. P., Chaplin, W. J., Charbonneau, D., Christensen-Dalsgaard, J., Clampin, M., Deming, D., Doty, J., De Lee, N., Dressing, C., Dunham, E. W., Endl, M., Fressin, F., Ge, J., Henning, T., Holman, M. J., Howard, A. W., Ida, S., Jenkins, J. M., Jernigan, G., Johnson, J. A., Kaltenegger, L., Kawai, N., Kjeldsen, H., Laughlin, G., Levine, A. M., Lin, D., Lissauer, J. J., MacQueen, P., Marcy, G., McCullough, P. R., Morton, T. D., Narita, N., Paegert, M., Palle, E., Pepe, F., Pepper, J., Quirrenbach, A., Rinehart, S. A., Sasselov, D., Sato, B., Seager, S., Sozzetti, A., Stassun, K. G., Sullivan, P., Szentgyorgyi, A., Torres, G., Udry, S., and Villasenor, J. *J. Astron. Telesc. Instrum. Syst.*, 1:014003, 2015.

Robertson, H. P. *MNRAS*, 97:423, 1937.

Rocchetto, M., Farihi, J., Gänsicke, B. T., and Bergfors, C. *MNRAS*, 449:574–587, 2015.

Romero, A. d., Campos, F., and Kepler, S. O. *MNRAS*, 450:3708–3723, 2015.

Rozner, M., Veras, D., and Perets, H. B. *MNRAS*, 502:5176–5184, 2021.

Rubincam, D. P. *Icarus*, 148:2–11, 2000.

Ryan, E. L., Mizuno, D. R., Shenoy, S. S., Woodward, C. E., Carey, S. J., Noriega-Crespo, A., Kraemer, K. E., and Price, S. D. *A&A*, 578:A42, 2015.

Safronov, V. S. *Evolution of the protoplanetary cloud and formation of the earth and planets*. Keter Publishing House, 1972.

Sanderson, H., Bonsor, A., and Mustill, A. *MNRAS*, 517:5835–5852, 2022.

Sandhaus, P. H., Debes, J. H., Ely, J., Hines, D. C., and Bourque, M. *ApJ*, 823:49, 2016.

Scheeres, D. J. *Icarus*, 188:430–450, 2007.

Schröder, K. P. and Cuntz, M. *ApJL*, 630:L73–L76, 2005.

Schröder, K. P. and Smith, R. C. *MNRAS*, 386:155–163, 2008.

Shakura, N. I. and Sunyaev, R. A. *A&A*, 24:337–355, 1973.

Shannon, A., Jackson, A. P., Veras, D., and Wyatt, M. *MNRAS*, 446:2059–2064, 2015.

Shara, M. M., Hurley, J. R., and Mardling, R. A. *ApJ*, 816:59, 2016.

Sibthorpe, B., Kennedy, G. M., Wyatt, N. C., Lestrade, J. F., Greaves, J. S., Matthews, B. C., and Duchêne, G. *MNRAS*, 475:3046–3064, 2018.

Sigurdsson, S., Richer, H. B., Hansen, B. M., Stairs, I. H., and Thorsett, S. E. *Science*, 301: 193–196, 2003.

Sinclair, A. T. *MNRAS*, 160:169, 1972.

Sion, E. M., Greenstein, J. L., Landstreet, J. D., Liebert, J., Shipman, H. L., and Wegner, G. A. *ApJ*, 269:253–257, 1983.

Smallwood, J. L., Martin, R. G., Livio, M., and Lubow, S. H. *MNRAS*, 480:57–67, 2018.

Smallwood, J. L., Martin, R. G., Livio, M., and Veras, D. *MNRAS*, 504:3375–2286, 2021.

Steckloff, J. K., Johnson, B. C., Bowling, T., Jay Melosh, H., Minton, D., Lisse, C. M., and Battams, K. *Icarus*, 258:430–437, 2015.

Steckloff, J. K., Debes, J., Amy, S., Johnson, B., Adams, E. R., Jacobson, S. A., and Springmann, A. *ApJL*, 913:L31, 2021.

Stephan, A. P., Naoz, S., and Zuckerman, B. *ApJL*, 844:L16, 2017.

Stephan, A. P., Naoz, S., and Gaudi, B. S. *ApJ*, 922:4, 2021.

Stephens, D. C. and Noll, K. S. *AJ*, 131(2):1142–1148, 2006.

Stone, N., Metzger, B. D., and Loeb, A. *MNRAS*, 448:188–206, 2015.

Su, K. Y. L., Rieke, G. H., Stansberry, J. A., Bryden, G., Stapelfeldy, K. R., Trilling, D. E., Muzerolle, J., Beichman, C. A., Moro-Martin, A., Hines, D. C., and Werner, M. W. *ApJ*, 653:675–689, 2006.

Swan, A., Kenyon, S. J., Farihi, J., Dennihy, E., Gänsicke, B. T., Hermes, J. J., Melis, C., and von Hippel, T. *MNRAS*, 506:432–440, 2021.

Tamanini, N. and Danielski, C. *Nature Astron.*, 3:858–866, 2019.

Tamayo, D., Rein, H., Shi, P., and Hernandez, D. M. *MNRAS*, 491:2885–2901, 2020.

Thommes, E. W. and Lissauer, J. J. *ApJ*, 597:566–580, 2003.

Thorsett, S. E., Arzoumanian, Z., and Taylor, J. H. *ApJL*, 412:L33, 1993.

Tittemore, W. C. and Wisdom, J. *Icarus*, 85:394–443, 1990.

Traxler, A., Garaud, P., and Stellmach, S. *ApJL*, 728:L29, 2011.

Tremblay, P.-. E., Cummings, J., Kalirai, J. S., Gänsicke, B. T., Gentile-Fusillo, N., and Raddi, R. *MNRAS*, 461:2100–2114, 2016.

Tremblay, P. E., Ludwig, H. G., Freytag, B., Fontaine, G., Steffen, M., and Brassard, P. *ApJ*, 799:142, 2015.

Tremblay, P. E., Fontaine, G., Gentile Fusillo, N. P., Dunlap, B. H., Gänsicke, B. T., Hollands, M., Hermes, J. J., Marsh, T. R., Cukanovaite, E., and Cunningham, T. *Nature*, 565:202–205, 2019.

Trevascus, D., Price, D. J., Nealon, R., Liptai, D., Manser, C. J., and Veras, D. *MNRAS Lett.*, 505:L21–L25, 2021.

Trujillo, C. A. and Brown, M. E. *ApJ*, 554:L95–L98, 2001.

van Lieshout, R., Kral, Q., Charnoz, S., Wyatt, M. C., and Shannon, A. *MNRAS*, 480(2): 2784–2812, 2018.

van Maanen, A. *PASP*, 29(172):258–259, 1917.

van Maanen, A. *ApJ*, 32:86–88, 1919.

Vanderbosch, Z., Hermes, J. J., Dennihy, E., Dunlap, B. H., Izquierdo, P., Tremblay, P. E., Cho, P. B., Gänsicke, B. T., Bell, K. J., Montgomery, M. H., and Winget, D. E. *ApJ*, 897 (2):171, 2020.

Vanderbosch, Z. P., Rappaport, S., Guidry, J. A., Gary, B. L., Blouin, S., Kaye, T. G., Weinberger, A. J., Melis, C., Klein, B. L., Zuckerman, B., Vanderburg, A., Hermes, J. J., Hegedus, R. J., Burleigh, M. R., Sefako, R., Worters, H. L., and Heintz, T. M. *ApJ*, 917: 41, 2021.

Vanderburg, A. and Rappaport, S. A. Transiting Disintegrating Planetary Debris Around WD 1145+017. In Deeg, H. and Belmonte, J., editors, *Handbook of Exoplanets*. Springer, Cham, 2018.

Vanderburg, A., Johnson, J. A., Rappaport, S., Bieryla, A., Irwin, J., Lewis, J. A., Kipping, D., Brown, W. R., Dufour, P., Ciardi, D. R., Angus, R., Schaefer, L., Latham, D. W., Charbonneau, D., Beichman, C., Eastman, J., McCrady, N., Wittenmyer, R. A., and Wright, J. T. *Nature*, 526(7574):546–549, 2015.

Vanderburg, A., Rappaport, S. A., Xu, S., Crossfield, I. J. M., Becker, J. C., Gary, B., Murgas, F., Blouin, S., Kaye, T. G., Palle, E., Melis, C., Morris, B. M., Kreidberg, L., Gorjian, V., Morley, C. V., Mann, A. W., Parvianen, H., Pearce, L. A., Newton, E. R., and Carrilo, A. *Nature*, 585:363–367, 2020.

Vassiliadis, E. and Wood, P. R. *ApJ*, 413:641, 1993.

Vennes, S., Pelletier, C., Fontaine, G., and Wesemael, F. *ApJ*, 331:876, 1988.

Veras, D. *Celest. Mech. Dyn. Astron.*, 118:315–353, 2014.

Veras, D. *Royal Society Open Science*, 3(2), 2016.

Veras, D. *MNRAS*, 493:4692–4699, 2020.

Veras, D. and Evans, N. W. *MNRAS*, 430:403–415, 2013.

Veras, D. and Fuller, J. *MNRAS*, 489:2941–2953, 2019.

Veras, D. and Fuller, J. *MNRAS*, 492:6059–6066, 2020.

Veras, D. and Gänsicke, B. *MNRAS*, 447:1049–1058, 2015.

Veras, D. and Heng, K. *MNRAS*, 496:2292–2308, 2020.

Veras, D. and Rosengren, A. J. *MNRAS*, 519:6257–6266, 2023.

Veras, D. and Scheeres, D. J. *MNRAS*, 492:2437–2445, 2020.

Veras, D. and Wolszczan, A. *MNRAS*, 488:153–163, 2019.

Veras, D., Crepp, J. R., and Ford, E. B. *ApJ*, 696:1600–1611, 2009.

Veras, D., Wyatt, M. C., Mustill, A. J., Bonsor, A., and Eldridge, J. J. *MNRAS*, 417: 2104–2123, 2011.

Veras, D., Hadjidemetriou, J. D., and Tout, C. A. *MNRAS*, 435:2416–2430, 2013a.

Veras, D., Mustill, A. J., Bonsor, A., and Wyatt, M. C. *MNRAS*, 431:1686–1708, 2013b.

Veras, D., Jacobson, A., S, and Gänsicke, T., B. *MNRAS*, 445:2794 – 2799, 2014a.

Veras, D., Leinhardt, Z. M., Bonsor, A., and Gänsicke, B. T. *MNRAS*, 445:2244–2255, 2014b.

Veras, D., Shannon, A., and Gänsicke, B. T. *MNRAS*, 445:4175–4185, 2014c.

Veras, D., Eggl, S., and Gänsicke, B. T. *MNRAS*, 452:1945–1957, 2015a.

Veras, D., Leinhardt, Z. M., Eggl, S., and Gänsicke, B. T. *MNRAS*, 451:3453–3459, 2015b.

Veras, D., Mustill, A. J., Gänsicke, B. T., Redfield, S., Georgakarakos, N., Bowler, A. B., and Lloyd, M. J. S. *MNRAS*, 458:3942–3967, 2016.

Veras, D., Carter, P. J., Leinhardt, Z. M., and Gänsicke, B. T. *MNRAS*, 465:1008–1022, 2017.

Veras, D., Efroimsky, M., Makarov, V. V., Boué, G., Wolthoff, V., Reffert, S., Quirrenbach, A., Tremblay, P. E., and Gänsicke, B. T. *MNRAS*, 486:3831–3848, 2019a.

Veras, D., Higuchi, A., and Ida, S. *MNRAS*, 485(1):708–724, 2019b.

Veras, D., McDonald, C. H., and Makarov, V. *MNRAS*, 492, 2020a.

Veras, D., Reichert, K., Flammini Dotti, F., Cai, M. X., Mustill, A. J., Shannon, A., McDonald, C. H., Portegies Zwart, S., Kouwenhoven, M. B. N., and Spurzem, R. *MNRAS*, 472:5062–5078, 2020b.

Veras, D., Tremblay, P.-E., Hermes, J. J., McDonald, C. H., Kennedy, G. M., Meru, F., and Gänsicke, B. T. *MNRAS*, 493, 2020c.

Veras, D., Birader, Y., and Zaman, U. *MNRAS*, 510:3379–3388, 2022.

Veras, D., Georgakarakos, N., and Dobbs-Dixon, I. *MNRAS*, 518:4537–4550, 2023.

Verbunt, F. and Rappaport, S. *ApJ*, 332:193–198, 1988.

Villaver, E., Livio, M., Mustill, A. J., and Siess, L. *ApJ*, 794:3, 2014.

Voyatzis, G., Hadjidemetriou, J. D., Veras, D., and Varvoglis, H. *MNRAS*, 430:3383–3396, 2013.

Walsh, K. J., Morbidelli, A., Raymond, S. N., O'Brien, D. P., and Madell, A. M. *Nature*, 475:206–209, 2011.

Wang, L., Zhang, X., Wang, J., Zhang, Z. X., Fang, T., Gu, W. M., Guo, J., and Jiany, X. *ApJ*, 944:23, 2023.

Wang, X. and Malhotra, R. *AJ*, 154:20, 2017.

Warner, B., Harris, P., and Pravec, P. *Icarus*, 202:134–146, 2009.

Weidenschilling, S. J. and Marzari, F. *Nature*, 384:619–621, 1996.

Weissman, P. R. and Levison, H. F. *ApJ*, 488:L133–L136, 1997.

Wilson, R. F., Barclay, T., Powell, B. P., Schlieder, J., Hedges, C., Montet, B. T., Quintana, E., McDonald, I., Penny, M. T., Espinoza, N., and Kerins, E. *Submitted to AAS, arXiv:2305.16204*, 2023.

Wisdom, J. *AJ*, 87:577–593, 1982.

Wisdom, J. *Icarus*, 63:272–289, 1985.

Wisdom, J. *AJ*, 94:1350, 1987a.

Wisdom, J. *Icarus*, 72:241–275, 1987b.

Wisdom, J. and Holman, M. *AJ*, 102:1528–1538, 1991.

Wolszczan, A. *Science*, 264(5158):538–542, 1994.

Wolszczan, A. and Frail, D. A. *Nature*, 355:145–147, 1992.

Wood, J. *The Dynamics of Small Solar System Bodies*. Springer Cham, 2019.

Wood, M. A. *ApJ*, 386:537, 1992.

Wu, Y. and Lithwick, Y. *ApJ*, 735:109, 2011.

Wyatt, M., Farihi, J., Pringle, J., and Bonsor, A. *MNRAS*, 439:3371–3391, 2014.

Wyatt, M. C., Bonsor, A., Jackson, A. P., Marino, S., and Shannon, A. *MNRAS*, 464: 3385–3407, 2017.

Xu, S. and Bonsor, A. *Elements*, 17:241, 2021.

Xu, S. and Jura, M. *ApJ*, 745:88, 2012.

Xu, S., Ertel, S., Wahhaj, Z., Milli, J., Scicluna, P., and Bertrang, G. H. M. *A&A*, 579:L8, 2015.

Xu, S., Zuckerman, B., Dufour, P., Young, E. D., Klein, B., and Jura, M. *ApJ*, 836:L7, 2017.

Xu, S., Dufour, P., Klein, B., Melis, C., Monson, N. N., Zuckerman, B., Young, E. D., and Jura, M. A. *AJ*, 158:242, 2019.

Yelverton, B., Kennedy, G. M., and Su, K. Y. L. *MNRAS*, 495:1943–1957, 2020.

Yoshida, F. and Nakamura, T. *Planet. Space Sci.*, 55:1113–1125, 2007.

Yu, Q. and Tremaine, S. *AJ*, 121:1736–1740, 2001.

Zahn, J. P. *A&A*, 220(1-2):112–116, 1989.

Zhang, Y. and Lin, D. N. C. *Nat. Astron.*, 2020.

Zhao, J. K., Oswalt, T. D., Willson, L. A., Wang, Q., and Zhao, G. *ApJ*, 746:144, 2012.

Zhou, G., Kedziora-Chudczer, L., Bailey, J., Marshall, J. P., Bayliss, D. D. R., Stockdale, C., Nelson, P., Tan, T. G., Rodriguez, J. E., Tinney, C. G., Dragomir, D., Colon, K., Shporer, A., Bento, J., Sefako, R., Horne, K., and Cochran, W. *MNRAS*, 463:4422–4432, 2016.

Zhou, G., Huang, C. X., Bakos, G. A., Hartman, J. D., Latham, D. W., Quinn, S. N., Collins, K. A., Winn, K. N., Wong, I., Kovács, G., Csubry, Z., Bhatti, W., Penev, A., K. Bieryla, Esquerdo, G. A., Berlind, P., Calkins, M. L., de Val-Borro, M., Noyes, R. W., Lázár, J., Papp, I., Sári, P., Kovács, T., Buchhave, L. A., Szklenar, T., Béky, B., Johnson, M. C., Cochran, W. D., Kniazev, A. Y., Stassun, K. G., Fulton, B. J., Shporer, A., Espinoza, N., Bayliss, D., Everett, M., Howell, S. B., Hellier, C., Anderson, D. R., Collier Cameron, A., West, R. G., Brown, D. J. A., Schanche, N., Barkoaui, K., Pozuelos, F., Gillon, M., Jehin, E., Benkhaldoun, Z., Daassou, A., Ricker, G., Vanderspek, r., Seager, S., Jenkins, J. M., Lissauer, J. J., Armstrong, J. D., Collins, K. I., Gan, T., Hart, R., Horne, K., Kielkopf, J. G., Nielsen, L. D., Nishiumi, T., Narita, N., Palle, E., Relles, H. M., Sefako, R., Tan, T. G., Davies, M., Goeke, R. F., Guerrero, N., Haworth, K., and Villanueva, S. *AJ*, 158: 141, 2019.

Zotos, E. E., Veras, D., Saeed, T., and Darriba, L. A. *MNRAS*, 497:5171–5181, 2020.

Zuckerman, B. and Becklin, E. E. *Nature*, 330:138–140, 1987.

Zuckerman, B., Melis, C., Klein, B., Koester, D., and Jura, M. *ApJ*, 722(1), 2010.

Zuckerman, B., Koester, D., Dufour, P., Melis, C., Klein, B., and Jura, M. *ApJ*, 739:101, 2011.